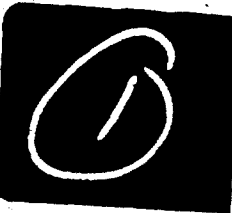
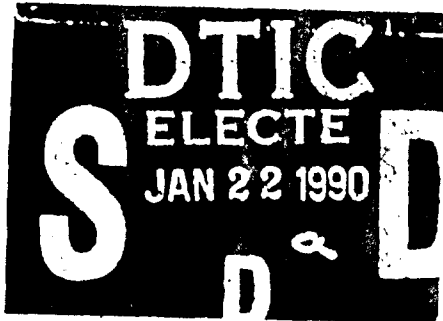


AD-A217 205

DTIC FILE COPY



VOLUME 1
EXCITATION AND VIBRATION
OF BLUFF BODIES IN CROSS FLOW



DISTRIBUTION STATEMENT A
Approved for public release
Distribution Unlimited

SYMPOSIUM on FLOW-INDUCED VIBRATIONS

VOLUME 1 EXCITATION AND VIBRATION OF BLUFF BODIES IN CROSS FLOW

Presented at

THE ASME WINTER ANNUAL MEETING
NEW ORLEANS, LOUISIANA
DECEMBER 9-14, 1984

Symposium co-sponsored by

Applied Mechanics, Fluids Engineering, Heat Transfer,
Noise Control and Acoustics, Nuclear Engineering,
and Pressure Vessels and Piping Divisions



Sessions in this Volume co-sponsored by

FLUIDS ENGINEERING, APPLIED MECHANICS, AND
NOISE CONTROL AND ACOUSTICS DIVISIONS

Edited by

M. P. PAIDOUSSIS (Principal Editor)
McGill University
Montreal, Quebec, Canada

O.M. GRIFFIN
Naval Research Laboratory
Washington, D.C.

Mr. SEVIK
David Taylor Naval Ship R & D Center
Bethesda, Maryland

Accession For	
NTIS	CRA&I
DTIC	TAB
Unannounced	
Justification	
31 36.00	
By 30.	
Distribution /	
Availability Codes	
Dist	Asst. Eng./Or Special
A-1 21	

THE AMERICAN SOCIETY OF MECHANICAL ENGINEERS

United Engineering Center 225 East 47th Street New York, N.Y. 10017

900118030

Library of Congress Catalog Card Number 84-72467

Statement from By-Laws: The Society shall not be responsible for statements or opinions advanced in papers . . . or printed in its publications (B7.1.3)

Any paper from this volume may be reproduced without written permission as long as the authors and publisher are acknowledged.

Copyright ©1984 by
THE AMERICAN SOCIETY OF MECHANICAL ENGINEERS
All Rights Reserved
Printed in U.S.A.

PREFACE

The 1984 ASME Symposium on Flow-Induced Vibration is a unique event in the annals of technical meetings organized by ASME. Apart from promising to be one of the most important symposia anywhere on this topic in recent memory (only time will tell exactly how important), it is the first time that such a large symposium on the subject has been organized by ASME. Furthermore, it is the first time that no less than six Divisions of the ASME have cooperated in co-sponsoring a symposium on any given subject, which surely bespeaks of the importance of the subject matter of this particular Symposium. The participating Divisions are:

Applied Mechanics, Fluids Engineering, Heat Transfer, Noise Control and Acoustics, Nuclear Engineering, and Pressure Vessels and Piping.

I should like to thank them all, for without their support this Symposium would not have been the success that it is promising to be.

The Proceedings of the Symposium are published in six bound volumes, containing sixty-eight papers in all, as follows:

Volume 1 Excitation and Vibration of Bluff Bodies in Cross Flow

Volume 2 Vibration of Arrays of Cylinders in Cross Flow

Volume 3 Vibration in Heat Exchangers

Volume 4 Vibration Induced by Axial and Annular Flows

Volume 5 Turbulence-Induced Noise and Vibration of Rigid and Compliant Surfaces

Volume 6 Computational Aspects of Flow-Induced Vibration

The organization of a Symposium of this size, with world-wide participation (from 12 countries), has been both a challenging and rewarding experience. It entailed a great deal of work by many people: the session developers, the reviewers, ASME Headquarters' staff, the 1984 WAM Organizers and, of course, the authors. Of the many people involved, too numerous to mention by name here, I am specially indebted to the session developers and co-editors (O. M. Griffin, M. Sevik, M. K. Au-Yang, S. -S. Chen, J. M. Chenoweth, M. D. Bernstein and A. J. Kalinowski), and would like to single out two: Dr. M. K. Au-Yang and Dr. S. -S. Chen, whom I would like to thank for their unswerving support from the very beginning, when the possibility of a "multidivisional symposium" looked like a pie in the sky! I would also like to thank my secretary, Ruth Gray, for efficiently handling the enormous amount of paperwork involved in several passes of sixty-eight-plus papers across my desk.

Michael P. Paidoussis
Principal Symposium Coordinator
and Principal Editor

FOREWORD

The dynamic response of a solitary bluff body in crossflow, the forces exerted on the body and the fluid mechanics of the flow around it have been studied very extensively and for a very long time, starting in earnest with Strouhal's work in 1878. Scientific fascination with the subject goes back to the time of Leonardo da Vinci, and even to the first mention in antiquity of the wind-induced vibration and sound of the Aeolian harp. However, despite the many advances and insights gained through the efforts of many researchers over the years, and despite the numerous conferences and symposia either largely or wholly devoted to flow-induced vibrations, there still remain questions to be answered and new facets to be explored. Thus researchers remain both interested and busy on this subject.

Not only is there interest on the dynamics of bluff bodies in cross-flow as a fundamental problem in fluid mechanics and fluid-elasticity, but there is also a great deal of interest from the viewpoint of engineering practice. Indeed, the scope of practical investigations is increasing as the subject becomes important in newer technological fields, while still retaining its importance in the older, traditional areas. Flow-induced vibrations of bluff bodies in cross-flow currently is important in wind engineering and structural design, naval and offshore technology, pressure vessel and piping design, and nuclear engineering, to name but a few. Each problem area brings its own set of peculiarities and special problems to the subject. For example, the behaviour of bluff bodies is different in dense fluids, as opposed to light fluids, and in two-phase flows, it is different in various ranges of the Reynolds number; it depends on the scale and level of the turbulence intensity; it is different when the separation points remain fixed during vibration (as with prismatic bluff bodies); it depends on whether body motions are large or small; and so on.

The fourteen papers in this volume give some idea of the wide spectrum of the various aspects and applications of flow-induced vibration. Some papers deal with the response of cylinders to vortex shedding; others with the turbulent buffeting of cylindrical and quasi-cylindrical bodies in wind or water currents, and with the suppression of the wind-induced motions; with the effects of high-turbulence cross-flow-induced forces and vibration; and with the presence of entrained air in liquid cross flows, in industrial environments.

On behalf of the Organizing Committee of this Symposium, we thank the authors for their cooperation in submitting papers of high quality on the topic of this Volume 1 of the Proceedings, *Excitation and Vibration of Bluff Bodies in Cross-Flow*. And we commend them for their willingness to participate and to share their experience with others who are interested in flow-induced vibrations. We also would like to thank the many reviewers for their thoughtful comments, which have contributed to the overall quality of the papers finally accepted for inclusion in the Symposium and its Proceedings.

M. P. Paidoussis

O. M. Griffin

M. Sevik

CONTENTS

Vibrations and Flow-Induced Forces Caused by Vortex Shedding, <i>O. M. Griffin</i>	1
Fluid Forces on a Rigid Cylinder in Turbulent Crossflow <i>T. M. Mulcahy</i>	15
Buffeting of Isolated Tubes in Cross Flow <i>S. D. Savkar</i>	29
Influence of Stream Turbulence Intensity and Eddy Size of the Fluctuating Pressure Forces on a Single Tube <i>C. Norberg and B. Sundén</i>	43
Unsteady Forces on a Cylinder in Cross Flow at Subcritical Reynolds Numbers <i>M. J. Moeller and P. Leehey</i>	57
Flow-Induced Oscillations of Cylinders in the Streamwise Direction <i>D. H. Turnbull and I. G. Currie</i>	73
Experiments on Flow-Induced Vibration of a Square-Section Cylinder <i>P. W. Bearman, I. S. Gartshore, D. J. Maull, and G. V. Parkinson</i>	85
Air-Bubble Effects on Vortex-Induced Vibrations of a Circular Cylinder <i>F. Hara</i>	103
Flow-Induced Vibrations of Mixing Vessel Internals <i>R. King</i>	115
Wind Effects on High Cooling Towers <i>J. F. Sageau and M. Robert</i>	129
Dynamical Behavior of Suspended Pipe in the Sea <i>T. Kawashima and T. Shimogo</i>	145
Vibration of Turbomachine-Blade Due to Viscous Wakes <i>K. Ishihara</i>	159
Nutation Dampers and Suppression of Wind Induced Instabilities <i>V. J. Modi and F. Welt</i>	173
Transient Loading of Pile-Shell-Type Supported Offshore Structures <i>V. A. Dzhupanov, D. D. Karagozova and V. M. Vassilev</i>	189

VIBRATIONS AND FLOW-INDUCED FORCES CAUSED BY VORTEX SHEDDING

O. M. Griffin
Marine Technology Division
Naval Research Laboratory
Washington, D. C.

ABSTRACT

This paper discusses available data for vortex-induced lift, drag, and displacement amplitude from numerous experiments which have been conducted over the past several years. Recent measurements of the component of the overall lift force which drives the oscillations are compared with previously-reported data. There is good agreement which further confirms the complex behavior of the lift force as a circular cylinder undergoes vortex-induced vibrations. It is clear from the results that there is a limiting amplitude of vibration as the exciting force (and force coefficient C_{LE}) first increases from zero to a maximum ($C_{LE} = 0.5$ to 0.6) and then decreases again to zero as the limiting vibration amplitude (± 1 or more diameters) is approached. Recent measurements of the mean in-line drag forces on freely-vibrating cylinders have shown that the drag coefficient is amplified by as much as 250 percent in water at large vibration amplitudes near the limiting value. Drag force measurements with cylinders which were forced to vibrate under similar conditions yielded comparable results. For both the lift and drag measurements the Reynolds numbers were in the range $Re = 10^3$ to 10^4 and slightly higher. Thus the results are suitable in many practical applications for structures both in air and in water.

NOMENCLATURE

C_D , C_{D0}	Steady drag coefficient on a vibrating (stationary) cylinder or cable.
C_L	Lift coefficient; see Eq. (6).
C_{LE}	Excitation lift force coefficient; see Eq. (6).
D	Body diameter (m or ft).
f_n	Natural frequency in the fluid medium (Hz).
f_s	Strouhal frequency (Hz).
I_t	Modal scaling factor; see Eq. (4).
k	Reduced damping; see Eq. (1).
L	Body length (m or ft).
m	Cable physical mass per unit length (kg/m or lb _m /ft).
m'	Cable virtual mass (physical plus added mass) per unit length (kg/m or lb _m /ft).
P	Power transmission to the cylinder, $\bar{P}/\rho_f^3 D^4$.
St	Strouhal number, $f_s D/V$.
V	Incident flow velocity (m/s or ft/sec).
V_r	Reduced velocity, $V/f_n D$.
w	Response parameter, $(1 + 2 \bar{Y}/D) (V/St)^{-1}$; see Eq. (10).
\bar{Y}	Cross flow displacement (m or ft).
\bar{Y}	Cross flow displacement amplitude (m or ft).
Y	Normalized displacement amplitude, \bar{Y}/D .
$Y_{EFF,MAX}$	Normalized displacement amplitude; see Eq. (4).
z	Coordinate measurement along the cylinder or cable (m or ft).

δ	Log decrement of structural damping; see Eq. (1).
γ_i	Normalizing factor; see Eq. (4).
ϕ	Phase angle (deg. or rad); see Eq. (6).
μ	Mass ratio, $\rho D^2/8\pi^2 S t^2 m$; see Eq. (2).
ν	Kinematic fluid viscosity (m^2/sec or ft^2/sec).
ρ	Fluid density (kg/m^3 or lb_m/ft^3).
$\psi_i(z)$	Mode shape for i th flexible beam mode; see Eq. (3)
ζ_s	Structural damping ratio; see Eq. (2).

INTRODUCTION

It is often found that bluff, or unstreamlined, structures display undesirable oscillatory instabilities arising from their motion relative to a surrounding fluid. A common mechanism for resonant, flow-excited oscillations is the organized and periodic shedding of vortices as the flow separates alternately from opposite sides of a long, bluff body. These vortices result in steady and unsteady drag forces in line with the flow and unsteady lift or side forces perpendicular to the flow direction. If the structure is flexible and lightly damped internally, then resonant oscillations can be excited normal or parallel to the incident flow direction. For the more common cross flow oscillations, the body and the wake usually oscillate in unison at a frequency near one of the characteristic frequencies of the structure. The shedding meanwhile is shifted away from the natural, or Strouhal, frequency at which pairs of vortices would be shed if the structure were restrained from oscillating. This phenomenon is known as "lock-on" or "wake capture."

The vortex-excited oscillations of marine cables, commonly termed *strumming*, result in increased steady and unsteady hydrodynamic forces, and amplified acoustic flow noise. They sometimes lead to early fatigue, structural damage and to failure. Flow-excited oscillations very often are a critical factor in the design of marine cable arrays, riser systems, and offshore platforms. Flow-induced vibrations also cause serious problems in nuclear reactors and reactor components. In air, chimney stacks, high-tension power lines and bus-bars commonly vibrate due to vortex shedding.

The dynamic analysis of structures and cable systems both in air and in water has become an important consideration in the prediction of stress distributions and fatigue lives. Reliable experimental data are now reasonably well in hand for the dynamic response characteristics and flow-induced forces on a model scale. Based upon these experiments, semi-empirical prediction models have been developed and favorably compared with field test data.

BASIC CHARACTER OF VORTEX SHEDDING

The frequency f_s of the vortex shedding from a circular cylinder is related to the other main flow parameters (D , the diameter of the cylinder; V , the flow velocity) through the nondimensional Strouhal number defined as

$$St = \frac{f_s D}{V}.$$

The value of the Strouhal number varies somewhat in different regimes of the Reynolds number and with the shape of the cylinder (circular, D -section, triangular, etc). For the range of the Reynolds number where the Strouhal number remains constant the relation between the shedding frequency and the velocity is linear for a given cylinder, i.e.

$$f_s = KV,$$

where $K = St/D$. If a cylinder immersed in a flowing fluid is free to oscillate in the cross-flow direction, then the latter relation does not hold in the vicinity of the natural frequency of the cylinder. This resonance phenomenon—called "lock-on" or "wake capture"—is discussed in this paper.

If the Reynolds number is lower than about 10^5 , then the vortex shedding is predominantly periodic and the value of the Strouhal number can be assumed to be about 0.2 for a circular cylinder or cable. Measurements of the frequencies, displacement amplitudes and forces which result from vortex-excited oscillations have been obtained by many investigators from experiments both in air and in water. Fairly detailed reviews of the basic aspects of the problem of vortex-excited oscillations in general has been made recently by Sarpkaya [1] and Bearman [2]. King [3], and Griffin and Ramberg [4,5] have discussed the subject in the context of ocean engineering applications. Simmons and Cleary [6] Rawlins [7], and Adami and Batch [8] recently have discussed problems caused by vortex shedding from structures in air. Paidoussis [9] has discussed the problem of vortex-induced vibrations as one part of an extensive review of flow-induced vibration problems in reactors and reactor components.

AMPLITUDES OF DISPLACEMENT

A typical structure used for experimental vortex shedding studies consists of a cylinder placed normal to the flow and flexibly supported in some manner at each end. Representative measurements for such a cylinder in air have been reported by Griffin and Koopmann [10] and in water by Dean, Milligan and Wootton [11]. The results obtained are generally the same in both media. As the incident flow velocity V , or the "reduced velocity" V_r , as in Fig. 1, is increased the unsteady displacement amplitude first builds up to a maximum, after which it begins to decrease as the upper limit of the resonance is approached. For one example shown in the figure the lock-on range, defined by vibration displacements greater than the resonant threshold (taken here as $2\bar{Y}/D = 0.1$), is given by reduced velocities between $V_r = 4.5$ and 7.5 in air, with the maximum of \bar{Y}/D occurring at $V_r \sim 6$. For the in-water experiments the resonance range is somewhat wider, from $V_r = 4$ to nearly 8 , but the peak value of \bar{Y}/D again is excited at $V_r \sim 6$.

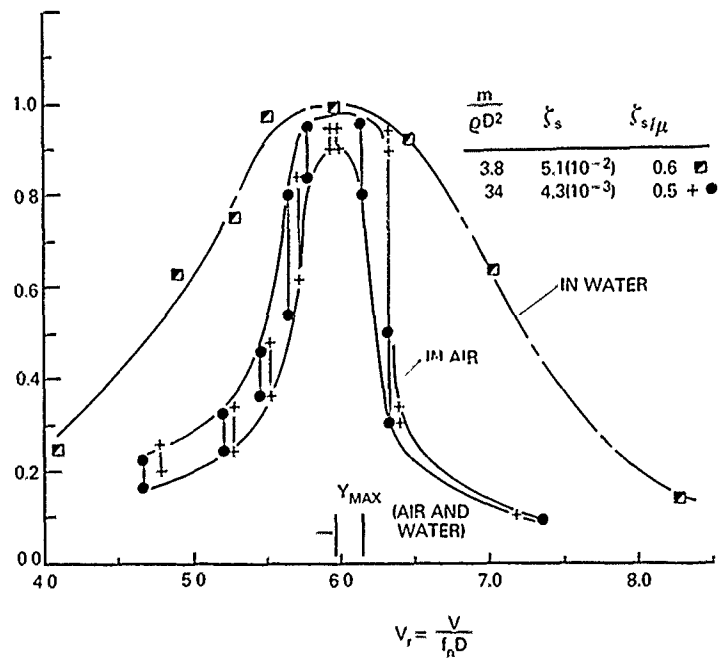


Fig. 1 — The cross flow displacement amplitude, $2\bar{Y}/D$, for a circular cylinder plotted against the reduced velocity, $V_r = V/f_n D$, from Ref. (5).

The value of V_r^{-1} at the peak amplitude of displacement yields a Strouhal number of $St \sim 0.17$. This is because the oscillation (and vortex shedding) frequency at resonance is about $f = 0.8$ to $0.85 f_s$ at the flow velocity V corresponding to \bar{Y}_{MAX} .

The narrow resonance band in air is typical of lightly-damped systems while the more broad resonance in water is typical of systems with relatively higher structural damping. It can be seen that even though the damping and mass ratios of the two systems differ by factors of ten, the *reduced damping* (the product of the mass ratio $m/\rho D^2$ and the structural damping ratio ξ_s) is very nearly the same and so are the peak displacement amplitudes for the two cases. This overall pattern of behavior is typical of measurements in water and in air at all Reynolds numbers where vortex shedding takes place.

It has been shown by numerous investigators that the displacement amplitude is a function primarily of a response or "reduced damping" parameter of the form

$$k_s = \frac{2m\delta}{\rho D^2}. \quad (1)$$

The reduced damping can be written in the analogous form

$$\xi_s/\mu = 2\pi St^2 k_s \quad (2)$$

when the damping is small and $\zeta_s = \delta/2\pi$. Here μ is an expression of the mass ratio. The importance of the reduced damping follows directly from resonant force and energy balances on the vibrating structure. It is important to note that the damping coefficients ζ_s and δ represent the damping measured in *still air*. For all practical purposes this is then equivalent to *in vacuo* structural damping. Moreover, the relation between Y_{MAX} and k_s or ζ_s/μ holds equally well for flexible cylindrical members with normal mode shapes given by $\psi_i(z)$, for the i th mode.

If the cross flow displacement (from equilibrium) of a flexible structure with normal modes $\psi_i(z)$ is written as

$$y_i = Y\psi_i(z) \sin \omega t \quad (3)$$

at each spanwise location z , then the peak displacement is scaled by the factor

$$Y_{EFF,MAX} = Y_{MAX} I_i^{1/2} / |\psi_i(z)|_{MAX} = Y_{MAX} / \gamma_i, \quad Y = \bar{Y}/D, \quad (4a)$$

where

$$I_i = \frac{\int_0^L \psi_i^2(z) dz}{\int_0^L \psi_i^2(z) dz}, \quad (4b)$$

and

$$\gamma_i = \frac{|\psi_i(z)|_{MAX}}{I_i^{1/2}}. \quad (4c)$$

The effective displacement amplitude Y_{EFF} is a scaled version of the displacement amplitude \bar{Y}_{MAX} which is derived from considerations based on several versions of the so-called "wake oscillator" approach to modelling vortex-excited oscillations [12,13].

Experimental data for Y_{EFF} as a function of ζ_s/μ are plotted in Fig. 2. These results encompass a wide range of single cylinders of various configurations and flexure conditions at Reynolds numbers from 300 to 10^6 . For *all* of the data points plotted in Fig. 2 the damping coefficients ζ_s and/or δ were measured in *still air*. This should minimize any further misconceptions among other investigators who have discussed various versions of this figure. The various types of structures represented by the data points available through 1982 are given by Grifin and Ramberg [5]. As a typical example, the deflections of a flexible cantilever in the fundamental mode have been measured under a variety of conditions. Peak-to-peak displacements as great as two to four diameters in water were measured for length/diameter ratios up to about 250. All available experiments conducted to date indicate that the limiting unsteady displacement amplitude for a flexible circular cylinder is about $Y_{EFF} = \pm 1$ to 1.5 at the lowest values of reduced damping.

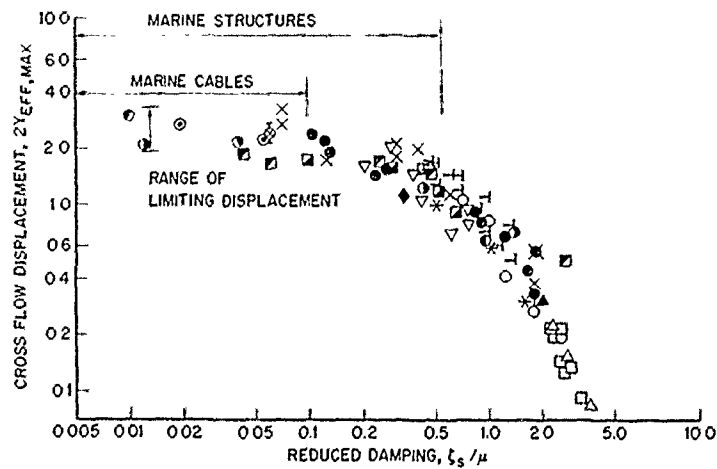


Fig. 2 -- The maximum peak-to-peak cross flow displacement amplitude, $2Y_{EFF,MAX}$, of circular cylinders, scaled as in Eq. (4), as a function of the reduced damping, $\zeta_s = 2\pi S_i^2 k_i$. The complete legend for the data points is given in Ref. (5), except for the recent data of Moe (1982), Q and of Every and King (1974), O.

The most recent measurements in water shown in Fig. 2 have been provided by Every and King [14] and by Moe [15] and are given by the symbols O and Q respectively. Both provide additional confirmation of the earlier trends shown in the figure. It is interesting to note that the reduced damping can increase from $\zeta_r/\mu = 0.01$ to 0.5 (a factor of f_0/f_p) and the displacement amplitude decreases only from two or three diameters to one diameter (a nominal factor of only *two or three*). This is why it is difficult to suppress the in-water oscillations by means of mass and damping control. Recent discussions of the suppression of vortex-excited oscillations in water are given by Every, King and Griffin [14,16] and by Zdravkovich [17].

The situation is somewhat different in air as shown in Fig. 3, which has been adapted from Adami and Batch [8]. The vibrations of a model bus-bar ($L/D = 114$) were measured in a wind tunnel with different end fixities. For the conditions tested the vibrations were nearly independent of the mode, end conditions and the aspect ratio [8]. The solid line in the figure is the prediction [18]

$$\bar{Y}_{MAX}/D = \frac{1.29 \gamma_f}{[1 + 0.43 (4\pi S t^2 m \delta / \rho D^2)]^{3.35}}. \quad (5)$$

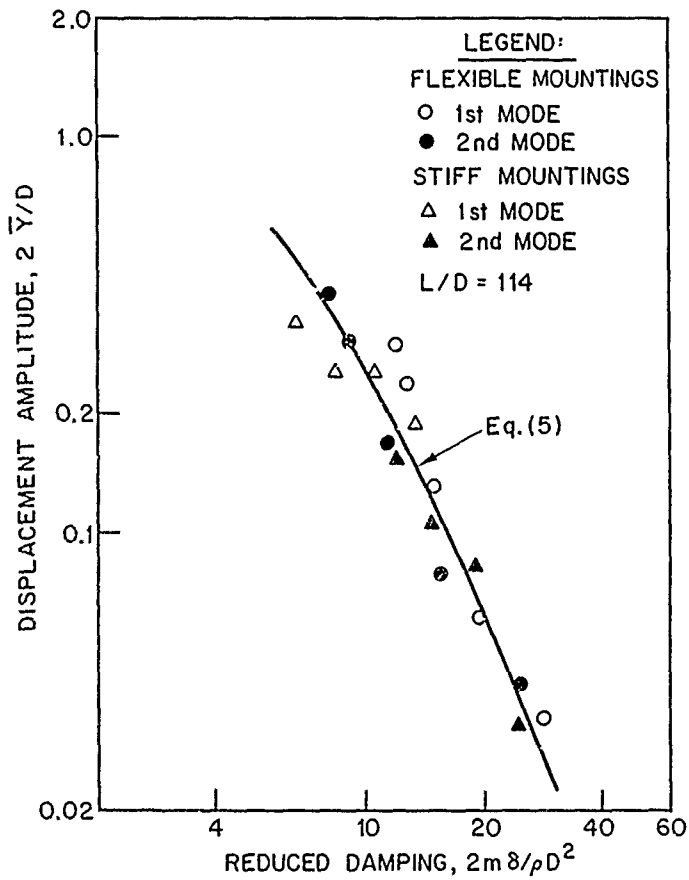


Fig. 3 — The cross flow peak-to-peak displacement amplitude, $2\bar{Y}/D$, for flexible circular cylinders in a wind tunnel as a function of the reduced damping, $k_r = 2m\delta/\rho D^2$, adapted from Adami and Batch (1981).

This is a least-squares fit to the data in Fig. 2 which were available in 1977. Other virtually identical prediction curves derived by different methods have been proposed by Sarpkaya [1] and Blevins [19]. The various approaches taken are discussed by Paidoussis [9]. The data plotted in Fig. 3 are typical of those obtained in air and would fall toward the right-hand side of Fig. 2. In that region the displacement amplitude is strongly dependent on the reduced damping. Control of the mass and damping of the member then provides a means for suppressing the vibrations.

These results have been obtained both in air and in water, even though the mass ratios of vibrating structures on the two media differ by two orders of magnitude. For typical structures vibrating in water the mass ratio $\frac{m}{\rho D^2}$ varies from slightly greater than 1 to about 5; in air the mass ratios corresponding to Fig. 2 typically vary from $\frac{m}{\rho D^2} = 15$ to 500.

LIFT FORCES

When a cylindrical body resonantly vibrates due to vortex shedding, the periodic motion is accompanied by increased coherence of the vortex shedding spanwise along the body and by an amplification of the unsteady fluid forces. Although some measurements of the forces have been made, only recently has attention been given to understanding the mechanisms by which this fluid-structural interaction force is generated and how the fluid forces may be scaled with some confidence to large Reynolds numbers.

The total fluid force which acts on a resonantly vibrating, cylindrical structure due to vortex shedding can be divided into several components [20,21], which are:

- An exciting force component, by which energy is transferred to the structure;
- A reaction, or damping force, which is exactly out-of-phase with the structure's velocity;
- An "added mass" force, which is exactly out-of-phase with the structure's acceleration; and
- A flow-induced inertial force.

These various components can be deduced from the total hydrodynamic force as measured, say, by Sarpkaya [1] or the various components can be measured individually as was done by Griffin and Koopmann [10], for example. The present discussion will deal essentially with the exciting force.

The excitation component of the total unsteady hydrodynamic force is defined as

$$C_{LE} = C_L \sin \phi \quad (6)$$

and is important because it is the component of the total force that transfers energy to the vibrating structure. Here ϕ is the phase angle between the hydrodynamic force coefficient C_L and the motion of the structure. A relatively large number of measurements of C_{LE} by various means are plotted against the effective displacement amplitude Y_{EFF} in Fig. 4. Table 1 describes the various conditions under which the experimental results were obtained. Several important characteristics of the unsteady lift and pressure forces that accompany vortex-excited oscillations are clear from the results. First there is a maximum of the excitation force coefficient at a peak-to-peak displacement amplitude of between 0.6 and 1 diameters for all the cases shown in the figure. Second, the maximum of the force coefficient is approximately $C_{LE} = 0.5$ to 0.6 for all but one case; the exception is the single result of $C_{LE} = 0.75$. C_{LE} then decreases toward zero and results in a limiting effective displacement amplitude between two to three diameters. This limiting amplitude is clearly shown at the low values of reduced damping in Fig. 2. Similar behavior in the pressure coefficient measured near the separation point on a forced-vibrating cylinder was obtained by Bearman and Currie [22].

Vortex-induced vibrations cause energy to be transferred to the cylindrical structure. This is caused at resonance by the excitation force component plotted in Fig. 4. A number of measurements of aerodynamic power have been made, primarily in the study of electrical transmission line vibrations, see, for example, the paper by Simmons and Cleary [6]. The time-averaged power input \bar{P} over a cycle of the oscillation is

$$\bar{P} = \pi f \bar{F}_L \bar{Y} \sin \phi \quad (7)$$

when the displacement of the cylinder is

$$\bar{y}(t) = \bar{Y} \cos 2\pi f t \quad (8a)$$

and the lift force is

$$\bar{F}(t) = \bar{F}_L \cos (2\pi f t + \phi). \quad (8b)$$

In nondimensional terms Eq. (7) reduces to

$$P = \frac{\bar{P}}{\rho D^4 f^3} = \frac{\pi}{2} Y C_L \sin \phi V_r^2 \quad (9a)$$

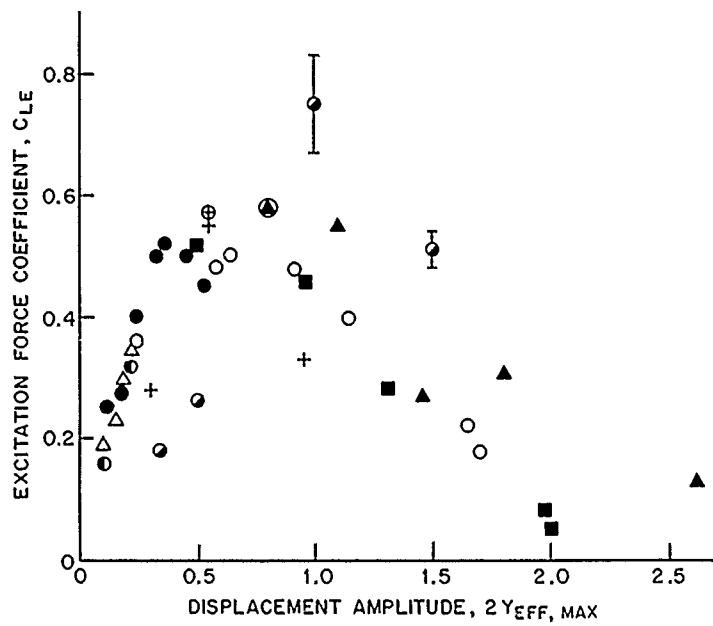


Fig. 4 — The excitation component, C_{LE} , of the lift force plotted against the displacement amplitude $2Y_{EFF, MAX}$, scaled as in Eq. (4). The legend for the data points is given in Table I.

Table I
The Excitation Force Coefficients on Vibrating Bluff Cylinders;
Description of the Data in Fig. 4

Symbol	Type of cylinder	Medium	Cylinder material	Investigator(s)
▲	Flexible cantilever	Water	PVC	King (1977)
■			PVC	
			Aluminum	
			Stainless steel	
○	Pivoted rigid cylinder	Water & Air	Brass	Vickery and Watkins (1964)
+	Spring-mounted rigid cylinder	Air	Aluminum tubing	Griffin and Koopmann (1977)
●	Rigid cylinder, forced oscillations	Water	Aluminum tubing	Sarpkaya (1978)
△	Flexible cantilever	Air	Aluminum	Hartlen, Baines and Currie (1968)
●	Flexible cylinder	Air	—	Farquharson and McHugh (1956)†
○	Rigid cylinder, forced oscillations	Air	Brass	Simmons and Cleary (1979)

†Quoted by Simmons and Cleary.

or, equivalently,

$$P = \frac{\pi}{2} Y C_{LE} V_r^2. \quad (9b)$$

Several examples of the measured and predicted time-average power P are given in Fig. 5. The measured values are from Simmons and Cleary and from Farquharson and McHugh. The latter examples were reduced by Simmons and Clearly from Ref. (23). The measured and predicted values are virtually indistinguishable for the case $V_r = 6$. The predictions of P are based upon a least-squares fit to the data in Fig. 4. As shown in Fig. 1 this condition is representative of the maximum power transmission in both air and water. The example given here is for the case of a vibrating transmission line in air, but a similar approach could be used to predict the hydrodynamic power transmission to and acoustic radiation from an oscillating member in water.

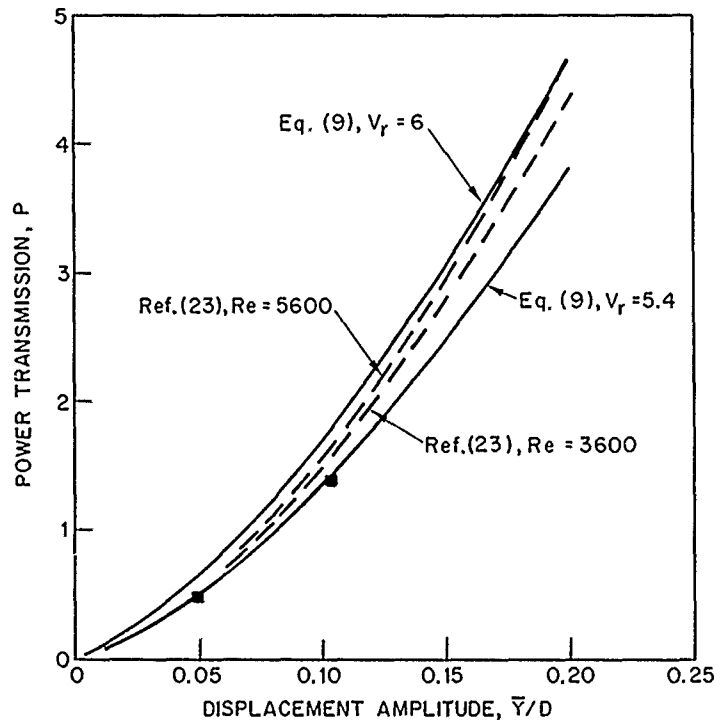


Fig. 5 — The measured and predicted time-averaged power transmission, P , to a vibrating circular cylinder plotted against the displacement amplitude, \bar{Y}/D . — — —, Farquharson and McHugh (1956), from Simmons and Cleary (1979); ■, Simmons and Cleary (1979).

DRAG FORCES

An important consequence of the resonant cross flow oscillations of structures and cables due to vortex shedding is an amplification of the steady drag force (or equivalently the drag force coefficient C_D). The drag amplification under a variety of conditions has been measured and the results have been summarized by Griffin and Ramberg [5]. A step-by-step method for employing these measurements in the analysis of marine cable structures was developed by Skop, Griffin and Ramberg [18]. One step in the method uses Eq. (5) to predict the cross flow displacement amplitude of the member. This procedure has been extended to the case of flexible, cylindrical marine structures by Griffin [4] in a study of OTEC cold water pipe vibrations. Measurements of the drag coefficient more recent than those discussed by Griffin and Ramberg are presented here.

Measurements of the vortex-induced cross flow vibrations of model marine piles were made by Fischer, Jones and King [26,27]. The steady deflection at the free end of the model pile also was measured; in this case the model was a simple, uniform cantilever beam with no tip masses, fully immersed in water, and normal to the incident flow. For low flow velocities the measured and predicted tip deflections coincided when the pile was effectively stationary. The deflection was predicted by assuming a uniform loading function

$$w(x) = 1/2 \rho V^2 D C_D(x)$$

over the length of the flexible beam in which the drag coefficient $C_D(x)$ was a constant, $C_D = 1.2$.

When the critical flow velocity for the onset of the vortex-induced vibrations was exceeded, the measured steady deflections in line with the flow departed significantly from the predicted reference curve. One example of the results obtained is given in Fig. 6. For the lower values of relative density the flow velocities above the threshold value caused steady deflections of up to twice the model's value predicted by assuming $C_D = 1.2$. For the higher values of relative density, the steady deflections of the model diverged from the predicted curve, reached a maximum as shown in Fig. 6, and then returned to the predicted curve as the flow velocity was increased still further. The region of divergence corresponds directly to the range of resonant, large amplitude cross flow vibrations. For example, the tip of the $SG = 3.5$ pile was deflected in line about 1.3 diameters at a water velocity V of 0.6 kt (0.3 m/s). At this same flow velocity the cross flow displacement amplitude was ± 1.5 diameters. When the pile was restrained from oscillating, the steady in-line deflection of the tip was predicted to be 0.6 diameters at the same flow velocity. The predicted tip deflections in Fig. 6 were computed using an approach which is discussed by Every, King and Griffin [16].

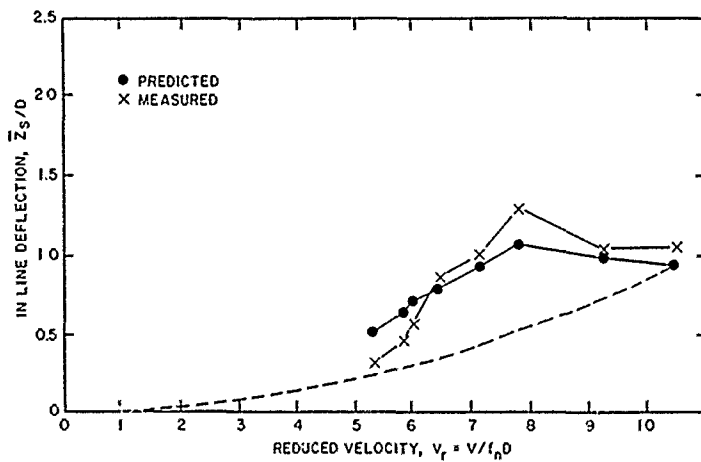


Fig. 6 — The predicted and measured steady up deflection, \bar{Z}_s/D , for a vibrating flexible cantilever in water; from Every, King and Griffin (1982). Relative density of the beam, $SG = 3.5$, — — —, beam restrained from oscillating, $C_{D0} = 1.2$.

The mean vortex-induced drag coefficient C_D on a freely-oscillating, spring-mounted cylinder is plotted against the reduced velocity V_r in Fig. 7. The measurements were made by Overvik [28] as a baseline case in a more extensive study of the effects of vortex shedding on marine risers. The drag on the cylinder clearly undergoes a resonant-like behavior in much the same manner as the cross flow displacement amplitude. Comparable measurements by Overrik of the displacement amplitude \bar{Y}/D correspond directly with the behavior of the drag coefficient C_D . At the peak value of the response, $\bar{Y} \sim 1.1 D$, the drag coefficient on the vibrating cylinder is $C_D \sim 2.5$. This is an amplification of about 250 percent, which is of sufficient magnitude to cause serious problems for the designer of marine structural members of cylindrical cross section. Less severe problems develop in the case of structures in air because of the smaller vibration amplitudes which are common there.

The drag amplification C_D/D_{D0} , where C_{D0} is the drag coefficient for the stationary cylinder, from a variety of recent experiments is plotted in Fig. 8 as a function of the "wake response" parameter

$$w_r = (1 + 2 \bar{Y}/D) (V_r S_l)^{-1}. \quad (10)$$

This parameter was introduced by Skop, Griffin and Ramberg [18] as a means for correlating the drag amplification that accompanies vortex-induced vibrations. In the particular form shown, the factor S_l^{-1} acts

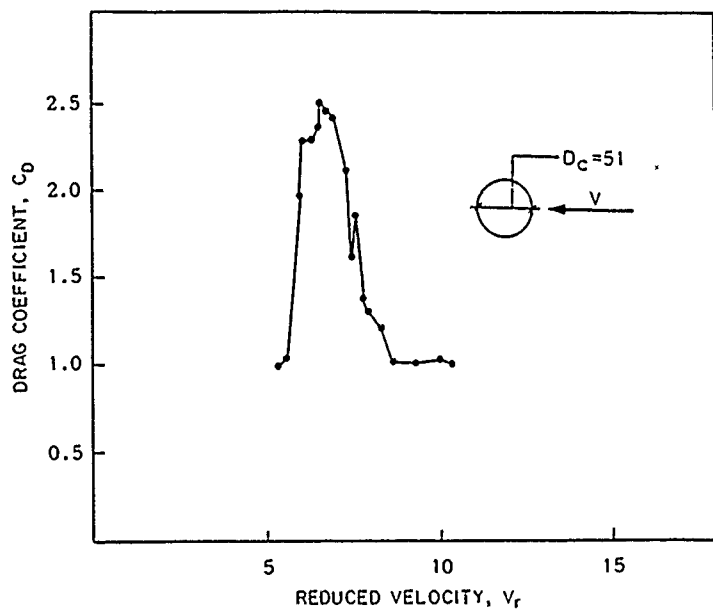


Fig. 7 — The drag coefficient, C_D , plotted against the reduced velocity, V_r , for a spring-mounted circular cylinder; from Overvik (1982). Peak cross flow displacement amplitude, $\bar{Y} = \pm 1$ to $1.1D$.

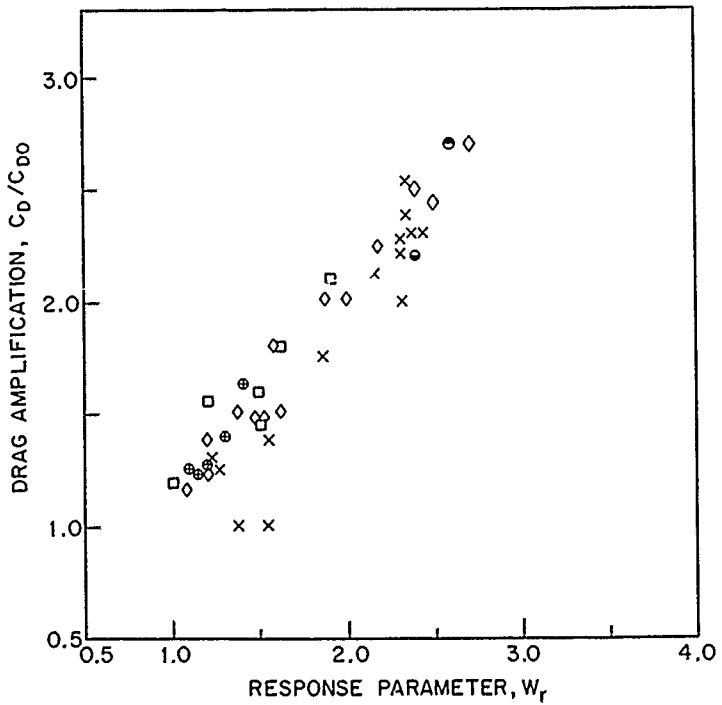


Fig. 8 — The drag coefficient amplification, C_D/C_{D0} , plotted as a function of the wake response parameter, $w_r = (1 + 2\bar{Y}/D) (St V_r)^{-1}$, for the cross flow vibrations of a circular cylinder. The legend for the data points is given in Table 2.

Table 2 Drag Force Amplification on Vibrating Circular Cylinders; Description of the Data in Fig. 8			
Symbol	Medium	Type of Vibration	Investigator(s)
⊕	Air	Cross flow, forced	Griffin and Ramberg (1975)
△	Water	Cross flow, forced	Sarpkaya (1977)
□	Water	Cross flow, forced	Scharge (1980)
X	Water	Cross flow, free	Overvik (1982)
○, ⊖	Water	Cross flow, free	Moe (1982)

to correct for any variations in Strouhal number (and Reynolds number) among the various sets of data. All of the data in Fig. 8 refer to conditions of lock-in between the vortex and vibration frequencies. A previous drag amplification-wake response plot was used by Every, King and Griffin [16] for the predictions shown in Fig. 6.

It is interesting to note the variety of data which are correlated in the figure. For instance, the drag coefficients from Griffin and Ramberg [29] were derived from wake measurements with a forced-vibrating cylinder in air. The drag measurements from Sarpkaya [30] and Scharge [31] were made on a forced-vibrating cylinder in water. Moe [15] and Overvik [28] measured the drag on a freely-vibrating cylinder in water. All of these different experiments resulted in substantial amplifications of the drag coefficient, with $C_D/C_{D0} > 2$ not uncommon for both free and forced vibrations in water.

Similar levels of hydrodynamic drag amplification were measured during the recent field experiments reported by Vandiver and Griffin [32,33]. Both a 23 m (75 ft) long pipe and a cable with and without attached masses underwent large-amplitude vibrations ($\bar{Y} \sim \pm 1D$) due to vortex shedding in a steady current. Mean drag coefficients of $C_D = 2.4$ to 3.2 were measured during the time intervals when the pipe and cable were oscillating at these large amplitudes. In another recent series of experiments Davies and Daniel [34] measured the strumming vibrations of submersible umbilical cables. The model cable of $L/D = 100$ to 300, which was tested in a large water channel, consistently was excited into large-amplitude cross flow oscillations which were comparable in level to those reported by Vandiver and Griffin. Consequently the normal mean drag coefficients measured by Davies and Daniel were in the range $C_D = 2.5$ to 3.4. This is an amplification factor of 2 to 2.8.

The overall implications for practical applications are that the relatively large amplitudes of vibration caused by vortex shedding, and the amplifications of the unsteady and steady fluid forces which are a consequence of the vibrations, can cause both large steady deflections and stresses and time dependent, fatigue-related unsteady forces and stresses.

SUMMARY AND CONCLUDING REMARKS

Until recent years problems associated with vortex shedding were given scant attention or approached on an ad hoc case-by-case basis, largely because reliable experimental data and design procedures were not available for general use. However, the dynamic analysis of modern structures and cable systems has become increasingly important and modern in order to predict stress distributions and operational lifetimes in hostile environments. This is largely because the amplitudes of vibration for a cylindrical structure such as a riser or pipeline in water are an order of magnitude greater than for a similar structure in air. The small mass ratio (structure to displaced fluid) in water produces small values of the reduced damping which in turn result in the relatively large vibration amplitudes shown here in Fig. 2.

There is a large range of reduced damping over which bluff cylindrical structures in water undergo large-amplitude vibrations due to vortex shedding. Thus it is not possible to suppress these oscillations by means of mass and damping control, and some form of external device such as a helical strake winding or fairing is required. The component of the lift coefficient which drives the motion is increased by vibration, as is the mean in-line drag coefficient which is increased by as much as 250 percent.

Structures in air experience vibration amplitude levels much smaller in magnitude, and consequently the drag amplification is not as extreme as in water. Mass and damping control often are used to suppress the in-air vibrations of such members as bus-bars and power transmission lines; external devices such as helical strakes are often used on chimney stacks and the protruding legs of jack-up drilling rigs under tow.

ACKNOWLEDGMENTS

This paper was prepared at the Naval Research Laboratory as part of a research program supported by the Minerals Management Service of the U.S. Department of the Interior. I am grateful to a number of colleagues who provided their own results and the results of others, especially J. L. Simmons of the University of Queensland, G. Moe and T. Overvik of the Norwegian Institute of Technology, C. B. Rawlins of the Alcoa Laboratories, and J. K. Vandiver of the Massachusetts Institute of Technology.

REFERENCES

1. T. Sarpkaya, "Vortex-Induced Oscillations, A Selective Review," *Trans. ASME, Series E, J. Applied Mechanics*, Vol. 46, 241-258, 1979.
2. P.W. Bearman, "Vortex Shedding From Oscillating Bluff Bodies," *Ann. Rev. Fluid Mech.*, Vol. 16, 195-222, 1984.
3. R. King, "A Review of Vortex Shedding Research and Its Applications," *Ocean Engineering*, Vol. 4, 141-171, 1977.
4. O.M. Griffin, "OTEC Cold Water Pipe Design for Problems Caused by Vortex-Excited Oscillations," *Ocean Engineering*, Vol. 8, 129-209, 1981.
5. O.M. Griffin and S.E. Ramberg, "Some Recent Studies of Vortex Shedding with Application to Marine Tubulars and Risers," *Trans. ASME, J. Energy Resources Tech.*, Vol. 104, 2-13, 1982.
6. J.M. Simmons and P.M.G. Cleary, "Measurement of Aerodynamic Power Associated with Vortex-Induced Vibration of Electrical Transmission Lines," *IEEE Power Engineering Society Paper F79 713-9*, 1979.
7. C.B. Rawlins, "Power Imparted by Wind to a Model of a Vibrating Conductor," *ALCOA Laboratories Report No. 93-82-1*, April 1982.
8. H. Adami and B.A. Batch, "Aeolian Vibrations of Tubular Busbars in Outdoor Substations," *Electra*, No. 75, 99-120, March 1981.
9. M.P. Paidoussis, "A Review of Flow-Induced Vibrations in Reactors and Reactor Components," *Nuc. Engrg. and Design*, Vol. 74, 31-60, 1983.
10. O.M. Griffin and G.H. Koopmann, "The Vortex-Excited Lift and Reaction Forces on Resonantly Vibrating Cylinders," *J. Sound and Vib.*, 54, 435-448, 1977.
11. R.B. Dean, R.W. Milligan and L.R. Wootton, "An Experimental Study of Flow-Induced Vibration," *E.E.C. Report 4*, Atkins Research and Development, Epsom (U.K.), 1977.
12. R.A. Skop and O.M. Griffin, "On a Theory for the Vortex-Excited Oscillations of Flexible Cylindrical Structures," *J. Sound and Vib.*, Vol. 41, 263-274, 1975; see also "The Vortex-Induced Oscillations of Structures," *J. Sound and Vib.*, Vol. 44, 303-305, 1976.
13. W.D. Iwan, "The Vortex-Induced Oscillation of Elastic Structural Elements," *Trans. ASME, Series B, J. Engrg. Indus.*, Vol. 97, 1378-1382, 1975.
14. M.J. Every and R. King, "Suppressing Flow-Induced Vibrations—An Experimental Study of Clamp-On Devices," *BIIRA Fluid Engineering Report RR 1576*, November 1979.
15. G. Moe, Private communication, 1983.
16. M.J. Every, R. King and O.M. Griffin, "Hydrodynamic Loads on Flexible Marine Structures due to Vortex Shedding," *Trans. ASME, J. Energy Resources Tech.*, Vol. 104, 330-336, 1982.

17. M.M. Zdravkovich, "Review and Classification of Various Aerodynamic and Hydrodynamic Means for Suppressing Vortex Shedding," *J. Indus. Aero. and Wind Engrg.*, Vol. 7, 145-189, 1981.
18. R.A. Skop, O.M. Griffin and S.E. Ramberg, "Strumming Predictions for the SEACON II Experimental Mooring," *Offshore Technology Conference Paper OTC 2884*, May 1977.
19. R.D. Blevins, *Flow-Induced Vibrations*, Van Nostrand Reinhold: New York, 1977.
20. S.S. Chen, "Crossflow-Induced Vibrations of Heat Exchanger Tube Banks," *Nuc. Engrg. and Design*, Vol. 47, 67-86, 1978.
21. O.M. Griffin, "Vortex-Excited Cross Flow Vibrations of a Single Cylindrical Tube," *Trans. ASME, J. Press. Vessel Tech.*, Vol. 102, 158-166, 1980.
22. P.W. Bearman and I.G. Currie, "Pressure Fluctuation Measurements on an Oscillating Circular Cylinder," *J. Fluid Mech.*, Vol. 91, 661-678, 1979.
23. F.B. Farquharson and R.E. McHugh Jr., "Wind tunnel investigation of conductor vibration with use of rigid models," *Transactions of the AIEE*, Vol. 75, 871-878, 1956.
24. B.J. Vickery and R.D. Watkins, "Flow Induced Vibration of Cylindrical Structures," *Proceedings of the First Australian Conference on Hydraulics and Fluid Mechanics*, R. Silvester (ed.), Pergamon Press: Oxford, 1964.
25. R.T. Hartlen, W.D. Baines and I.G. Currie, "Vortex-Excited Vibrations of a Circular Cylinder," University of Toronto Technical Report 6809, 1968.
26. F.J. Fischer, W.T. Jones and R. King, "Current-Induced Oscillations of Cognac Piles During Installation," in *Practical Experiences with Flow-Induced Vibrations*, E. Naudascher and D. Rockwell (eds.), Springer-Verlag: Berlin, 570-581, 1980.
27. R. King, "Model Tests of Vortex-Induced Motion of Cable Suspended and Cantilevered Piles for the Cognac Platform," BHRA Fluid Engineering Report RR 1453, January 1978.
28. T. Overvik, "Hydroelastic Motion of Multiple Risers in a Steady Current," Ph.D. Thesis, Norwegian Institute of Technology, August 1982.
29. O.M. Griffin and S.E. Ramberg, "On vortex strength and drag in bluff body wakes," *J. Fluid Mech.*, Vol. 69, 721-728, 1975.
30. T. Sarpkaya, "Transverse Oscillation of a Circular Cylinder in Uniform Flow," *Proc. ASCE, J. WPCO Div.*, Vol. 104, 275-290, 1978.
31. R.S. Schargel, "The Drag Coefficient for a Randomly Oscillating Cylinder in a Uniform Flow," M.S. Thesis, MIT Ocean Engineering Department, September 1980.
32. J.K. Vandiver, "Drag Coefficients of Long, Flexible Cylinders," *Offshore Technology Conference Paper OTC 4490*, May 1983.
33. O.M. Griffin and J.K. Vandiver, "Flow-Induced Vibrations of Long Cables with Attached Masses," Naval Civil Engineering Laboratory Report CR 84.004, November 1983.
34. M.E. Davies and A.P. Daniel, "The Hydrodynamics of a Model of a Vibrating Umbilical Cable," *Offshore Technology Conference Paper OTC 4832*, May 1984.

FLUID FORCES ON A RIGID CYLINDER IN TURBULENT CROSSFLOW

T. M. Mulcahy
Argonne National Laboratory
Argonne, Illinois

ABSTRACT

Fluctuating lift and drag force coefficients are presented which were obtained in water flows with Reynolds numbers in the range 3×10^4 to 2×10^5 . Turbulence intensities were varied from 1.5 to 15% while integral scale lengths ranged from 0.5 to 2 tube diameters. The turbulence generated is described and the method of force measurement is outlined. Empirical bounds on the force spectra are given, and available information on spanwise correlation lengths are identified so that the data can be used to make RMS vibration response predictions where fluid-structure interaction does not occur.

1. INTRODUCTION

The response of a circular cylinder to flow normal to its longitudinal axis, called crossflow, involves very complex physical phenomena. However, a single tube in crossflow is not an uncommon reactor geometry and a sometimes strong fluid excitation mechanism, vortex shedding, exists. Therefore the associated response must be accounted for in fatigue or fretting and wear design. Several methods of response analysis and bodies of data describing the fluid forces are available. Although the methods of structural analysis are classical, the applicability of the force data available and the modeling of the fluid-structure interaction are controversial.

To date, most force data have been obtained for cylinders with very smooth surfaces subject to the two-dimensional (uniform), very low turbulence, crossflow producible in wind and water tunnels. These conditions shall be referred to as "ideal crossflow." For ideal crossflow, large responses are predictable, especially when the frequency of the vortex shedding and the natural frequency of the structure coincide (lock-in) [1]. However, not uncommonly, reactor scale model response measurements with potentially detrimental, but other than ideal, crossflow conditions show only low level random motion [2] with no hint of periodic vortex shedding induced excitation. In short, current design methods based on ideal crossflow information appear conservative.

As more and more knowledge is gained about the crossflow induced forces, design methods can be made more system specific, and, as a result, less conservative. Toward that goal, an experiment was performed to obtain

additional fluctuating lift and drag force data for a rigid, smooth surfaced cylinder in flows with different free stream turbulence typical of those expected in power generation systems. Although many other factors can influence the fluid forces, free stream turbulence was identified for study first, because highly turbulent flows are the norm in heat generation and exchange systems.

2. TURBULENCE EFFECTS

Assuming no fluid-structure interaction (lock-in), prediction of the dynamic (RMS) response of a cylinder in crossflow requires, at a minimum, knowledge of the fluctuating lift and drag force/length coefficients, C_L and C_D , spanwise correlation lengths, λ_c , and single point spectral densities, ϕ_L and ϕ_D . For ideal crossflow, quantitative characterization is available and the fluid forces are of three different types for three distinct Reynolds number ranges. In the subcritical range, $10^4 < N_R < 2 \times 10^5$, where the attached boundary layer is laminar, the forces are nearly periodic and, for example $\lambda_c \sim 6 D$ [3], $C_L \sim 0.5$ (see Fig. 1), and the vortex shedding frequency is determined by a Strouhal number $S \sim 0.2$ (see Fig. 2). In the transcritical range, $N_R > 3 \times 10^6$, where the attached boundary layer is turbulent, the forces are narrow band random in character and $\lambda_c \sim D$. The lift coefficient, for example, is smaller ($C_L \sim 0.1$) and the shedding frequency is centered around $S \approx 0.26$. In the critical through the supercritical range, $2 \times 10^5 < N_R < 3 \times 10^6$, where the attached boundary layer is in transition, the forces are wide band random in character with the smallest force coefficients and the shortest correlation lengths ($\lambda_c < D$) [5].

Adding turbulence to otherwise ideal crossflow is known to change the fluid forces in several ways, but not as much quantitative information characterizing the forces is available as for ideal crossflow.* One reason for the deficiency is logistical: different turbulence intensities I and length scales L produce different results. For instance, the addition of turbulence to the free stream has been known [14], for a long time, to shift the critical range to smaller (up

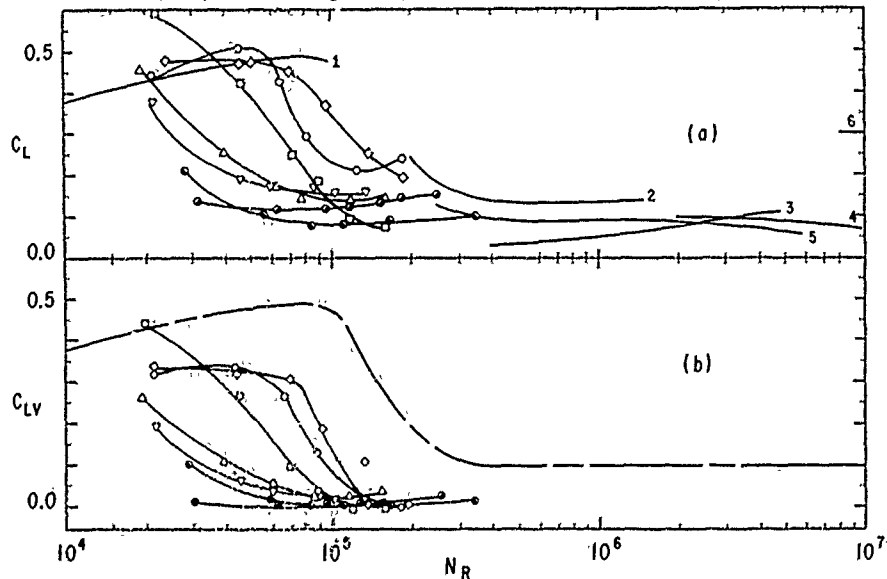


Fig. 1. (a) Total lift force coefficients C_L . (b) Narrow band lift coefficients C_{LV} . Ideal crossflow curves: 1 [13], 2 [12], 3 [11], 4 [10], 5 [7], and 6 [9]. Upper bound curve — for ideal crossflow data. See Table 1 for turbulent flow data notation.

* The author was made aware of very recent and pertinent experimental results [27] which could not be included.

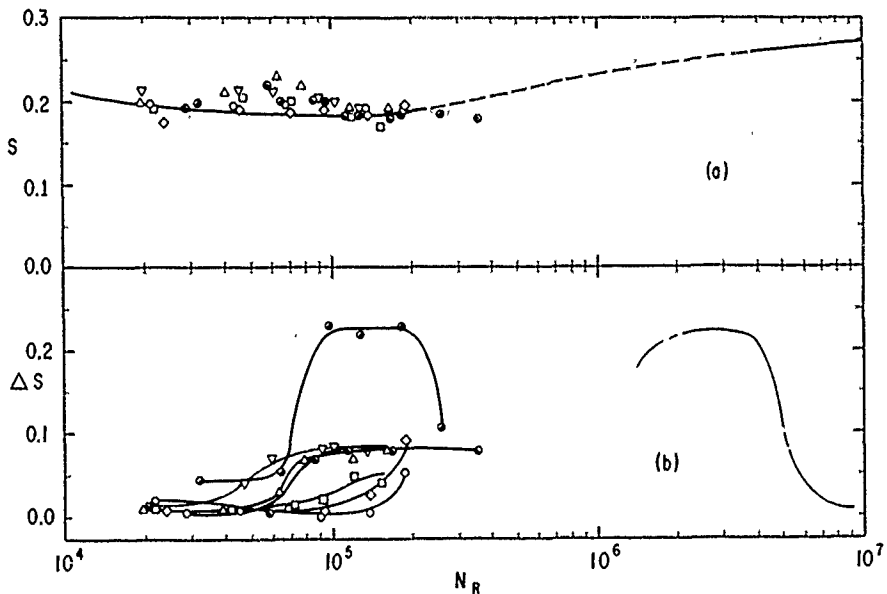


Fig. 2. (a) Strouhal number S . (b) Half-power bandwidth ΔS . Ideal crossflow S —, with - - - representing trend for sporadic data [5]. Ideal crossflow ΔS — [10]. See Table 1 for turbulent flow data notation.

to an order of magnitude) Reynolds numbers. However, I is much more effective in lowering the critical range than L , as reflected in recent correlations [15] of new and existing data with the Taylor number, $T = I/(L/D)^{0.2}$. The location of the upper end of the supercritical region has not been quantified, because experiments to characterize fluid forces have not been performed for $N_R > 3 \times 10^6$.

If the effect of turbulence in the flow were only to shift the ranges (critical, etc.) to different Reynolds numbers which could be quantified, then the character of the forces in turbulent flow could be extrapolated from the available ideal flow information. However, turbulence added to ideal flow is known to penetrate the attached boundary layer on the front half of the cylinder, at least, and increase the pressure fluctuations and decrease their axial correlation in proportion to the flow turbulence intensity and scale [15-17]. Also, turbulent kinetic energy added to the attached boundary layer means larger negative pressure gradients will be overcome, the separation line will move rearward, the wake will narrow, and the wake will shorten if reattachment does not occur [17-19]. Thus, the character of the fluid forces must be assumed different for different turbulent flows.

Partial characterization of the fluid forces in turbulent flow with $N_R < 3 \times 10^6$ are available and can be useful in a response analysis. Most of the available data for the drag coefficient C_D were found [15] to collapse into a relatively narrow band when plotted versus $(N_R^{1.34}T)$ for $10^4 < N_R < 3 \times 10^6$. Also, when plotted versus $(N_R^{1.34}T)$, the spanwise correlation lengths of the pressure fluctuations at 90° circumferentially from the stagnation line were found to collapse into a narrow band. Although scant data was available for plotting and a correspondence to the lift force spanwise correlation must be assumed, the correlation lengths given in [15] probably are adequate estimates of ℓ_c for response prediction: all are small, 0.5 to 3.0 D, in comparison to the length of most beam structures.

Little information exists for fluctuating force coefficients and spectral densities in turbulent flow. For $I \sim 0.15$ and $L = 4.8$ D, surface pressure crosscorrelations were determined [20] at $N_R = 4 \times 10^4$ and integrated to determine a lift coefficient comparable to those obtained in ideal flow,

$C_L \sim 0.5$, although the pressure spectral peaks were lowered and broadened in comparison to those of ideal flow. The fluctuating drag coefficient in turbulent flow ($C_D' \sim 0.25$) was considerably higher than that measured in ideal flow ($C_D' \sim 0.05$). The large intensity, the broad drag spectrum, and the lack of a spectral peak at twice the Strouhal frequency were attributed to the dominance of the incident turbulence over the vortex shedding in producing the fluctuating drag force. The influence of the incident turbulence was also reflected in the spanwise correlations of the lift and drag which were nearly equal to the spanwise scale for homogeneous turbulence, $1/2 L$.

For $I = 0.095$, $0.16 D < L < 1.3 D$, the fluctuating lift and drag forces on isolated spans were measured [21] with a force transducer over the Reynolds number $3 \times 10^4 < N_R < 5 \times 10^5$. Because blockage of the cylinder in the water tunnel was 16%, the force coefficients, as expected, were higher than for an isolated cylinder; for example $C_L \sim 1.0$ for ideal flow at $N_R = 4 \times 10^4$. However, the variations in the data with turbulence, N_R , and active span lengths were revealing. In turbulent flow at $N_R = 4 \times 10^4$, the lift coefficient was half of that in smooth flow, in contrast to [20]. The spectral content was only quasi-periodic, closer to a Gaussian random than periodic. The critical range was shifted to lower N_R by the addition of turbulence in the flow, and by $N_R = 10^5$ the lift force was wide band random in spectral content. These trends are similar to the effects of turbulence on the steady drag and surface pressure discussed previously. Also of interest, the magnitude of C_L was a function of the active span length of the force measurement system. With a change in active span lengths from $3 D$ to D , the coefficient was increased by a factor between 2 and 3, depending on N_R .

3. EXPERIMENT DESIGN

A flow-induced vibration test facility (FIVTF) was available which could pump $\sim 8,000$ gpm ($0.5 \text{ m}^3/\text{s}$) of water, with an available head of $\sim 75 \text{ lb/in.}^2$ (0.52 mPa), through an 18-in. (0.46-m) pipe. Heat exchangers provided constant temperature control near room temperature. A 12-in. (0.31-m) square liner was inserted in the pipe to form a flow channel upstream and downstream of a similar sized turbulence generator section and a test section. A 1-in. (25.4 mm) diameter cylinder was mounted in crossflow and flow turbulence measurements could be made through view ports of the test section using a Laser-Doppler anemometer. Deionized water, with 15-megohm resistance, was used to maintain water quality and instrumentation isolation. Reynolds numbers in the range $2 \times 10^4 < N_R < 2 \times 10^5$ could be attained with the system described. Reynolds numbers in reactor flows are typically in this range or larger.

Testing in both the smooth (nonturbulent) flow conditions of a water tunnel with grids added to produce the desired turbulence would have been desirable. But an expansion and contraction section was not available nor affordable. Instead, by including $\sim 20 \text{ ft}$ (6.1 m) of channel upstream of the test section, nearly fully developed pipe flow was attained (grid OP in Table 1) at the

Table 1. Grid and turbulence characteristics

Grid No. (X (mm))	Symbol	I%	L (mm)	d (mm)	b (mm)	SB	ϕ_{DO}	C_{DC}'
OP	◇	3	51-54	-	-	0	0.100	0.15
HC	○	1-2	40-85	-	-	0	0.100	0.15
2(493)	□	4-5	12-14	17.4	8.9	0.58	0.032	0.09
24(191)	●	8-10	6-12	22.6	8.9	0.50	0.010	0.05
24(107)	●	12-18	7-28	22.6	8.9	0.50	0.014	0.06
52(493)	△	10-11	23-27	26.7	25.4	0.75	0.027	0.08
52(338)	▽	13-15	23-30	26.7	25.4	0.75	0.026	0.08

location of the test cylinder. To produce less turbulent flows [22], two honeycombs in series could be inserted 7.25 ft (2.21 m) upstream of the test cylinder. The upstream honeycomb of the flow-smoothing device (grid HC in Table 1) had 6-in. (152-mm) long hexagonal cells with 0.25-in. (6.4-mm) wide flat sides which were 0.002-in. (0.051-mm) thick. Located 0.125 in. (3.2 mm) downstream, to suppress the turbulent wake of the first honeycomb, was a smaller honeycomb which had 0.5-in. (12.70-mm) long hexagonal cells with 0.125-in. (3.2-mm) wide flat sides which were 0.004-in. (0.1-mm) long. To produce flows more turbulent than the open channel flow, turbulence generator grids were located from $x = 4.2$ to 19.4 in. (107 to 493 mm) upstream of the test cylinder. The grids were constructed by drilling holes uniformly in a close-packed array through 1.125-in. (28.6-mm) thick plates. The grid number, the distance from the cylinder x , the hole diameter d , the average bar (web) size b between holes, and the solid blockage SB are given in Table 1. Based on typical reactor flows, the grids were chosen to produce turbulence intensities up to 15% and scales slightly more and less than the diameter of the test cylinder, $\sim 0.5 D$ to $2 D$.

The flows produced by the method described were less than ideal from the standpoint of producing homogeneous, isotropic turbulent flows. However, they are expected to suffer less distortion than will exist in reactor flows, for which the data obtained is primarily intended.

To mount and seal the 1-in. (25.4-mm) diameter test cylinder to the test section walls, and to measure the fluid forces, the cylinder was built in several parts. Complete details are provided in [23] and summarized below and in Fig. 3. End supports mounted on the test section walls held the central bar which, in turn, provided a rigid base to mount dummy sleeves and a force sensing ring over the 7.5-in. (191-mm) long central section of the cylinder. The 0.5-in. (12.7-mm) long sensing ring was separated from the dummy sleeves and mounted on the central bar with a force measurement ring which could monitor lift and drag direction forces via two, four-arm strain gauge bridges. The sensing ring and dummy sleeves were machined and sanded to a surface finish having less than $0.5 \times 10^{-4} D$ surface roughness. The short length of the sensing ring was deemed necessary to resolve lift forces with short correlation lengths, as discussed in the previous section. The force measurement ring was designed to resolve force magnitudes as small as 0.05-lb (0.22 N) and did not statically deflect more than 0.001 in. (0.025 mm) under maximum loading. The natural frequency of the submerged force measurement system was 5 times the vortex shedding frequency

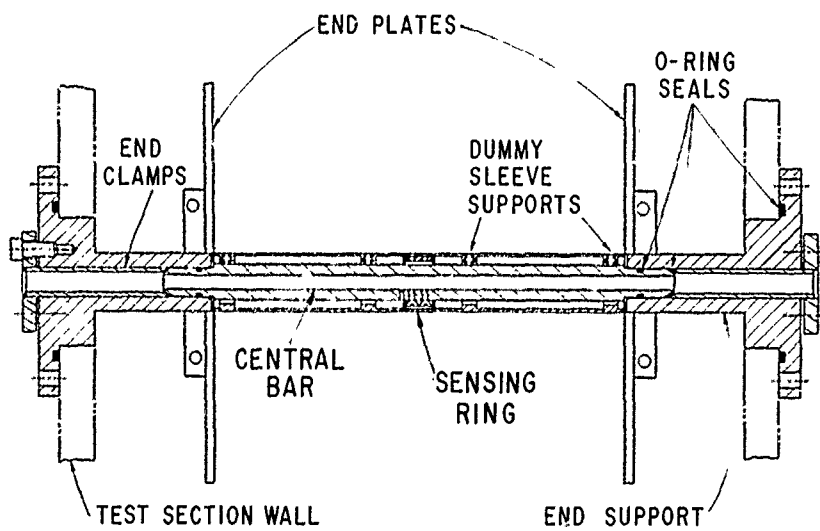


Fig. 3. Force-transducer assembly mounted in end supports attached to test-section walls

based on $S = 0.2$. The resonant response signals of the transducer could be filtered from the force signal, and no significant interaction between the two were observed.

The major concern in the transducer design was the diametral gaps between the force sensing ring and the dummy sleeves, even though the dummy sleeves had been lapped to the sides of the force sensing ring to minimize the gap to ~ 0.001 in. (0.025 mm). Near the transition range of Reynolds numbers, the two-dimensionality of the boundary layer separation lines has been found by many to be sensitive to flow or surface discontinuities. These cause three-dimensionality in the flow, reduction of spanwise correlation, and early transition of the boundary layer. Initial measurements in the smoothest flow possible, grid HC in Table 1, showed the periodicity expected in the subcritical lift forces, but the coefficients were a factor smaller than those of ideal flow. After completely sealing the diametral gaps and measuring the same low force coefficient, the known nonuniformity of the flow near the boundaries of the square section became suspect. End plates were constructed based on a successful design [8] and installed 7.5 D apart on the end supports as shown in Fig. 3, and the lift coefficients measured were similar to those of ideal flow [13]. Flows in reactors are expected to be much more three-dimensional, and therefore force data obtained in the experiment should provide upper bound estimates.

4. FLOW MEASUREMENTS

Plexiglass windows, 6-in. (152-mm) high \times 2-in. (50.8-mm) wide, were provided in two opposite test section walls so that flows, occurring in the cross-section where the test cylinder would be mounted vertically, could be measured with a TSI Laser Doppler velocimeter (LDV) in the forward scatter, dual-beam mode. The laser, beam splitter, frequency shifter, transmitting optics, receiving optics, and photodetector were all mounted on a milling machine bed which allowed measured traverses over the full width and central 6 in. (152 mm) of the height of the test section. A tracker type of signal processor was employed, and the water was seeded with 0.6×10^{-6} in. (1.5×10^{-3} mm) mean diameter silicon carbide particles to achieve an almost continuous signal, $(20-50) \times 10^3$ samples/s. Although the LDV is self-calibrating when tracking properly, a successful comparison was made with the mean flow velocity measurements of a pitot tube.

Data were obtained at ~ 4000 gpm ($0.25 \text{ m}^3/\text{s}$) and ~ 7000 gpm ($0.44 \text{ m}^3/\text{s}$) for each of the grid conditions of Table 1. The mean velocity V was measured at 1.5-in. (38.1-mm) intervals along the central 6 in. (152 mm) of the vertical and horizontal axes of the test section, at least, and flow direction velocity fluctuations u were measured along the central 3 in. (76.2 mm) of the axes, at least. An HP 5451B fast Fourier transform (FFT) analyzer was used to obtain mean velocities and single-point spectra from 20 minutes of FM taped (3-3/4 ips) data. One-hundred time records, each uniformly sampled from 2048 to 4096 times, were analyzed and averaged to obtain spectra with maximum frequencies from 100 to 2500 Hz. The integral of the average spectrum provided the mean square velocity fluctuation $\langle u^2 \rangle$, and the transform of the spectrum divided by $\langle u^2 \rangle$ provided an autocorrelation normalized to unity at zero time lag. An integral length scale was obtained from Taylor's hypothesis for homogeneous turbulence

$$L = \tau V, \quad (1)$$

where the integral of the normalized autocorrelation to the first zero crossing was used as a very approximate measure of the integral time scale τ .

The mean velocities over the 6 in. (152 mm) central area of the test section were within $\pm 5\%$ of the centerline value, except for grid 24(107). At a given flowrate, the turbulence intensities I and integral scale lengths L over the 3 in. (76 mm) central area of the test section were within $\pm 7\%$ and $\pm 15\%$, respectively, except for grids 24(107) and HC. In the case of grid HC, the absolute variations in I were small, see Table 1, even though the percent variations were substantial ($< 25\%$). The large variations in L , up to 40%, were due to the concentration of the correlation at low frequencies. These correlations have the greatest influence on the shape of the autocorrelation

curve at large τ and therefore the location of the first zero crossing. Such large variations would not be expected if the autocorrelation could have been calculated and integrated for very large time lags. However, due to the very low frequency unsteadiness in the loop pumping, valving, and reservoir levels, all information below 1 Hz had to be deleted any way from all the autocorrelation calculations. The up to 20, 30, and 52% variations in V , I , and L , respectively, indicate that measurements for grid 24(107) are being taken in the very nonhomogeneous jet region of the grid. As such, this represents the most severe, three-dimensional flow condition created for testing. Absolute variations in I and L for all grids are summarized in Table 1. All attempts to create more uniform, high intensity, small scale turbulence failed, and production just may not be possible for the water flow facility size available and the Reynolds number range of interest.

One measure of the degree the grids produce homogeneous, isotropic turbulent flow can be seen in Fig. 4, where the normalized spectral densities of the centerline measurements for all grid conditions are shown to lie in a narrow band close to

$$\frac{V\phi}{4\langle u^2 \rangle L} = \frac{1}{1 + (4\pi f^2/V^2)L^2}, \quad (2)$$

a theoretical spectrum for one-dimensional flow [24]. Also, transverse (spanwise) velocity fluctuations were measured for grid conditions 2 and 52, and the turbulence intensities were within $\sim 15\%$ and the integral scales were $\sim 50\%$ of those in the longitudinal direction.

5. FORCE MEASUREMENTS

The cylinder's force transducer system was calibrated by hanging known dead weights from the force sensing ring. The flatness of the transducer's frequency response to above 100 Hz in water was verified by measuring the transfer function between the transducer's output and the input from an instrumented impulse hammer (PCB K2981A02) during impact with the force sensing ring. See [23] for details.

Typically, lift and drag force data were measured and FM taped (3-3/4 ips) over 20 minutes at 12.5, 25, 37.5, 50, 75, and 100% of the maximum flow rates for all the grid conditions of Table 1. Steady drag forces were calculated by

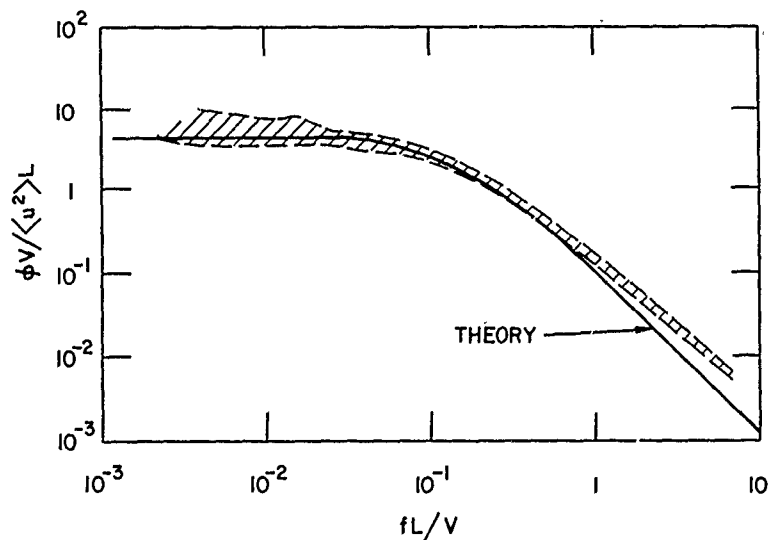


Fig. 4. Centerline spectral density scatter band for all grid conditions compared to theory — [24]

inspection of condensed and low pass filtered (~ 4 Hz) time histories. The FFT analyzer was used to obtain spectra of the fluctuating forces. Either 100 or 175 time records, sampled uniformly 1024 times, were analyzed and averaged with maximum frequencies of 100 or 250 Hz, respectively. The calibrated spectra were integrated and divided by the force sensing ring width to obtain, for example, the mean square lift force/length, $\langle p_L^2 \rangle$. The lift coefficient C_L was calculated from the usual

$$\langle p_L^2 \rangle^{1/2} = \frac{1}{2} \rho V^2 C_L . \quad (3)$$

The steady and fluctuating drag coefficients, C_D and C_D^f , were calculated similarly. No flow blockage corrections were made for the coefficients plotted in Figs. 1, 2, 5, and 6 as a function of N_R and the turbulence grid conditions of Table 1. Note information exists for correcting ideal crossflow [26], and the ideal crossflow data given in the figures is for zero blockage.

The Strouhal numbers of the peak in the lift force spectra were calculated and are shown in Fig. 2. As a measure of the sharpness of the peaks, the half-power bandwidth Strouhal number ΔS was calculated and is shown in Fig. 2 along with the only set of data available for ideal crossflow. Of course, ΔS is very small in ideal crossflow at subcritical N_R .

The effect which different turbulent flows and Reynolds numbers have on the periodicity of the lift forces can be seen best by comparing the example normalized spectra given in Fig. 7 for relatively small and large amounts of turbulence in the flow. The spectral density of the lift force/length ϕ_L are normalized in Fig. 7 according to

$$\phi_L = \phi_L (V/D) (1/2 \rho V^2 D)^{-2} . \quad (4)$$

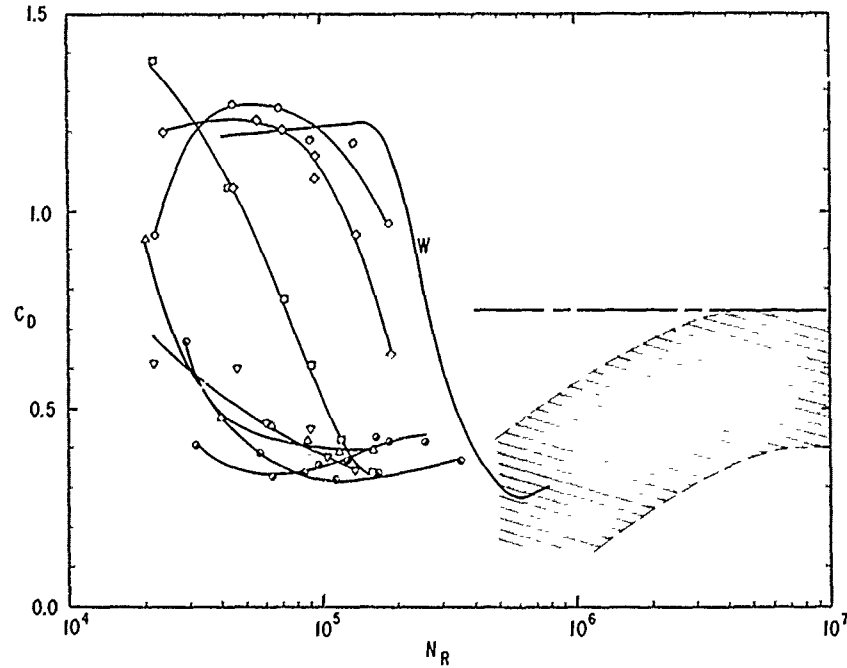


Fig. 5. Mean drag coefficient C_D . Ideal crossflow data notation: Wieselberger from [4] — W, scatter band (////) of existing data, and bounding curve - - - - - See Table 1 for notation.

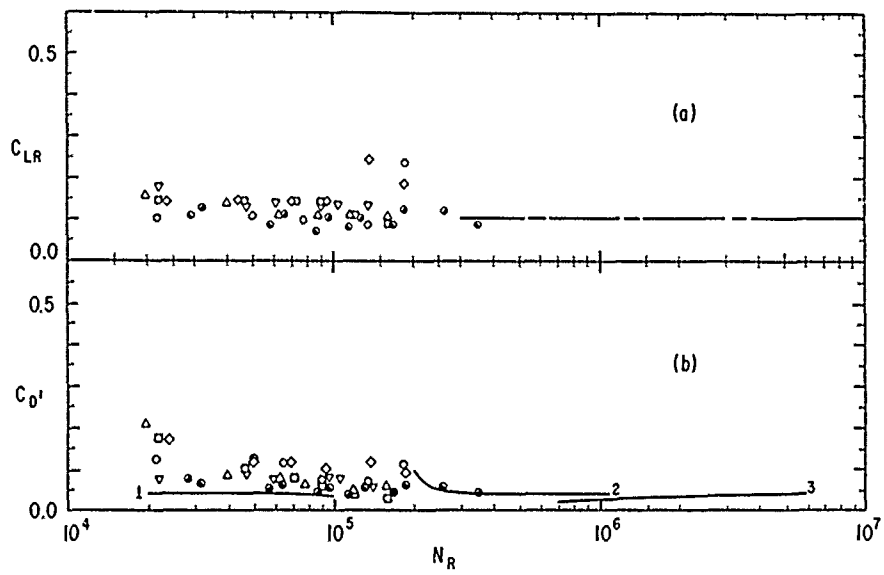


Fig. 6. (a) Wide band lift coefficient C_{LR} . (b) Fluctuating drag coefficient C_D' . See Table 1 and Fig. 1 for notation.

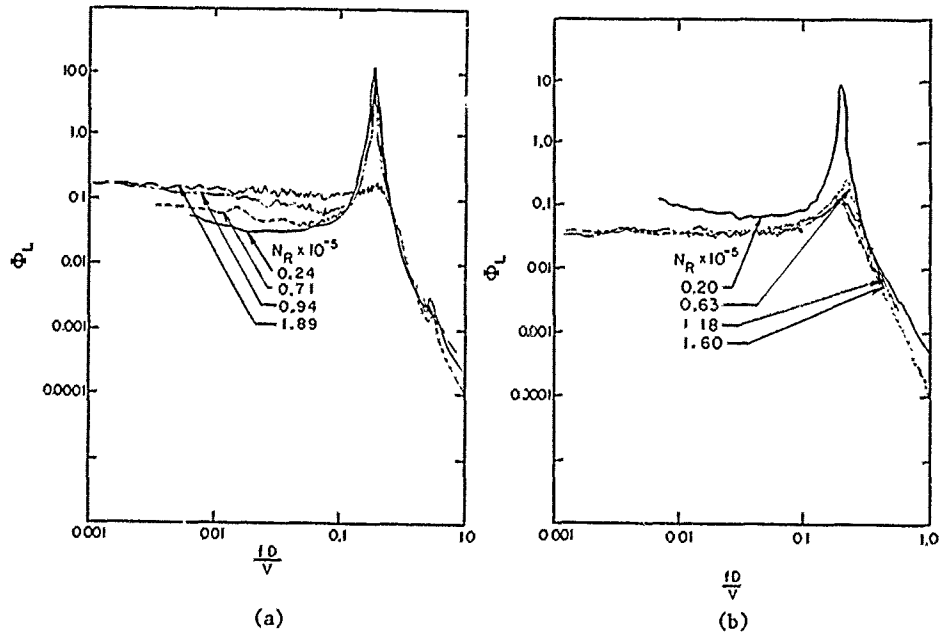


Fig. 7. Normalized lift force spectrum at several Reynolds numbers. (a) Open channel, grid OP, (b) grid 52(493)

Whereas some periodicity exists in the lift force for the open channel (grid OP) at every N_R tested, except the highest, almost no periodicity exists for grid 52 (493), except for the lowest N_R tested. The open channel's spectra are typical for grid HC and grid 2, while grid 52(493)'s spectra are typical for grid 52(338) and grid 24(107). The spectra for grid 24(107) contained almost no periodicity and were typical of a low-pass random signal.

The fluctuating drag force spectra were undistinguished with most energies contained at low frequencies over a wide band. Relatively insignificant amounts of periodicity were observed mainly at the vortex shedding frequency and less at higher harmonics of the shedding frequency. The periodicity at the vortex shedding frequency was probably due to crosstalk with the lift direction forces. The force transducer sensitivity in the drag direction was less than one-third that in the lift direction to provide sufficient drag-direction transducer stiffness [23], and therefore the drag coefficients are very approximate estimates.

6. DISCUSSION

Adding turbulence to the flow affects the fluctuating fluid forces in three ways, at least, with all effects resulting in spectral densities which are more random than periodic. First, the Reynolds number at which the attached boundary layer undergoes transition from laminar to turbulent flow is reduced. This has been observed before [21] and can be seen in the relatively sharp declines in C_L and C_D in Figs. 1(a) and 5, as well as in the increase in ΔS in Fig. 2(b). Thus, the critical region appears to occur over a larger Reynolds number range, and the associated wake forces are random at N_R where they would be periodic in ideal crossflow. Also, the more turbulent flows produce smaller subcritical ranges of Reynolds numbers.

Interpreting the first effect in another way, the C_L in Fig. 1 and the C_D in Fig. 5 can be seen to be greatly reduced as I is increased to $\sim 15\%$ for a given $N_R < 10^5$. By comparing the C_L for grids with similar I (OP and 2(493), 24(191) and 52(493), and 52(338) and 24(107)), there appears to be a tendency for smaller L to produce smaller C_L . Such a trend is less distinguishable for C_D . Even though the variation in L used in testing is not large, flows with small $L < D$ have been observed to be most effective in interacting with the boundary layer flow on the cylinder [17]. In response analysis, use of the C_L and C_D corresponding to the largest L would be conservative.

The second effect of turbulence in the flow is the degradation of the two-dimensional vortex shedding process: the reduction of the spanwise correlation of the surface pressures [15,16] and forces [21], to less than D in some cases. Since the width of the force sensing ring was small, $1/2 D$, the spanwise correlation degradation also is reflected in the broadening and reduction of the amplitude of the peaks in the lift force spectra of Fig. 7, for example. Therefore, the second effect is difficult to distinguish from the first effect of early transition.

The third effect is pressure fluctuations are created on the upstream side of the cylinder surface [15,16] by the impinging turbulence in the flow. As a result, the magnitude of the drag coefficient is larger in turbulent flow than in ideal crossflow (see Fig. 6(b)), and the lift force spectra are large at frequencies below the vortex shedding peak frequency (see Fig. 7). Periodicity may still exist in the drag direction at twice the shedding frequency, but for the most part it is submerged in the wide band random forces which the turbulence in the flow creates.

In summary, the lift force spectra in turbulent flow appear to consist of a component in a narrow band of frequencies, due to organized vortex shedding, superimposed on a component which occurs over a wide band of frequencies primarily below the vortex shedding frequency. The relative size of the two components depends upon N_R and the turbulence of the free stream. The fluctuating drag spectra are similar to the lift spectra but without any significant periodic component. The C_L and C_D provide a measure of the amplitude of the spectra, but the distribution of the spectra is needed for response analysis.

7. BOUNDING SPECTRA

Because the velocity fluctuation spectra of the turbulent flow was fit well by (2), see Fig. 4, attempts were made to fit a similar form

$$\phi_D(\bar{f}) = \phi_{D0}(1 + 4\pi^2 f^2)^{-1} \quad (5)$$

to the fluctuating drag force spectra. ϕ_D is graphed in Fig. 8 (without D subscripts) for $\phi_0 = 4.5$. The ϕ_D is related to the single-sided spectra for the fluctuating drag force/length as ϕ_L is related to ϕ_L in (4), and \bar{f} is the reduced frequency fD/V . Although good fits to the data across the entire frequency spectrum could not be achieved with (5), a ϕ_{D0} could be chosen for each turbulence condition such that ϕ_D formed an upper bound on the wide band part of the spectra for all values of Reynolds number N_R . Table 1 associates the ϕ_{D0} chosen with the turbulence condition and the RMS fluctuating drag force coefficient C_{DC}' calculated by integrating (5) from zero to infinity

$$(C_{DC}')^2 = 0.225 \phi_{D0} \quad (6)$$

The degree to which (5) approximates the measured spectra is well represented by the differences between the calculated C_{DC}' , given in Table 1, and the measured C_D' shown in Fig. 6(b). Except for the lowest N_R and grid 2(493) data, (5) represented the spectra well: the spectra are nearly the same for the same turbulence condition and different N_R . By adding a deterministic force at $\bar{f} = 0.4$ with a coefficient of $(C_D' - C_{DC}')$, when $C_D' > C_{DC}'$, to the wide band excitation forces, an upper bound on the fluctuating fluid drag force is generated.

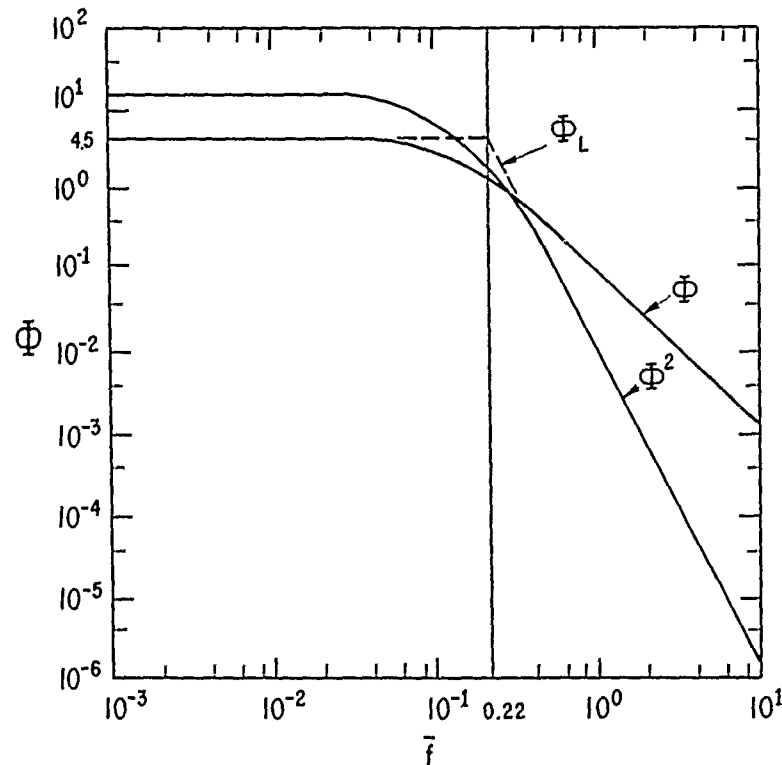


Fig. 8. $\Phi(\bar{f})$ shown with $\Phi^2(\bar{f})$ and a linear bound Φ_L to Φ , $\bar{f} < 0.22$, and Φ^2 , $\bar{f} > 0.22$

The spectra of the fluctuating lift force/length could not be as simply approximated as Φ_p , because of the often relatively large narrow frequency band component centered at the vortex shedding Strouhal number S . Again, empirical formulations were sought which would bound the measured spectra and lead to upper bounds in a response analysis. The wide band component of the lift force spectra for $\bar{f} < S$ appeared to be representable by Φ in Fig. 8, while for $\bar{f} > S$ it appeared to be representable by Φ^2 , except where the narrow band component existed. Thus the wide band component of the normalized lift spectra was represented by the linear approximation

$$\begin{aligned}\Phi_L &= \Phi_{LO} & \bar{f} < 0.22 \\ &= (2.34 \times 10^{-3})\Phi_{LO}\bar{f}^{-4} & \bar{f} > 0.22\end{aligned}\quad (7)$$

The narrow band component was represented by a deterministic force at $\bar{f} = 1/S = 0.2$ with a lift coefficient

$$C_{LV} = C_L - C_{LR}, \quad (8)$$

where C_L is the measured lift coefficient and C_{LR} is a calculated value associated with the wide band component: the area under the curve (7) from $\bar{f} = 0$ to ∞ ,

$$C_{LR}^2 = 0.293 \Phi_{LO}. \quad (9)$$

The Φ_{LO} selected to best fit (visually) the experimental data, and the lift coefficients are given in Figs. 1 and 6(a).

8. CONCLUSIONS

The data obtained verifies the observation of others [21] that C_L will be smaller for flows with larger turbulence intensities I at the same Reynolds number in the range $2 \times 10^4 < N_R < 10^5$. Also, flows with smaller integral length scales ($L \sim 0.5 D$) showed a trend to produce smaller C_L than flows with the same I but $D < L < 2D$.

Very turbulent flows eliminate periodic vortex shedding forces, probably through a combination of causing early transition to a turbulent boundary layer and disturbance of the two-dimensional spanwise correlation necessary to produce significant vortex shedding. Intermediate turbulent flows produced both random and periodic components in the lift force spectra, and the drag force spectra were primarily random.

Although exact modeling of the spectra was not possible, analytical forms of bounding spectra were given. These could be used with the fluid force coefficients presented in Figs. 1, 5, and 7, and spanwise correlation lengths available in the literature, to predict upper bounds on the RMS vibration response of cylinders in some turbulent flows assuming fluid-structure interaction (lock-in) does not occur [25].

ACKNOWLEDGMENTS

Work supported by the U.S. Department of Energy, Office of Breeder Technology Projects, under Contract W-31-109-Eng-38.

The help of Art Miskevics in performing the tests, the hardware designs of Ed Bielick, and the continued support and consultation of Marty Wambsganss are greatly appreciated.

REFERENCES

1. Blevins, R. D., Flow-Induced Vibration, Van Nostrand, 1977.
2. Turula, P., and Mulcahy, T. M., "Computer Modeling of Flow-Induced In-Reactor Vibrations," Journal of Power Division, Proc. ASCE, Vol. 103, No. 1, 1977, pp. 37-49.

3. Graham, C., "A Survey of Correlation Length Measurements of the Vortex Shedding Process behind a Circular Cylinder," Engineering Projects Laboratory Report 76028-1, Massachusetts Institute of Technology, 1966. Available from U. S. Dept. of Commerce Clearinghouse, AD 650 849.
4. Roshko, A., "Experiments on the Flow Past a Circular Cylinder at Very High Reynolds Number," Journal of Fluid Mechanics, Vol. 78, 1961, pp. 561-576.
5. Ericson, L. E., and Redding, J. P., "Criterion for Vortex Periodicity in Cylinder Wakes," AIAA Journal, Vol. 17, No. 9, 1979, pp. 1012-1013.
6. Sarpkaya, T., "Vortex-Induced Oscillations - A Selective Review," Trans. ASME, Journal of Applied Mechanics, Vol. 46, 1979, pp. 241-258.
7. Loiseau, H., and Szechenyi, E., "Analyse Expérimentale Des Portances sur un Cylindre Immobile soumis à un Écoulement Perpendiculaire à son Axe à des Nombres de Reynolds Elevevés," La Recherche Aérospatial, No. 5, 1972, pp. 279-291.
8. Stansby, P. K., "The Effects of End Plates on the Base Pressure Coefficient of a Circular Cylinder," Aeronautical Journal, Vol. 78, 1974, pp. 36-37.
9. Szechenyi, E., "Supercritical Reynolds Number Simulation for Two-Dimensional Flow over Circular Cylinders," Journal of Fluid Mechanics, Vol. 70, No. 3, 1975, pp. 529-542.
10. Jones, G. W., "Unsteady Lift Forces Generated by Vortex Shedding about a Large, Stationary, and Oscillating Cylinder, ASME Paper 68-FE-36, 1968.
11. Schmidt, L. V., "Fluctuating Force Measurements upon a Circular Cylinder at Reynolds Numbers up to 5×10^6 ," Meeting on Ground Wind Load Problems in Relation to Launch Vehicles, NASA Langley Research Center, June 7-8, 1966, NASA TM 57779, 1966, pp. 19.1-19.17.
12. Fung, Y. C., "Fluctuating Lift and Drag acting on a Cylinder in a Flow at Supercritical Reynolds Numbers," Journal of Aerospace Sciences Vol. 27, No. 11, 1960, pp. 801-814.
13. Keefe, R. T., "An Investigation of the Fluctuating Forces acting on a Stationary Circular Cylinder in a Subsonic Stream and of the Associated Sound Field," Report No. 76, 1961, University of Toronto Institute for Aerospace Studies.
14. Fage, A., and Warsap, J. H., "The Effects of Turbulence and Surface Roughness on the Drag of a Circular Cylinder," London R and M No. 1283, 1929, Aeronautical Research Council.
15. Kiya, M., et al., "A Contribution to the Free-Stream Turbulence Effect on the Flow Past a Circular Cylinder," Journal of Fluid Mechanics, Vol. 115, 1982, pp. 151-164.
16. Bruun, H. H., and Davies, P. O. A., "An Experimental Investigation of the Unsteady Pressure Forces on a Circular Cylinder in Turbulent Crossflow," Journal of Sound and Vibration, Vol. 40, No. 4, 1975, pp. 535-559.
17. Sadeh, W. Z., and Brauer, H. J., "Coherent Substructure of Turbulence near the Stagnation Zone of a Bluff Body," Journal of Wind Engineering, Vol. 8, 1981, pp. 52-72.
18. Simiu, E., "Modern Developments in Wind Engineering: Part 2," Engineering Structures Vol. 3, 1981, pp. 242-248.
19. Vermeulen, P. E. J., "Turbulence Effects on High Reynolds Number Flow Past Circular Cylinders," Designing with the Wind Symposium, June 15-19, 1981, Vol. 1, Theme V, Paper V-3, Centre Science and Technology, Nantes, France (1981).
20. Surry, D., "Some Effects of Intense Turbulence on the Aerodynamics of a Circular Cylinder at Subcritical Reynolds Number," Journal of Fluid Mechanics, Vol. 52, No. 3, 1972, pp. 543-563.
21. So, R. M. C., and Savkar, S. D., "Buffeting Forces on Rigid Circular Cylinders in Crossflows," Journal of Fluid Mechanics, Vol. 105, 1981, pp. 397-425.
22. Loehrke, R. I., and Nagib, H. M., "Control of Free-Stream Turbulence by Means of Honeycombs: A Balance between Suppression and Generation," Journal of Fluids Engineering, Vol. 98, No. 3, 1976, pp. 342-353.

23. Mulcahy, T. M., "A Crossflow Force Transducer," ANL-CT-82-11, 1982, Argonne National Laboratory, Argonne, IL. Also "Measurement of Crossflow Forces on Tubes," ASME Paper No. 83-PVP-77, presented at ASME PVP Meeting, June 1982, Portland, Oregon.

24. Hinze, J. O., Turbulence, McGraw Hill, New York, 1975.

25. Mulcahy, T. M., "Design Guide for Single Circular Cylinders in Turbulent Crossflow," ANL-CT-82-7, 1982, Argonne National Laboratory, Argonne, IL.

26. Richter, A., and Naudascher, E., "Fluctuating Forces on a Rigid Cylinder in Confined Flow," Journal of Fluid Mechanics, Vol. 78, 1976, pp. 561-576.

27. Cheung, J. C. K., and Melbourne, W. H., "Turbulence Effects on Some Aerodynamic Parameters of a Circular Cylinder at Supercritical Reynolds Numbers," Journal of Wind Engineering and Industrial Aerodynamics, Vol. 14, 1983, pp. 399-410.

APPENDIX I - NOMENCLATURE

b	Average web size of turbulence generator grid (pitch = 0.95 d)
C_D	Steady drag force/length/(1/2 $\rho V^2 D$)
C'_D	RMS fluctuating drag force/length/(1/2 $\rho V^2 D$)
C'_{DC}	Calculated C'_D
C_L	RMS lift force/length/(1/2 $\rho V^2 D$)
C_{LR}	Random component of C_L
C_{LV}	Periodic component of C_L
d	Hole diameter of turbulence generator grid
D	Cylinder diameter
f	Frequency, cycles/sec (Hz)
f_v	Vortex shedding frequency
Δf	Half-power bandwidth of lift force spectra
\tilde{f}	fD/V , reduced frequency
I	Flow direction turbulence intensity, $\langle u^2 \rangle^{1/2} / V$
λ_c	Spanwise correlation length of fluid forces
L	Flow direction turbulence integral scale length
N_{R_2}	VD/v , Reynolds number
$\langle p_L^2 \rangle$	Mean-square lift force/length
S	Strouhal number, $f_v D / V$
ΔS	$\Delta f D / V$
SB	Solid blockage of grid
t	Time
T	Taylor number, $L_u / (L_u / D)^{0.2}$
u	Fluctuating component of crossflow in mean flow direction
$\langle u^2 \rangle$	Mean square velocity in the flow direction
V	Mean crossflow velocity
v	Fluid kinematic viscosity
ρ	Fluid mass density
τ	Flow direction turbulence integral time scale
ϕ	Longitudinal velocity fluctuation spectral density ($0 < f < \infty$)
ϕ_D	Spectral density of fluctuating drag force/length ($0 < f < \infty$)
ϕ_L	Spectral density of fluctuating lift force/length ($0 < f < \infty$)
ϕ	Normalized spectral density
ϕ_D	Normalized fluctuating drag spectral density
ϕ_{D0}	ϕ_D for $\tilde{f} = 0$
ϕ_L	Normalized lift force spectral density
ϕ_{L0}	ϕ_L for $0 < \tilde{f} < 0.22$

BUFFETING OF ISOLATED TUBES IN CROSS FLOW

S. D. Savkar
General Electric Company
Corporate Research and Development
Schenectady, New York

ABSTRACT

A study of the unsteady forces induced on rigid isolated cylinders immersed in cross flows of varying levels of inflow turbulence is presented. Experimental measurements on which the study is based were conducted primarily in a water tunnel. An analogy is found to exist between the steady and unsteady forces induced on isolated cylinders. Indeed, as a function of the Reynolds number, the functional behavior of the fluctuating forces can be divided into subcritical, transitional and supercritical regimes. Correlations are also presented between the fluctuating base pressure of the cylinder and forces respectively induced by the vortex wake in uniform flow and buffeting forces induced in turbulent flows.

NOMENCLATURE

a	Axial separation of vortices used in the Karman model
b	Transverse separation of vortices used in the Karman model
C_C	Critical damping ratio
\bar{C}_D	Steady (time averaged) drag coefficient = $D/\left(\rho \frac{U^2}{2} \cdot d\right)$
C'_d	Fluctuating (RMS) drag coefficient = $D'/\left(\rho \frac{U^2}{2} \cdot d s\right)$
C'_L	Fluctuating (RMS) lift coefficient = $L'/\left(\rho \frac{U^2}{2} \cdot d s\right)$
C_0	Damping
C_p	Pressure coefficient = $(P - P_\infty)/\left(\rho \frac{U^2}{2}\right)$
$(C_p)_b$	Base pressure coefficient
d	Test cylinder diameter
D	Steady drag per unit span
D'	Fluctuating drag measured over a span s
f	Frequency in Hz, f_S the Strouhal frequency
k	Base pressure parameter = $\sqrt{1 - (C_p)_b}$
K_2	Modal stiffness of the cylinder
l	Length scale
l_x	Axial integral scale of turbulence
l_y	Transverse integral length of turbulence
L'	Fluctuating lift measured over a span s
m_0	Modal mass of the cylinder
M	Grid mesh dimension
P	Static pressure on the cylinder

P_∞	Freestream static pressure
Re	Reynolds number $U_\infty d/\nu$
s	Active span over which the fluctuating force is measured
St	Strouhal number $= fd/U_\infty$
U, U_∞	Freestream speed
V	Speed of propagation of vortices in the Karman model
X	Distance between the grid and centerline of test cylinder
ν	Kinematic viscosity
ω	Circular frequency
ω_0	Natural frequency of the test cylinder system including load cells
γ	Critical damping ratio
ρ	Density of test fluid
$\Psi(\omega)$	Power spectrum of applied load
$\Phi(\omega)$	Power spectrum of measured load

INTRODUCTION

A systematic overview of the buffeting forces induced on cylinders and cylindrical arrays by cross flows is offered in this and the accompanying paper.¹ By buffeting, it is meant the unsteady forces induced by both a uniform flow and a flow rendered turbulent by means of suitably designed grids. In the literature, the former is often referred to as Strouhal or vortex wake excitation where as the latter is referred to as buffeting. As a result of the present series of papers, this distinction is somewhat blurred. Instead, what differences there are appear to stem from the flow regime of operation. However, because of common usage and the concise description it affords, this paper will continue the loose, separate usage of the two terms.

The present study was conducted on rigid cylinders. The forces induced on rigid cylinders are important for design calculations since they represent the excitation experienced in incipient vibrations. It is the magnitude and spectral character of these forces that the designer needs to avoid or minimize vibrations in his design. The precise definition of what is meant by a rigid body is very important from the point of view of the experimental technique. The usage here is based on a dynamic rather than a static consideration.

Early research on isolated cylinders concentrated on characterizing the time-averaged drag forces as a function of Reynolds number, Re .² An important observation that was made was the identification of, broadly-speaking, three regimes of uniform flow as a function of Reynolds number. The three regimes are illustrated in Figure 1, in which the steady (i.e., the time-averaged) drag coefficient C_D is plotted against the Reynolds number. In the transitional regime, the boundary layer on the cylinder goes from laminar to turbulent and the point of separation moves from the upstream location ($\approx 80^\circ$ from the stagnation point) to a downstream location $\approx 110^\circ$. At the same time the wake substantially narrows and the pressure component of steady (time-averaged) drag substantially decreases.

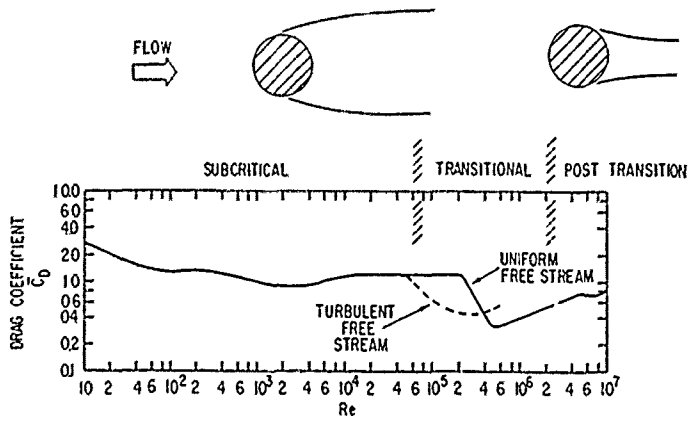


Figure 1. Drag coefficient and flow regimes of an isolated cylinder.

* $Re = U_\infty d/\nu$, where U_∞ is the freestream velocity upstream of the cylinder, d the cylinder diameter and ν the fluid kinematic viscosity.

Because it disturbs the boundary layer on the cylinder, the effect of turbulence in the freestream is to advance the transition of the boundary layer from laminar to turbulent. In so doing, the point of transition, in terms of the $\overline{C_D}$ - Re dependence, shifts to a lower Reynolds number,⁵ as in Figure 1. Below this shifted transition, the freestream turbulence does not appear to significantly affect the steady drag values. The question naturally arises as to the unsteady response of the cylinder in the two flow (uniform and turbulent) situations.

Despite many attempts, the unsteady response of the cylinder has not, until recently, been on as firm a footing. In part, this had to do with the difficulty of measuring the unsteady forces. Indeed, the best available data were only recently measured by Richter and Naudascher,⁶ who moreover have carefully examined the effect of tunnel blockage (or interference) on the Strouhal frequency, lift and drag of an isolated rigid cylinder. Prior data concentrated largely on measuring the Strouhal number or normalized vortex shedding frequencies St (Roshko⁷). Eventually, it was discerned that the behavior of $1/St$ was analogous to $\overline{C_D}$ as a function of Re (e.g., Morkovin⁸). The effect of a turbulent freestream has not been as extensively investigated. Surry⁹ and Batham¹⁰ represent the typical studies available which have largely drawn their insights from local pressure measurements.

EXPERIMENTAL APPARATI

Two different facilities were employed in the course of this study. One was a wind tunnel and one a water tunnel facility at Pennsylvania State University. The wind tunnel served to develop the piezoelectric force measurement system.² The water tunnel was employed for the isolated cylinder study to cover a range of Reynolds numbers up to 2×10^6 and forms the basis of this paper. A test rig designed around the piezoelectric force measurement scheme was employed in both the study presented here and in Reference 1. In what follows, the design principles of the direct force measurement scheme and the test tunnels will be given.

Description of the Technique to Measure Unsteady Buffeting Forces

A schematic of the test cylinder and its mounting within the test tunnel is shown in Figure 2. The test cylinder was constructed of a thin-walled aluminum tube. To avoid end effects, measurements were carried out only over the central exposed part of the span. This was accomplished by stepping down the ends of the cylinder and passing it through dummy end sleeves. The sleeves thereby avoided the local disruption of the mean flow. The span of the cylinder over which the forces were measured could be changed by changing the location of the end steps and making compensatory changes in the length of the end sleeves.

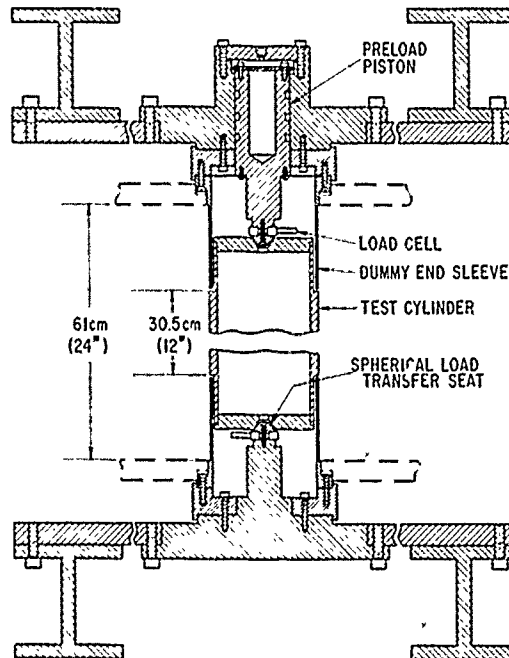


Figure 2. Schematic of the load cell instrumented test cylinder used in the tube array testing.

At the heart of the measurement system are two Kistler 9251A three-axis load cells located at the two ends of the test cylinder. The load is transmitted from the cylinder to the load cells by friction, hence the level of friction between the contacting parts must be sufficiently high. This is accomplished in the apparatus by a pneumatic preload device.

As has been pointed out, the unsteady loads can only be measured accurately if the system is rigid. The notion of rigidity has to be dynamically based. The dynamics of the load cell mounted test cylinder can be represented as a simple spring mass system (see Figure 3) since the load cells are much stiffer than the cylinder. Given the modal description of the system and considering only the lowest flexural mode of vibration, the governing system can be represented as

$$m_0 \ddot{x} + c_0 \dot{x} + k_0 x = F(t) \quad (1)$$

where m_0 is the mode weighted mass of the cylinder, c_0 the damping, k_0 the stiffness and $F(t)$ the applied unsteady load. The question is the relationship between $f(t)$, the load sensed by load cell, and the applied load, $F(t)$. Assuming a harmonic loading $F(t) = F_0 e^{i\omega t}$ and that $f = f_0 e^{i\omega t}$,

$$\frac{f_0}{F_0} = \frac{\sqrt{1 + \left(2\gamma \frac{\omega}{\omega_0}\right)^2}}{\left[\left(1 - \frac{\omega^2}{\omega_0^2}\right)^2 + \left(2\gamma \frac{\omega}{\omega_0}\right)^2\right]^{1/2}} \quad (2)$$

where ω_0 is the lowest flexural mode frequency, $\omega_0 = \sqrt{k_0/m_0}$, $\gamma = c_0/c_c$ and c_c is the critical damping = $2m_0\omega_0$. This is of course the equation for vibration isolator. Since the load measuring system has to behave opposite to the isolator, it is clear that the dominant frequency of the applied load ω must be much less than ω_0 . Ignoring the damping for $\omega/\omega_0 = 1/4$ the dynamic contamination of the loads registered by the load cell would be about 7%. In the apparatus used, γ was about 1 to 2% so that the error introduced by ignoring damping, even up to $\omega/\omega_0 = 0.5$, was less than two orders of magnitude lower. It follows that a simple correction to the load cell output can be devised provided that ω/ω_0 sufficiently less than 1.

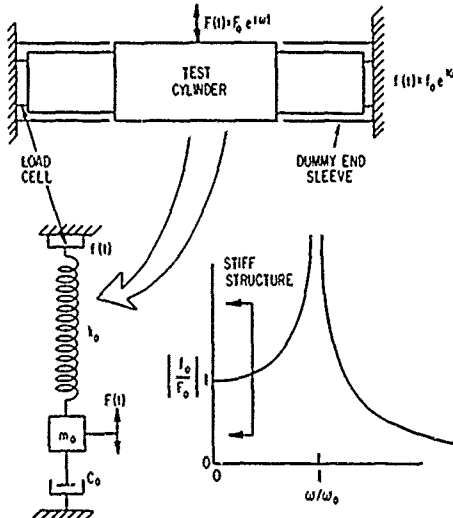


Figure 3. Dynamic behavior of load cell mounted test cylinder.

Suppose that the power spectrum of $f(t)$ is $\phi(\omega)$ and that of the applied load $F(t)$ is $\Psi(\omega)$, then to the first order it can be shown that

$$\Psi(\omega) = \phi(\omega) \cdot (1 - \omega^2/\omega_0^2)^2 \quad (3)$$

It was a simple matter to design a filter to automatically make this correction by using the block multiplication feature of the Hewlett-Packard Fourier analyzer system used. Even so, every attempt was made to operate at conditions such that the bulk of the applied load spectrum fell below $\omega_0/4$. The resultant corrections rarely resulted in changing (reducing) the RMS values by more than 7% and were generally more on the order of 1 to 3%.

Description of Water Tunnel Facility

The Penn State water tunnel used in this study is a closed-circuit tunnel and has a cross section that is circular at most points. The average velocity in the working section can be continuously varied from 0 to 24 m/s. A detailed description of this facility is given by Lehman¹⁶ and So and Savkar.³

Grids of the square mesh type were used to produce homogeneous turbulence of approximately the same intensity, but different length scale at $x/M = 10$, where x is the stream coordinate and M is the mesh size, in the tunnel test section. The mesh sizes chosen were 25.4, 50.8, and 76.2 mm, respectively. Square bars of different dimensions were used to make up the grid so that a blockage of $\approx 34\%$ results for all three grids. Turbulence characteristics were measured by a DISA hot film anemometer. The measured intensity level at $x/M = 10$ for all three grids was $\approx 9.5\% \pm 1\%$ while the measured integral axial length scale to mesh size ratios at $x/M = 10$ were respectively 0.34, 0.36 and 0.31.

Although the water tunnel was capable of delivering a flow with a mean velocity up to 24 m/s in the test section at an operating pressure of 400 kPa, cavitation considerations at the grid and test cylinders limited the maximum mean velocity to 9.1 m/s with grids and 12.0 m/s without grids.

Steady Drag Measurements

The steady drag measurements were made by integrating the static pressure measured around a cylinder. This procedure yields primarily the pressure drag; however, the skin friction drag over the range of Reynolds numbers tested contributes less than 3% of the total drag. The static pressure distribution was measured on specially designed cylinders.

Calibration of Load Cells

The calibration of the load cell cylinders was done in situ using dead weights both before and after each series of tests to be reported herein. The two sets of calibrations never disagreed with each other more than 1%. Both the lift and drag directions were separately calibrated. The cross talk between the two channels was less than 1%.

Data Recording and Data Analysis

All the fluctuating force data have been stored on tape. The data recording was carried out at 7 1/2 ips. Both the recording and playback of the data was carried out on a Bell and Howell 4020A fourteen channel tape recorder. All the data reduction of the fluctuating forces was carried out on a Hewlett-Packard 5451 Model C Fourier analyzer. The spectral plots were recorded directly on to a Hewlett-Packard 9872 S plotter coupled to the Fourier analyzer. RMS values were typically recorded by integrating the spectra up to the frequency sufficiently below the structural frequency to which the integrals remained flat.

RESULTS

Mean Drag of an Isolated Cylinder

Sample plots of the the C_d distribution around a single cylinder (uncorrected for blockage) in uniform as well as turbulent cross flows are given in Figure 4. Figure 4 shows the distributions for the 38.1 mm diameter cylinder at three different Reynolds numbers in a uniform stream and a turbulent stream created by the 50.8 mm grid. The turbulent intensities for these two streams were 0.5% and 9.5%, respectively. It can be seen that at pretransitional Reynolds number (2.6×10^4), the 9.5% turbulent intensity in the approach flow does not significantly disturb the boundary layer development around the cylinder. As a result, a laminar separation of the viscous layer still occurs and approximately the same C_d distribution is obtained for the two cases (Figure 4). As the Reynolds number, Re , is increased to approximately 10^5 , a laminar separation of the viscous layer still persists in the uniform flow case, but the separation seems to change to a turbulent one for the turbulent flow case. This gives rise to a big difference in the base pressure between the two cases, with the base pressure being higher in the case of a turbulent cross flow (Figure 4). Further increase in Re to 3×10^5 causes the viscous layer to have a turbulent separation in the uniform flow case, too, and the C_d distributions for the two cases, with or without the grid, are again identical (Figure 4). Changing the grids but not the turbulent intensity does not have an appreciable effect on the general development of the flow and essentially the same C_d distributions are obtained at the same Re for turbulent cross flows created by different grids.

Characteristics of the Fluctuating Forces

The Strouhal frequencies of the lift and drag signals were determined from the auto-power spectra of the signals. At low Re , the lift and drag spectra are similar to those obtained by Richter and Naudasher. Therefore, they are not shown here. There is only one distinct peak in the spectra and the Strouhal frequencies can be identified without ambiguity. As Re is increased, the peak in the spectra becomes less and less distinct, resulting in no identifiable peak for the Strouhal drag at $Re = 3 \times 10^5$. The calculated Strouhal numbers, $St = f_s d/U_d$, is plotted vs. Re in Figure 5. It can be seen that St remains fairly constant at 0.21 for Re less than 2×10^5 . Beyond this point, the spectra often contained two distinct peaks. This resulted in two legs to the St vs. Re curve. The upper leg appears to match the data of Richter and Naudasher. The lower leg, on the other hand, generally defined the frequency through which most of the spectral energy was concentrated. There are reasons to believe that the lower leg is the more appropriate frequency as will be suggested presently. A sample spectrum with the double peak is illustrated in Figure 6.

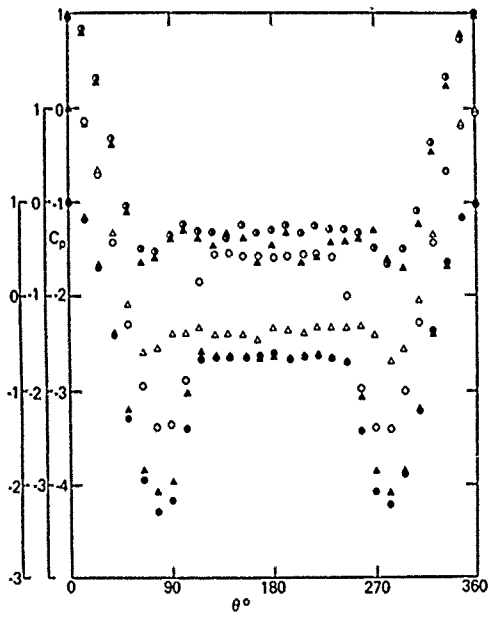


Figure 4. Pressure distributions around the 38.1 mm diameter test cylinder in cross flows at three different Re . Measurements: with no grid, Δ , $Re = 2.62 \times 10^4$; \square , $Re = 10.0 \times 10^4$; \diamond , $Re = 30.6 \times 10^4$; with 50.8 mm grid, \circ , $Re = 2.67 \times 10^4$; \bigcirc , $Re = 10.4 \times 10^4$; \bullet , $Re = 34.5 \times 10^4$.

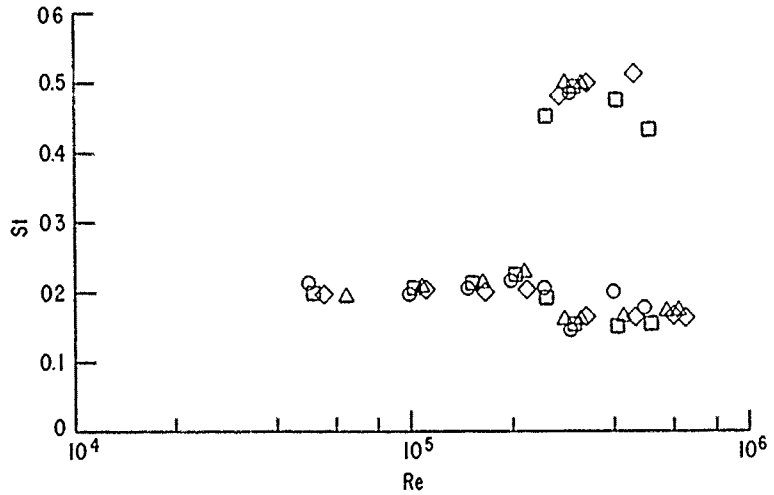


Figure 5. Transitional Strouhal spectrum showing the double peak. The symbols used match Figure 12.

The spectral character of the buffeting data have been examined in Reference 3. There was in fact some variation in the spectral character as a function of the active span. The data for the largest active span showed a distinct peak for all three grids and over the whole range of flows tested. This allowed a ready definition of a Strouhal frequency. The spectra for the other situations were not always so sharp. After carefully evaluating all the data and noting the resemblance between the buffeting and grid spectra, it was decided that unless the spectrum showed a distinct peak, the Strouhal frequency was defined as the "knee" in the spectrum. The knee appeared to be a logical choice since the Strouhal peak, when present and distinct, as with the largest active span, always coincided with it. This is illustrated in Figures 7a and 7b. When viewed this way, the plot illustrated in Figure 8 resulted for buffeting. Whereas in the subcriti-

cal regime the frequency was well defined, a certain amount of ambiguity appeared in the transitional region. This dual peak character of the spectra is very similar to the Strouhal data. Again, for consistency, it is the lower leg that is picked as the definition of the Strouhal frequency.

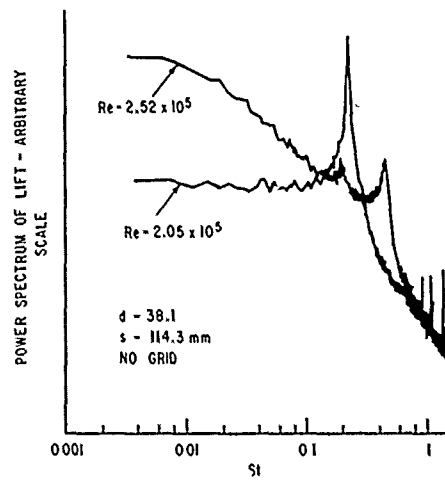


Figure 6. Variation of the uniform flow Strouhal number St with Reynolds Number, Re .

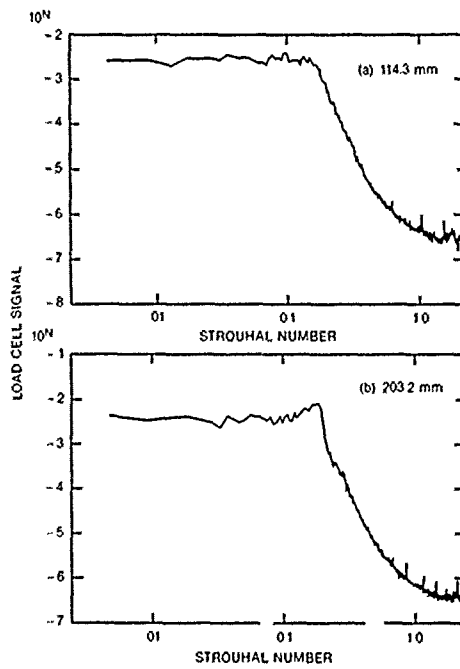


Figure 7a,b. Buffeting spectra for 114.3 mm and 203.2 mm spans with 50.8 mm grid turbulence. Note the correspondence of the larger span Strouhal peak with the knee of the smaller span spectrum.

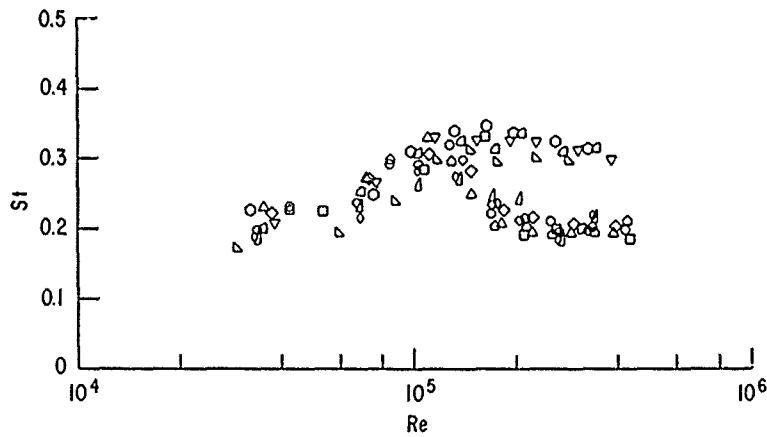


Figure 8. Variation of the turbulent flow Strouhal numbers St with Reynolds number Re . The symbols used match Figure 14.

The general behavior of both the uniform and turbulent flow buffeting lift C'_L and steady drag \bar{C}_D with Re (uncorrected for blockage) are shown in Figure 9. The agreement between the uniform flow C'_L presented (16% area blockage) and those of Richter and Naudascher⁶ for 25% blockage is rather remarkable. The major importance of Figure 9 is the behavior of the C'_L and \bar{C}_D curves and the effects of turbulent intensity on the steady and unsteady forces. Both the Strouhal C'_L and \bar{C}_D go through a transition region where the values drop by ten-fold for the Strouhal C'_L and somewhat less for \bar{C}_D . The same behavior is observed for the buffeting C'_L and \bar{C}_D ; however, the transition now occurs at a lower value of Re . This similarity between the behavior of the fluctuating forces and that of \bar{C}_D with Re is an important observation. It is evident that the magnitudes of \bar{C}_D and C'_L are about the same order for the active span of 3d and for the range of Re illustrated. This suggests that for design purposes, an estimate of the C'_L can be obtained from the \bar{C}_D vs. Re curves for both Strouhal and buffeting forces. An exactly similar behavior was found for the fluctuating drag although its amplitude was an order of magnitude lower.³

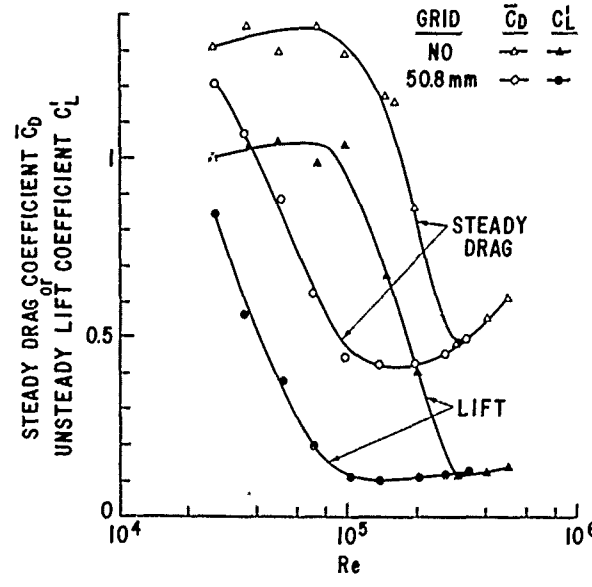


Figure 9. The correspondence between the steady drag of an isolated cylinder and its fluctuating lift in uniform and turbulent flow.

The data illustrated in Figure 9 are for one active span s ($s = 114.3$ mm) and for one mesh M grid ($M = 76.2$ mm). As the grid and the active span are changed, the spanwise correlation of the forces induced changes. As the active span is reduced, the flow appears increasingly better correlated in uniform flow and the amplitude of the fluctuating lift coefficient (and fluctuating drag) is expected to increase. In a like manner, in turbulent flow, one expects the spanwise correlation of the fluctuating forces to be proportional to the statistically defined average eddy scale (in the spanwise direction). Thus as the ratio of the eddy scale to the active span increases, one expects an increase in the measured fluctuating force coefficient. It is physically arguable that as this ratio becomes very large, one should begin to approach uniform flow conditions. The trends suggested by the above arguments are illustrated for four active spans and three different grids in Figures 10a, b, c and d. In these figures, the ordinate is the ratio of the fluctuating (RMS) lift to steady drag coefficient. The parameter between the different figures is the active span over which the force was measured. For reference, the Strouhal data measured in each case are reproduced in each figure. All data are uncorrected for blockage. The evidence suggests that for all three of the tested grids, the transition moves to a lower Reynolds number with the post-transition lift forces being higher as the grid size is increased.

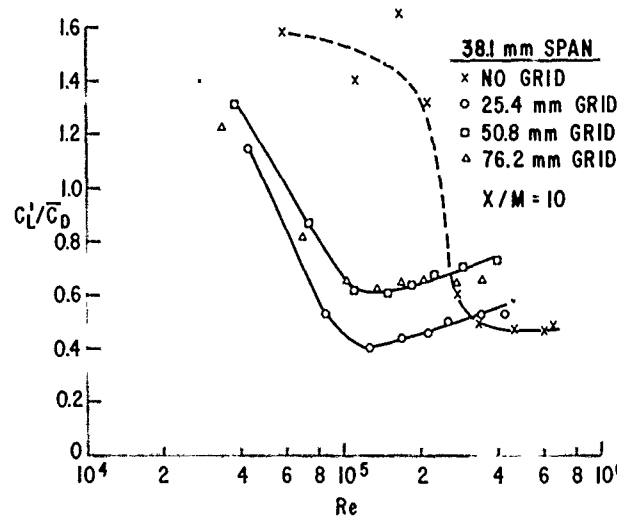


Figure 10a. Fluctuating lift coefficient for 38.1 mm active span with parametric dependence on the three grids (varying turbulent scale).

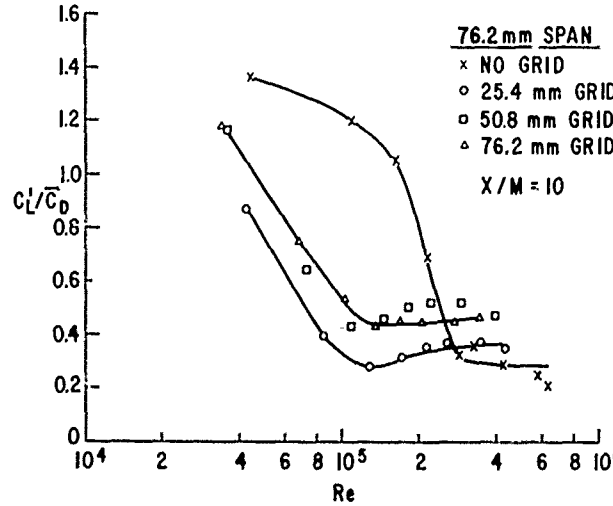


Figure 10b. Fluctuating lift coefficient for 76.2 mm active span with parametric dependence on the three grids (varying turbulent scale).

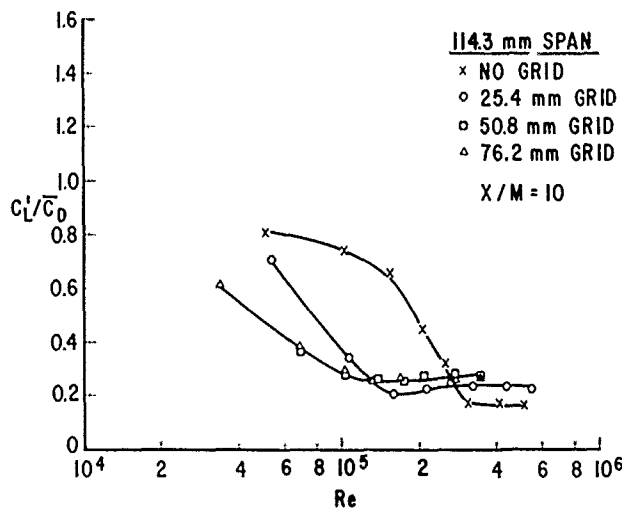


Figure 10c. Fluctuating lift coefficient for 114.3 mm active span with parametric dependence on the three grids (varying turbulent scale).

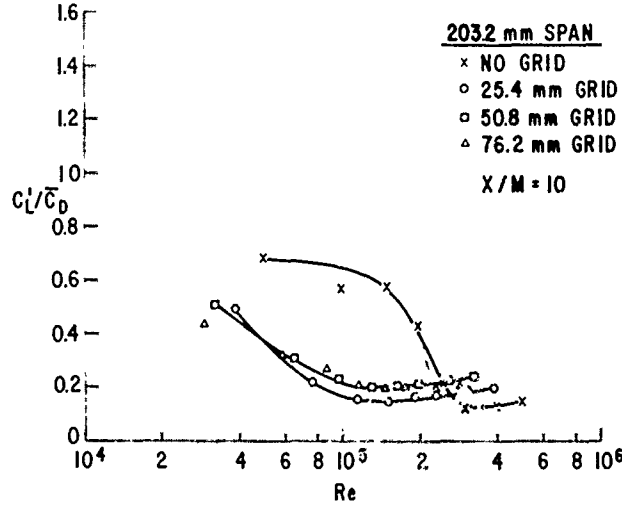


Figure 10d. Fluctuating lift coefficient for 203.2 mm active span with parametric dependence on the three grids (varying turbulent scale).

The following section will take up the question of some scaling relationships to come from an examination of the data from Figure 10. In anticipation, consider the cross plots in Figure 11. The parameter held fixed in the two plots is the ratio of the grid mesh dimension M to the active span s . Since all the data were obtained at a fixed number of mesh dimensions from the grid, $x/M = 10$, this translates directly to an equivalent ratio in terms of integral scale to span keeping the intensity approximately fixed. Indeed, since the turbulence is approximately homogeneous at $x/M = 10$, there is a simple relation between the axial length scales actually measured and the transverse scales which were not. This fact will be made use of in what follows. However, it is clear from Figure 11 that it should be possible to develop some useful scaling insights from the data obtained.

Scaling of Isolated Cylinder Forces

Several analogies and possible scaling relationships have been already discussed. It is now the objective to attempt to draw these together. Bearman,¹¹ following up on Roshko's postulate¹³ that changes in base pressure are closely related to changes in \bar{C}_D , developed a semi-empirical relationship between the product of the drag coefficient \bar{C}_D , Strouhal number St and a base pressure parameter $k = [1 - (C_p)_b]^{1/2}$. The

latter actually represents a measure of the separated flow streamline speed. The base pressure coefficient is referenced to the freestream static pressure P_∞ and velocity V_∞ .

The formation of the vortex wake behind a cylinder, or a bluff body, significantly affects both the amplitude of the pressure drag and the fluctuating lift. Indeed, Bearman developed his correlation from a model for the mean vortex wake drag deduced by von Karman.¹⁴ In light of the analogy found to exist between the fluctuating lift and mean drag, it is natural to seek an extension of the Bearman correlation to the fluctuating lift and drag. The discussion here will be limited to the fluctuating lift, the extension to the fluctuating drag being obvious.

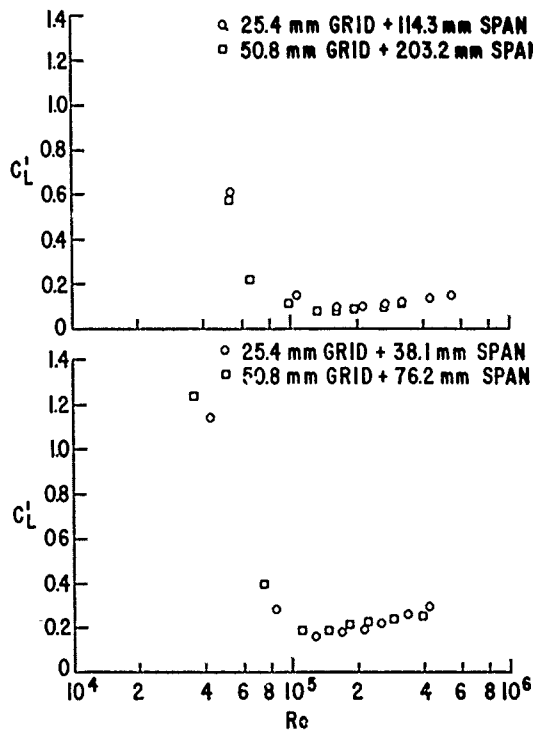


Figure 11. Cross plot of buffeting data keeping the ratio of grid mesh to active span fixed.

Consider a cylinder in motion with a velocity, U , in a liquid otherwise at rest. Let the axial or streamwise separation of the shed vortices be "a" and the distance between the two rows shed be "b." The vortex street will advance with a velocity

$$V = \frac{\Gamma \pi}{a} \tanh \frac{\pi b}{a} \quad (4)$$

where Γ is the strength of each vortex. Then by applying Euler's momentum theorem¹⁴ over a cycle, one obtains Karman's well-known relation for the mean pressure drag

$$C_D = \frac{4}{\pi} \left[\left(\frac{V}{U} \right)^2 \left[\coth^2 \frac{\pi b}{a} + \left(\frac{U}{V} - 2 \right) \frac{\pi b}{a} \coth \frac{\pi b}{a} \right] \right] \quad (5)$$

Repeating the above calculation for the fluctuating lift, there obtains the relation

$$C_D \cdot St = \frac{b}{a} \left[2 \sqrt{1 - V/U} \sqrt{C'_L \cdot St \tanh^{-1}(\pi b/a)} - \frac{b}{a} C'_L \cdot St \tanh^{-1} \frac{\pi b}{a} \right] \quad (6)$$

or upon substituting Karman's constants

$$C_D \cdot St = 0.629 \sqrt{C'_L \cdot St} - 0.111 C'_L \cdot St \quad (7)$$

In other words, if a relationship exists between $C_D \cdot St$ and base pressure $(C_p)_b$, one should also exist between $C'_L \cdot St \cdot f(s/d)$ and $(C_p)_b$. The factor $f(s/d)$ is an unknown function and is included here to correct the two-dimensional potential flow calculation to a three-dimensional flow as would be encountered in practice. Indeed, it is experimentally known that in uniform flow the spanwise correlation of vortex shedding typically extends over three diameters. The precise definition of $f(s/d)$ is not clear; however, in

in the present study, the function $f(s/d) = \sqrt{s/3d}$ was found to yield the best fit. The square root function has some rationale based on the work of Schmidt¹² and Liepmann.¹⁶ The resulting correlation for the Strouhal data are illustrated in Figure 12. Included in the figure also are some data obtained from Richter and Naudascher.⁶ The agreement between the semi-empirical model and the vortex shedding lift data are reasonably good. Also shown in the figure, for comparison, is the original-Bearman curve for $C_D \cdot St$, with the function $f(s/d)$ set equal to unity for the steady drag. It should be noted that the data are drawn from four different active spans of the water tunnel tests. The same grouping, $C'_L \cdot St \cdot \sqrt{s/3d}$ is also found to correlate the data with respect to the Reynolds number as illustrated in Figure 13.

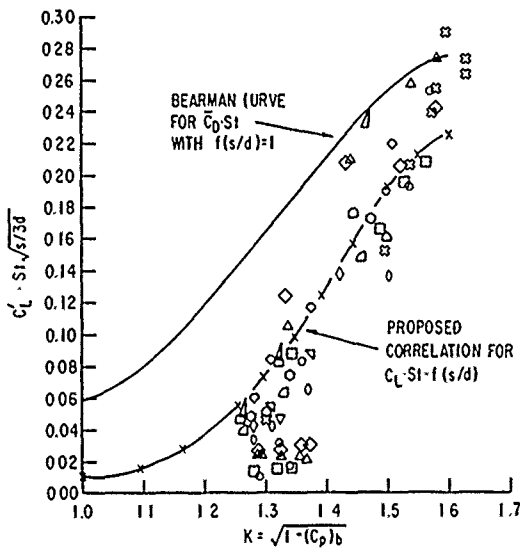


Figure 12. Correlation of $C'_L \cdot St \cdot f(s/d)$ vs. the base pressure parameter K . Broken line is based on Equation 3.3.5, the solid line is the Bearman curve for $C_D \cdot St$ with $f(s/d) = 1$. Data are all from the uniform flow case in the water tunnel and Richter and Naudascher.⁶ \times , Richter and Naudascher data;⁶ \diamond , 38.1 mm span, present tests; Δ , 76.2 mm span, present tests; \square , 114.3 mm span, present tests; \circ , 203.2 mm span, present tests. The remaining data are subcritical data points from the buffeting measurements.

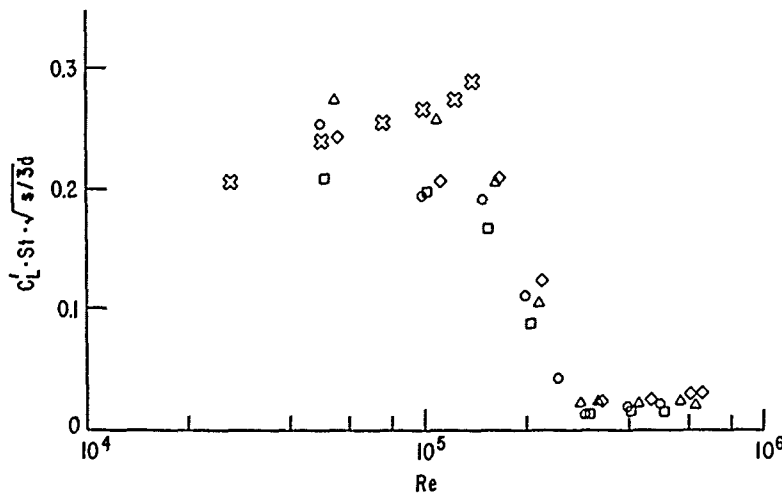


Figure 13. Correlation of Strouhal forces, $C'_L \cdot St \cdot \sqrt{s/3d}$, with Reynolds number. The symbols are the same ones used in Figure 12.

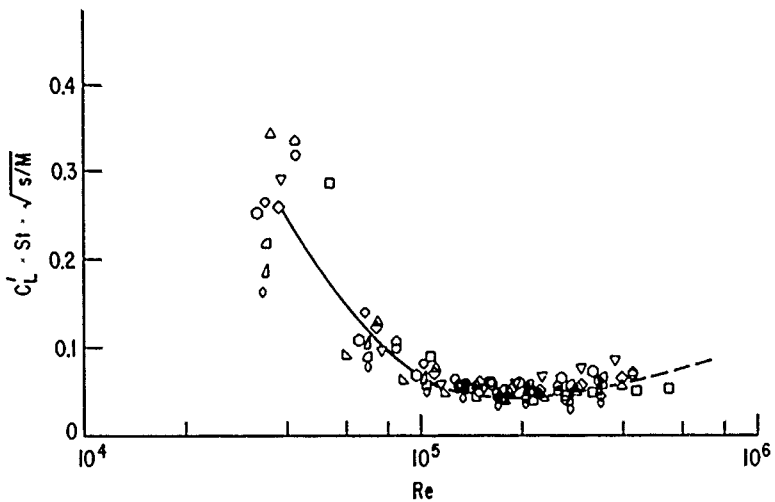


Figure 14. Correlation of buffeting forces, $C'_L \cdot St \cdot \sqrt{s/M}$ with Reynolds number. All buffeting data for 38.1 mm diameter cylinder:

Span s	Grid M	25.4 mm	50.8 mm	76.2 mm
38.1		○	◇	△
76.2		□	△	○
114.3		□	□	○
203.2		▽	○	△

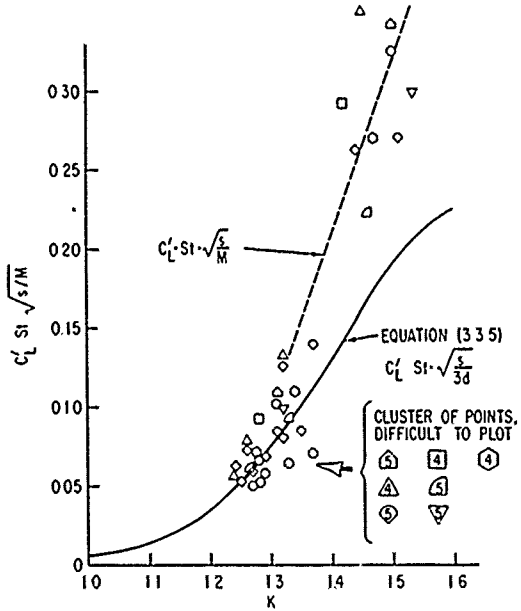


Figure 15. Modified Bearman correlation for the fluctuating buffeting forces. Ordinate and the symbols are the same as Figure 14 and abscissa same as Figure 12.

Given that a grouping of the type $C'_L \cdot St \cdot f(s/\bar{l})$, where \bar{l} is a measure of the spanwise coherence of the fluctuating forces, is found to work for the Strouhal forces, one is tempted to speculate whether a similar correlation can be found for buffeting forces. Upon testing various groupings, a reasonably simple correlation was found for the grouping $C'_L \cdot St \cdot \sqrt{s/M}$, where M is the grid mesh dimension. This choice is somewhat arbitrary except that the turbulent scales are closely related to the mesh dimension as a function of x/M . In the current tests, x/M was held fixed at 10 for all the grids. In fact, the subcritical correlation (as has been discussed already) is rather better if the grid turbulence is ignored and the factor

$3d$ is used instead of M . The undefined symbols in Figure 12 are in fact the subcritical buffeting points correlated using $3d$ as the factor. The resultant correlation using the water tunnel data, with the s/M factor, for four different active spans is examined in Figures 14 and 15. While this simplified approach does appear to work reasonably well for the Strouhal lift, the scatter in the buffeting situation is somewhat greater. That is not surprising considering both the transitional character of the data and the simplicity of the parameter grouping.

In examining the above plots, two points should be carefully borne in mind. All of the water tunnel data here discussed were obtained on a single diameter cylinder of 38.1 mm. None of the water tunnel data here presented were corrected for blockage. While both lift and drag can be corrected for blockage by the relationships suggested by Richter,⁶ such blockage correction is not available for the base pressure coefficient (C_p)_b. Additional work is required to pin down the effect of blockage on the base pressure before the curves can be viewed as true correlations. However, the plots do suggest the approximate form of the correlations (especially Figures 12-14) and offer the promise that the fluctuating forces could perhaps be estimated from a single base pressure measurement.

REFERENCES

1. S.D. Savkar, "Buffeting of Cylindrical Arrays in Cross Flow," 1984 ASME WAM Symposium on Flow Induced Vibration.
2. S.D. Savkar and R.M.C. So, "On the Buffeting Response of a Cylinder in a Turbulent Crossflow," TIS Report No. 78CRD119, General Electric Corporate Research and Development, 1978.
3. R.M.C. So and S.D. Savkar, "Buffeting Forces on Rigid Circular Cylinders in Cross Flows," *J. Fluid Mech.*, 105, 1981.
4. S.D. Savkar, T.A. Litzinger, and R.M.C. So, "Fluctuating Lift and Drag Forces Induced on Large Span Bluff Bodies in a Turbulent Cross Flow," ASME Special Publication HTD, 9, *Flow Induced Heat Exchanger-Tube Vibration*, 1980.
5. S. Goldstein, *Modern Developments in Fluid Dynamics*, Dover, 1965.
6. A. Richter and E. Naudascher, "Fluctuating Forces on a Rigid Circular Cylinder in Confined Flow," *J. Fluid Mech.*, 78, 561, 1976. See also A. Richter, "Stromungskräfte auf Starre Kreiszylinder Zwischen Pellen Wänden," Ph.D. Dissertation, University of Karlsruhe, 1973.
7. A. Roshko, "Experiments on the Flow Past a Circular Cylinder at Very High Reynolds Number," *J. Fluid Mech.*, 10, 345, 1961.
8. M.V. Morkovin, "Flow Around Circular Cylinder - A Kaleidoscope of Challenging Fluid Phenomena," ASME Symposium on Fully Separated Flows (ed., A. G. Hansen), 1964.
9. D. Surry, "Some Effects of Intense Turbulence on the Aerodynamics of a Circular Cylinder at Subcritical Reynolds Number," *J. Fluid Mech.*, 52, 543, 1972.
10. J.P. Batham, "Pressure Distributions on Circular Cylinders at Critical Reynolds Numbers," *J. Fluid Mech.*, 57, 209, 1973.
11. P.W. Bearman, "On Vortex Street Wakes," *J. Fluid Mech.*, 28, 625, 1967. See also P.W. Bearman, "On Vortex Shedding from a Circular Cylinder in the Critical Reynolds Number Regime," *J. Fluid Mech.*, 37, 577, 1969.
12. L.V. Schmidt, "Influence of Spatial Correlation upon Load Resolution," *J. Spacecraft*, 7, 363, 1970.
13. A. Roshko, "On the Wake and Drag of Bluff Bodies," *J. Aero. Sci.*, 22, 124-132, 1955.
14. Y.N. Chen, "Flow Induced Vibration and Noise in Tube Bank Heat Exchangers Due to von Karman Streets," 1968 *Trans. ASME*, Series B, *J. Eng. for Industry*, 90, pp. 134-146.
15. A.F. Lehman, *The Garfield Thomas Water Tunnel*, The Pennsylvania State University, Report No. Nord 16597-57, 1959.
16. H. Liepmann, "Extension of the Statistical Approach to Buffeting and Gust Response of Wings of Finite Span," *J. Aero. Sci.*, March 1955.

INFLUENCE OF STREAM TURBULENCE INTENSITY AND EDDY SIZE ON THE FLUCTUATING PRESSURE FORCES ON A SINGLE TUBE

C. Norberg and B. Sundén

Chalmers University of Technology

Department of Applied Thermo and Fluid Dynamics

Gothenburg, Sweden

ABSTRACT

This paper presents a systematic investigation of the influence of stream turbulence on the pressure forces on a single tube. Grids were used to produce different turbulent flow fields with longitudinal integral scale (eddy size) ranging from 0.1 to 0.5 tube diameters and turbulence intensities ranging from 0.1 to 3.2%. The measurements were carried out at two Reynolds numbers, $2.7 \cdot 10^4$ and $4.1 \cdot 10^4$, respectively.

Results are presented for the mean and fluctuating pressures including spectral distributions, skewness and flatness factors of the fluctuating pressure. The rms force coefficients were estimated using the phase differences and rms pressure coefficients around the tube.

The results indicate considerable influence of the turbulence intensity but weaker influence of the eddy size and of the Reynolds number.

NOMENCLATURE

C_D = mean drag coefficient
 C'_D = rms drag coefficient
 C_p = mean pressure coefficient = $(\bar{p} - p_r)/q$
 C'_p = rms pressure coefficient = p'/q
 D = tube diameter
 f = frequency
 f_n = natural frequency of pinhole system
 f_s = vortex shedding frequency
 p_r = reference static pressure
 \bar{p} = mean static pressure
 p' = rms pressure fluctuation on the tube surface
 q = dynamic head = $\rho U^2/2$
 Re_D = Reynolds number = UD/v
 S_D = Strouhal number = $f_s D/U$
 Tu = turbulence intensity = u'/U
 U = mean velocity
 u' = rms velocity fluctuation

α = angle from forward stagnation point
 $\Delta\phi = \phi(\alpha) - \phi(-\alpha)$
 ζ = damping parameter of pinhole system
 Λ = macroscale of velocity fluctuation
 λ = microscale (Taylor) of velocity fluctuation
 ν = kinematic viscosity
 ρ = density
 $\varphi(\alpha)$ = phase between reference and $p(\alpha)$

Subscripts

b = base
 m = maximum

INTRODUCTION

In the flow through the interstices of a tube bundle of the type used in heat exchangers, very high level of turbulence may be generated. This turbulence causes buffeting of the tubes, and this is one of the mechanisms by which tube vibration is initiated and sustained. When the dominant frequency of the turbulent flow matches the natural frequency of the tube, a considerable transfer of energy may occur leading to significant vibration.

Turbulent buffeting is not always identified as the primary cause of tube damage but it might initiate the tube motion leading to fluid-elastic instability. Also the buffeting may be the cause of long term damage.

An empirical equation for estimation of the dominant frequency for turbulent buffeting has been proposed by Owen [1]. This equation, obtained from investigations with gas flowing across an ideal tube bundle, does however not include any leading turbulence parameter (e.g. turbulence intensity or eddy size). Thus there is a great need for further investigation.

Although earlier investigations have dealt with the effect of incident turbulence fields on the pressure forces on circular cylinders, the influence of the stream turbulence intensity and eddy size (integral scale) has not been fully revealed. The interaction between the incident turbulence and e.g. vortex shedding is not fully understood and thus there is need for additional investigations. For recent reviews, see [2,3].

The overall objective of the present work is to measure the fluctuating pressure on the surfaces of single tubes and tube bundles and to establish adequate correlations relating these forces to the intensity and scale (eddy size) of the turbulence.

Another objective is to study the interaction of the vortex shedding and stream turbulence and the corresponding influence on the vibration characteristics.

The present paper reports results for a single tube and is a brief account of a comprehensive work on the buffeting phenomenon.

EXPERIMENTAL EQUIPMENT AND INSTRUMENTATION

Windtunnel and turbulence generating grids

The experiments were performed in a closed-circuit low-speed windtunnel, see Fig. 1. The dimensions of the working section are 2.9 m (length), 0.5 m (height) and 0.4 m (width). With a honeycomb and two screens in the settling chamber together with a long contraction, the longitudinal turbulence intensity in the working section is less than 0.1 %.

Turbulent flows can be generated by placing grids across the entrance of the working section. In this investigation, three different grids were used. They were all biplanar with square meshes and circular rods, see Table 1.

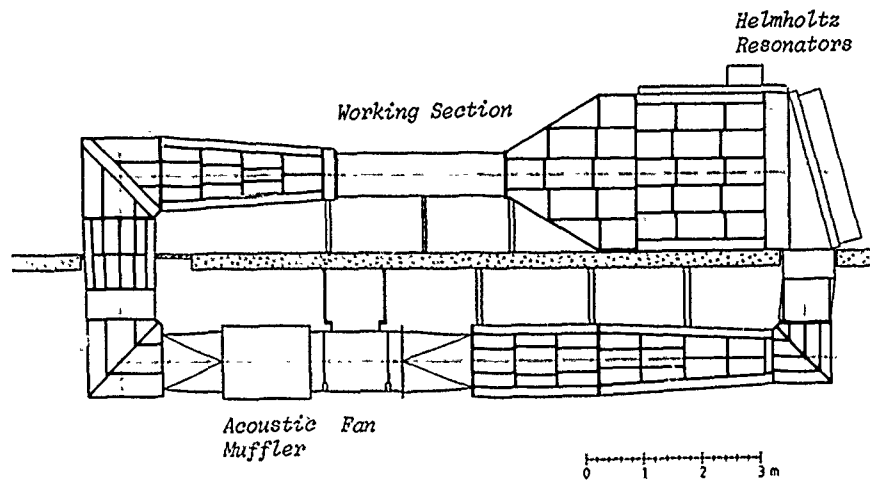


Fig. 1. The windtunnel

Table 1 Data for the turbulence generating grids

Grid No	Bar Size mm	Mesh Size mm	Pressure loss coeff
1	1	5	0.63
2	4	20	0.54
3	7	35	0.56

Velocity field measurements

The measurements of mean and fluctuating velocities upstream the tube were carried out with a Pitot-static tube and single DISA hot wires of 5 μm diameter.

The turbulence structure downstream the grids was at first measured in the empty tunnel. The distributions of the turbulence intensity T_u and the eddy size to diameter ratio Λ/D are shown in Fig. 2.

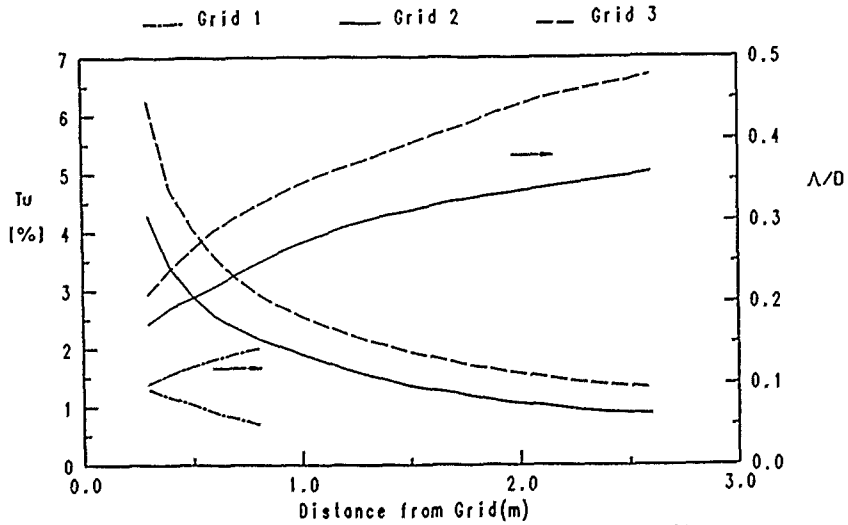


Fig. 2. Turbulence structure downstream the grids

With the tube in place there will be a complex interaction between the mean flow around the tube and the approaching stream turbulence. At some distance upstream the tube, this interaction will be negligible. Typical distributions of the turbulence intensity and the eddy size are depicted in Fig. 3. As is evident, the approaching turbulence undergoes amplification close to the tube surface.

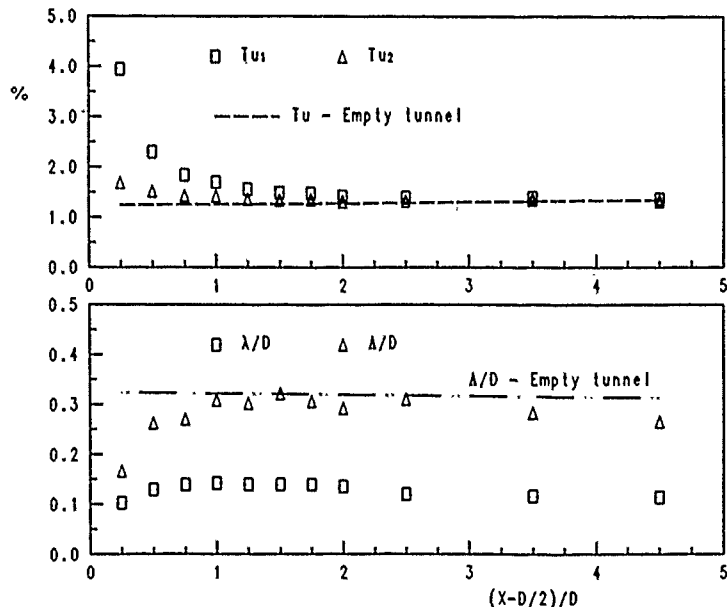


Fig. 3. Turbulent structure in the working section with and without the tube in place. Tu_1 - local Tu , Tu_2 - Tu based on freestream velocity.
Note: X from tube axis, stagnation line.

The position where the turbulence intensity is independent of the presence of the tube can be taken as the definition point for the approaching turbulence. This definition has been used in related heat transfer studies [4-6]. However, in the present work, the definition is taken from the curves in Fig. 2 at the position downstream the grids where the tube is placed during the measurements. The relation between these two methods of definition can be found from Fig. 3.

To enable a systematic variation in the turbulent parameters, the tube was placed at different positions downstream the grids. In that way, the turbulence intensity can be kept constant while the eddy size is varied or alternatively, the eddy size can be kept constant while the intensity is varied.

In these flow measurements, a digital data aquisition system with a VAX 11/750 computer was employed. A sampling frequency of 10 kHz was used and 200 ksamples were taken at each point of measuring. The eddy size (Λ) was obtained as the mean value of the macroscale from the autospectrum (low frequency limit) and the integral time scale using Taylor's hypothesis.

Measurements of the fluctuating pressures on the tube

The tube had an outer diameter of 41 mm and was divided in two sections. One section was a steel pipe while the other was made of aluminium and contained a microphone which was connected to the tube surface through a cannula (pinhole arrangement) which was 9.5 mm long and had an inner diameter of 0.4 mm, see Fig. 4.

In the spanwise direction pressure taps of 0.5 mm, connected to a manometer, were placed. The outer surface of the tube was polished.

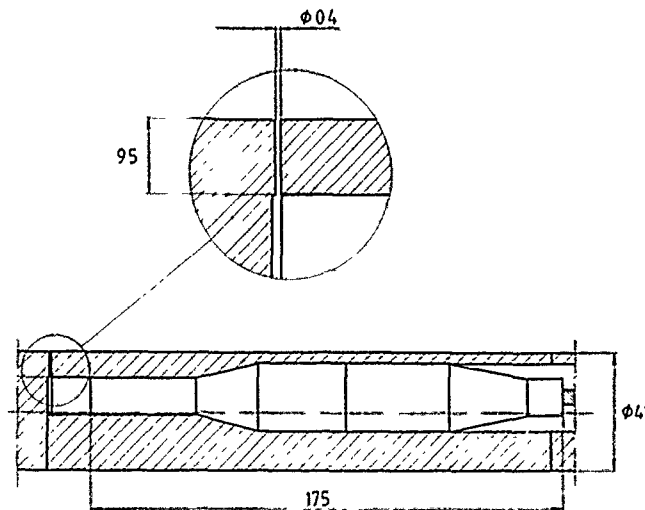


Fig. 4. Test tube with microphone in pinhole arrangement.
Dimensions in mm.

The tube was mounted horizontally and rigidly between the side-walls of the working section but could be rotated in steps of 1 deg and positioned at different locations.

In order to obtain a two-dimensional flow around the tube and to obtain correct levels of the measured pressure distribution and the calculated drag coefficient, it was found necessary to use end plates on the tube. To find the proper placement of the end plates, an investigation was carried out. This investigation suggested that if the end plates were placed approximately 35 - 40 mm from the side-walls of the windtunnel (just outside the wall layers) results sufficiently independent of the end plate position were obtained. Similar problems have been investigated and discussed in [7,8]. With the end plates (similar design as in [7,8]) in place, a blockage ratio of 8.3 % and a span length to diameter ratio of 8.0 prevailed.

The acoustic pressure field in the tunnel was measured by microphones flush-mounted in the tunnel floor and by microphones (equipped with nose cones) placed in the stream.

The microphone system employed was of Brüel and Kjaer fabrication (1/2" microphone Type 4147 with Carrier System Type 2631) and had a frequency response ranging from 0.01 Hz to 16 kHz (± 1 dB). The sensitivity checked by a Sound Level Calibrator (B & K Type 4230) and the in-built calibration signal was typically 20 mV/Pa.

The frequency response for the pinhole arrangement showed a Helmholtz resonance which could be described as a second-order system ($f_n = 635$ Hz, $\zeta = 0.31$). The calculated spectral distributions were corrected for this frequency response. The unfiltered output from the pinhole microphone was dominated by frequencies below 250 Hz and therefore it was of secondary importance.

Vibration studies were made with an accelerometer (B & K Type 4368, Conditioning Amplifier Type 2626).

When necessary, the outputs from the transducers were filtered and amplified

(Krohn Hite Model 3340 and 3700). For accurate measurements of the root mean square (rms) and mean voltages a HP Digital Voltmeter 3456A was used.

In the sampling and evaluation of data the VAX 11/750 computer again was used. The sampling frequency and the number of samples taken were chosen in such a way that suitable resolution and high statistical accuracy were achieved. In the spectral analysis the signals were low-pass filtered at half the sampling frequency in order to avoid aliasing errors.

Fluctuating lift and drag forces

The spanwise and circumferential correlations between the fluctuating pressures at two points on the tube surface are of great engineering importance in that they yield information about the rms-values and spanwise coherence of the fluctuating lift and drag forces.

For these correlation measurements we are using a technique similar to the one used by Kiya et al. [9] and Arie et al. [10]. These measurements are not completed but will be reported in a later paper. However, estimations for the fluctuating forces using a simplified procedure will be given.

Disturbances

Acoustic disturbances in a windtunnel may influence the fluctuating flow field and the associated forces on an object placed in the flow but to which extent is not fully revealed, see [11,12].

An extensive study of the acoustic disturbances in our windtunnel showed that the sound level in the working section was high, typically 2 % of the dynamic head at 10 m/s (no grid). Spectral and correlation analysis showed that the major contribution was concentrated in a frequency band around 30 Hz associated with a longitudinal standing acoustic wave. The corresponding wavelength matched with the distance between the corners in the upper part of the tunnel system.

An installation of 17 tuned Helmholtz resonators and an ordinary acoustic muffler reduced the sound level by a factor greater than 2.

Also, the standing wave pattern implies that the associated wave-components at different locations are coherent. By measuring the coherence function between an additional microphone flush-mounted in the tunnel floor far upstream the tube (≥ 10 diameters) and the pinhole microphone it was possible to subtract or compensate for the remaining part of these disturbances.

It is worth noting that on the major part of the tube surface the flow-induced pressure fluctuations are of such a magnitude that the disturbances are negligible. However, in the stagnation zone the fluctuations are small, especially if the oncoming flow is non-turbulent. At this region of the tube surface the subtraction technique was applied.

The use of end plates to reduce the interference effect from the tunnel walls has been described earlier.

Other common types of disturbances present in investigations like this were controlled without any large difficulties.

RESULTS

Results from ten different cases are reported, see Table 2. At first no end plates were fitted to the tube. This resulted in pressure distributions and drag coefficients which for the non-turbulent cases deviated much from the generally accepted values. The cause of this was found to be interference effects from the boundary layers on the tunnel walls. To remedy this, end plates had to be used as outlined in an earlier section.

All cases were in the subcritical range where the flow is dominated by vor-

tex shedding.

Table 2 Parameters for cases investigated.
 X - Distance downstream the grids, U -
 Nominal velocity.

Case	Grid No	X[m]	U[m/s]	Tu[%]	A/D	λ/D	C_D	S
0	-	1.7	10	0.1	-	-	1.18	0.192
1	-	1.7	15	0.1	-	-	1.21	0.189
2	3	0.7	10	3.25	0.31	0.11	1.26	0.189
12	3	0.7	15	3.15	0.29	0.11	1.25	0.188
4	1	0.3	10	1.30	0.10	0.08	1.21	0.187
11	1	0.3	15	1.33	0.10	0.07	1.22	0.186
3	2	1.7	10	1.28	0.32	0.16	1.26	0.190
8	2	1.7	15	1.26	0.31	0.14	1.26	0.187
7	3	2.6	10	1.34	0.49	0.20	1.20	0.188
10	3	2.6	15	1.28	0.46	0.18	1.20	0.186

Mean quantities

Fig. 5 depicts the mean pressure coefficient for some of the cases in Table 2. Data were corrected for tunnel blockage by the method of Allen and Vincenti as described in [13,14]. The maximum correction applied for the mean velocity and the drag coefficient were 3.4 and 7.9 %, respectively.

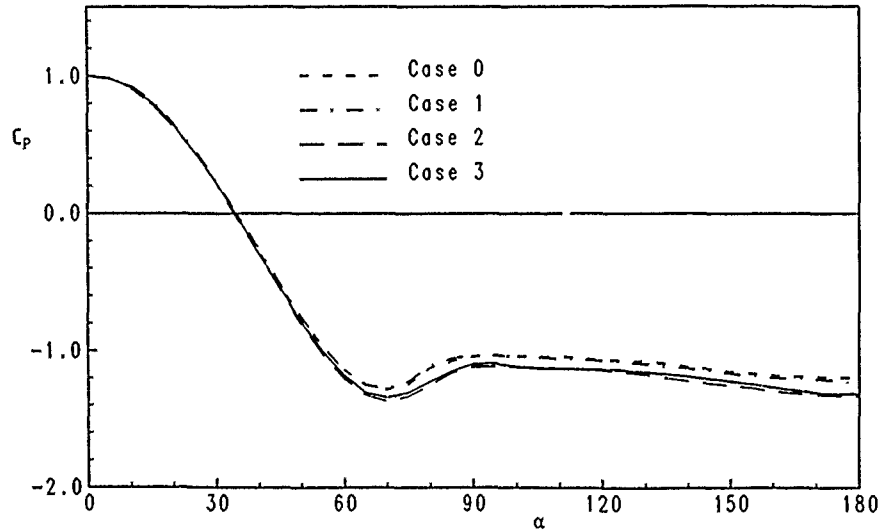


Fig. 5. Distributions of the mean pressure coefficient, $C_p(\alpha)$, on the tube surface. Cases refer to Table 2.

From Fig. 5 it is evident that the mean pressure coefficient on the upstream side of the tube is almost unaffected by the stream turbulence. This is in agreement with the assumptions and findings in [4-6]. The base pressure in the wake region is however slightly altered by the stream turbulence and thus there is an interaction between the external turbulence and the wake flow.

The mean drag coefficients were determined by integration of the mean pressure distributions. The vortex shedding frequencies were determined from spec-

tral measurements at $\alpha = 60$ deg (resolution ≈ 0.2 Hz). Table 2 shows that when the Reynolds number was changed from $2.7 \cdot 10^4$ (≈ 10 m/s) to $4.1 \cdot 10^4$ (≈ 15 m/s) a slight increase in the drag coefficient appeared. The corresponding Strouhal number ($S = f_s D/U$, f_s shedding frequency) decreased slightly (non-turbulent cases). However, these variations were smaller for the turbulent cases. For the non-turbulent cases the values of the mean drag coefficient are in agreement with the standard data reported in e.g. [15]. This confirms that for all cases, the flow is in the pre-transitional range.

RMS - distributions

The distribution of the rms pressure coefficient C'_p are presented in Fig. 6 for the same cases as in Fig. 5.

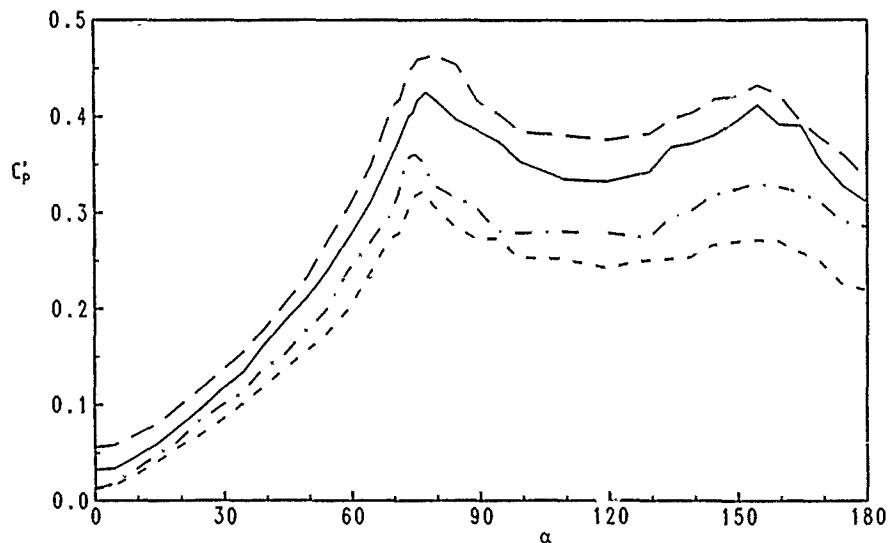


Fig. 6. Distributions of the rms pressure coefficient, $C'_p(\alpha)$, on the tube surface. For legend, see Fig. 5.

All distributions exhibit a maximum at an angle of about 77 deg, which is close to the separation point. The similarity between the distributions is significant. This is in accordance with other investigations, for instance [9, 16]. The span in C'_p covered by the different cases clearly demonstrates the sensitivity to variations in the turbulence of the oncoming flow. The Reynolds number effect on C'_p was small except for the non-turbulent flow. The non-turbulent cases are in agreement with i.e. [17].

The rms-pressure fluctuations around the tube are increased by the blockage (see e.g. Modi and El-Sherbiny [18]). The similarity in the C'_p - distributions therefore suggests that an increase in the dynamic head is an appropriate correction to the rms-pressure coefficient. However, this blockage effect is not fully understood and therefore no correction was applied in this investigation.

The maximum value of the rms-pressure coefficient ($C'_{p_{\max}}$) increased by the stream turbulence by as much as 45 %. The rms-pressure coefficient at the base (C'_{p_b}) is also affected by the turbulence. Changes of order 30 - 50 % occur compared to the non-turbulent flow. Both the turbulence intensity and the integral scale (eddy size) influence these coefficients although the effect of the scale is weaker.

A direct comparison with other studies is not possible since the effect of the turbulence intensity and eddy size have not usually been separated.

Spectral and statistical analysis

When the oncoming flow was turbulent the levels of the pressure fluctuation spectra were increased for all values of α . The angular variation of the power spectral density (PSD) for case 12 (see Table 2) is shown in Fig. 7. The peak at the fundamental Strouhal frequency (f_S) disappears at the rear stagnation point ($\alpha = 180$ deg) where the energy around the second harmonic ($2f_S$) has a maximum. The component at three times the shedding frequency ($3f_S$) is discernible, in particular between $\alpha = 130 - 160$ degrees. Except for high frequencies the spectral distributions are similar for all the cases investigated.

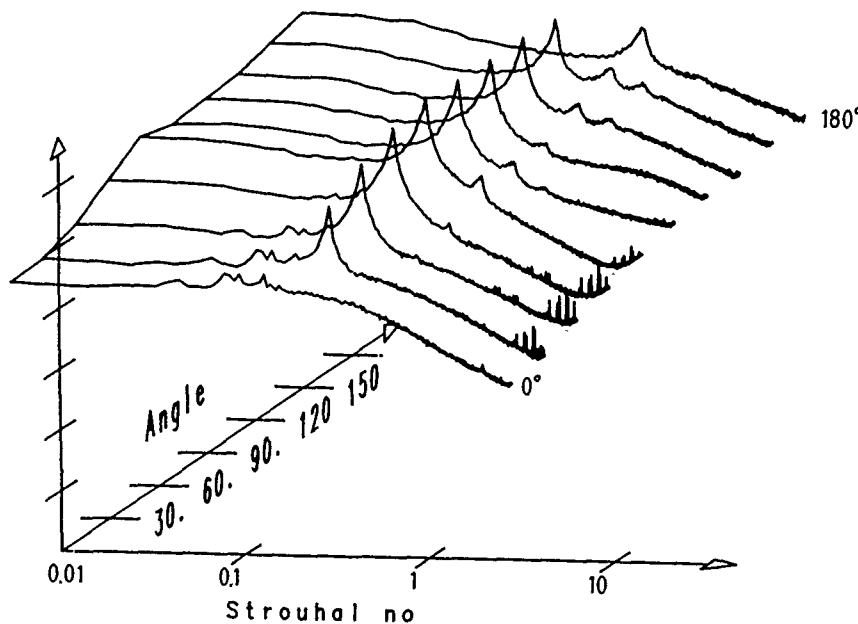


Fig. 7. Power spectral density distribution. Case 12.
Note: 20 dB between tickmarks on vertical axis.
Strouhal no = fD/U .

The pressure signals showed a strong low-frequency amplitude modulation which increased from the stagnation point. The importance of these modulations was pointed out by Sonneville [19], who suggested that they were associated with slow changes in the region of formation of the shedding.

The distributions in different Strouhal-bands at different positions are shown in Fig. 8 (Case 11, see Table 2).

The energy around the fundamental Strouhal frequency ($fD/U = 0.1 - 0.3$) dominates the spectra except near the rear region. This level, which is associated with the strength of the vortices shed, was influenced by the turbulence. The half-power (-3 dB) bandwidth was increased by the velocity but the turbulence effect was small.

Further measurements are needed to clarify phase- and coherence-relations for different spectral components.

The statistical analysis was based on computation of the probability density function (PDF) of the pressure signals (statistical moments, minimum and maximum pressures). The distributions in Fig. 9 are typical in a general view for all cases.

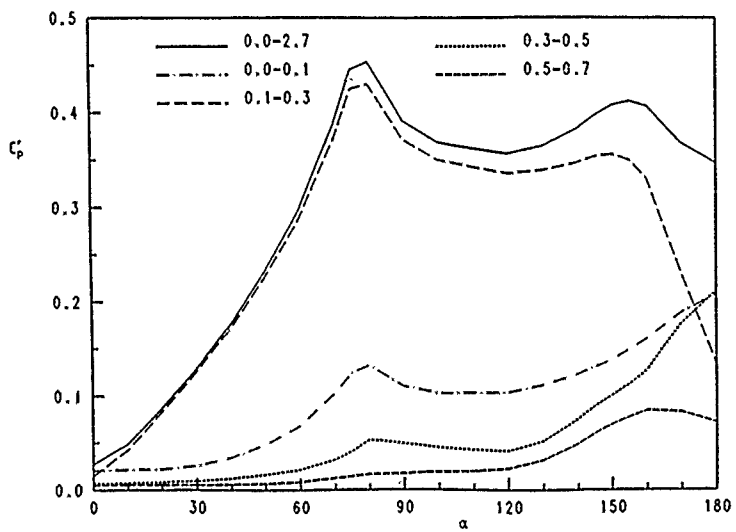


Fig. 8. Distribution of C_p' in different Strouhal-bands around the tube surface. Case 11 (see Table 2).

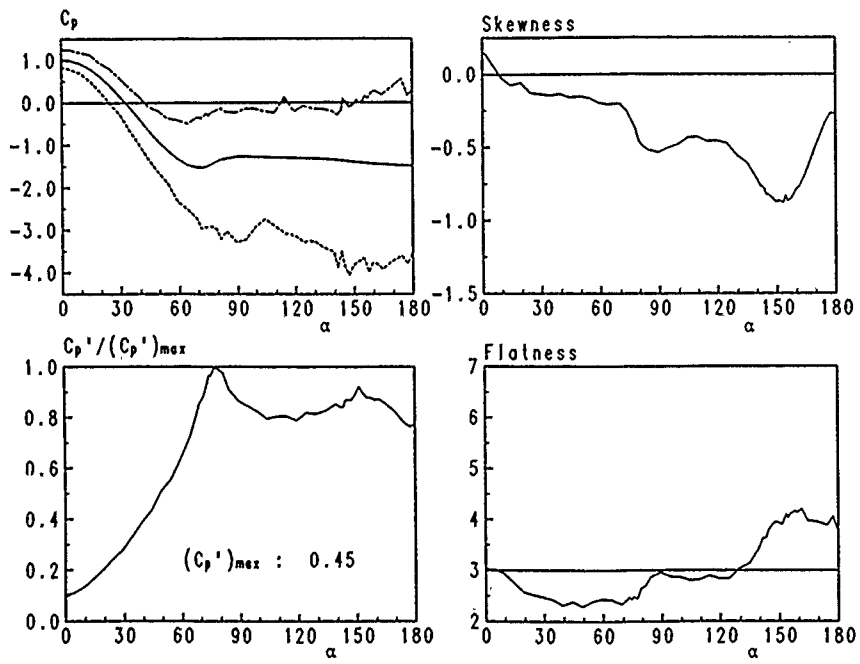


Fig. 9. Statistical moments, minimum and maximum pressures at different positions on the tube surface. Case 12.

On the stagnation line ($\alpha = 0$ deg) the distributions are almost Gaussian (skewness = 0, flatness = 3) and the amplitude is dependent on the upstream turbulence level. The fluctuations grow in magnitude in the boundary layer region up to the separation point. In the region of decelerated flow (adverse pressure gradient), the minimum pressure coefficient reaches a minimum and the rms-distribution a maximum ($\alpha \approx 77$ deg). The higher order moments change very rapidly in this region. For angles between 90 and 120 degrees, the variations are small. The most striking feature is the variations in the region $\alpha \approx 130 - 160$ degrees. The intermittency of the pressure in this region is reflected in the extreme values of the higher order moments (rms, skewness, flatness). This seems to be associated with the entrainment of fluid bearing vorticity of opposite sign (secondary circulation) discussed by Surry [16] and Gerrard [20].

Estimation of the fluctuating forces

So and Savkar [2] found that for Reynolds numbers between $10^4 - 10^5$, conservative estimates of the fluctuating lift force coefficient C'_L and the fluctuating drag coefficient are obtained by the relations $C'_L/C_D = 0.8$ and $C'_D/C_D = 0.1$, respectively.

The distance between the tube and the place where the periodic wake is formed decreases at a Reynolds number of about $2 \cdot 10^3$ and the wake is formed close to the shoulder ($\alpha = 90$ deg) at a Reynolds number of about $5 \cdot 10^4$ (non-turbulent flow), see Bloor [21]. The measurements by Gerrard [22,23] show that the flow in this Reynolds number range is highly sensitive to disturbances (e.g. freestream turbulence). He also found that the variations in the rms-pressure coefficient and the turbulence intensity at the shoulder are similar to the variations in C'_L . In another investigation by Kiya et al. [9] it was found that $C'_L/C'_D(90) \approx 2$.

In order to estimate the fluctuating forces on the tube, the phase-difference between the fluctuating velocity 0.1 diameter above the tube at $\alpha = 90$ deg and the fluctuating pressures around the tube surface was measured (mid-span position). Fig. 10 shows the phase-difference between the corresponding angles 30, 60, 90, 120 and 150 degrees from the stagnation point for fD/U (Strouhal no) below 0.75 (Cases 0 and 3).

A simple calculation procedure using these phase-differences and the rms-pressure coefficients (weighted by an estimation of the coherence between the corresponding angles) in different Strouhal bands gave an estimation of the sectional pressure forces on the tube. The major contribution to the fluctuating lift came from energy around the fundamental Strouhal frequency (f_S) while the contributions to the fluctuating drag were dominated by energies at low Strouhal numbers ($fD/U < 0.1$) and from energy around the second harmonic ($2f_S$). A comparison between cases 0 and 3 ($Re_D = 2.7 \cdot 10^4$, $Tu = 0.1, 1.3\%$) is summarized in Table 3.

Table 3 Calculated fluctuating force coefficients and measured quantities for cases 0 and 3. $Tu =$ turbulence intensity at $\alpha = 90$ deg, 0.1 diameter above the tube surface.

Case	C'_{p_m}	$C'_p(90)$	C'_{p_b}	$-C'_{p_b}$	$Tu[\%]$	C'_D	C'_L
0	0.32	0.27	0.22	1.20	4.0	0.07	0.54
3	0.41	0.37	0.30	1.32	5.4	0.09	0.73

These variations are in accordance with the estimates just given. For instance, the variations in C'_L are very similar to the variations in $C'_p(90)$ and the turbulence at the shoulder. As judged from [23], the turbulence effect seems to be a reduction in the length of the formation region. The alterations in the base pressure coefficients clearly demonstrates that the wake flow is affected by the stream turbulence.

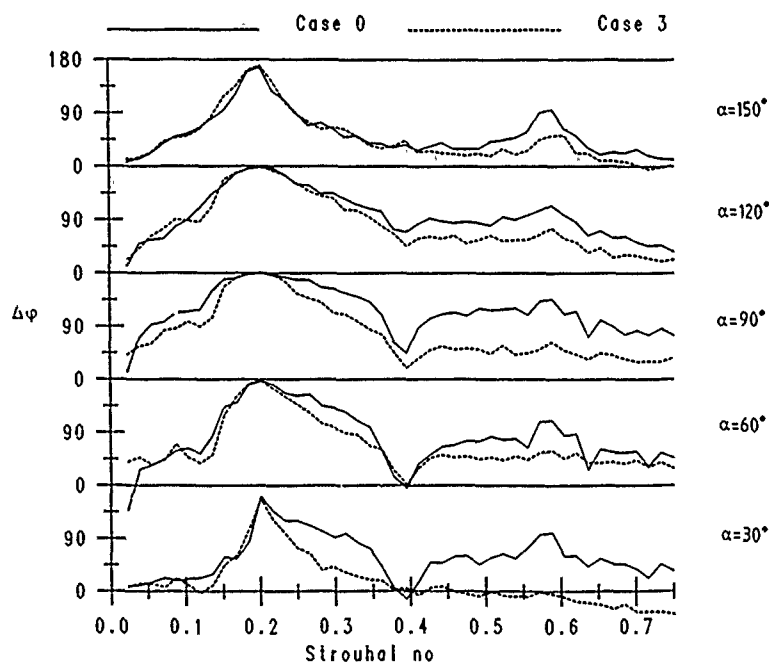


Fig. 10. Phase-difference between corresponding angles on the tube surfaces. Cases 0 and 3.

A more rigorous determination of C_L^1 and C_D^1 will be possible when the spanwise and circumferential correlation coefficients are available.

CONCLUSIONS

The results of the experimental investigation presented in this paper provide new and additional information concerning fluctuating pressures on a single tube placed in a turbulent stream.

The investigation was carried out at two different Reynolds numbers ($2.7 \cdot 10^4$ and $4.1 \cdot 10^4$) with varying turbulence intensity (0.1 - 3.2 %) and eddy size ($\Lambda/D = 0.1 - 0.5$) of the approaching stream.

For the flow ranges considered, the Reynolds number effect was small while the influence on the mean drag coefficient and maximum pressure coefficient by the stream turbulence was such that increases of order 5 % and 15 - 45 % occurred, respectively, compared with the non-turbulent flow.

The experiments were all in the subcritical or pre-transitional range where the vortex shedding dominates the flow but an interaction between the stream turbulence and the vortex shedding was found.

Spectral and statistical analysis indicated that different physical mechanisms take place at various angular positions on the tube surface.

ACKNOWLEDGEMENTS

The present project is the Swedish contribution to the IEA - cooperative work on Heat Transfer and Heat Exchangers, Annex III Tube Vibration. The project is financially supported by the National Swedish Board for Technical Development.

REFERENCES

1. Owen, P.R., "Buffeting Excitation of Boiler Tube Vibration," J. Mech. Eng. Sci., Vol. 7, 1965, pp. 431-439.
2. So, R.M.C. and Savkar, S.D., "Buffeting Forces on Rigid Circular Cylinders in Cross Flows," J. Fluid Mech., Vol. 105, 1981, pp. 397-425.
3. Farrell, C., "Flow around Fixed Circular Cylinders: Fluctuating Loads," J. Eng. Mech. Div., ASCE, Vol. 107, No. EM3, 1981, pp. 565-588.
4. Sunden, B., "A Theoretical Investigation of The Effect of Freestream Turbulence on Skin Friction and Heat Transfer for a Bluff Body," Int. J. Heat Mass Transfer, Vol. 22, No. 7, 1979, pp. 1125-1135.
5. Hanarp, L. and Sunden, B., "Structure of The Boundary Layers on a Circular Cylinder in the Presence of Freestream Turbulence," Lett. Heat Mass Transfer, Vol. 9, No. 3, 1982, pp. 169-177.
6. Hanarp, L. and Sunden, B., "An Investigation of the Influence of Free-stream Turbulence on the Thermal Characteristics around a Single Tube," Symposium Series No. 86, I. Chem. Eng., Vol. 2, 1984, pp. 1125-1135.
7. Stansby, P.K., "The Effects of End Plates on the Base Pressure Coefficient of a Circular Cylinder," Aeronautical Journal, Vol. 78, Part 3, 1974, pp. 543-563.
8. West, G.S. and Apelt, C.J., "The Effects of Tunnel Blockage and Aspect Ratio on the Mean Flow Past a Circular Cylinder With Reynolds Number Between 10^4 and 10^5 ," J. Fluid Mech., Vol. 114, 1982, pp. 361-377.
9. Kiya, M., Suzuki, Y., Arie, M. and Hagino, M., "A Contribution to the Freestream Turbulence Effect on the Flow Past a Circular Cylinder," J. Fluid Mech., Vol. 115, 1982, pp. 151-164.
10. Arie, M., Kiya, M., Moriya, M. and Mori, H., "Pressure Fluctuations on the Surface of two Circular Cylinders in Tandem Arrangement," ASME J. Fluids Eng., Vol. 105, 1983, pp. 161-167.
11. Peterka, J.A. and Richardson, P.D., "Effects of Sound on Separated Flows," J. Fluid Mech., Vol. 37, Part 2, 1969, pp. 265-287.
12. Hatfield, H.M. and Morkovin, M.V., "Effect on an Oscillating Free Stream on the Unsteady Pressure on a Circular Cylinder," ASME J. Fluids Eng., Vol. 95, 1973, pp. 249-254.
13. Roshko, A., "Experiments on the Flow Past a Circular Cylinder at Very High Reynolds Number," J. Fluid Mech., Vol. 10, 1961, pp. 345-356.
14. Sadeh, W.Z. and Saharon, D.B., "Turbulence Effect on Crossflow around a Circular Cylinder at Subcritical Reynolds Number," NACA CR 3622, 1982.
15. Schlichting, H., Boundary Layer Theory, 7th ed., McGraw-Hill, New York, 1979.
16. Surry, D., "Some Effects of Intense Turbulence on the Aerodynamics of a Circular Cylinder at Subcritical Reynolds Number," J. Fluid Mech., Vol. 52, Part 3, 1972, pp. 543-563.
17. Igarashi, T., "Correlation Between Heat Transfer and Fluctuating Pressure in Separated Region of a Circular Cylinder," Int. J. Heat Mass Transfer, Vol. 27, No. 6, 1984, pp. 927-937.

18. Modi, V.J. and El-Sherbiny, S., "Effect of Wall Confinement on Aerodynamics of Stationary Cylinders," Proc. Wind Effects on Buildings and Structures, 1971, pp. 365-375.
19. Sonneville, P., "Etude de la Structure Tridimensionnelle des Ecoulement Autour d'un Cylindre Circulaire," Bulletin de la Direction des Etudes et Recherches, Ser. A, No. 3, 1976, pp. 1-260.
20. Gerrard, J.H., "The Mechanisms of Formation Region of Vortices Behind Bluff Bodies," J. Fluid Mech., Vol. 25, No. 2, 1966, pp. 401-413.
21. Bloor, S., "The Transition to Turbulence in the Wake of a Circular Cylinder," J. Fluid Mech., Vol. 19, No. 2, 1964, pp. 290-304.
22. Gerrard, J.H., "An Experimental Investigation of the Oscillating Lift and Drag of a Circular Cylinder Shedding Turbulent Vortices," J. Fluid Mech., Vol. 11, 1961, pp. 244-256.
23. Gerrard, J.H., "A Disturbance-sensitive Reynolds Number Range of the Flow Past a Circular Cylinder," J. Fluid Mech., Vol. 22, No. 1, 1965, pp. 187-196.

UNSTEADY FORCES ON A CYLINDER IN CROSS FLOW AT SUBCRITICAL REYNOLDS NUMBERS

M. J. Moeller
Massachusetts Institute of Technology
Cambridge, Massachusetts
Now at General Dynamics/Electric Boat
Groton, Connecticut

P. Leehey
Massachusetts Institute of Technology
Cambridge, Massachusetts

ABSTRACT

The effect of large amplitude cylinder motion on the vortex shedding process was investigated using a small flush mounted force transducer. The experiments were carried out in the MIT Marine Hydrodynamics Laboratory's closed circuit water tunnel. The test cylinder was subject to forced harmonic motion in a direction transverse to the cross flow at amplitude to diameter ratios up to 0.5 in the reduced frequency range $0.1 < fd/U_\infty < 0.3$. Lock-in boundaries were determined for a Reynolds Number of 19,300. Both the locked-in and non locked-in behaviours were investigated.

The test cylinder was spring mounted in the water tunnel to determine its vibratory response to vortex shedding excitation. The system showed hysteresis in that the response was different for increasing flow velocities as compared to decreasing flow velocities. The forced vibration data were used to explain this hysteretic behaviour.

1. INTRODUCTION

The vibration of cylindrical structures due to vortex shedding excitation can be an important mechanism leading to structural failure. Destructive levels of vibration have been observed in towing lines (Blevins [1]), power lines (Blevins [1]), and trash racks (Crandall [2]). Due to the complexity of the vortex shedding process, much of the information about it comes from model experiments and full scale measurements. A review of the recent work on the topic can be found in King [3] or Sarpkaya [4]. The vortex shedding process is sensitive to several different disturbances such as: freestream turbulence, cylinder end conditions, surface roughness, and cylinder motion. Cylinder motion plays an important role in the vortex shedding process. It causes the magnitude of the vortex shedding forces to increase and tends to organize the normally random shedding of vortices along the length of the cylinder as can be seen in data taken by Toebe [5]. The mean drag of the cylinder also increases due to the cylinder motion. These effects result in large increases in the loads carried by cylindrical structural elements and can lead to premature structural failure.

The effect of cylinder motion on the vortex shedding process was investigated in the MIT Marine Hydrodynamics Laboratory's closed circuit water tunnel. The test cylinder was subjected to forced harmonic motion in a direction transverse to the freestream flow. The results of the forced motion experiments were used to estimate the motion of a spring mounted cylinder that was constrained to move transverse to the flow direction.

2. EXPERIMENTAL PROGRAM

2.1 Water Tunnel

The experiments were conducted in the MIT Marine Hydrodynamics Laboratory's closed circuit water tunnel. The test section of the water tunnel is 50.8 cm square and 137 cm long. The contraction ratio leading to the test section is 4.5:1. There is a honeycomb of one inch diameter acrylic tubes upstream of the contraction to reduce the turbulent intensity levels. The range of speeds used was from 0.12 m/sec to 10.0 m/sec. The velocity profile was uniform across the test section and the freestream turbulence level was 0.9%. The water tunnel was selected for use because it was possible to achieve controlled large amplitude two dimensional cylinder motions at Reynolds Numbers above 10,000. The test cylinder was mounted in a yoke and was forced to vibrate by a mechanical shaker as shown in Figure 1.

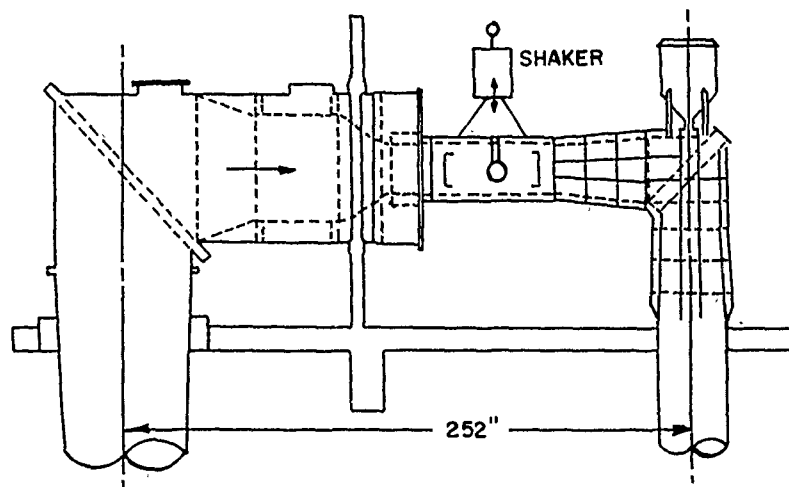


Figure 1. Schematic of Water Tunnel Facility

2.2 Force Transducer and Yoke

The force transducers used in this investigation were developed in the MIT Acoustics and Vibration Laboratory and are described in more detail in Moeller [6]. A schematic of the force transducer is shown in Figure 2. The transducer consists of a ring element that is flush mounted in the center of the test cylinder. The ring element is attached to a cantilever beam element that is fixed in the test cylinder. The transducer is sensitive to the relative displacement of the beam element with respect to the test cylinder. This relative motion was kept as small as possible (10E-6 cylinder diameters maximum). This small relative motion did not interfere with the vortex shedding process under investigation. transducers were sealed with a commercially available RTV elastomer.

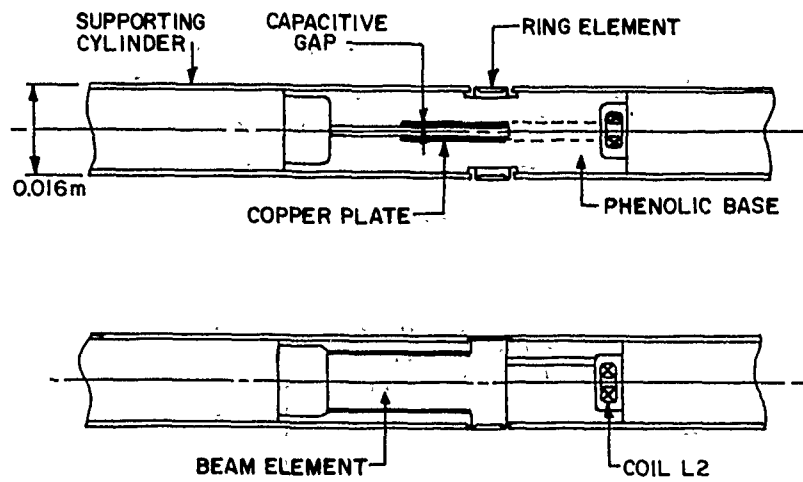


Figure 2. Schematic of Force Transducer

The transducers were calibrated with a specially developed magnet and coil calibrator. The transducers had a bending resonance at 1.6 kHz. This resonance was well above the frequency range of interest, 0 - 50 Hz. The transducer calibration was verified in situ.

The apparatus used to oscillate the test cylinder in water was designed by Schargel [7]. A schematic of this apparatus is shown in Figure 3. The cylinder was supported in a yoke. The aspect ratio of the test cylinder was 25.6. The yoke consisted of a pair of struts with endplates at the end of the test cylinder. The endplates were ten cylinder diameters in diameter. The struts were supported in a frame attached to the top of the water tunnel. Mounted inside the frame were four ball bushings (two per side). The ball bushings were aligned so that the yoke could only oscillate in the vertical direction. The struts of the yoke extended vertically downward through the plexiglass window of the water tunnel. The window was sealed with 3/8 inch thick neoprene compression seals.

The yoke was attached to a B+K model 4801 shaker using a B+K 4818 mode study shaker head. The power was supplied by a B+K model 2707 power amplifier. The shaker had a displacement limit of 25.4 cm and a force limit of 381 Newtons. The shaker was used to oscillate the test cylinder at a controlled amplitude and frequency. At low frequencies the displacement limit of the shaker controlled the maximum amplitude. At high frequencies the maximum force controlled the maximum displacement that could be achieved.

2.3 Stationary Cylinder Results

The transducer was used to determine the unsteady force coefficients for a stationary cylinder spanning the water tunnel. The cylinder had end plates to isolate the center of the test cylinder from end conditions. The transducer was used to measure the unsteady lift forces and then rotated 90 degrees and used to measure the drag forces. The spectrum levels for the unsteady lift and drag forces are shown in

Figure 4. The spectrum levels for the lift forces show a peak at the vortex shedding frequency. The spectrum levels for the unsteady drag show a peak at twice the vortex shedding frequency and the spectrum levels of the drag tend to increase with decreasing frequency for low frequency. The measured values of lift coefficient are plotted versus Reynolds Number in Figure 5. The measured drag coefficients are shown in Figure 6. The mean drag coefficient was approximately 1.35 for $6000 < Re < 45,000$. The measured lift coefficients compare well to those measured in air by Moeller (6) in the MIT Acoustics and Vibration Laboratory's low noise wind tunnel using a similar force transducer modified for in air testing.

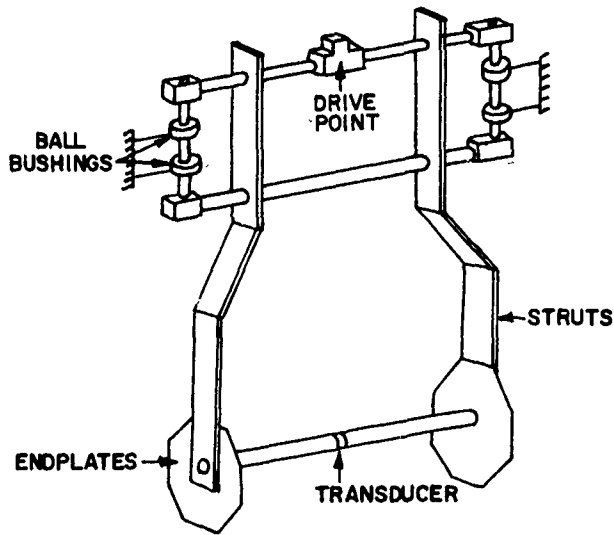


Figure 3. Schematic of Yoke

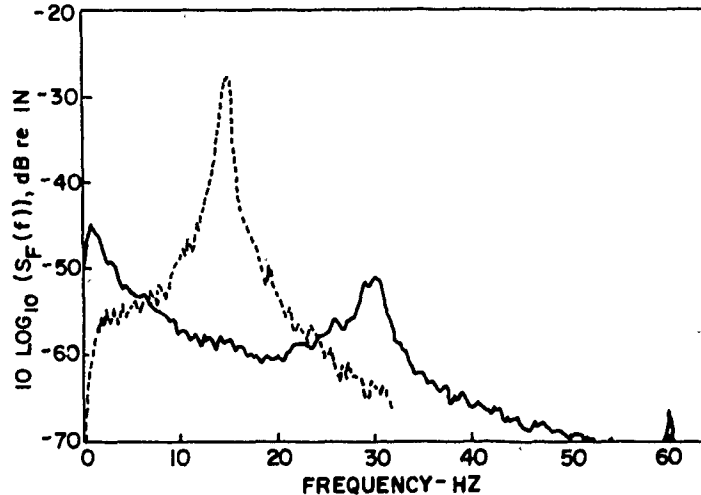


Figure 4. Spectrum Levels Lift and Drag Force
---- Lift, — Drag

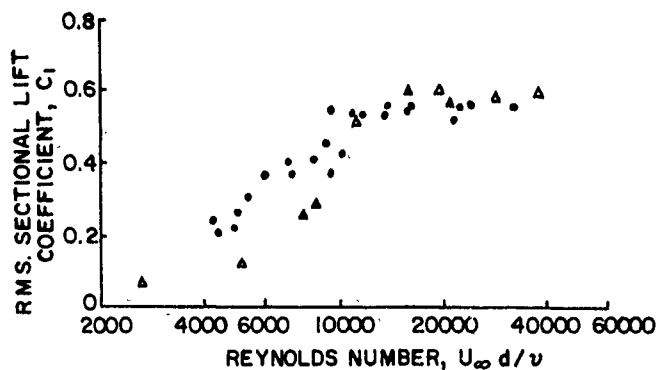


Figure 5. RMS Sectional Lift Coefficient for a Stationary Cylinder, Δ Water TI = 0.9%, \bullet Air TI = 1.2% Moeller (6)

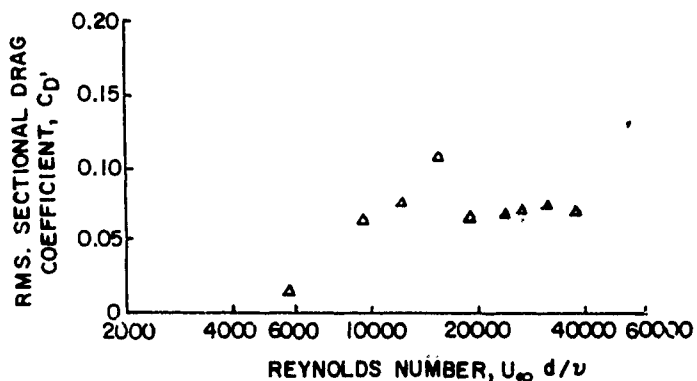


Figure 6. RMS Sectional Drag Coefficient for a Stationary Cylinder, TI = 0.9%

2.4 Forced Oscillation Results

The force transducer was placed in the yoke and oscillated by the B+K shaker system. An accelerometer on the yoke sensed the motion of the yoke and transducer. The result was a simultaneous measurement of unsteady force and cylinder motion. The experiments were performed by first setting the desired flow velocity and setting the desired frequency on the oscillator. The cylinder motion was then changed from rest to the desired amplitude of motion. The flow was allowed to stabilize and the data were taken. The data were analyzed using a Hewlett Packard Structural Dynamics Analyzer type 5423A.

The transducer was used to investigate the forces on the test cylinder while it underwent forced harmonic oscillation in a direction transverse to the flow. When the cylinder was stationary, the force transducer responded to forces on it due to the vortex shedding. These forces occurred in a narrow band about the vortex shedding frequency, f_s . The cylinder was oscillated in the

presence of a mean flow at the forcing frequency, f_f (different from the shedding frequency, f_s) at a fixed amplitude. The response was observed at both the shedding frequency and the forcing frequency. The excitation was a pure tone at the forcing frequency and the measured acceleration was nearly pure tone. The force and acceleration data were analyzed in the frequency domain. The magnitude of the force and acceleration were monitored at the forcing frequency. The magnitude of the force at the shedding frequency was also monitored. The cross-spectrum of the force and acceleration was used to determine the relative phase of the force and acceleration at the forcing frequency. The force at the driving frequency was broken down into two components; the force in phase with the acceleration and the force out of phase with the acceleration. The force in phase with the acceleration included the response of the transducer to its effective mass. The force in phase with the velocity was the work producing force.

A phenomenon that has been observed before is that the shedding frequency would change from the Strouhal frequency to the forcing frequency under certain conditions. This phenomenon was termed lock-in by Bishop and Hassan [8]. The lock-in effect has been observed for in-line oscillations as well as transverse oscillations (Crandall et al [2]). In this paper we deal only with transverse oscillations. The lock-in effect was investigated at discrete points in the nondimensional displacement, nondimensional frequency space. The amplitude displacement, δ was nondimensionalized on the cylinder diameter, $\delta_n = \delta/d$. The frequency was nondimensionalized using the shedding frequency, $f^* = f_s/f_f$. This nondimensionalization was selected to facilitate the use of the forced data in interpreting naturally oscillating cylinder phenomena. The lock-in effect was investigated in the region $0.0 < \delta_n < 0.5$ and $0.6 < f^* < 1.4$. This corresponds to a fd/U range of $0.10 < fd/U_\infty < 0.30$. This range was determined by shaker displacement limit and peak power. The data show the frequencies and amplitudes required for lock-in to occur. Both the locked-in and non locked-in behaviours were investigated.

The region of $f^*-\delta_n$ space where lock-in occurred is shown in Figure 7 for a Reynolds Number of 19,300. The trend in the data was that the closer the forcing frequency was to coincidence with the shedding frequency, the smaller the amplitude of motion required for lock-in to occur. Lock-in boundaries have been determined by other investigators. Koopman [9] and Mercier [10] used flow visualization techniques to determine when the flow was locked-in. The current data is in good agreement with the lock-in boundaries determined by other investigators in spite of significant differences in Reynolds Numbers.

In the non lock-in region the response of the force transducer showed two peaks in its response: a broad peak associated with the vortex shedding and a peak associated with the cylinder motion. Figure 8 is an example of the non locked-in spectrum levels of the lift force for $f^* = 1.36$ and $\delta_n = 0.21$. The peak at the forcing frequency includes the inertial force of the transducer ring element. At the forcing frequency for amplitudes up to $\delta_n = 0.4$ the fluid loading was predominately mass-like. The motion of the cylinder did not completely disrupt the shedding of vortices at the vortex shedding frequency. There was still the same character to the force spectrum as when the cylinder was stationary at the same Reynolds Number, except for the peak at the forcing frequency due to the cylinder motion.

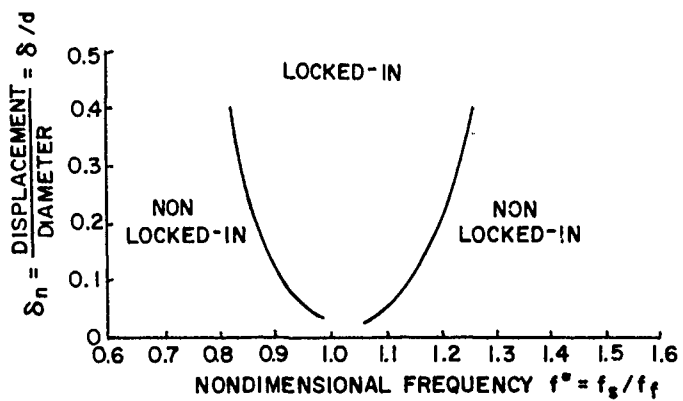


Figure 7. Lock-in Boundaries in $f^* - \delta_n$ Space

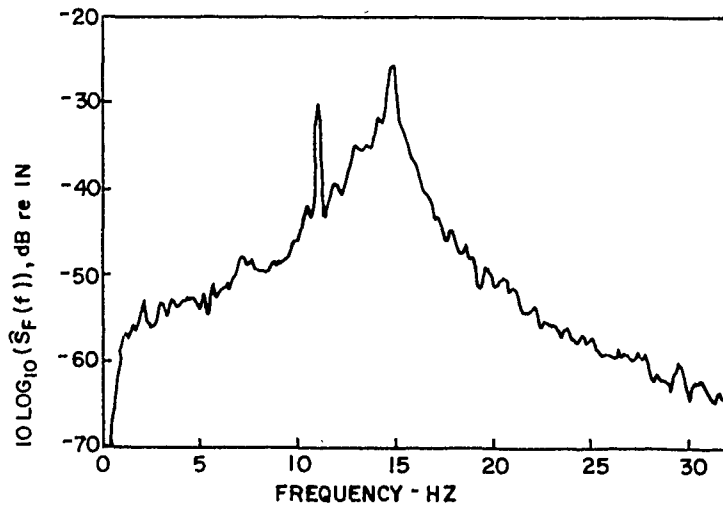


Figure 8. Spectrum Levels Lift Force, Forced Oscillation
 $Re = 19,300, f^* = 1.36, \delta_n = 0.21$

In the locked-in region the shedding frequency changed from the Strouhal frequency to the forcing frequency and only one peak occurred. An example of the lock-in behaviour is shown in Figure 9 for an $f^* = 1.0$ and a $\delta_n = 0.20$. The spectrum levels for a stationary cylinder are also shown in Figure 9. The cylinder motion has organized the flow as can be seen from the narrowness of the peak for the locked-in case. An example of locked-in and non

locked-in behaviour at the same forcing frequency is shown in Figure 10 for an $f^* = 0.91$ and $\delta_n = 0.05$ and $\delta_n = 0.32$. This shows that at a fixed frequency the flow can be either locked-in or not locked-in depending on the amplitude of motion. The non locked-in case shows two peaks and the locked-in case has only one.

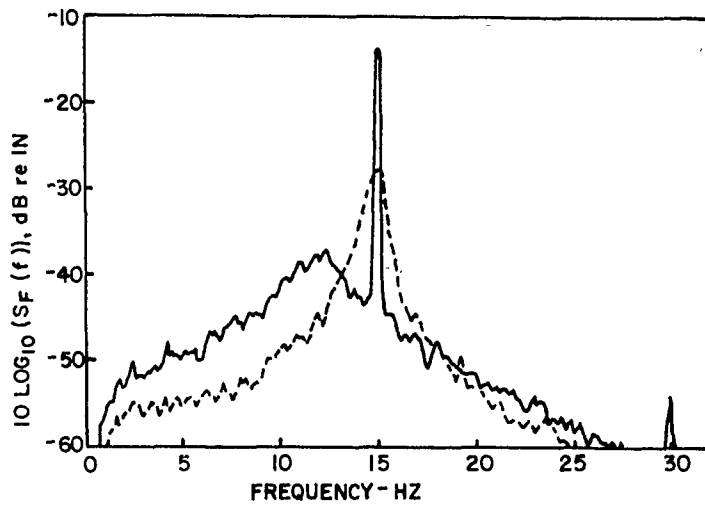


Figure 9. Spectrum Levels Lift Force, Forced Oscillation
 $Re = 19,300$, $f^* = 1.0$, $\delta_n = 0.0$,
 $\delta_n = 0.21$

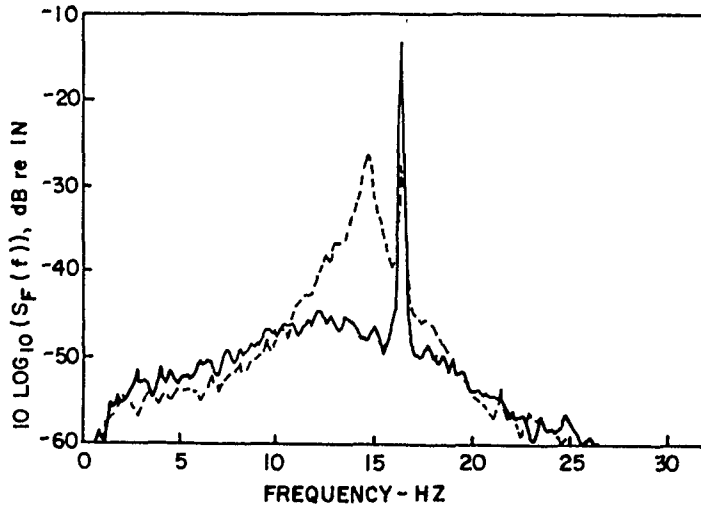


Figure 10. Spectrum Levels Lift Force, Forced Oscillation
 $Re = 19,300$, $f^* = 0.91$, $\delta_n = 0.05$,
 $\delta_n = 0.32$

3. SPRING MOUNTED CYLINDER RESULTS

Tests were undertaken to determine the response of a spring mounted cylinder to vortex shedding excitation. The arrangement utilized the existing frame and yoke. Springs were mounted on the yoke outside the water tunnel as in Figure 11. The springs were located such that there was a set holding the yoke to the water tunnel and another set that was tied to a chain hoist that was used to pretension all the springs. The pretensioning was necessary so that the springs would operate in their linear domains. The pretensioning was large enough so that the springs were in tension throughout the tests. The system was designed to have a resonant frequency as close to 15 Hz as possible so that the Reynolds Number range would correspond to the forced oscillation tests.

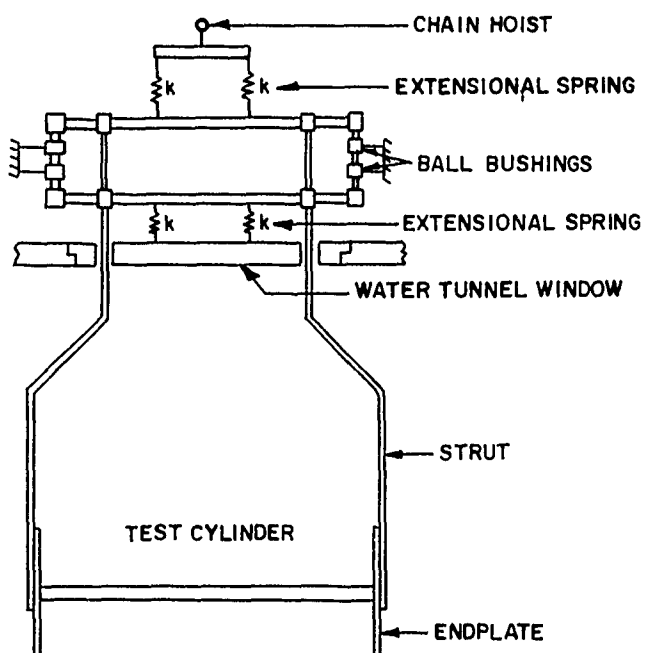


Figure 11. Schematic of Spring Mounted Cylinder

The system characteristics were determined experimentally. The moving mass was measured to be 2.4 Kg. The natural frequency was measured by plucking the cylinder and observing its response. The damping was determined from the same tests. The tests were done in air and then the water tunnel was filled with water and the tests were repeated. The results are summarized in Table 1.

Condition	Resonant Frequency	Quality Factor
dry	13.8 Hz	25.0
wet	13.4 Hz	14.4

An accelerometer was placed on the yoke outside the water tunnel and used to determine the acceleration response of the structure. The flow was initiated and stabilized. The acceleration response spectrum levels were determined for each flow condition using the Hewlett-Packard Analyzer. The path the system followed in the displacement frequency space is plotted in Figure 12. Also shown in Figure 12 are the lock-in boundaries determined from the forced motion experiments. The corresponding frequency v.s. nondimensional frequency plot is shown in Figure 13.

The ordinate in Figure 12 is the nondimensional frequency. It is defined to be the shedding frequency for a stationary cylinder at that velocity ($f_s = 0.2U_\infty/d$) divided by the resonant frequency of the spring mounted cylinder in water. Defined this way, The nondimensional frequency increases with flow velocity. In Figure 12 the dots represent the path followed when the flow velocity was increasing and the x's represent the path followed when the flow velocity decreased. Similarly, Figure 13 shows the variation of the cylinder response frequency with nondimensional frequency. The dots show the path followed with increasing flow velocity and the x's show the path followed with decreasing flow velocity.

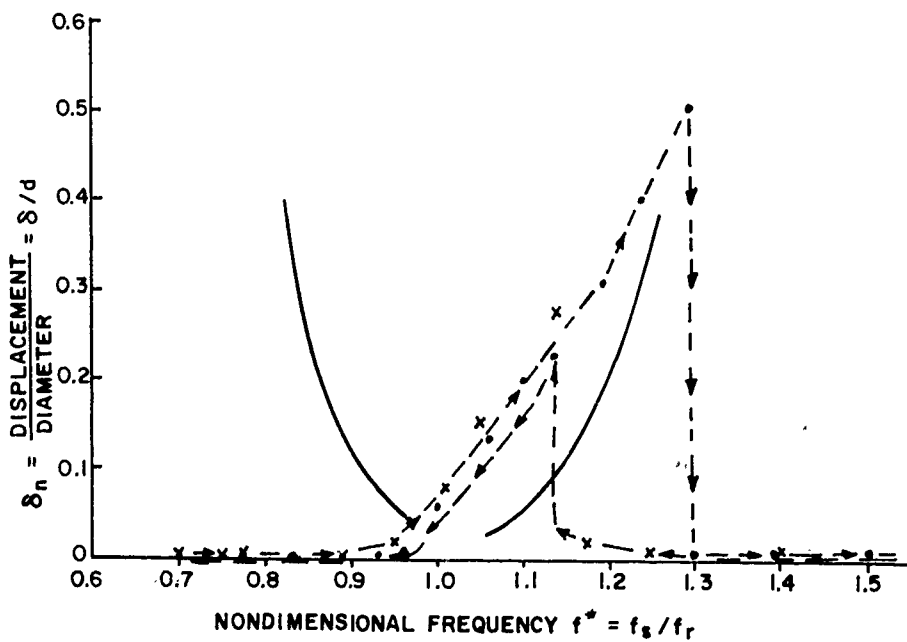


Figure 12. Response Diagram, Spring Mounted Cylinder
 • Increasing Velocity, x Decreasing Velocity

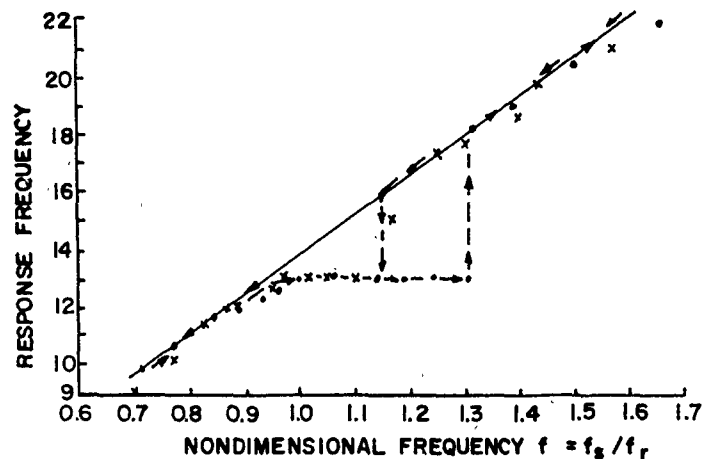


Figure 13. Variation of Cylinder Response Frequency with Nondimensional Frequency
 • Increasing Velocity
 × Decreasing Velocity

The spring mounted cylinder showed a definite hysteresis loop with the amplitude and spectrum levels of the acceleration response depending on whether the point was approached from a higher or lower velocity. This type of double amplitude response has been observed by Feng [11] and Tsahalis and Jones (12). The maximum amplitude of cylinder response did not occur at the coincidence of the natural frequency with the shedding frequency. The cylinder did not lock-in with increasing velocity until coincidence. The maximum amplitude occurred just before the cylinder detuned from the locked-in condition and returned to a non locked-in response.

The hysteretic behaviour was investigated by both stopping the cylinder and releasing it from rest and by displacing the cylinder and releasing it. When the cylinder was released from rest it rose to the lower branch of the hysteresis loop when the flow conditions corresponded to the hysteresis region. Outside this region, the cylinder returned to its initial amplitude. This is the same behaviour observed by Feng [11]. When the spring mounted cylinder was displaced and released, the observed behaviour depended on the nondimensional frequency. When the nondimensional frequency was outside the hysteresis region, the cylinder would settle to the same conditions observed without the initial disturbance. When the nondimensional frequency was in the hysteresis region, the observed response depended on how close the nondimensional frequency was to unity and on the amplitude of the initial disturbance. At a fixed nondimensional frequency, the cylinder would not lock-in if the disturbance was small. If the disturbance was large enough, the cylinder would lock-in and respond at a large amplitude. The size of the disturbance necessary to cause lock-in was smaller the closer the nondimensional frequency was to unity. At the largest nondimensional frequency that lock-in occurred with increasing velocity, it was not possible to give the test cylinder a large enough initial amplitude to achieve the lock-in condition. The result is that a naturally oscillating cylinder can be locked-in or not locked-in depending on the cylinders' initial conditions.

4.0 ANALYSIS OF DATA

An attempt to utilize the information gained from the forced oscillation experiments has been made. This description is only valid for cylinders constrained to move in a direction transverse to the flow. A description of a naturally oscillating cylinder has been formulated using the lock-in boundaries in a displacement-frequency space. The result from experiments at one Reynolds Number have been utilized to make predictions over a range of Reynolds Numbers. The shedding frequency for a stationary cylinder was nondimensionalized by the still water resonant frequency of the naturally oscillating cylinder, $f^* = f_s/f_r$. The stationary cylinder shedding frequency f_s is $f_s = 0.19U_\infty/d$. The displacement was nondimensionalized using the cylinder diameter and the lock-in boundaries of Figure 7 were utilized. The resonant frequency replaces the forcing frequency in the nondimensionalization. In the resonant case the shedding frequency changes from the Strouhal frequency to the natural frequency, whereas in the forced case it changes from the Strouhal frequency to the forced frequency. In both cases it is the motion of the cylinder that causes the change in character of the flow.

The stationary cylinder lift spectrum levels were used to compute the nonlocked-in response. The non locked-in data showed that the cylinder motion does not drastically alter the spectrum levels of the force for small amplitude displacements. The unsteady lift coefficients do not change much in the Reynolds Number range from 15,000 to 50,000 and the shedding occurs at the Strouhal frequency. A simple fit to the spectrum levels of the force was used to predict non locked-in response amplitudes. A simple mechanical oscillator was used to estimate the response of the spring mounted cylinder to flow. The equation for the squared magnitude of the transfer function from displacement response due to an input force is

$$|H(f)|^2 = \frac{1}{[k - M(2\pi f)^2]^2 + (C2\pi f)^2} \quad (1)$$

The response spectrum was estimated by multiplying the structural response function by the forcing function. The local force coefficients were corrected for cylinder length using stationary cylinder correlation lengths. This assumes that the motion does not correlate the flow for the conditions of interest, i.e. non locked-in low amplitude motions. The result of correcting for the cylinder length is

$$\hat{S}_g(f) = \frac{|H(f)|^2 q^2 d^2 l_c (l - \gamma) d / U_\infty}{[5 - (\frac{f_1}{U_\infty})^2 |38|^2 + (0.9 f d / U_\infty)^2]} \quad (2)$$

The result is the displacement spectrum levels for the cylinder at a fixed flow velocity. This estimate of the response neglects the damping due to the fluid for low amplitude, non locked-in flows. The displacement spectrum levels are then integrated to determine the rms displacement. The rms displacement and nondimensional frequency are checked against the lock-in boundaries in Figure 7 to see if the point corresponds to a locked-in condition or not. If it does not correspond to a locked-in condition then the response estimate is assumed to be valid.

When the lock-in boundary in displacement-frequency space is encountered the previous model is no longer valid. The vortex shedding frequency changes from the Strouhal frequency to the resonant

frequency. The constraint for determining the response amplitude in the locked-in region is that the power flow from the fluid to the structure must be dissipated by the structural damping mechanism. The structural damping can be described in terms of a quality factor, $Q = 1/\eta = 1/2 C_{cr}/C$. The damping force is

$$F_d = \frac{M(2\pi f_r)^2 \delta_{nd}}{\sqrt{2} Q} \quad (3)$$

where f_r is the resonant frequency of the system. This damping force must be offset by the lift force for the cylinder to remain in a steady state condition. The required total lift coefficient for the cylinder to respond at nondimensional amplitude, C_{LR} is

$$C_{LR} = \frac{F_d}{1/2 \rho U_\infty^2 d \ell} = \frac{1/Q M 2\pi f_r^2 \delta_{nd}}{\sqrt{2} 1/2 \rho d f^* U_c^2} \quad (4)$$

where $f^* = f_s/f_r$, and U_c is the flow velocity for which $f_s' = f_r$. To determine the allowed amplitudes of response it is necessary to know both the variation of the local force coefficients and the variation of the correlation lengths with the nondimensional displacement. The variation of correlation length with amplitude was measured by Toebees (5) for a δ_n up to 0.125 at a Reynolds Number of 68,000. Koopman (9) used a pair of hot wires in the wake to determine the lock-in boundaries. Lock-in was defined when the cylinder motion fully organized the wake.

This algorithm was used to predict the response of the spring mounted cylinder. The cylinder mass was 2.4 Kg, diameter 1.6 cm, length 40 cm, quality factor 14.4, and resonant frequency of 13.4 Hz. The correlation length was assumed to be 7 diameters long for the non lock-in response estimate. For the locked-in response estimate, the lift coefficient for $f^* = 1.0$ was used to estimate the power input. The variation of the local unsteady force for $f^* = 1.0$ with δ_n is shown in Figure 14. The flow was assumed to be fully correlated for the locked-in estimates.

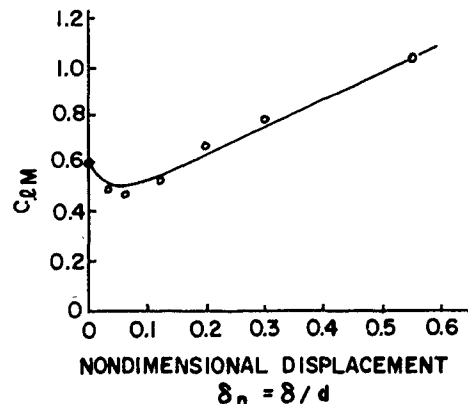


Figure 14. Variation of RMS Sectional Lift Coefficient with δ_n , $f^* = 1.0$, $Re = 19,300$

The estimated response is shown in Figure 15. The response shows a region in $f^*-\delta_n$ space where the cylinder can be locked-in or not locked-in depending on the path followed in $f^*-\delta_n$ space. This region corresponds to $1.15 < f^* < 1.3$. This hysteretic behaviour was observed in the spring mounted cylinder tests.

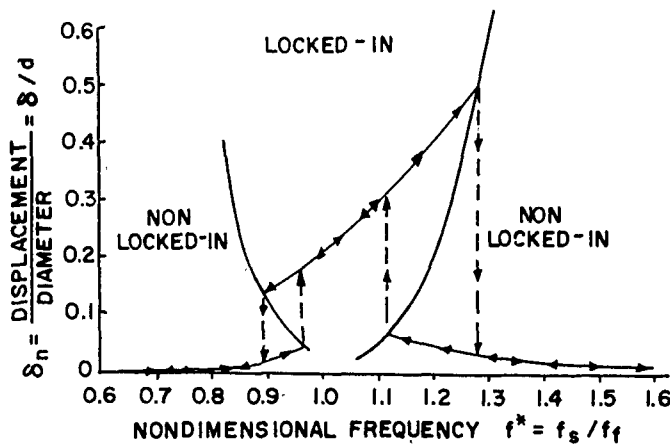


Figure 15. Estimated Cylinder Response Diagram
Spring Mounted Cylinder in Water

5. RESULTS AND CONCLUSIONS

- 1) Lock-in boundaries were determined in the reduced frequency range $0.1 < f_d/U_\infty < 0.3$ for amplitude to diameter ratios up to $\delta_n = 0.5$.
- 2) The vibratory response of a spring mounted cylinder was observed. The cylinder was constrained to move transverse to the flow direction. The response showed a region where the cylinder could be locked-in or not locked-in at the same velocity.
- 3) The response of the spring mounted cylinder was estimated using forced vibration data. The lock-in boundaries in the $f^*-\delta_n$ space were used to describe the state of the cylinder motion. The hysteretic behaviour that was observed was due to the fact that the lock-in boundaries were amplitude dependant as well as frequency dependant.

Acknowledgements: The funding for this work was provided by the office of Naval Research, Contract No. N00014-76-6-0696.

REFERENCES

1. Blevins, R. D., Flow-Induced Vibration, Von Reinhold Co., 1977.
2. Crandall, S. H., Vigander, S., and March, P. A., "Destructive Levels of Vibration of Trashracks Due to Fluid Structure Interaction," Journal of Engineering for Industry, Nov. 1975, pp. 1359-1365.
3. King, R., "A Review of Vortex Shedding Research and Its Application," Ocean Engineering, Vol. 4, 1977, pp 147-172.
4. Sarpkaya, T., "Vortex-Induced Oscillations - A Selective Review," Journal of Applied Mechanics, Vol. 46, No. 2, 1979, pp. 241-258.
5. Toebe, G. H., "The Unsteady Flow and Wake Near an Oscillating Cylinder," Journal of Basic Engineering, Vol. 91, 1969, pp. 493-505.
6. Moeller, M. J., "Measurement of Unsteady Forces on a Circular Cylinder in Cross Flow at Subcritical Reynolds Numbers," MIT PhD Thesis, September 1982.
7. Scharge, R. S., "The Drag Coefficient for a Randomly Oscillating Cylinder in Uniform Flow," MSc. Thesis, MIT, 1980.
8. Bishop, R. D. E. and Hassan, A. Y., "The Lift and Drag Forces on a Cylinder Oscillating in a Flowing Fluid," Proc. Royal Society, Ser. A, 277, 1963, pp. 51-75.
9. Koopman, G. H., "The Vortex Wakes of Vibrating Cylinders at Low Reynolds Numbers," Journal of Fluid Mechanics, Vol. 28, 1967, pp. 501-512.
10. Mercier, J. A., "Large Amplitude Oscillations of a Circular Cylinder in a Low-Speed Stream," PhD Thesis, Stevens Institute of Technology, Hoboken, N.J., 1973.
11. Feng, C. C., "The Measurement of Vortex Induced Effects in Flow Past Stationary and Oscillating Circular and D Section Cylinders," MSc Thesis, University of British Columbia, 1968.
12. Tsahalis, D. T., and Jones, W. T., "Vortex Induced Vibrations of a Flexible Cylinder Near a Plane Boundary in Steady Flow," Proceedings of the Offshore Technology Conference, Vol. 2, 1981, pp 367-372.

FLOW-INDUCED OSCILLATIONS OF CYLINDERS IN THE STREAMWISE DIRECTION

D. H. Turnbull and I. G. Currie
Department of Mechanical Engineering
University of Toronto
Toronto, Ontario, Canada

ABSTRACT

The purpose of the research reported here is to attempt to clarify the conditions under which in-line oscillations of a circular cylinder occur, and to establish the oscillation characteristics.

A mathematical model has been developed which attempts to represent a cylinder vibrating in the streamwise direction. This mathematical model is based on the Van der Pol equation and is similar in many respects to one series of models which exists for cross-flow oscillations. Solutions to the mathematical model indicate the possibility of in-line oscillations and the results so obtained have been fitted to experimental data, thus evaluating the free parameters in the mathematical model.

An experiment was carried out to establish the effects of reduced velocity, Reynolds number, surface roughness, and freestream turbulence on the stability of a circular cylinder to in-line oscillations. Results obtained from the test program indicate that, within the range of conditions covered, in-line oscillations occur when the Reynolds number is in the critical range, and then only when free-stream turbulence exists. Surface roughness of the test cylinders did not appear to play a significant role.

1. INTRODUCTION

Investigations into the nature of flow-induced oscillations of cylinders in the streamwise direction began to appear in the literature after the problems encountered during the construction of an oil jetty at Immingham, England, in the tidal flow of the Humber estuary [1], [2]. The main results emerging from the Immingham experience are summarized below:

- (a) Flow-induced oscillations in the streamwise direction developed over a Reynolds number range $2 \times 10^5 - 6 \times 10^5$, which is expected to be close to the critical range for a smooth cylinder.
- (b) These oscillations occurred over two distinct ranges of reduced velocity, $V_r = V/f_r D$:
(i) close to $V_r \approx 2.0$, accompanied by symmetric vortex shedding;

(ii) close to $V_r = 2.5$, where alternate vortex shedding was observed.

The response peak at $V \approx 2.5$ was easiest to explain, being a simple harmonic of the well documented cross-flow vibration peak in which the frequency of cylinder vibration is twice the vortex shedding frequency. The response peak at $V \approx 2.0$ corresponded to a self-excited cylinder oscillation that was completely unexpected. The amplitudes of oscillation ($a/D \approx 0.1$) were an order of magnitude smaller than those associated with cross-flow oscillations, but were still large enough to make construction difficult and to potentially damage the jetty structure. Symmetric vortex shedding was observed to accompany the in-line oscillations at $V_r = 2.0$, the two symmetric vortices being shed once every cycle of oscillation.

Subsequent investigations have confirmed the existence of two response peaks for in-line oscillations, and have demonstrated that the Reynolds number need not be in the critical range for in-line oscillations to occur. Flow-induced streamwise oscillations of flexible cantilevered cylinders in flowing water have been reported at Reynolds numbers well below the expected critical range [3]. This leads to the notion that there are two distinct types of in-line oscillation and that they have different fundamental mechanisms.

Based on in-line cylinder oscillations in the critical Reynolds number range, a quasisteady model was proposed, reference [4], to explain a possible mechanism for these oscillations. This model is based on an instability criterion which is only satisfied in the critical Reynolds number range, where the mean drag coefficient vs. Reynolds number curve has a negative slope.

Almost nothing is known of the mechanism responsible for the symmetric vortex shedding phenomenon associated with the first instability range of in-line oscillations near $V_r = 2.0$. In this paper it is proposed that the symmetric vortex shedding is due to a cycle of vortex formation and shedding on a time scale which is short compared to the time scale necessary for the development of a (stable) alternate vortex shedding pattern. If the Reynolds number is low enough when the cylinder is moving downstream, then a pair of symmetric vortices (Föppl vortices) form behind the cylinder and remain attached [5]. As the Reynolds number increases, this pattern of vortex formation breaks down and the vortices are shed alternately. However, if the time scale of vortex formation is long compared to the time scale of the cylinder oscillation, then an alternate pattern may never develop before the Reynolds number again falls. This could account for the observation of a pair of symmetric vortices being shed once each cycle of cylinder oscillation.

2. THEORETICAL DEVELOPMENT

2.1 Van der Pol Oscillator Model

Vortex-induced cylinder oscillations in the transverse (or cross-flow) direction have been described mathematically using a lift-oscillator model in which the lift coefficient satisfies the Van der Pol oscillator equation [6], [7]. In this paper a similar approach is taken to describe vortex-induced cylinder oscillations in the streamwise (or in-line) direction.

The Van der Pol oscillator model has traditionally been employed in this area of fluid mechanics as a relatively simple description of the periodic separated flow around an oscillating bluff body. The model predicts self-excited (self-limiting) oscillations, the frequency of which can be related to the Strouhal frequency to describe the role of vortex shedding in exciting the cylinder oscillations. The interaction of the cylinder motion with the oscillator is through a forcing term which will be discussed.

2.2 Mathematical Formulation

The physical problem of a cylinder subjected to vortex-induced oscillations in the streamwise direction will be modelled as a damped mass-spring system for the equation of the cylinder motion, coupled through the forcing

terms to a Van der Pol equation for the instantaneous fluctuating drag coefficient.

The equation of motion in the streamwise direction may be written as

$$Mx_1'' + cx_1' + kx_1 = (\text{forcing})$$

where M is the cylinder mass, including the added mass. The simplest forcing term that could be proposed is $\frac{1}{2}\rho DLV^2 C_D$, where C_D is the fluctuating drag coefficient. A somewhat more general forcing term involved C_D^1 as well as C_D^2 , where C_D^1 is the mean drag coefficient. The mean drag force term is omitted because it does not contribute to the cylinder oscillations.

Introducing the dimensionless variables $t = \omega_0 t_1 = \sqrt{k/M} t_1$ and $x = x_1/D$, this equation can be written in nondimensional form:

$$\ddot{x} + 2\xi\dot{x} + x = (\text{forcing}), \quad (1)$$

where $\xi = \frac{c}{2M\omega_0}$ and a dot (\cdot) denotes differentiation with respect to t .

The instantaneous drag coefficient satisfies a Van der Pol equation:

$$\ddot{C}_D - \delta\omega_0 \dot{C}_D + \frac{1}{\omega_0} \dot{C}_D^3 + \omega_0^2 C_D = (\text{forcing}), \quad (2)$$

where ω_0 is the oscillator frequency, and for the second instability range of in-line oscillations is taken to be twice the dimensionless Strouhal frequency $\omega_0 = 2 \frac{f_s}{f_n} = 2 \frac{f_s}{f_n}$. The approximate solution to equation (2) for small forcing is

$$C_D = C_{D0} \sin \omega_0 t,$$

where $C_{D0} = \sqrt{\frac{4\delta}{3}}$ has a natural physical interpretation as the fluctuating drag drag coefficient of a stationary cylinder, which is approximately 0.2, see reference [8].

The forcing term in equation (1) can be taken to be

$$\alpha_1 C_D + \beta_1 \dot{C}_D,$$

$$\text{where } \alpha_1 = \frac{\frac{1}{2}\rho DLV^2}{MD\omega_0^2} = \frac{\rho D^2 L}{8\pi^2 M} \left(\frac{V}{f_s D} \cdot \frac{2f_s}{f_n} \right)^2 = \frac{\rho D^2 L}{32\pi^2 M S^2} \cdot \omega_0^2 = \alpha \omega_0^2,$$

and for lack of more detailed information, β_1 is taken to be equal to α_1 . The forcing term in equation (2) is taken to be a linear function of the cylinder displacement and velocity, and is written

$$ax + bx,$$

where a and b must be chosen to fit physical data.

The general model for in-line cylinder oscillations may, therefore, be written as

$$\ddot{x} + 2\xi\dot{x} + x = \alpha\omega_0^2 (C_D + \dot{C}_D), \quad (3)$$

$$\ddot{C}_D - \delta\omega_0 \dot{C}_D + \frac{1}{\omega_0} \dot{C}_D^3 + \omega_0^2 C_D = ax + bx, \quad (4)$$

$$\text{where } \zeta = \frac{c}{2M\omega_n}, \quad (5)$$

$$\alpha = \frac{\rho D^2 L}{32\pi^2 M S^2}, \quad (6)$$

$$\sqrt{\frac{4\delta}{3\gamma}} \approx 0.2, \quad (7)$$

$$\text{and } w_0 = 2 \frac{w_s}{w_n} = 2 \frac{f_s}{f_n} = 2 S_t \cdot v_r \quad (8)$$

is assumed to be close to unity.

2.3 Model Solutions

To obtain approximate solutions to equations (3) and (4), it is assumed that all the coefficients are small, of order $0(\varepsilon)$ where $\varepsilon \ll 1$, except w , which is $1 + O(\varepsilon)$. That is, the coefficients are taken to be $\zeta = \varepsilon \zeta$, $\alpha = \varepsilon \alpha$, etc., and $w_0 = 1 + \varepsilon \Omega$, where now ζ , α , etc., and Ω are of order $0(1)$. Physically, these assumptions correspond to small damping, coupling (forcing), and small nonlinearities. Under these assumption, equations of the type (3) and (4) can be solved using a two-time perturbation expansion [9], [10]. The introduction of two time scales makes sense physically, as explained previously, if the fast time is equated to the time scale of the cylinder oscillation while the slow time is the time scale of the formation of an alternate vortex pattern.

The assumption is made that x and C_D depend not only on t , but also on a slow time $\tau = \varepsilon t$. To order ε , the solution to equations (3) and (4) is assumed to have the form

$$\begin{aligned} x &= x_0(t, \tau) + \varepsilon x_1(t, \tau), \\ C_D &= C_{D0}(t, \tau) + \varepsilon C_{D1}(t, \tau). \end{aligned}$$

Substituting this assumed solution into equations (3) and (4), and noticing that $w^2 \approx 1 + 2\varepsilon\Omega$, " \cdot " = $\frac{\partial}{\partial t} + \varepsilon \frac{\partial}{\partial \tau}$, one obtains a hierarchy of equations to be solved:

$$\frac{\partial^2 x_0}{\partial t^2} + x_0 = 0 \quad (9a)$$

$$\frac{\partial^2 x_1}{\partial t^2} + x_1 = -2 \frac{\partial^2 x_0}{\partial t \partial \tau} - 2\zeta \frac{\partial x_0}{\partial t} + \alpha C_{D0} + \alpha \frac{\partial C_{D0}}{\partial t} \quad (9b)$$

and

$$\frac{\partial^2 C_{D0}}{\partial t^2} + C_{D0} = 0 \quad (10a)$$

$$\frac{\partial^2 C_{D1}}{\partial t^2} + C_{D1} = -2 \frac{\partial^2 C_{D0}}{\partial t \partial \tau} - \gamma \left(\frac{\partial C_{D0}}{\partial t} \right)^3 + \delta \frac{\partial C_{D0}}{\partial t} - 2\Omega C_{D0}$$

$$+ a x_0 + b \frac{\partial x_0}{\partial t}. \quad (10b)$$

The general solutions of equations (9a) and (10a) are

$$x_0(t, \tau) = X_0(\tau) \cos(t + \phi_0(\tau)), \quad (11)$$

$$C_{D0}(t, \tau) = C_{D0}(\tau) \cos(t + \psi_0(\tau)). \quad (12)$$

The standard procedure in the two-time perturbation method is to substitute (11) and (12) into equations (9b) and (10b), and equate the coefficients of $\cos(t + \phi_0)$, $\cos(t + \psi_0)$ and $\sin(t + \phi_0)$, $\sin(t + \psi_0)$ to be zero, in order to avoid "secular" solutions (solutions which diverge as $t \rightarrow \infty$). When this is done, four equations are obtained for $X_0(\tau)$, $C_{D0}(\tau)$, $\phi_0(\tau)$ and $\psi_0(\tau)$:

$$\begin{aligned} \frac{dX_0}{d\tau} &= -\zeta X_0 + \frac{1}{2}\alpha C_{D0}(\cos\mu_0 - \sin\mu_0) \\ \frac{d\phi_0}{d\tau} &= -\frac{1}{2}\alpha \frac{C_{D0}}{X_0} (\cos\mu_0 + \sin\mu_0) \\ \frac{dC_{D0}}{d\tau} &= \frac{1}{2}\delta C_{D0} - \frac{3}{8}\gamma C_{D0}^3 + \frac{1}{2}X_0(b\cos\mu_0 + a\sin\mu_0) \\ \frac{d\psi_0}{d\tau} &= \Omega - \frac{1}{2}\frac{X_0}{C_{D0}} (\alpha\cos\mu_0 - b\sin\mu_0) \end{aligned} \quad (13)$$

Here $\mu_0 = \mu_0(\tau) = \phi_0(\tau) - \psi_0(\tau)$.

To obtain steady-state, single-frequency solutions to equations (13), one assumes the response frequency is $1 + \epsilon\omega$, where ω is of order $O(1)$. The amplitudes X_0 and C_{D0} are assumed constant, while the phases ϕ_0 and ψ_0 both drift at the slow rate $\epsilon\omega$. Then equations (13) become

$$\begin{aligned} \zeta X_0 - \frac{1}{2}\alpha C_{D0}(\cos\mu_0 - \sin\mu_0) &= 0 \\ \omega + \frac{1}{2}\alpha \frac{C_{D0}}{X_0} (\cos\mu_0 + \sin\mu_0) &= 0 \\ \frac{1}{2}\delta C_{D0} - \frac{3}{8}\gamma C_{D0}^3 + \frac{1}{2}X_0(b\cos\mu_0 + a\sin\mu_0) &= 0 \\ \omega - \Omega + \frac{1}{2}\frac{X_0}{C_{D0}} (\alpha\cos\mu_0 - b\sin\mu_0) &= 0. \end{aligned} \quad (14)$$

Equations (14) can be manipulated to obtain approximate steady-state, single-frequency solutions to equations (13) in the following form:

$$\text{Frequency: } \Omega \approx \omega + \frac{k_1\zeta - k_2\omega}{4(\omega^2 + \zeta^2)} \quad (15)$$

$$\text{Amplitude: } C_{D0}^2 = \frac{4}{3\gamma} \left\{ \delta - \frac{k_1\omega + k_2\zeta}{2(\omega^2 + \zeta^2)} \right\} \quad (16)$$

$$X_0^2 = \frac{\alpha^2}{2(\omega^2 + \zeta^2)} C_{D0}^2 \quad (17)$$

$$\text{Phase: } \tan\mu_0 = \frac{\omega + \zeta}{\omega - \zeta}. \quad (18)$$

Here $k_1 = \alpha(a+b)$ and $k_2 = \alpha(a-b)$. In these solutions, Ω and ω may be thought of as "detuning" variables: Ω represents the detuning between the cylinder natural frequency and the Van der Pol oscillator frequency, while ω represents the detuning between the response frequency and the cylinder natural frequency.

The stability of the steady state solutions given by equations (15)-(18) can be checked by linearizing equations (13) about the steady state solution.

Positive real parts of eigenvalues of the resulting Jacobian matrix then correspond to unstable solutions of (13).

2.4 Model Predictions

The theory outlined in the preceding sections can be utilized, with a suitable choice of model parameters, to predict cylinder oscillations in the streamwise direction. The model parameter a is determined from equation (6) while δ and γ are chosen so that relationship (7) is satisfied. The damping factor ζ can be determined from equation (5) if the damping coefficient c is known. A more useful formula in the case of small-amplitude vibrations in a high Reynolds number flow [11] is given below:

$$\zeta = \frac{1}{4\pi} \left(\frac{\rho D^2 L}{M} \right) \left(\frac{V}{f_D} \right) C_D, \quad (19)$$

where C_D is the mean drag coefficient. Finally, since there is no known physical reasoning guiding the choice of model parameters a and b , these are chosen to fit physical data.

The model can be fitted to data obtained at Immingham [2] in both instability regions of in-line oscillations. The mass ratio of the steel piles used at Immingham can be estimated as

$$\frac{\rho D^2 L}{M} \approx 0.4.$$

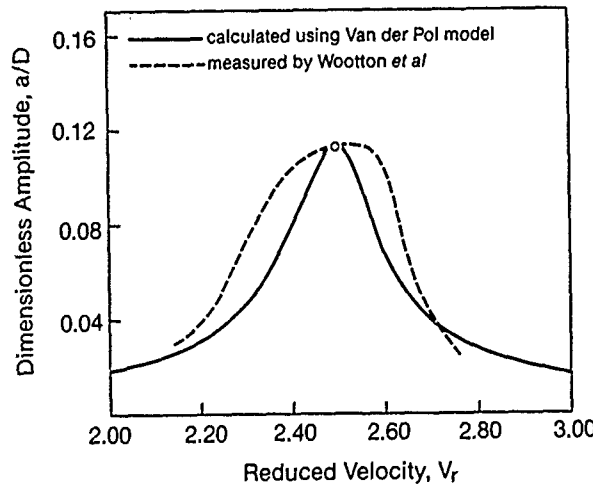


FIGURE 1: AMPLITUDE RESPONSE FOR ALTERNATE VORTEX SHEDDING

In the second instability region (near $V_r = 2.5$), where the Reynolds number was approximately 5×10^5 , and the mean drag coefficient is estimated to be 0.5, the model parameters determined from (6), (7) and (19) are $\epsilon = 0.01$, $\zeta = 4$, $a = 2.2$, $\delta = 2$, $\gamma = 50$. It is seen that the assumption that all the parameters are of order $O(1)$ is not strictly adhered to, but reasonable results are obtained nevertheless. Based on Van der Pol oscillator models of cross-flow vibrations [6], $a = 0$ is a sensible choice for the alternate vortex shedding induced oscillations in the second instability region. The model parameter b was chosen to fit the Immingham data [2] and was selected to be $b = 4$. Finally, the frequency was translated into reduced velocity using equation (8):

$$V_r = \frac{1 + \epsilon \Omega}{2S_t},$$

where the Strouhal number was assumed to be $S_t = 0.2$. Stable, steady-state solutions were computed using equations (15)-(18), and these are shown in Figure 1 with the Immingham data superimposed.

The Van der Pol oscillator model can also be fitted to the first instability region of vortex-induced, in-line cylinder oscillations (near $V_r = 2.0$). In this case the Reynolds number was approximately 3.5×10^5 , and the mean drag coefficient is estimated to be 0.6. The model parameters determined from (6), (7) and (19) are $\varepsilon = 0.01$, $\zeta = 4$, $\alpha = 2.8$, $\delta = 3$, $\gamma = 50$. The main difference in the modelling of the two instability regions of in-line oscillations is the forcing term of the Van der Pol equation. It has been suggested that the first instability region might depend on the oscillation amplitude, rather than velocity [2]. This was the motivation for taking $b = 0$ and selecting a to fit the Immingham data. The model parameter a was selected to be $a = 5$. It should be noted that there is no obvious way to translate frequency into reduced velocity in the first instability region. Based on the observation that $V_r \approx 2.0$, the translation to reduced velocity was made rather arbitrarily using

$$V_r = (1 + \varepsilon \Omega) (2)$$

Stable, steady-state solutions, computed using equations (15)-(18), are shown in Figure 2 with the Immingham data superimposed.

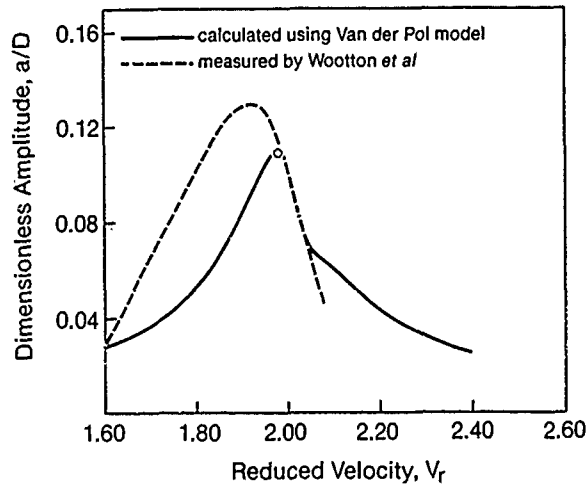


FIGURE 2: AMPLITUDE RESPONSE FOR SYMMETRIC VORTEX SHEDDING

The Van der Pol oscillator model shows reasonable agreement with the physical data in the amplitudes of oscillation in both instability regions, and in the reduced velocity range over which the oscillations occur in the second instability region. The fluctuating drag coefficient, C_{D0} , is approximately 0.2, as was desired. It is seen that for the second instability region, the fluctuating drag coefficient takes on a maximum value near the point of maximum oscillation amplitude, while for the first instability region, C_{D0} is decreasing to a minimum at the point of maximum oscillation amplitude. The model also predicts that the phase difference between the Van der Pol forcing and the cylinder response is close to zero in the first instability region, which is just what one might predict for cylinder oscillations excited by two symmetric vortices being shed once every cycle of oscillation. The corresponding phase difference for the second instability region of in-line oscillations is approximately 45° .

These results indicate that the cylinder oscillations in the second instability region are indeed a simple harmonic of the "velocity driven" transverse cylinder oscillations, while those in the first instability region may be "amplitude driven".

. EXPERIMENTAL RESULTS

.1 Test Facilities

Experiments were performed to study some aspects of streamwise oscillations of circular cylinders. The test rig, operated in a 400-foot long towing channel, consisted of an aluminum frame around which two hydrofoil sections were placed, creating a uniform, two-dimensional flow over the test cylinders. This rig was pulled through the water by a towing carriage with very accurate speed control at speeds of up to 20 feet/sec. The 4-foot long test cylinders were mounted between the hydrofoils on specially designed bearings which allowed motion of up to 2 inches in amplitude in any direction in a plane perpendicular to the free surface of the water.

Two test cylinders were employed, one being 6.5 in. diameter and the other being 14 in. diameter. The width of the towing tank was 16 feet and the water depth was 9 feet. This gave a blockage ratio of 3.24% or less. The models were located 3 feet below the free surface of the water. Each cylinder could be fitted with a surface roughening layer on which the height of the protuberances was about 1 mm.

For the experiments described in this paper, only the horizontal (streamwise) cylinder motions were of interest, so the bearings were clamped in the vertical direction. Support for the test cylinders in the horizontal (streamwise) and vertical (transverse) directions was provided by 1/16 inch cables attached to the bearings, drawn over pulleys of minimal friction, and cleated to the frame of the test rig. Springs of various stiffness were connected into the cables to provide various vibrational frequencies of the cylinders, and load cells were connected at the same point to measure the forces on the cylinder. The motion of the test cylinders was measured with differential transformer displacement transducers which followed the cylinder endplates. The support arrangement for the test cylinder is shown in Figure 3.

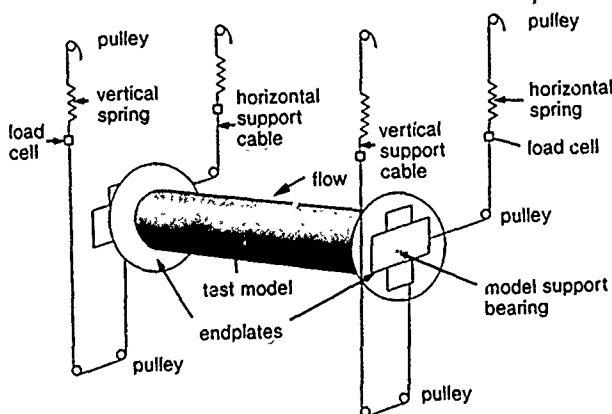


FIGURE 3: MODEL SUSPENSION SYSTEM

The flow over the cylinder could be made turbulent by pulling a screen through the water approximately 7 mesh lengths upstream of the cylinder. This screen was designed to provide a "flat" mean velocity profile along the cylinder axis, and a scale of turbulence approximately equal to the cylinder diameter. Measurements of the flow characteristics behind the screen were made

with a cylindrical hot-film probe and constant temperature anemometer. The signals from the hot-film probe, as well as the load cells and displacement transducers, were recorded directly onto an on-board computer, and stored for later analysis.

3.2 Test Results

Flow-induced, in-line cylinder oscillations were observed for a smooth 14-inch outer-diameter cylinder in turbulent flow. Figure 4 shows a portion of the output from the displacement transducers. The unstable condition occurred when the cylinder natural frequency was $f_n = 0.52$ Hz, the Reynolds number was $R_e = 1.7 \times 10^5$ and the reduced velocity was $V_r = 2.6$. This was in the critical Reynolds number range for this cylinder in turbulent flow, and was close to the reduced velocity expected for the second instability region of in-line oscillations.

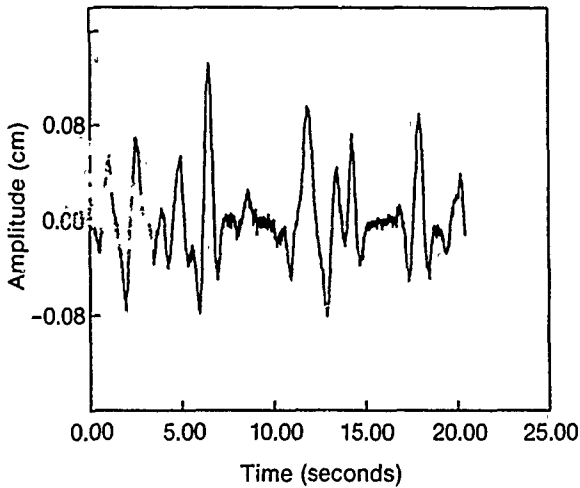


FIGURE 4: DISPLACEMENT TRANSDUCER RECORDING

These single-frequency, in-line cylinder oscillations were observed in the turbulent flow over a reduced velocity range of approximately 2.0-3.0. This also corresponded to the critical Reynolds number range for the cylinder in turbulent flow.

The oscillations observed were very small, indicative of a highly damped system. By studying the decay of cylinder oscillations in water after release from an initial displacement, the logarithmic decrement of the system was estimated to be $\delta_s \approx 1.8$. The damping factor can be computed from

$$\zeta = \frac{\delta_s}{\sqrt{(2\pi)^2 + \delta_s^2}} \quad (20)$$

and it is found that $\zeta \approx 25$ (for $\varepsilon = 0.01$). Thus the damping factor is about six times greater than that present at Immingham.

When the turbulence was removed from the flow, but conditions were otherwise matched to the unstable condition (critical $R_e, V_r \approx 2.5$), no in-line cylinder oscillations were observed. It should be noted that for undisturbed flow the critical Reynolds number range is considerably greater than in turbulent flow, and consequently the springs required to match the reduced velocity are stiffer and provide more constraint to cylinder motion. With the high damping present in the system, this added constraint is probably more than enough to prevent oscillations from occurring.

The test cylinder was also surface roughened by gluing to it 1 mm silicon spheres, and it was tested under the same unstable conditions as the smooth cylinder (turbulent flow, $V \approx 2.5$). In this case no single-frequency, in-line cylinder oscillations were observed. This lends some support to the explanation, mentioned earlier, that the mechanism responsible for streamwise cylinder oscillations depends on an instability criterion which is sensitive to the drag characteristics of the cylinder [4]. Figure 5 shows the drag coefficient as measured for the test cylinder. The results show that the steepest slope and the minimum absolute value of the drag are associated with a smooth surface in turbulent flow.

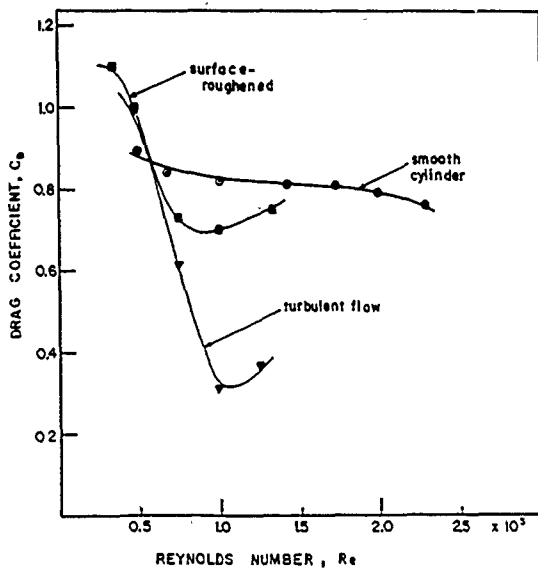


FIGURE 5: DRAG COEFFICIENT vs. REYNOLDS NUMBER

The Van der Pol oscillator model can be fitted to the data obtained in these experiments. Using equations (6), (7) and the value of ζ determined experimentally above, the model parameters are $\varepsilon = 0.01$, $\zeta = 25$, $\alpha = 1$, $\delta = 1$, $\gamma = 50$, and b is taken to be $b = 4$. The parameter a was chosen to be zero since the observed oscillations occurred near the reduced velocity range expected for the second instability region of in-line oscillations. The stable, steady-state model solution is shown in Figure 6 with values of the nondimensionalized amplitude (a/D) from the experiments superimposed.

4. CONCLUSIONS

A Van der Pol oscillator model has been adapted to flow-induced cylinder oscillations in the streamwise direction, and approximate model solutions have been computed by taking into account two inherent time scales in the problem. The model has been fitted to experimental data in the two instability regions of in-line oscillations with good agreement in the amplitude of oscillation. The model predictions make sense when viewed against the physical characteristics of the two instability regions.

Experimental data have been obtained which lends support to an explanation for one form of streamwise cylinder oscillations which is based on an instability criterion satisfied only in the critical Reynolds number range. It appears that the occurrence of in-line oscillations may depend on a number of conditions (critical R , critical V , damping threshold, freestream turbulence level) being met simultaneously. The other form of in-line oscillation was not observed, presumably due to our high level of damping.

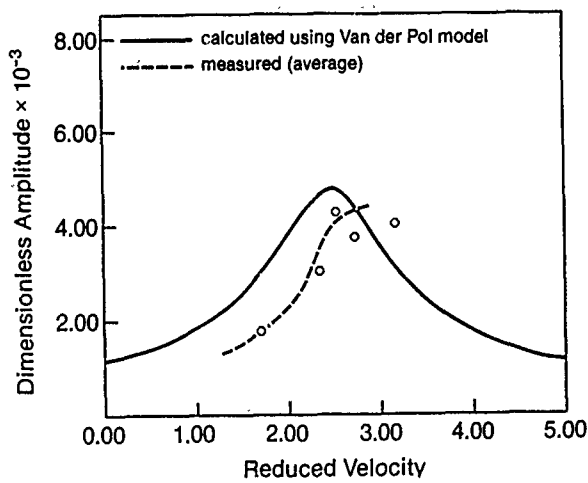


FIGURE 6: CALCULATED AND MEASURED AMPLITUDES OF OSCILLATION

APPENDIX

List of Symbols

- a = amplitude of cylinder oscillation
- C_D = mean drag coefficient (mean drag force = $\frac{1}{2}\rho DV^2C_D$)
- D = cylinder diameter
- f_n = cylinder natural frequency ($\omega_n = 2\pi f_n$)
- f_s = vortex shedding or Strouhal frequency ($\omega_s = 2\pi f_s$)
- L = cylinder length
- M = cylinder mass (including added mass)
- R_e = Reynolds number, VD/v (v = fluid kinematic viscosity)
- S_t = Strouhal number, $f_s D/V$
- V = mean flow speed
- V_r = reduced velocity, $V/f_n D$
- ρ = fluid density

REFERENCES

- [1] Sainsbury, R.N., and King, D., "The Flow Induced Oscillation of Marine Structures," Proc. Instn. Civ. Engrs., Vol. 49, 1971, pp. 269-301.
- [2] Wootton, L.R., Warner, M.H., and Cooper, D.H., "Some Aspects of Oscillations of Full-Scale Piles," in Flow-Induced Structural Vibrations, E. Naudascher, ed.; Springer-Verlag, Berlin, Germany, 1974, pp. 587-601.
- [3] King, R., Prosser, M.J., and Johns, D.J., "On Vortex Excitation of Model Piles in Water," J. Sound and Vibration, Vol. 29, 1973, pp. 169-188.
- [4] Martin, W.W., Currie, I.G., and Naudascher, E., "Streamwise Oscillations of Cylinders," J. Eng. Mech. Div., ASCE, Vol. 107, No. EM3, 1981, pp. 589-607.
- [5] Schlichting, H., Boundary Layer Theory, (7th edition), McGraw-Hill Book Co., New York, N.Y., 1979.
- [6] Hartlen, R.T., and Currie, I.G., "Lift-Oscillator Model of Vortex-Induced Vibration", J. Eng. Mech. Div., ASCE, Vol. 96, No. EMS, 1970, pp. 577-591.
- [7] Skop, R.A., and Griffen, O.M., "A Model for the Vortex-Excited Resonant Response of Bluff Cylinders," J. Sound and Vibration, Vol. 47, 1973, pp. 225-233.
- [8] King, R., "A Review of Vortex Shedding Research and Its Application," Ocean Engineering, Vol. 4, 1977, pp. 141-171.
- [9] Cole, J.P., Perturbation Methods in Applied Mathematics, Blaisdell Pub. Co., Waltham, Mass., 1968.
- [10] Hall, S.A., "Vortex-Induced Vibrations of Structures", Ph.D. thesis, California Institute of Technology, 1981.
- [11] Blevins, R.D., Flow-Induced Vibration, Van Nostrand Reinhold Co., New York, N.Y., 1977.
- [12] Vierck, R.K., Vibration Analysis, (2nd edition), Harper and Row, New York, N.Y., 1979.

EXPERIMENTS ON FLOW-INDUCED VIBRATION OF A SQUARE-SECTION CYLINDER

P. W. Bearman

Department of Aeronautics
Imperial College
London, England

I. S. Gartshore

Department of Mechanical Engineering
University of British Columbia
Vancouver, Canada

D. J. Maull

Engineering Department
University of Cambridge
Cambridge, England

G. V. Parkinson

Department of Mechanical Engineering
University of British Columbia
Vancouver, Canada

ABSTRACT

A long elastic body of aerodynamically bluff cross section, capable of exhibiting either galloping or vortex-induced transverse vibrations in a flow normal to its length, can, if lightly damped, also exhibit large-amplitude vibrations related to the two above forms but not predictable from information available for either form considered separately. Before a rational explanation of this behaviour can be given it is necessary to have some detailed experimental evidence of the exciting forces on the body during these vibrations. To this end the authors have made wind tunnel measurements on a freely-oscillating cylinder of square section under closely two-dimensional conditions in both smooth and turbulent flow. The test cylinder was constrained to one degree of freedom by air bearings in an elastic system mounted on a rigid external frame independent of the wind tunnel structure. Linear springs and variable magnetic system damping were used. The aerodynamic excitation was measured using a pressure manifold connected to pressure taps along a streamwise line on one face of the test model at mid-span, and reporting to a transducer. Two key theoretical parameters are dimensionless wind speeds U_r , for system resonance with the wake vortex street, and U_o , for the initiation of galloping. With the highest damping U_o was well above U_r , and for all turbulence levels the measurements of both excitation and response supported the predictions of galloping theory. With the lowest system damping U_o was less than U_r for all turbulence levels, and in these cases oscillation always began at U_r , and cylinder amplitude increased monotonically with U , while the fluctuating pressure excitation was dominated by the component synchronized with the body motion, except near $U = 3U_r$, where a peak of the same order occurred in the component at three times body frequency, with corresponding kinks in the body amplitude curves. Generally the spectrum of the excitation was found to depend strongly on the ratio U_o/U_r . All of the parameters appearing in theoretical models of vortex-induced and galloping oscillations were measured in the experiments, and the observed phenomena are analyzed in the light of existing knowledge of the two basic forms of oscillation and of existing and possible theoretical models.

NOMENCLATURE

$C'_y N$	component at frequency Nf_c , $N=1,2,3,\dots$	$U_r = \frac{1}{2\pi S}$	reduced velocity for vortex resonance
f_c	body frequency	U_i	experimental critical velocity for oscillation
$f_n = \frac{\omega_n}{2\pi}$	system natural frequency	v	air velocity
f_v, f_{v_s}	wake vortex frequencies	v	streamwise turbulent fluctuation
h	size of square section	y	lateral displacement of body
L_x	streamwise turbulence scale	$\bar{Y} = \frac{Y}{h}$	reduced displacement
M	mass of oscillating system per unit span	\bar{Y}	reduced amplitude
$n = \frac{\rho h^2}{2M}$	mass parameter	α	angle of incidence
s	asymptotic slope of \bar{Y} - U curve	β	system critical damping ratio
$S = \frac{f_{v_s} h}{V}$	Strouhal number	β_e	effective system damping during oscillation
$U = \frac{V}{\omega_n h}$	reduced velocity	ρ	air density
$U_0 = \frac{2B}{nA_1}$	velocity for galloping	ϕ	phase angle between C'_y and \bar{Y}
		()'	r.m.s. value

1. INTRODUCTION

Flow-induced transverse vibrations of long elastic or elastically mounted cylinders of bluff section have been studied in many laboratories, and the phenomena of two forms, galloping and vortex-induced, have become widely known.

Galloping vibrations were originally studied in relation to their occurrence in ice-covered electric transmission lines, excited by winds normal to the span, where the low-frequency large-amplitude displacement waves along the lines gave rise to the name. Galloping represents a classical instability mechanism, in that a small transverse body motion creates an aerodynamic force that increases the motion. It has been most extensively studied for rigid cylinders of square section in wind tunnel experiments under two-dimensional conditions, and it has been shown by Parkinson and Smith [1] and others that a quasi-steady theory accurately predicts the phenomena of galloping if the reduced frequency is sufficiently low. In this theory the two important parameters are s , the slope of the asymptote from the origin in the \bar{Y} - U plane approached by the dimensionless cylinder amplitude \bar{Y} at high values of dimensionless wind speed U , and U_0 , the wind speed for the initiation of galloping. Slope s is a function of the cross-sectional shape of the cylinder, which determines the variation of static transverse force coefficient C_y with angle of attack α . The initial galloping speed is given by $U_0 = 2B/nA_1$, where B is the system damping constant expressed as a fraction of critical viscous-type damping, n is the mass parameter, proportional to the ratio of displaced fluid mass to body mass, and $A_1 = dC_y/d\alpha|_{\alpha=0}$, positive for the cross-section of a cylinder which will gallop from rest.

Vortex-induced vibrations can occur for any bluff cylinder whose cross-section has an appreciable afterbody, the part downstream of the flow separation points. However, it has been most widely studied for the circular cylinder, which of course cannot gallop. The phenomena have been documented by many, including Feng [2]. Vibrations occur only over a discrete range of U containing U_r , for which the wake vortex frequency f_{v_s} for the stationary cylinder is equal to the system natural frequency f_n . In the portion of this range for which amplitude \bar{Y} exceeds a threshold value, the wake vortex frequency f_v is synchronized with cylinder frequency f_c at values close to f_n , and exciting force coefficient C_y leads cylinder displacement \bar{Y} by a phase angle ϕ . The maximum

cylinder amplitude increases with decreasing system damping β , but is self-limiting to a value of the order of one diameter. No complete theory exists for vortex-induced oscillation, but the lift oscillator models, first proposed by Hartlen and Currie [3] and since studied in different versions by many others, can correctly duplicate most of the observed phenomena, and their development continues.

Any bluff cylinder that can gallop can also exhibit vortex-induced vibrations, since an appreciable afterbody is a requirement for both. Most such cylinders have Strouhal numbers S in the range $1 < S < 2$, and since $U_r = \frac{2\pi S}{U}$ this means that vortex-induced vibrations occur near $U=1$. On the other hand, pure galloping occurs for $U \gg 1$, since U is the reciprocal of reduced frequency. The two forms of wind-induced oscillation are then quite separate, and do not interact. However, in both forms the excitation is a pressure loading over the afterbody surface arising from the kinematics of the separated shear layers, and the response frequency is always close to f_p . Therefore, if the wind speed ranges for the two forms are brought relatively close together it is not surprising that interaction effects appear.

The current investigation of these interaction effects for cylinders of square section was prompted partly by scientific interest in a complex problem involving phenomena of separated flow and of nonlinear oscillations, and partly by an earlier study by Parkinson and Sullivan [4] which showed that there could be important engineering implications for the behaviour of towers. In this study models of tall towers of square section were tested in a large boundary layer wind tunnel in a wind closely simulating to model scale wind conditions in a suburban area. With high system damping the towers exhibited galloping behaviour in accordance with predictions of the quasi-steady theory. However, when the damping was low enough for the predicted wind speed ranges for vortex-induced and galloping vibrations to be relatively close, the vibration behaviour changed.

Vibrations began at a reference wind speed (measured at the top of the tower) corresponding closely to vortex resonance, and tower tip amplitude increased nearly linearly with wind speed, approaching the galloping asymptote at high values. Thus, large-amplitude vibrations were observed in a range of wind speeds over which no vibrations should have occurred according to the theories for galloping and vortex-induced vibrations, considered separately. Moreover, these same conditions could occur, using reasonable values of system parameters, for full-scale towers, thereby creating a vibration hazard not anticipated by design engineers.

In a subsequent investigation by Wawzonek [5] cylinders of square section were tested in smooth flow under two-dimensional conditions with elastic and damping parameters adjusted so that U_0 could be varied from below to well above U_r , and observations of Y vs U confirmed the existence of strong interaction effects, similar to those observed for the tower models, for sufficiently low values of the ratio U_0/U_r . There were, however, puzzling features of the $Y-U$ variations, and it became clear that a rational explanation of the phenomena required measurements of the excitation during vibration. This requirement led to the present experiments.

It has been less common to make measurements of pressure excitation of cylinders in flow-induced vibration than to infer details of such excitation from fluctuating fluid pressure or force measurements on cylinders in forced harmonic vibration in a uniform flow. This method has the advantage that all characteristics of the body motion, as well as the incident flow, are controlled, so that the only unknowns to be measured or observed are properties of the surface pressure fluctuations and of the wake. Equivalent phenomena for the flow-induced vibration of the cylinder can then be inferred from data for which all of the relevant parameters correspond in the two situations. Studies of this type have been carried out for the circular cylinder by Bishop and Hassan [6], Bearman and Currie [7], and Staubli [8], among others, and for the square-section cylinder by Otsuki et al [9], Nakamura and Mizota [10], and Bearman and Obasaju [11], with a recent extension by Obasaju [12].

However, the present wind tunnel experiments were performed on an elastically mounted square-section cylinder in wind-induced vibration, partly because of the experience with and the availability of equipment for this kind of test in the laboratory of the department of mechanical engineering of the University of

British Columbia (U.B.C.), and partly because of a belief in the usefulness of directly observing the phenomena of the wind-induced vibrations. The experimental arrangements are described in the next section.

2. EXPERIMENTAL ARRANGEMENTS

For the experiments, the instantaneous local cross stream force was to be measured from a two dimensional square section model free to oscillate in a pure plunging motion across the uniform air stream inside a wind tunnel. For this purpose a heavy rigid free-standing frame was constructed to fit around the outside of the U.B.C. aeronautical wind tunnel. This tunnel, which has a test section size 0.69 m high, 0.91 m wide and 2.44 m long, is of closed circuit type and has a relative turbulence level of less than 0.05%. Light aluminum guide tubes sliding through low friction air bearings on the frame, were rigidly connected to the vertical model by slender fingers which passed through slits in the tunnel walls as shown in Fig. 1. Four identical helical coil springs stretched from the frame to the guide tubes provided elastic support for the system so that the model and guide tubes could oscillate in the cross stream direction as required. This general arrangement is very similar to that used earlier at U.B.C. by Smith [1], Feng [2] and others. In fact preliminary experiments in these tests used the frame and air bearings designed by Smith, but all measurements reported here were made using a new frame which was considerably more rigid than the earlier version.

Displacement of the model was measured using a linear displacement transducer (Schaevits Model 3000 H.R.) with suitable circuitry added. The resulting output voltage was linear with displacement within $\pm 1.5\%$ over a range of ± 63 mm, and was independent of velocity for the frequency range used in the tests (less than 6 Hz), within the same accuracy of measurement.

Damping of the model could be increased using eddy current dissipation, provided by surrounding the moving aluminum guide tubes by steady magnetic fields. The minimum system damping, with no magnetic field applied, was $\beta = 0.0009$ (± 0.00015), and this could be increased to over 0.006 using the electromagnetic dampers. The level of damping was measured by observing, with wind off, the decay of free oscillations following an initial displacement. (The still-air aerodynamic damping was found to be negligibly small in a test in which a streamlined bar of the same mass replaced the test cylinder). A slight variation with amplitude was found but, over the range of calibration (r.m.s. dimensionless displacement $Y' < .5$), this was within the accuracy already quoted (see also Table 2).

The effective mass of the moving system was deduced by observing the natural frequency of the model with an additional mass m added to it. Plotting m against $1/\omega_n^2$, where ω_n is the corresponding circular natural frequency of vibration, the effective mass of the model above can be found by dividing the average slope of the curve, (which is equal to the stiffness of the system) by its intercept at $m = 0$ (which is equal to the inverse of the square of the natural frequency of the model alone). Using this method, the total effective mass of all the model mounting tubes, springs etc. together with the model itself, was found to be 1.21 ($\pm .01$) kgms.

The model, made of thin aluminum sheet fastened to light ribs, was square in cross section, 38.1 mm on each side and 686 mm in span. With the springs used, the natural frequency of the model and its connecting mounts was $f_n = 5.60$ ($\pm .025$) Hz. Seventeen pressure taps were located at the mid span of the model, eight equally spaced on each side to measure the instantaneous side force (as shown in Fig. 2) and one at the centre of the rear face to measure the base pressure. Each set of eight taps was connected through suitable light plastic tubing inside the model to a symmetrical pressure manifold fastened to one guide tube outside the tunnel. This manifold, which followed the design of Surry and Stathopoulos [13] provides a single output pressure whose magnitude is the average of the eight input pressures, under static conditions. For time-varying input pressures, the tubing lengths and manifold dimensions alter the output pressure so that it deviates from the required average in both magnitude and phase. Suitable calibrations of the manifold and its tubing, made with input pressures varying at a single adjustable frequency, resulted in the curves shown in Figs. 3(a) and (b) for amplitude and phase respectively. At the model

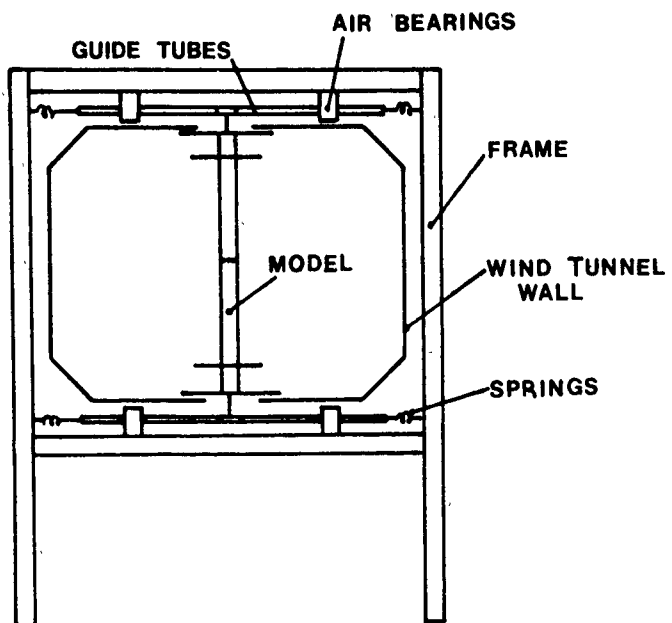


Fig.1 Experimental Arrangements

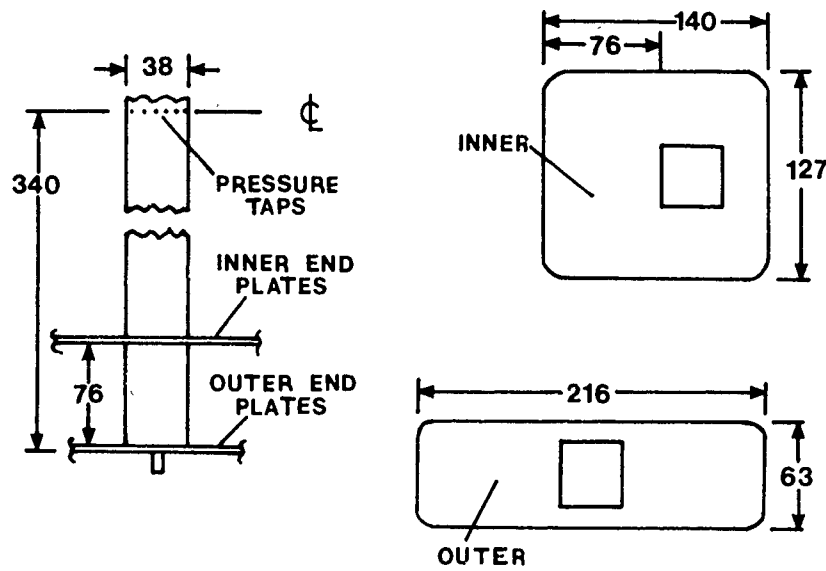


Fig.2 Details of model. Dimensions in millimetres

natural frequency of 5.6 Hz, the output pressure is expected to exceed the correct average by 2 to 3 percent, while its phase would lag the correct average by about 4° . With these corrections considered the RMS output of the manifold connected to one side of the model, when divided by the free stream dynamic pressure, would evidently measure one-half of the local r.m.s. lateral force coefficient C'_y imposed at the mid span of the model, assuming on grounds of symmetry that forces on either side of the model were equal and 180° out of phase. All pressures from the model were measured using a Setra ± 1 psi pressure transducer.

For direct measurements of the mean lateral force imposed by the wind on the stationary model at various angles of incidence α , needed in the quasi-steady theory of galloping, the model was detached from its frame and mounted vertically on a turntable. The integrated mean pressures occurring on either side of the model were then measured, using the pressure manifolds just described, and subtracted from each other to give the net side force. The side force coefficient C_y was found from these results and the slope $A_1 = (\frac{dC_y}{d\alpha})_{\alpha=0}$ was found from plots of C_y versus α . The coefficient A_1 could also be deduced from the rate of growth of oscillation amplitude of the model starting with a small initial amplitude. This indirect method, previously used by Nakamura [10], involved the measurement of total damping β_{TOT} from a series of transient amplitude observations. For growing amplitudes, which were recorded for the purpose on a suitable chart recorder, the value of β_{TOT} is negative, and can be used with the equation of motion, after taking account of the structural damping present with no wind effects imposed, to deduce A_1 .

A further correction to the measurements of fluctuating pressure from the manifold involved the oscillatory pressure in the tubing and manifold arising from the model motion only, that is with the input pressure taps blocked. This pressure fluctuation was observed to have a dominant component 80° out of phase with the body motion. At each displacement amplitude, this spurious pressure fluctuation was measured with pressure taps securely taped and was then subtracted from subsequent measurements wherever it was significant.

Average phase angles were measured between the body motion and the component of imposed aerodynamic force at the same frequency by correlating signals representing these two quantities, using a PAR time-delay correlation unit. This unit averages over about 2 minutes, or about 670 cycles at the frequency of 5.6 Hz. The peak of the correlation, occurring at a time delay τ_M (say) and expressed as a fraction of the time period for one cycle, is then the phase angle (as a fraction of 360°) between the two quantities concerned. Corrections for body motion, just described, and for phase lag in the manifold, were included in the data reduction, to provide measured phase angles accurate to $\pm 10^\circ$ at least.

Two pairs of end plates were fastened to the model, as shown in Fig.2. The outer pair, whose purpose was to cover the slits in the wind tunnel walls, were at the ends of the model and were identical in shape to those used by Wawzonek [5]. The second or inner pair of end plates were more conventional in size and shape and were attached to produce flow conditions as nearly two-dimensional as possible. Their dimensions are sketched in Fig.2. No explicit tests of the flow around the model were conducted but it was observed that, with the model fixed, a significant increase in C'_y occurred when the inner pair of end plates was attached. Their position, 76 mm from each end in all tests, was not critical, no effective difference in C'_y occurring with the plates fixed at 25 mm from the model ends.

Instrumentation used in the tests included a true RMS voltmeter with variable integration time and a Spectral Dynamics SD335 spectroscope unit. The latter was capable of displaying (and holding in memory) the spectrum of an incoming signal so that, through the use of moveable cursors and digital readouts, the frequency and height of spectral peaks could be quickly measured.

Two biplanar grids were used in the tests to produce free stream turbulence; both had square mesh arrangements of square bars with mesh to bar size ratios of 4:1. The mesh sizes were 229 mm (grid 1) and 114 mm (grid 2). Placed at distances of 1.86 m and 1.80 m (respectively) from the model front face, these produced longitudinal turbulence integral scales and intensities as shown in Table 1. The experimental accuracy of other reduced results is estimated in Table 2.

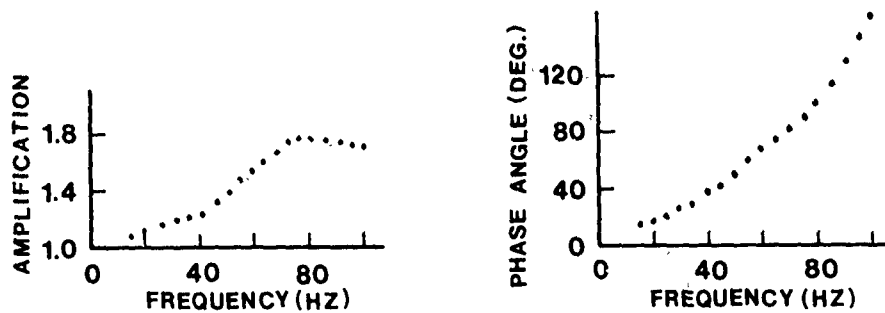


Fig. 3 Calibration of manifold
(a) Amplitude (b) Phase angle

3. RESULTS

3.1 Preliminary Results Measured with Model Fixed

Three results obtained in the low-turbulence flow with the model at rest were the mean base pressure coefficient C_{pb} , the root mean square amplitude of the lift force C'_y , and the Strouhal number S , all measured over a range of wind speeds ($10^4 < Re < 3 \times 10^4$ equivalent to $3 < U < 9$).

The mean base pressure coefficient was found to be effectively constant at a value of $-1.5 (\pm .1)$. Similarly, the Strouhal number, found by observing the frequency of the largest peak in the spectrum of the oscillating pressure measured through the pressure manifold from one side of the fixed model, was found to remain close to $0.133 (\pm .005)$. The fluctuating side force, corrected for the frequency response of the manifold, was found to be most sensitive to the addition of end plates, but, with the final configuration used for all the tests, was also effectively constant at $C'_y = 1.40 (\pm .07)$.

3.2 Displacement Versus Wind Speed

The experiments whose results are reported here were all carried out with the model described in Section 2 mounted in a spring-mass system with $f_n = 5.6 \text{ hz}$. Nine combinations of system damping β and turbulence intensity in the incident flow were tested. Through the test series, there were minor variations from nominal values of β , due to the sensitivity of the configuration to the alignment of the air bearings, and of the turbulence intensity, due to Reynolds number effects, but essentially the 9 tests were for low, medium, and high values of β and of turbulence intensity. In each test the wind speed was increased in small steps from a value below the range for wind-induced oscillations. At each wind speed the model was released by supplying air to the bearings and any wind-induced oscillation was allowed to reach steady state conditions, when all data were recorded.

Fig. 4 shows the variation of dimensionless r.m.s. model displacement Y' vs dimensionless wind speed U for the 9 tests. The general form a particular curve was likely to take was of course already known from the previous work described in Section 1, but the new mounting frame permitted extension of the tests to higher values of U and β , and gave more confidence in the observation and interpretation of detailed behaviour. It can be seen from Fig. 4 that the three curves for low β all show oscillation commencing at initial wind speeds U_i equal or very close to U_r , which varied from 1.22 in low turbulence to 1.27 in high turbulence due to small changes in the stationary-cylinder Strouhal number. The interesting features of the curves of Fig. 4, in addition to the values of U_i , are the slopes $\frac{dY'}{dU} = \frac{S}{\sqrt{2}}$ approached asymptotically at high U , and the details of the shape where it departs from the usual almost linear trend. For the three

Reduced Velocity	GRID 1		GRID 2	
	$v'/V(\%)$	Lx/h	$v'/V(\%)$	Lx/h
$U = 2$	11.5($\pm .3$)	1.3($\pm .2$)	7.0($\pm .2$)	1.2($\pm .2$)
$U = 4$	10.5($\pm .3$)	1.4($\pm .2$)	6.5($\pm .2$)	1.2($\pm .2$)

Table 1. Turbulence Characteristics

Reduced Quantity	Typical Range	Estimated Accuracy
U	1 to 5	$\pm .10$
Y'	0 to 1	$\pm 5\% \text{ of reading} \quad \text{whichever or } \pm 0.003 \quad \text{is greater}$
C_y^t	1 to 1.5	$\pm 5\%$
β	9×10^{-4} to 6×10^{-3}	$\pm 1.5 \times 10^{-4}$

Table 2. Experimental Accuracy of Basic Results

low-damping curves the slope s is seen to decrease with increasing turbulence intensity. This would be predicted by the galloping theory from the $C_y - \alpha$ curves of Fig. 5 for the stationary model in the same incident flows as suggested by Laneville and Parkinson [14]. The interesting shape feature for the low-damping curves is the consistent kink in each of the three curves near $U = 3$. Like the coincidence of U_i with U_r , this is not accounted for by the quasi-steady theory of galloping.

The three high-damping curves, for which all data points have relatively high values of U , considerably greater than U_r , appear to be in agreement with predictions of galloping theory, at least qualitatively. (Aspects of the quantitative agreement are examined in Section 3.3). The initial wind speeds U_i for strong vibrations (disregarding some low-amplitude buffetting, with $Y' < .03$, from the incident turbulence) increased with increasing turbulence intensity, in agreement with the behaviour of the theoretical initial speed U_o as it varies with coefficient A_1 for the three levels of turbulence. The asymptotic slopes s for the medium-and high-turbulence curves are close to those for the corresponding low-damping curves, as they should be, and the lower slope and different shape of the low-turbulence curve is a direct consequence of the different shape of the $C_y - \alpha$ curve for the low-turbulence case in Fig. 5, which leads to the prediction of 2 stable galloping amplitudes of oscillation over a range of wind speeds. The curve of Fig. 4 represents the variation with U of the lower of these two amplitudes. The upper amplitudes are outside the range of the test apparatus.

The three medium-damping curves of Fig. 4 also appear to be in general qualitative agreement with predictions of galloping theory, and the remarks above about the high-damping curves apply again, except that the sequence of initial velocities U_i is different. This is examined in Section 3.3.

3.3 Parameters for Galloping Theory

The measurement of lateral force as a function of angle of attack on the stationary cylinder in the same flow for which galloping behavior is desired is a required input to the quasi-steady theory. Fig. 5 shows C_y vs α from such measurements on cylinders of square section. Values inferred from the present measurements of manifold pressure on a side are shown in comparison with three different sets of force measurements, using different models and techniques. The

data for a given turbulence level are seen to be in quite good agreement, particularly for $0 < \alpha < 8^\circ$, and the markedly different shape of the low-turbulence curve from the others is significant in producing a different galloping response, as mentioned in Section 3.1. Also, the decrease in the asymptotic slope s of the displacement-wind speed curves with increasing turbulence is a direct consequence of the corresponding decrease in the range of α for positive C_y in Fig. 5.

It can also be seen from Fig. 5 that the slope A_1 of the curves at $\alpha = 0$ lies in a fairly small range, $2.5 < A_1 < 5.5$, but that it would be difficult to make a precise determination for a particular combination of Reynolds number and turbulence intensity because of the scarcity and limits on the accuracy of the data points. However, with the realization that the error in a given value is likely to be at least $\pm 10\%$, values of A_1 determined by a polynomial fit to the present data points for values of $\alpha < 4^\circ$ are given in the first column of Table 3.

The alternative dynamic method of determining A_1 mentioned in Section 2 provides a useful comparison. In the galloping theory, the transient build-up of oscillation from rest can be approximated as a linear process for small amplitudes, so that the transient amplitudes are proportional to $e^{-\beta_{TOT} \omega_n t}$, where

$$\beta_{TOT} = \beta - \left(\frac{A_1 n}{2} \right) U .$$

If $U > U_o$, β_{TOT} is negative and can be measured from a chart record of cylinder displacement vs time. If this is done for several values of U in the same conditions of turbulence, values of $(\beta - \beta_{TOT})$ vs U should plot on a straight line, assuming Reynolds number effects are negligible, and the slope $\frac{A_1 n}{2}$ can then be used to determine A_1 . Fig. 6 shows such a plot for each of the three turbulence conditions, with data points for 2 or 3 values of β used to determine each line. The scatter is seen to be reasonably small, and the only organized departure from the linear variation is with the data points for $U < 2.5$, where the proximity to U_r apparently leads to increased excitation from the synchronized wake vortex system, and thus to higher values of the coefficient corresponding to A_1 . Values of A_1 from the straight lines of Fig. 6 are given in the second column of Table 3.

The two values of A_1 for each turbulence condition in Table 3 are in reasonably good agreement, with $\pm 11\%$ deviation from the mean for low turbulence, $\pm 1\%$ for medium, and $\pm 8\%$ for high turbulence. Therefore, the mean values have been used to calculate the theoretical initial velocity $U_o = \frac{2\beta}{nA_1}$ for each of the 9 test combinations of β and turbulence. These are compared in Table 3 with the observed initial values U_i . The agreement is good for the 3 high- β cases, the ones to which the quasi-steady theory is most applicable, with U_o ranging from 4% high for the low-turbulence case to 13% low for the medium-turbulence case, and an overall average of 4.4% low. For the 3 low-damping curves any agreement is fortuitous, since $U_i = U_r$ in all cases. Finally, for the 3 medium-damping cases, the agreement is good for the low-turbulence case, but there is poor agreement for the other 2 cases, and it appears that U_r is close enough to U_r for significant effects of the vortex excitation on the galloping behaviour.

3.4 Fluctuating Pressure Characteristics

Using the calibrated manifold, described in Section 2, it is possible to observe the instantaneous side force on the moving model. The contribution from various frequencies, and in particular from frequencies close to the body motion (or its higher harmonics) can be estimated by noting the height of appropriate spectral peaks and the total signal strength from all frequencies. In each test, these quantities were available from the spectrograph, each measured as an RMS quantity. The band width for the spectral measurements was .06 Hz (3 db down) on the 0-20 Hz range, and the measurement sensitivity for frequencies was .04 Hz because of the discrete steps used in the instrument. Only the maximum value of each spectral peak was measured, and not the integration under the peak as would be strictly necessary to obtain precise values. The results are therefore estimates of the relative importance of each harmonic, and their approximate

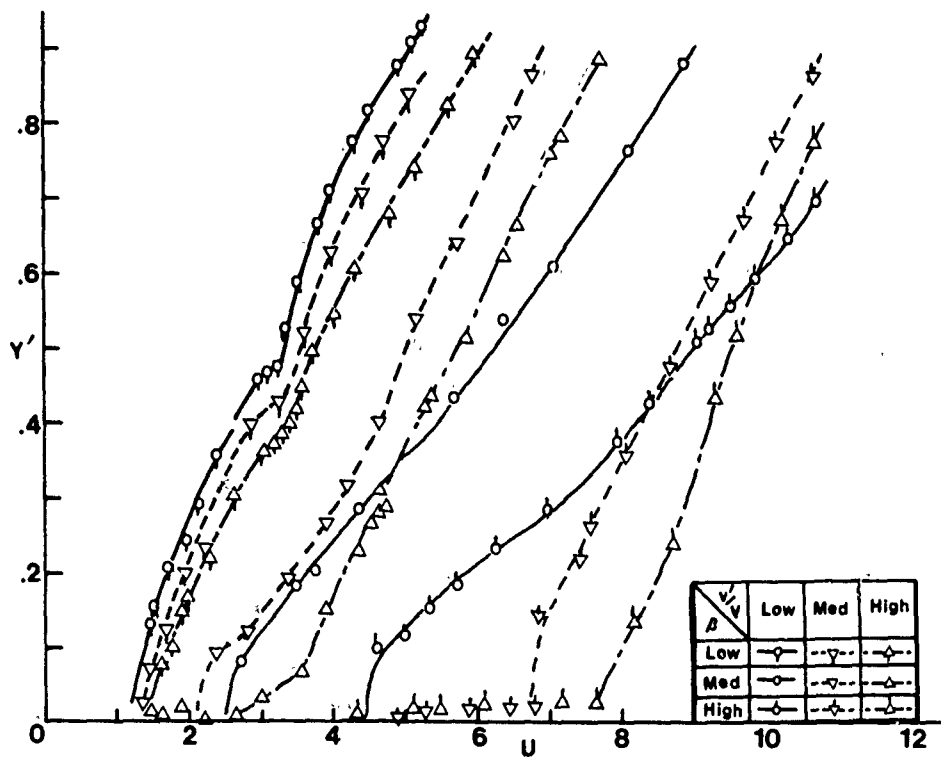


Fig.4 Displacement vs wind speed.

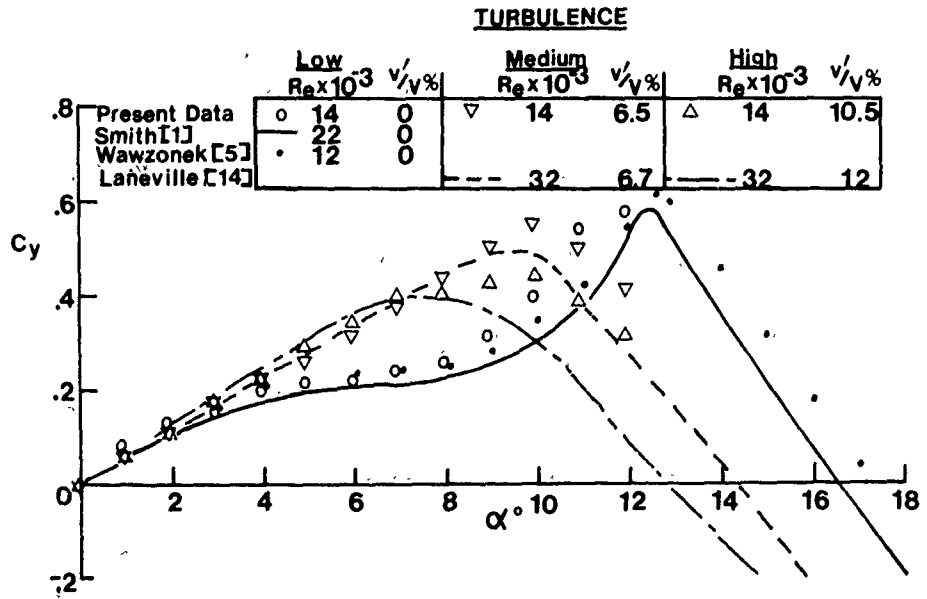


Fig.5 Latéral force coefficients for square section.

relationship to the spectrally complete value of C'_y . Where broad peaks in the spectrum occurred, no measurements of the harmonics were made.

In cases in which body motion was significant, the fluctuating side force had observable components near the body frequency. The exact frequency at which the spectral peak occurred was not usually the wind-off body frequency f_n (which was measured before each test and was effectively constant) but was found to vary from f_n to as much as 4% lower. Phase angles could still be estimated under these circumstances using the correlation method described in Section 2. The component of the force coefficient associated with frequencies near that of the body motion is designated as C'_{y1} , with subsequent harmonics as C'_{y2} , etc.

Turbulence Intensity	A ₁			B		
	C_y vs α	$(\beta - \beta_{TOT})$ vs U		Low	Medium	High
Low	5.4	4.3	U_o/U_i	.75/1.22	2.57/2.51	4.72/4.5
			β_e/β	2.31	1.13	1.24
			S		.128	.128
Medium	3.9	4.0	U_o/U_i	1.11/1.27	3.16/2.09	5.79/6.7
			β_e/β	1.76	1.20	1.22
			S	.140	.132	.128
High	3.4	2.9	U_o/U_i	1.16/1.27	3.96/2.5	7.26/7.6
			β_e/β	1.53	1.32	1.22
			S	.139	.131	.127

Table 3 Derived Results

Measured values of C'_{y1} , C'_{y2} , etc. are plotted in Fig. 7 for the low damping, low turbulence case. This figure shows that much of the side force exerted on the body occurs at (or very close to) the body frequency for $2 < U < 5$, a range of wind speeds for which significant motion of the body was observed. Near $U = 3$, where the kink occurs in the amplitude vs wind speed plots of Fig. 4 for this case, C'_{y3} rises sharply, indicating the presence of strong force components at about three times the body frequency. At the upper limits of the amplitude range for the apparatus ($Y' = 1$), occurring for low damping and low turbulence at $U = 5$, C'_{y5} rises sharply showing now the presence of the fifth harmonic of body motion in the force. The even harmonics, C'_{y2} and C'_{y4} remain low throughout.

It appears from this figure that progressive "lock in" at odd harmonics of the body motion occurs sequentially as the velocity increases, the force of the fundamental remaining significant but decreasing slightly.

The phase angle between the body motion and the force at the fundamental frequency is plotted for the three low turbulence cases in Fig. 8. The measured phase angle increases progressively as U increases, although considerable scatter is evident. This angle is taken as 90° in the quasi-steady theory in which $C_y(t)$ is assumed to be in phase with dy/dt at every velocity, so that the present measurements show a progressive approach to the quasi-steady conditions. For the low damping, low turbulence case, phase angles are still far from the quasi-steady value even at the highest velocity ($U \approx 5$) however.

Similar decompositions of the force, and measurements of phase angle were made for all other test conditions. Phase angles for the highest damping, low turbulence case were closer to 90° , as shown in Fig. 8, but still not equal to 90° as expected from previously described agreement with the quasi-steady galloping theory for this case (Section 3.3, and appropriate entry in Table 3). The accuracy of measurement of phase angle is not very good, however, ($\pm 10^\circ$), which makes close comparisons impossible. The values of C'_{y1} for the highest damping cases were much lower than the total C'_y (about in the ratio 1:9) and no evidence of significant higher harmonics was observed. This is in agreement with quasi-steady theory.

When the two levels of turbulence were added to the low damping case, patterns similar to the cases without turbulence of Figs. 7 and 8 were again formed, although not as clearly. In these cases, a rise of the third harmonic was again observed around $U = 3$ where the amplitude curve of Fig. 4 shows a kink, and relative phase angles between 13° and 50° were measured. For the three cases with medium damping the values of C'_{y1} were again small in comparison with overall C'_y and phase angles were intermediate between the values for low and high damping cases. Low-amplitude harmonics were observed for all but the high-turbulence case, where none could be detected.

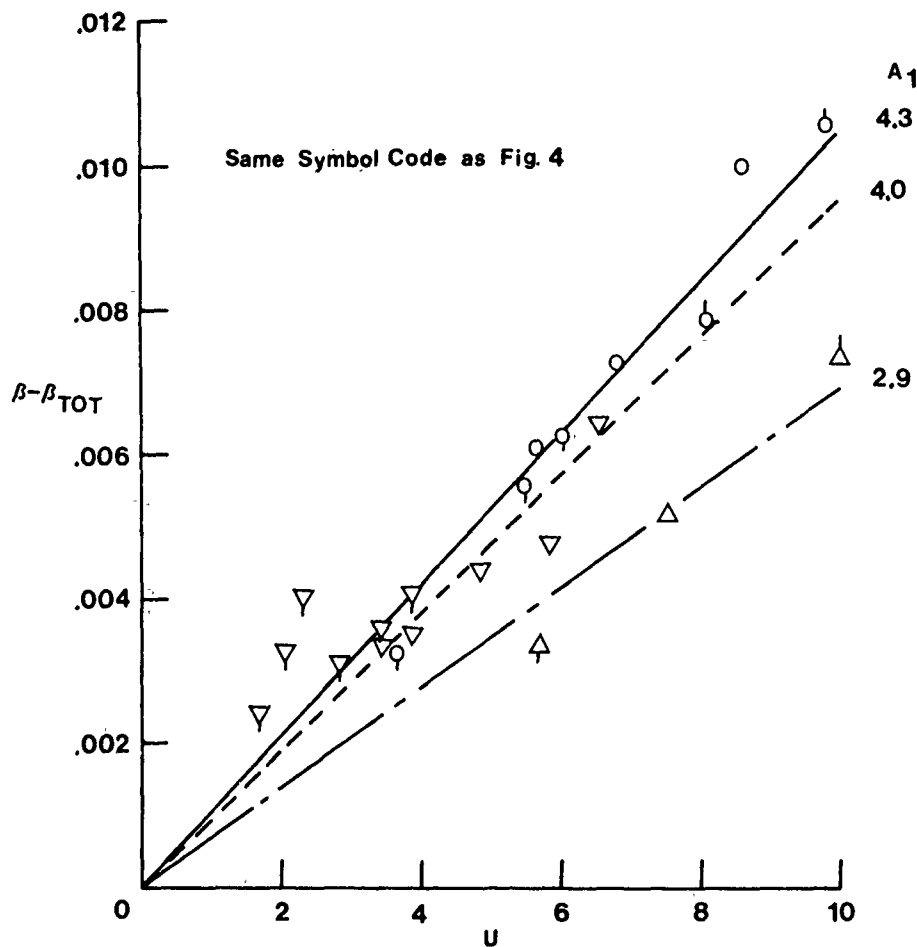


Fig.6 Dynamic method of determining A_1 .

3.5 Effective Damping and Strouhal Number

If the reasonable assumption is made that the displacement of the oscillating cylinder is caused by that part of the fluctuating pressure force synchronized with the body motion, and leading the displacement by phase angle ϕ , then in steady-state oscillation the dissipative force of the system damping is balanced by the $\sin\phi$ component of the exciting force. All quantities entering into this force balance were measured in the experiments, including the system damping parameter β , and it is useful to solve the balance equation for an effective damping parameter β_e and compare it with the nominal measured value. This was done for all data points for which $Y' > .1$ and C'_{y1} and ϕ could be measured, and Table 3 shows mean values of β_e/β for each of the 9 tests. Scatter of individual data points in a given test averaged $\pm 19\%$, but the mean results show an interesting trend. For all tests $\beta_e/\beta > 1$, and for the high and medium damping cases the value is nearly constant, averaging $1.22 \pm .09$. For the low damping cases the values were much higher and increased with decreasing turbulence intensity. These results are discussed in the next section.

Finally, in all but the first test run (low damping, low turbulence) a search was made for spectral peaks other than at the body frequency and its harmonics, and in all cases such a peak was found corresponding to the Strouhal frequency for the stationary cylinder. The corresponding Strouhal number was remarkably constant, considering that it was measured during oscillations with amplitudes as large as $Y' = 0.9$. Mean values for each test are given in Table 3. For high damping cases the excitation at the Strouhal frequency was much stronger than at the body frequency, and S from individual data points was constant within 3%. For medium damping cases the Strouhal and body-frequency excitations were of the same order, and S was constant within 4%. For low damping cases the Strouhal excitation was weaker than that at the body frequency, and S was constant within 7%. The overall mean value was $S = .132$, very close to the value of $.133$ measured for the same cylinder at rest in the same Reynolds number range in low-turbulence flow.

4. DISCUSSION

4.1 Results that Can Be Explained by Existing Theory

The observed and calculated results for the 3 cases of high system damping are all in good agreement with predictions of the quasi-steady theory of galloping. These include the values of U_1 , all close to U_r , and the variation of Y' with U in Figure 4, the fact that C'_{y1} values were small and ϕ close to 90° , and the fact that values of A_1 measured dynamically were in good agreement with the corresponding static values. Therefore, since $U_1 > 3.7 U_r$ in these tests, it seems safe to conclude that phenomena of wind-induced oscillation of cylinders of square section can be predicted by the quasi-steady theory of galloping for $U > U_r > 4U_r = 5$.

Some of the results for the 3 medium-damping cases are also in at least qualitative agreement with predictions of the theory. The shape of the $Y' - U$ curves shows the predicted dependence on the $C_y - \alpha$ curves of Figure 5, and the values of U_1 lie between U_r and the high-damping values, $1.6 U_r < U_1 < 2.1 U_r$, as they should. C'_{y1} values remain small and for higher values of U phase angles ϕ again approach 90° and dynamic values of A_1 are in good agreement with static values. However, the general quantitative agreement is poor.

For the 3 low-damping cases it is understandable that if no oscillation has occurred for $U < U_r$ (forced oscillation tests [9, 10, 11, 12] indicate the reason to be that ϕ is negative), oscillation would commence at or near U_r because of resonance with the wake vortex system. It is also to be expected that the $Y' - U$ curves at high values of U would approach the asymptotic slopes predicted by the quasi-steady theory. Otherwise the results do not conform to predictions of either galloping or vortex-induced flow models.

4.2 Results that Require Additional Explanation

Transverse flow-induced oscillations of long bodies of bluff section are a consequence of the behaviour of the shear layers that separate from the body, including the formation of wake vortices and interaction with the section after-body. The vortex formation process is of particular interest. The stationary

square-section cylinder at $\alpha = 0$ creates a Kármán wake vortex street with $S = 1.13$. Remarkably, when the same cylinder is in large-amplitude flow-induced oscillation with instantaneous relative values of α reaching $\pm 15^\circ$ (greater than α for reattachment of a shear layer on the stationary cylinder), the same Strouhal number is detected from the surface pressure signal, as shown in Section 3.5. On the other hand, any transversely oscillating body in a flow will shed vortices at the oscillation frequency, thus creating a second organized wake vortex system, whose flow field will exert a pressure loading on the body synchronized but out of phase with the body motion. These two wake vortex systems apparently coexist in the present experiments through the entire range of conditions tested, but with a progressive change in their relative strengths. When $U \gg U_r$, the Strouhal signal is much stronger than the body-frequency signal, for which ϕ is near 90° , while when U is close to U_r , the reverse is true for the signal

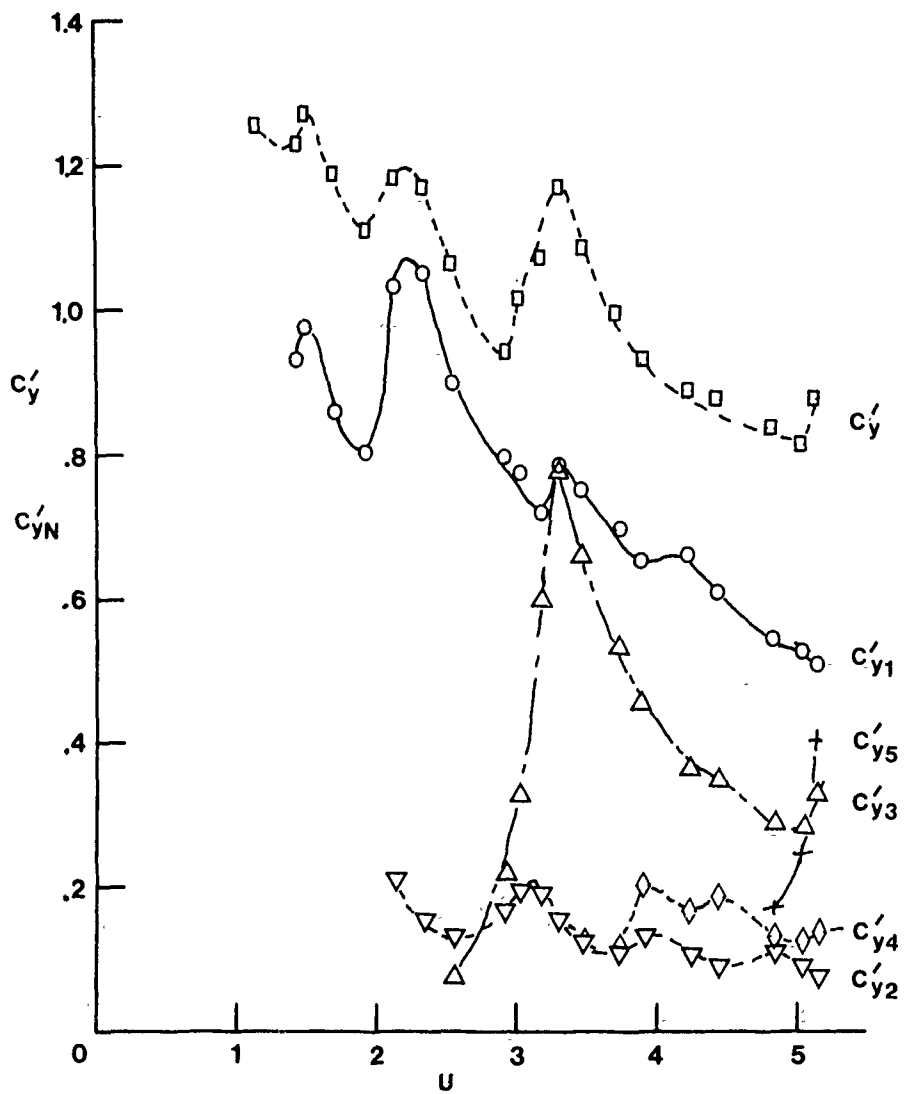


Fig.7 Force coefficients and harmonic components.

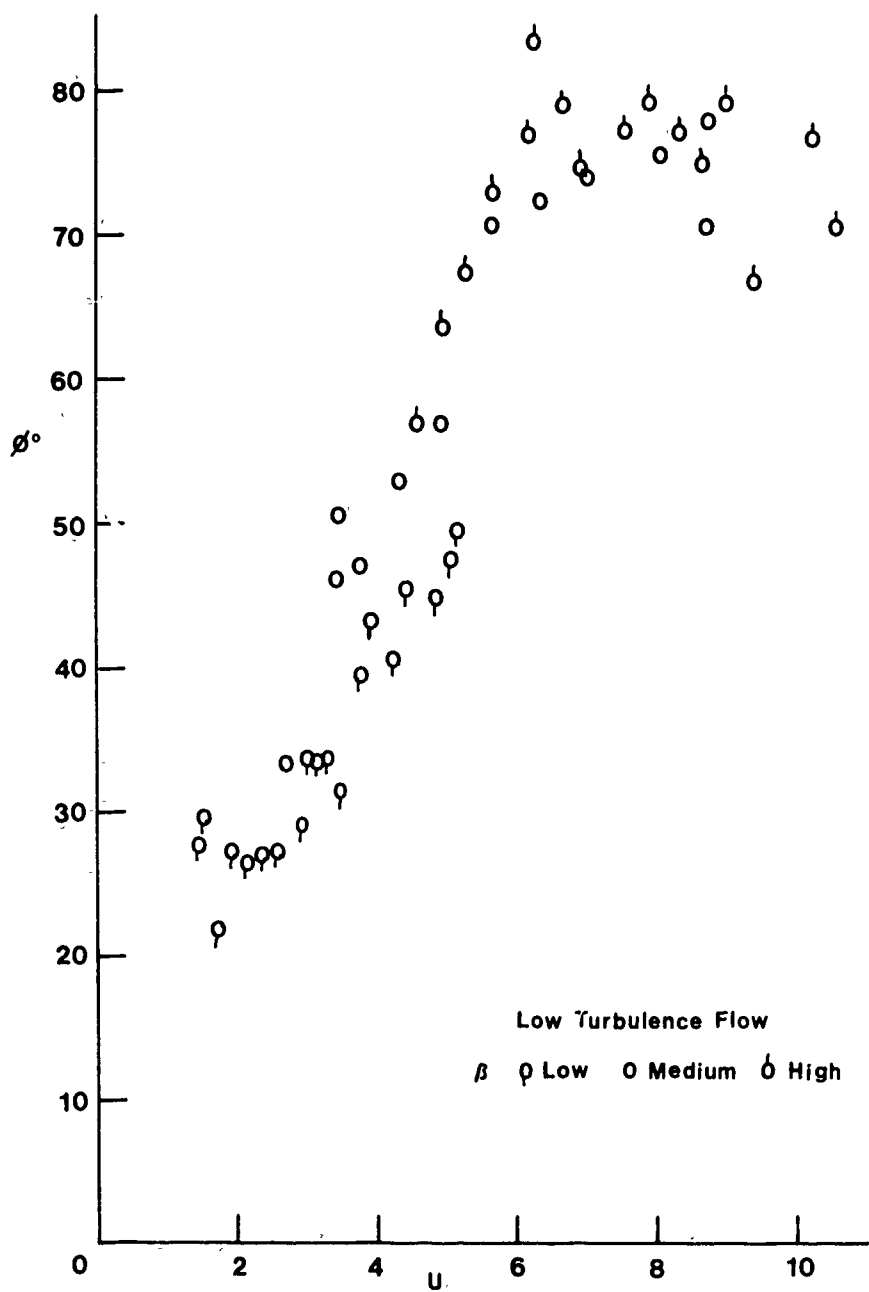


Fig.8 Phase angle between C'_{y1} and Y' .

strengths, and ϕ is small. Thus the term 'lock-in' usually applied to vortex frequency when U is near U_r here corresponds merely to a strong magnification of the body-frequency signal at the expense of the Strouhal signal.

The most interesting phenomenon of the experiments was the occurrence in the three low damping tests of a strong signal C'_p_3 at three times the body frequency, and the corresponding kink in each of the three $Y'-U$ curves. Over the range $2 < U < 4$ in which the kink occurred C'_p_1 was strong, decreasing slightly with increasing U , C'_p_3 reached a sharp peak near $3U_r$ and of the same order as C'_p_1 , and the Strouhal signal was also present, although relatively weaker. Thus again the phenomenon does not appear to involve lock-in in the sense of a single vortex shedding frequency synchronized at three times the body frequency. Rather, the evidence indicates that C'_p_1 and C'_p_3 are the fundamental and third harmonic of a periodic but non-sinusoidal signal which co-exists with the regular Strouhal signal. This is probably the result of a complex vortex formation process, perhaps influenced by the periodic proximity of the separated shear layers to the corners of the square section afterbody during the oscillation cycle. Work is in progress in an attempt to employ the above form of excitation in a mathematical oscillator model to explain the kink in the $Y'-U$ curves.

The first author and his students, in References 11 and 12 and in recent unpublished work, have discussed forced-oscillation experiments on square-section cylinders which have produced results generally consistent with those of the present paper. These forced-oscillation results done only in low-turbulence flow suggest the existence of three zones in the $Y'-U$ plane, a quasi-steady zone which would contain the present high-damping results, a multiple harmonic zone, in which strong progressively higher odd harmonics would appear in the C' signal as Y' and U increase, and which would contain the present low-damping results, and an intermediate transition zone which would contain the present medium-damping results, except at low amplitude, since the two zone boundaries converge on U_r at $Y' = 0$. According to this suggested zone model the present medium-damping results for small Y' should be predictable from quasi-steady theory, and it is interesting to note from Table 3 that the theory did give a good prediction of U_o in low-turbulence flow (on which the zone model is based).

Finally, the results in Table 3 demonstrate that β_e during wind-induced oscillation is consistently higher than the nominal β measured in wind-off amplitude decay tests, despite the effort expended in providing a rigid external mounting frame for the cylinder and its elastic and damping system, isolated from the wind tunnel structure. Work is in progress to attempt to identify the sources of the increase in system damping so that a more correct damping term can be incorporated in the quasi-steady theory.

ACKNOWLEDGEMENTS

The participation of two of the authors in the experiments was made possible by a NATO research grant. The mounting frame was designed by Mr. William Bell, on leave from the Institute of Ocean Sciences, and calibrations and wind tunnel tests were performed by Mr. Allen Lee, a 1983 graduate in Mechanical Engineering at UBC.

REFERENCES

1. Parkinson, G.V. and Smith, J.D., "The Square Prism as an Aerelastic Non-linear Oscillator," Quart. Jour. Mech. App. Math. 17, 2, 1964, pp. 225-239.
2. Feng, C.C., "The Measurement of Vortex-Induced Effects in Flow Past Stationary and Oscillating Circular and D-Section Cylinders," M.A.Sc.Thesis, UBC, 1968.
3. Hartlen, R.T., and Currie, I.G., "Lift-Oscillator Model of Vortex-Induced Vibration," Proc. ASCE, Jour. Eng. Mech., EM5, 1970, pp. 577-591.
4. Parkinson, G.V., and Sullivan, P.P., "Galloping Response of Towers," Jour. Ind. Aero. 4, 1979, pp. 253-260.
5. Wawzonek, M.A., "Aerelastic Behavior of Square Section Prisms in Uniform Flow," M.A.Sc. Thesis, UBC, 1979.
6. Bishop, R.E.D. and Hassan, A.Y., "The Lift and Drag Forces on a Circular Cylinder Oscillating in a Flowing Fluid," Proc. Roy. Soc. Lond. A, 277, 1964, pp. 51-75.

7. Bearman, P.W., and Currie, I.G., "Pressure-Fluctuation Measurements on an Oscillating Circular Cylinder," *Jour. Fluid Mech.* 91, 1979, pp.661-677.
8. Staubli, T., "Calculation of the Vibration of an Elastically Mounted Cylinder Using Experimental Data from Forced Oscillation," *Jour. Fluids Eng.*, 105, 1983, pp. 225-229.
9. Otsuki, Y., Washizu, K., Tomizawa, H. and Ohya, A., "A Note on the Aero-elastic Instability of a Prismatic Bar with Square Sections," *Jour. Sound Vib.* 34, 1974, pp. 233-248.
10. Nakamura, Y. and Mizota, T., "Unsteady Lifts and Wakes of Oscillating Rectangular Prisms," *Proc. ASCE, Jour. Eng. Mech.*, EM6, 1975, pp. 855-871.
11. Bearman, P.W. and Obasaju, E.D., "An Experimental Study of Pressure Fluctuations on Fixed and Oscillating Square-Section Cylinders," *Jour. Fluid Mech.* 119, 1982, pp. 297-321.
12. Obasaju, E.D., "Forced-Vibration Study of the Aeroelastic Instability of a Square-Section Cylinder Near Vortex Resonance," *Jour. Wind Eng. and Ind. Aero.*, 12, 1983, pp. 313-327.
13. Surry, D. and Stathopoulos, T., "An Experimental Approach to the Economical Measurement of Spatially-Averaged Wind Loads," *Jour. Ind. Aero.* 2, 1977, pp.385-397.
14. Laneville, A. and Parkinson, G.V., "Effects of Turbulence on Galloping of Bluff Cylinders," *Proc. 3rd Int. Conf. Wind Effects*, Tokyo, 1971, pp.787-798.

AIR-BUBBLE EFFECTS ON VORTEX-INDUCED VIBRATIONS OF A CIRCULAR CYLINDER

F. Hara
Department of Mechanical Engineering
Science University of Tokyo
Tokyo, Japan

ABSTRACT

This paper indicates, experimentally, the influence that air bubbles have in drastically reducing vortex-induced vibration and in exciting vibration of a single circular cylinder, and discusses the mechanisms involved. This air-bubble effect occurs in both in-line and cross-flow vibrations. Vibration reduction, which occurs at low void fractions, is especially marked under conditions of resonance between cylinder oscillation and vortex shedding. The cylinder is, however, strongly excited at higher void fractions in a two-phase flow.

Experimental results concerning Karman vortex shedding, unsteady lift and drag forces acting on a stationary circular cylinder, and two-phase flow characteristics around the cylinder, all indicate an idea that the mechanism reducing vibrations is air bubbles detuning the synchronization of vortex shedding with cylinder oscillation, because fluid forces due to the two-phase flow are rather random. The excitation mechanism is considered to be due to buffeting produced by air-bubble motion in the flow, which is very strong and random for high void fractions.

1. INTRODUCTION

Vortex shedding is one of well-known causes of violent oscillation in a cylinder immersed in a single-phase cross flow, and many papers have already been published on this problem. Sarikaya[1] selectively reviewed vortex-induced oscillations, and Durgin[2] reported low-mode response of circular cylinders in cross flow, which occurred when the natural frequency was approximately one-third the normal vortex shedding frequency. Botelho[3] and Staubli[4] individually studied calculation models for vortex-induced vibrations of an elastically mounted cylinder. The foregoing studies were confined to single-phase gas or liquid flows.

Many situations exist in our technological field, however, where two-phase gas-liquid flow plays an inevitable but often troublesome role in the operation of facilities such as steam generators, condensers, and civil engineering structures, such as pilings, submerged in a wave flow containing bubbles. Vibrations induced by a two-phase flow aggravate troubles in such facilities.

Among the very few researches done in this area are the works by

Pettigrew and Gorman[5], Heilker and Vincent[6], and Every et al.[7]. Two-phase air-water or steam-water flow-induced vibrations present a new side of on-site flow-induced vibration problems, and increasing attention is being paid to safety in operating affected facilities. Most experiments were done with the aim of obtaining information of immediate usefulness in preventing the problem in specific designs, and little understanding was reached about two-phase flow-induced vibrations in highly complicated vibration systems such as tube banks for steam generators or heat exchangers.

In the most simple, therefore fundamental, vibration study on two-phase cross flow-induced vibrations, Hara and his colleagues did a series of experiments involving two-phase flow: (1) pressure fluctuations on a stationary circular cylinder immersed perpendicular to the flow, (2) unsteady lift and drag force characteristics of a two-phase flow, (3) in-line vibration of a circular cylinder, and (4) cross-flow vibration of a circular cylinder.

Hara and Ohtani[8] investigated experimentally two-phase flow vortex shedding and pressure fluctuations using a 60 mm circular cylinder, 30 mm in diameter, installed rigidly and perpendicular to the flow at the center of a 200 mm x 60 mm rectangular test channel in which the flow was vertically upward. The maximum flow velocity was 0.6 m/s, corresponding to a Reynolds number of 1.8×10^4 , based on the cylinder diameter. Black ink was injected from two small holes, 90 degrees from the stagnation point in the cylinder's midsection, into the two-phase bubble flow. Air bubbles in the flow had an average diameter of 6.6 mm. The oscillatory motion of black ink trails following the cylinder was detected by a CdS photodiode, enabling the measurement of vortex shedding frequency.

The dominant wave-motion frequency of the wake--defined as the peak frequency in the PSD of signals from the CdS photodiode--was slightly larger than that estimated from the Strouhal number, 0.2, but seemed to be associated with Karman vortex shedding just the same. Wake oscillation demonstrated a clear-cut dominant frequency when the void fraction was less than 7%. The peak PSD frequency of differential pressure fluctuation between two points across the cylinder's horizontal center line indicated a good agreement between the dominant frequencies of wake motion and pressure fluctuation for single-phase water flow and two-phase flow with a low void fraction under almost 10%. The pressure fluctuation, however, was very random and large when the void fraction was high.

The RMS values for differential pressure fluctuation, referred to above, indicated two trends: one being a rather weak pressure-fluctuation dependence on void fraction, and the other being a stronger dependence on void fraction at higher void fractions. The intersection of the two trends was a critical void fraction, about 10%, for transition from vortex shedding to nonvortex shedding in a two-phase bubble flow.

Hara[9, 10] examined the characteristics of unsteady lift and drag forces acting on a circular cylinder in a two-phase cross flow, employing the same size cylinder as above, but one flexibly mounted with cross-configured flat springs, each of which detected a lift or drag force component. The natural frequency of the cylinder-spring system was about 100 Hz in each direction--sufficiently large compared to the dominant frequency of two-phase flow-induced unsteady forces. He showed the RMS of fluctuating lift and drag forces against void fraction, depicting two trends: one being a weak dependence of flow-induced forces on void fraction at low void fractions, and the other a stronger dependence at higher void fractions the same as for RMS pressure fluctuation. A precise comparison of lift and drag forces indicated that unsteady lift was greater than drag for lower void fractions, while both became comparable for higher void fractions.

Due to vortex shedding, the two-phase flow-induced lift force was still rather narrow-banded for lower void fractions. However, it contained more higher-frequency components at high void fractions. The unsteady drag was less periodic even in low void fractions.

Recently, Hara and Ogawa[11] reported two-phase flow-induced in-line vibrations in a circular cylinder, revealing the significant influence of air bubbles on vibration: when the cylinder oscillated with a large ampli-

tude due to synchronization of vortex shedding with the oscillation in a water flow, the introduction of small amount of air bubbles--about 5% in void fraction--drastically reduced vibrations. In contrast, in-line vibration became markedly large and random for higher void fractions.

Ogawa and Hara[12] encountered interesting experimental results concerning the cross-flow vibration of a circular cylinder immersed perpendicular to a two-phase bubble flow. Cross-flow vibration was also drastically reduced by the injection of air bubbles in amount less than 10% in void fraction when cylinder oscillation was synchronized with vortex shedding. In contrast, vibration was strongly excited for flow velocities where there was no synchronization.

Hara and Ogawa did not sufficiently explore the mechanisms of vibration reduction and excitation due to the injection of air bubbles in the flow in their papers[11, 12]. Thus this paper is the first to briefly describe experimental results of in-line and cross-flow vibrations of a single circular cylinder immersed in a two-phase air-water bubble flow, which was vertically upward, and shows air-bubble effects on the vibrations. We then discuss in detail the mechanisms of vibration reduction and excitation generated by injecting air bubbles in a water flow surrounding a flexibly mounted single cylinder. In the discussion, we take into account available experimental results[8, 9, 10] such as flow visualization, two-phase flow characteristics with respect to flow pattern around a stationary circular cylinder, magnitude and frequency characteristics of pressure fluctuation on the cylinder surface, and two-phase flow unsteady lift and drag force characteristics. From the discussions, an idea for vibration reduction mechanism is proposed for in-line and cross-flow vibrations, as well as for the vibration excitation mechanism for nonresonant conditions and for higher void fractions.

2. TWO-PHASE CROSS-FLOW INDUCED VIBRATIONS

2.1 In-line Vibration

A 58 mm vibration-test cylinder, 30 mm in diameter, was horizontally installed, as shown in Fig. 1 (a), with a wire spring, in a 200 mm x 60 mm rectangular test section where the flow was vertically upward. The

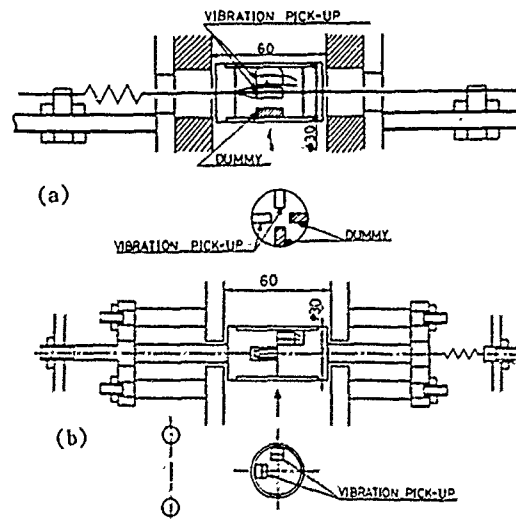


Fig. 1 A circular test cylinder for two-phase cross-flow induced vibrations, (a) in-line vibration, and (b) cross-flow vibration

ratio of channel area to cylinder area was 200/30 for the test section, which produced a rather small blockage effect[13, 14] on vortex shedding from a rigidly fixed circular cylinder of the same diameter as the tested cylinder, i.e., the Strouhal number was 0.22 to 0.19 in a range of $Re \approx 0.9$ to 1.8×10^4 . The aspect ratio of the test cylinder was almost 2, which was small. However, the cylinder's end was very close to the test-channel wall, i.e., the gap between them was 1 mm, so the test-channel wall seemed to suppress some of the three-dimensional flow effects similarly as for end plates at both sides of a cylinder[4]. Noted here that, although this small aspect ratio detracts from generality of the results from the viewpoint of fluid mechanics, they are considered to indicate a new problem involving vortex-induced vibrations of a circular cylinder in a two-phase flow.

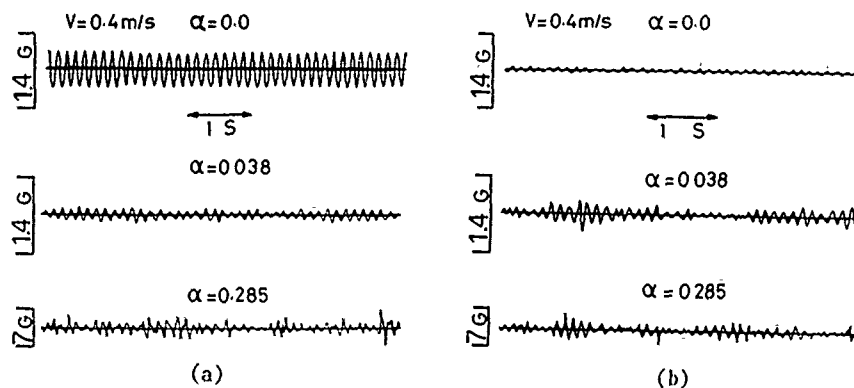


Fig. 2 Typical wave forms of cylinder vibrational accelerations
in (a) in-line and (b) cross-flow directions

Figs. 2 (a) and (b) show typical time traces for the vibrational acceleration of the cylinder at flow approaching-velocity $V=0.4$ m/s, where the in-line component of acceleration is indicated in Fig. 2 (a) and the cross-flow component in 2 (b). For a single-phase water flow (volume-metric void fraction: $\alpha = 0.0\%$), in-line vibration was harmonic and large.

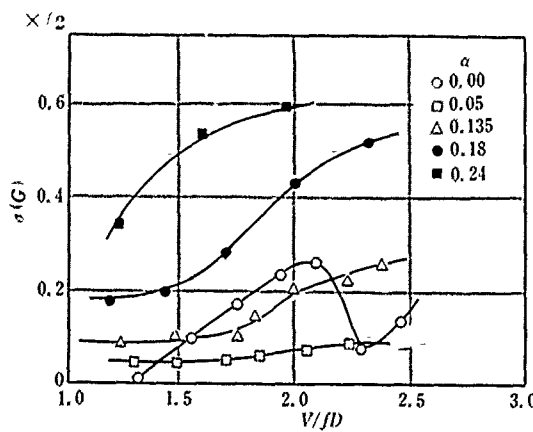


Fig. 3 RMS of in-line vibrational acceleration of a cylinder
as a function of reduced velocity V/fD

However, for $\alpha = 3.8\%$, it was drastically reduced (Fig. 2 (a)). Further increasing the void fraction, e.g., to $\alpha = 28.5\%$, yielded a rather random but very large in-line vibration.

Corresponding to Fig. 2 (a) for $\alpha = 3.8\%$ and 28.5% , Fig. 2 (b) shows that cross-flow vibration at that flow was little influenced by air bubbles injected into the flow for low void fractions, e.g., $\alpha = 3.8\%$, but a large amount of air bubbles in the flow ($\alpha = 28.5\%$) generated strong vibrations in both cross-flow and in-line directions.

Using f to designate the peak frequency in PSD for in-line vibrational acceleration, the reduced velocity is defined as V/fD , where D is the cylinder diameter and V the water approaching-velocity. Fig. 3 shows the RMS of in-line vibrational acceleration plotted against reduced velocity. A single-phase water flow induced a large in-line vibration in the cylinder system when $V/fD = 2.1$, agreeing with King's findings[15]. When the void fraction was 5%, two-phase flow-induced in-line vibration became much smaller than that in water flow, for reduced velocities ranging from 0.5 to 2.5. Note that, at $V/fD = 2.1$, vibration was markedly reduced to about 1/4 that in water flow. Even for $\alpha = 13.5\%$, air bubbles in the flow damped in-line vibration by about 20% for V/fD of nearly 2. For higher void fractions, e.g., $\alpha = 18\%$ or 24% , cylinder vibration increased with V/fD , and was very large compared with that for water flow.

2.2 Cross-flow Vibration

A cylinder the same size as that described in Section 2.1 was used to investigate two-phase flow-induced cross-flow vibration. Flat-plate springs were employed to flexibly support the test cylinder as shown in Fig. 1 (b). The natural frequency of the cylinder-spring system in this case was 3.4 Hz in a cross-flow direction in still water, and 13 Hz in an in-line direction. The cylinder was thus able to oscillate primarily in a cross-flow direction. The damping ratio of the test cylinder system was 3.7% in water. Two vibration pickups, fixed inside the cylinder, measured oscillatory acceleration in both cross-flow and in-line directions.

Fig. 4 shows the RMS value of cross-flow vibration acceleration plotted against void fraction. For $V = 0.3$ m/s, vibration increased with void fraction. For higher velocity, e.g., $V = 0.6$ m/s, vibration was very

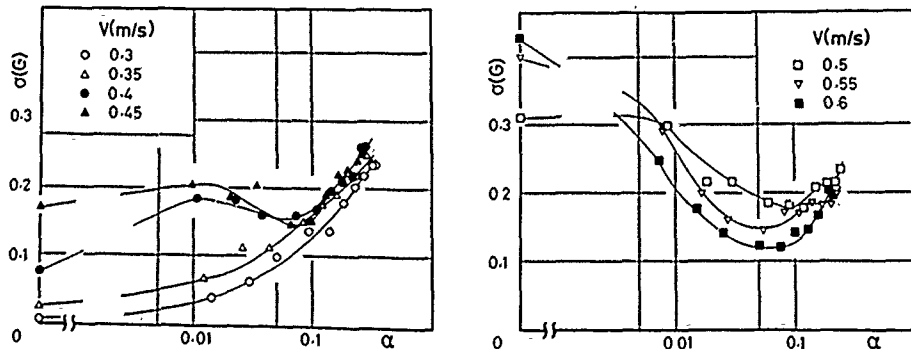


Fig. 4 RMS cross-flow vibrational acceleration of a cylinder as a function of void fraction

large at $\alpha = 0.0\%$, i.e., in water flow. This is clearly due to the lock-in of vortex shedding with cylinder oscillation. Injecting air bubbles up to about 7% in void fraction into the flow reduced vibration markedly, as the figure shows. Above a void fraction of $\alpha = 7\%$, however, cross-flow vibration again increased. Maximum vibration reduction for these velocities was observed to occur at a void fraction of about 7%.

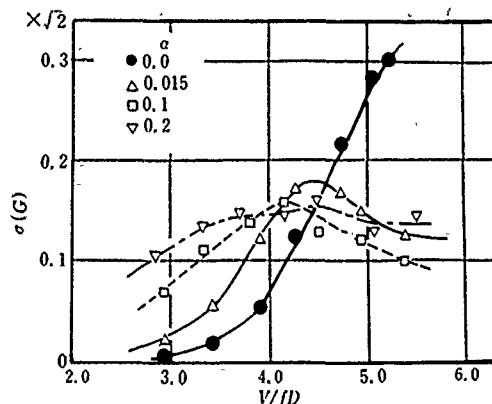


Fig. 5 RMS cross-flow vibrational acceleration of a cylinder as a function of reduced velocity V/fD

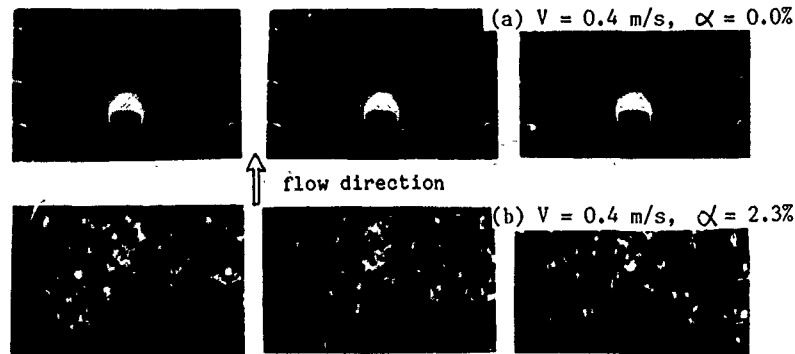


Photo 1. Wake patterns from an in-line oscillating circular cylinder (a) in single-phase water flow, and (b) in two-phase flow

These results are plotted next, in Fig. 5, against reduced velocity, V/fD . For a single-phase flow ($\alpha = 0.0\%$), cross-flow vibration increased with reduced velocity, falling into a so-called lock-in state at $V/fD \approx 5$, where there were large-amplitude vibrations of the cylinder. For a two-phase flow with a void fraction $\alpha \leq 20\%$, vibration increased almost linearly with reduced velocity up to $V/fD = 4.5$. Over $V/fD = 4.5$, however, vibration decreased for $\alpha < 10\%$; for higher void fractions, e.g., $\alpha = 20\%$, it kept an almost constant magnitude. As the figure indicates, cross-flow vibration was drastically reduced for $V/fD \geq 5$ by injecting a certain amount of air bubbles into the flow. For $V/fD \leq 4.5$, however, the two-phase flow-induced vibration was much stronger than that excited by vortex shedding in a water flow. For a two-phase flow with a low void fraction, e.g., $\alpha = 1.5\%$, the peak response in Fig. 5 at $V/fD = 4.5$ corresponded to the "resonance" of the cylinder system caused by a narrow-banded fluid force of two-phase vortex shedding, because the vortices shed at a frequency of 3.3 Hz calculated from a Strouhal number of 0.22.

3. VIBRATION EXCITATION AND REDUCTION MECHANISMS

3.1 In-line Vibration

(a) Excitation mechanism. Photo 1 (a) shows a series of wake patterns generated by in-line vibration of the circular cylinder described

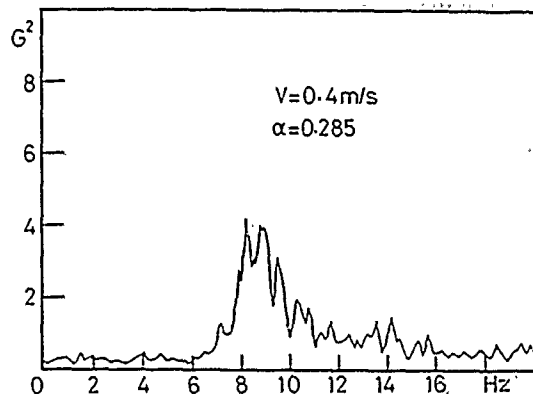


Fig. 6 PSD of in-line vibrational acceleration induced by two-phase flow ($V = 0.4$ m/s, and $\alpha = 28.5\%$)

in Section 2.1. Water flow velocity was 0.4 m/s, corresponding to a reduced velocity V/fD of 1.75. The wake did not oscillate, but rose straight. According to King[15], in-line vibration is excited by symmetric vortex shedding at each cycle of cylinder vibration. The wake is therefore considered to form the pattern in Photo 1 (a). Because a cylinder system is most inclined to vibrate at its natural frequency, symmetric vortex shedding is thought to synchronize with cylinder oscillation, meaning a large in-line vibration will be generated. King[15] also pointed out a threshold amplitude for the onset of in-line vibration instability, i.e., 1-2% cylinder diameters. For $V/fD = 2.1$ in Fig. 3, the estimated vibration amplitude was 1.6 mm, yielding an amplitude-to-diameter ratio of 5.3%. A large in-line vibration was thus concluded to occur at $V/fD = 2.1$.

For higher void fractions, for instance $\alpha = 28.5\%$, the cylinder was very strongly excited in both in-line and cross-flow directions (Figs. 2 (a) and (b)). Two-phase flow vortex shedding did not occur at higher void fractions [8], e.g., $\alpha \geq 0\%$. Vortex shedding was thus not a candidate for the excitation mechanism in this case. On the other hand, two-phase flow-induced unsteady forces are very large and rather random[8, 9], apparently generated by buffeting of the cylinder by a very random flow which includes air bubbles. The cylinder was thus considered to be forced to vibrate by these strong, random, extraneous buffeting fluid forces. This is supported by the shape of the PSD distribution for in-line vibration acceleration for $V = 0.4$ m/s and $\alpha = 28.5\%$, as shown in Fig. 6, corresponding to one example in Fig. 2 (a).

(b) Reduction mechanism. Photo 1 (b) shows a series of two-phase flow patterns around the flexibly mounted cylinder, exhibiting a slightly oscillatory motion in the wake generated. Air bubbles flow closely along the cylinder surface with a slip-velocity to water flow due to buoyancy, and are thus considered to strongly disturb the boundary layer. Symmetric vortices are therefore probably not generated at each cycle of oscillation. Photo 1 (b) supports this hypothesis by indicating two-phase flow alternate vortex shedding as described in Section 1.

A vibration amplitude, estimated from the RSM of cylinder vibrational acceleration and the natural frequency for $V/fD = 2.1$ and $\alpha = 5\%$ in Fig. 3 yields an amplitude-to-diameter ratio of about 1.3%, meaning the cylinder is essentially stationary in the flow. Fluid forces acting on the flexibly mounted cylinder are thus considered to have almost the same character as that acting on a stationary cylinder for a low void fraction[9, 10]. This means that two-phase flow-induced forces are not dominant, but are rather random over a range 4 Hz to 10 Hz including the cylinder natural frequency[9, 10]. The cylinder thus does not resonate with fluid forces at its natural frequency. For this reason, in-line vibration was markedly reduced by injecting a small amount of air bubbles in the flow.

3.2 Cross-flow Vibration

(a) Excitation mechanism for small, reduced velocity. For $V/fD \leq 4$ in Figs. 4 and 5, there are two possible excitation mechanisms in the two-phase flow-induced vibrations. One is vortex shedding generating an alternative fluid force on the cylinder system, and the other is the buffeting force due to random air-bubble motion against the cylinder.

As shown in Fig. 5, the vibration response $\sigma^2(G)$ increases rapidly with V/fD for small void fractions; for example, $\alpha = 1.5\%$ or 10% , and takes a peak at about $V/fD = 4.4$ to 4.1 . From the viewpoint of linear random vibration, two major factors produce a large vibration response in the cylinder-spring system: One is the magnitude of an unsteady fluid force acting on the cylinder, and the other the dominant frequency of the fluid force. Hara[9] already demonstrated that, for low void fractions $\alpha \leq 10\%$, two-phase flow-induced unsteady lift increased rather gradually with flow velocity V ; for instance, the force acting on a stationary circular cylinder, 30 mm in diameter, at $V = 0.5\text{ m/s}$ (or $V/fD = 4.6$) was about 50% larger than that for $V = 0.3\text{ m/s}$, corresponding to $V/fD = 3$ in Fig. 5. On the other hand, the increase in vibration response from $V = 0.3\text{ m/s}$ to 0.5 m/s is almost 8 times for $\alpha = 1.5\%$ as shown in Fig. 5. Thus, this high response at $V/fD = 4.6$ is considered due to the dominant frequency of the fluctuating lift rather than the magnitude of unsteady lift, approaching the cylinder natural frequency with the increase in V/fD and bringing the vibration into a resonance with vortex shedding.

Buffeting is not sinusoidal but random[9, 10], and increases with void fraction and water velocity in the flow, as indicated in [9, 10]. Furthermore, when reduced velocity is small, e.g., $V/fD = 3$, vortex shedding

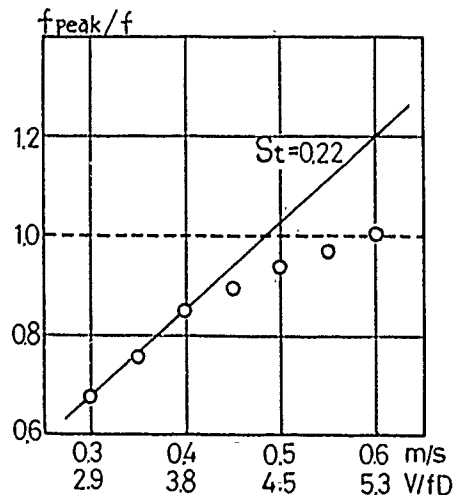


Fig. 7 Peak frequency in PSD of cross-flow vibrational acceleration at $\alpha = 0.0\%$ plotted against reduced velocity V/fD

frequency is much smaller than the cylinder natural frequency (Fig. 7). Thus, vibration of the cylinder system is due mostly to the buffeting force and becomes narrow-banded, with a dominant component at the cylinder natural frequency as shown in Fig. 8 for $V = 0.3\text{ m/s}$ and $\alpha = 1.4\%$, and increases with the void fraction as shown in Figs. 5 and 8. The buffeting, unsteady, impulsive force due to air bubble random motion in the flow is, therefore, considered the major excitation mechanism in cross-flow vibration at low reduced velocities.

Karman vortex shedding apparently does not occur[8] for void fraction $\alpha > 10\%$. Hara[9, 10] showed that unsteady fluid forces were very large

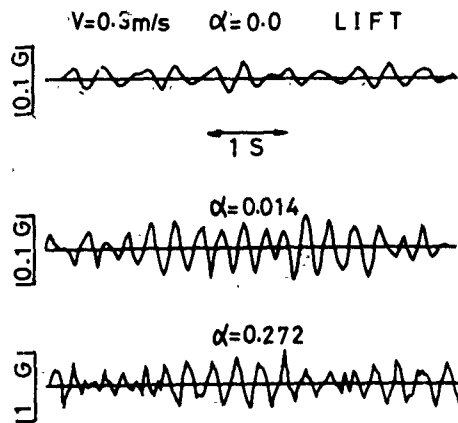


Fig. 8 Cross-flow acceleration waveforms at $V = 0.3$ m/s for different void fractions

and random, indicating that a major excitation mechanism for high void fractions is most likely the impinging air bubbles and the unsteady, random buffering force, due to random bubble motion, acting on the cylinder. Fig. 8 supports this, because the cylinder, which is a one-degree-freedom vibration system, has a narrow-banded response character with the dominant component at its natural frequency.

(b) Vibration reduction. When vortex shedding is synchronized with cylinder oscillation, a small amount of air bubbles injected in the flow can drastically reduce cross-flow vibration (Figs. 4, 5). Photos 2 (a) and (b) show wake patterns generated by a single cylinder flexibly mounted in a



(a) $V = 0.6$ m/s, $\alpha \approx 0.0\%$



(b) $V = 0.6$ m/s, $\alpha = 5.0\%$

Photo 2. Wake patterns from a cross-flow oscillating circular cylinder (a) in single-phase flow, and (b) in two-phase flow

cross flow. Photo 2 (a) is for $V = 0.6$ m/s and $\alpha = 0.0\%$ (water flow) and (b) for $V = 0.6$ m/s and $\alpha = 5\%$. Photo 2 (a) and Fig. 8 indicate the vibration is locked in. The injection of air bubbles in the water flow is thought to strongly disturb the cylinder's boundary layer due to the random motion of air bubbles flowing with a slip velocity to water flow and to produce a random buffeting force. Synchronization is thereby probably detuned and the lock-in state destroyed, and two-phase flow vortices shed at the appropriate Strouhal number--which is already much higher, for this case, than the cylinder natural frequency (Fig. 7). Unsteady fluid forces acting on the cylinder, however, which remains almost stationary, are random and impulsive, but have a dominant frequency component corresponding to two-phase flow vortex shedding for low void fraction[9, 10]. This character is considered due to random air bubble motion in the flow. Cross-flow vibration response to random fluid forces without a dominant component at the cylinder natural frequency is thereby significantly reduced. This is also supported by the fact that, as demonstrated in experiments, when the random forces have a dominant frequency component at the cylinder natural frequency, for example, $V = 0.5$ m/s or $V/fD = 4.5$, the vibration is not reduced significantly, as indicated in Fig. 4.

Major mechanisms in reducing vortex-induced cross-flow vibration in water flow are, thus, considered to be (1) detuning of synchronization between vibration and vortex shedding and (2) randomness of unsteady fluid forces induced by the stochastic motion of air bubbles in the flow.

4. CONCLUDING REMARKS

This paper (1) examines in-line and cross-flow vibration characteristics of a flexibly, horizontally mounted circular cylinder in a two-phase vertical flow, and (2) discusses the major fluid dynamic and vibrational mechanisms exciting and reducing in-line and cross-flow vibration, taking into account major experimental results on phenomenological characteristics of two-phase air-water bubble flow around a single circular cylinder, which is horizontally installed and perpendicular to the flow.

A small amount of air bubbles injected in the flow markedly reduces both in-line and cross-flow vibrations when they are in resonance with vortex shedding. A large amount of air bubbles injected in the flow, however, excites vibration strongly and randomly.

Thus, the major vibration mechanisms for excitation in two-phase cross flow found from the experimental data are (1) buffeting forces due to the random motion of air bubbles in the flow and (2) two-phase flow vortex shedding generating a narrow-banded random force on the cylinder at low void fractions.

Major mechanisms for vibration reduction are found to be (1) detuning of synchronization between cylinder oscillation and vortex shedding through strong disturbance of the cylinder boundary layer caused by injecting a small amount of air bubbles in the flow and (2) randomness in two-phase flow-induced unsteady forces.

ACKNOWLEDGMENTS

The author wishes to thank Mr. N. Ogawa, who assisted in carrying out most of the experimental work. Research for this work was supported in part by grants from the Japanese Ministry of Education and Culture and the Saneyoshi Foundation.

REFERENCES

- 1 Sarpkaya, T., "Vortex-induced Oscillations: A Selective Review", ASME Journal of Applied Mechanics, Vol. 46, 1979, pp. 241-258
- 2 Durgin, W. W. et al, "Lower Mode Response of Circular Cylinders in Cross Flow", ASME Journal of Fluids Engineering, Vol. 102, 1980, pp. 183-190
- 3 Botelho, D. L. R., "An Empirical Model for Vortex-induced Vibrations",

California Institute of Technology, Earthquake Engineering Research Laboratory, Report No. EERL 82-02, 1982, pp. 1-111

4 Staubli, T., "Calculation of the Vibration of an Elastically Mounted Cylinder Using Experimental Data from Forced Oscillation", ASME Journal of Fluids Engineering, Vol. 105, 1983, pp. 225-229

5 Pettigrew, M. J. and Gorman, D. J., "Vibration of Heat Exchange Components in Liquid and Two-Phase Cross Flow", Atomic Energy of Canada Limited, AECL-6184, 1978, pp. 1-20

6 Heilker, W. J. and Vincent, R. Q., "Vibration in Nuclear Heat Exchangers Due to Liquid and Two-phase Flow", ASME Journal of Engineering for Power, Vol. 103, 1981, pp. 358-366

7 Every, M. J. et al, "Hydrodynamic Loads on Flexible Marine Structures Due to Vortex Shedding", ASME Winter Meeting 1981, 81-WA/FE-24, 1981, pp. 1-9

8 Hara, F. and Ohtani, I., "Vibration of a Circular Cylinder in a Two-phase Cross Flow, 1st Report, Karman Vortex Shedding and Pressure Fluctuation", Trans. of JSME, Vol. 48, No. 431-c, 1982, pp. 962-971, (in Japanese)

9 Hara, F., "Two-phase Cross Flow-induced Forces Acting on a Circular Cylinder", ASME Flow-induced Vibration of Circular Cylindrical Structures, PVP-Vol. 63, 1982, pp. 9-17

10 Hara, F., "Two-Phase Cross Flow-induced Vibrations in a Circular Cylinder, 2nd Report, Characteristics of Unsteady Lift and Drag", Trans. of JSME, Vol. 48, No. 433-c, 1982, pp. 1371-1379, (in Japanese)

11 Hara, F. and Ogawa, N., "Vibrations of a Circular Cylinder Immersed Perpendicular to a Two-phase Air-water Bubbly Flow, 3rd Report, Response Characteristics of In-line Vibrations and Vibration Reduction and Excitation due to a Bubbly Flow", Trans. of JSME, Vol. 49, No. 445-c, 1983, pp. 1624-1629, (in Japanese)

12 Ogawa, N. and Hara, F., "Cross-flow Vibrations of a Circular Cylinder due to a Bubbly Two-phase Flow, 4th Report, Response Characteristics and Vortex Shedding", Trans. of JSME (to be published in Japanese)

13 Richter, A. and Naudascher, E., "Fluctuating Forces on a Rigid Circular Cylinder in Confined Flow", Journal of Fluid Mechanics, Vol. 78, Part 3, 1976, pp. 561-576

14 Blevins, R. D., "Flow-induced Vibration", Van Nostrand Reinhold Comp., 1977, pp. 1-363

15 King, R., "A Review of Vortex Shedding Research and Its Application", Ocean Engineering, Vol. 4, 1977, pp. 141-171

FLOW-INDUCED VIBRATIONS OF MIXING VESSEL INTERNALS

R. King
BHRA, The Fluid Engineering Centre
Cranfield, Bedford, England

ABSTRACT

This paper draws together the results of research work undertaken at BHRA on cylindrical members excited to oscillate by flow within unbaffled mixing vessels. Oscillations of an anchor mixer and parallel sided and stepped dip tubes are described, including those cases in which the cylinders are mounted close to the vessel wall. The results are used to define guidelines for use in calculating safe operating limits of cylinders dipping into water. Recommendations are made for avoiding vortex excited oscillations of an anchor mixer by a device which actually improves its efficiency as a mixer.

1. INTRODUCTION

This paper describes work recently completed with elastic cylinders undergoing vortex-excited oscillations in flowing fluids. Two examples have been selected: a fully immersed cylinder in nominally rotary flow and cylinders dipping into linear and rotary flow from above.

Considerable research effort has been directed towards the problems of sustained oscillations of cylinders due to vortex shedding in steady flow. In the majority of cases, the cylinders have been completely immersed in the fluid (chimneys, underwater pipelines) or have protruded through the fluid surface from below (marine piles, submarine periscopes). In other equally practical situations, the cylinder dips into the flowing fluid from above, and this configuration has not received the same detailed experimental attention. Typical applications of these cylinders would be draught tubes and stilling wells for submersible pumps on offshore oil rigs or thermometer pockets and dip tubes in reaction vessels in the nuclear or process industries. This geometrical arrangement differs from the more conventional cylinder/water set-up in at least two ways (i) the fluid excitation is applied where the elastic resistance of the cylinder is lowest and (ii) for very shallow depths of immersion the three-dimensional flow effects over the end of the cylinder cause disruption of the vortex shedding correlation with respect to length.

Both of the examples to be described have application to the process industries because both are associated with batch mixing vessels in which chemical reactions are to be carried out. It is essential that the reactants or components

are brought into contact and distributed uniformly throughout the vessel, and for this purpose, mechanical mixers, or agitators are used. Typically, the vessels are up to 7 m³ in volume and the majority are each fitted with a central shaft and driven from above through an external motor and gearbox supported on a steel lid.

Many of the liquids are extremely corrosive and the vessels are glass-lined as a protection. The mixer too must be protected and this means that the shape selected is one that can be readily glass coated rather than that which would give the best mixing.

In viscous corrosive media an agitator shaped like an anchor frequently is used; this sweeps past the walls of the vessel (which are usually heated) to prevent local accretion or hot spots. Normally anchor blades or arms would be oval in cross section, with the larger axis radial to the vessel wall and equal to one tenth of the vessel diameter. However, in the first example, a model anchor mixer with arms of circular cross-section was tested in a mixing vessel under an industrial contract. The rotating arms created a concentric flow pattern within the vessel; the fluid did not rotate at the same rate as the arms, due to slippage and the arms thus experienced cross-flow relative to them. In addition, the clearance between the anchor arms and the vessel wall was varied to observe the changes induced by this practice.

In the second example, several model dip-tubes were tested in a mixing vessel and also in a water channel. Dip tubes are used for measuring temperatures, adding reagents, and for extracting samples from mixing vessels. These tubes are generally of circular cross-section, are cantilevered from the lid of the vessel and may extend almost to its base. Not all dip tubes are straight or of constant diameter. Some gas sparge pipes are tapered: some are stepped, having a silencer at the end to reduce noise levels; others may be curved for emptying the contents from vessels not equipped with bottom outlets. In mixing vessels in which nominally rotating flow is created, the dip tubes are subject to relative cross flow. Dip tubes are often placed close to the walls of the vessel and proximity effects must be considered, just as in the case of the arms of the anchor mixer.

Vortex shedding occurs from the anchor arms and from the dip tubes, and sustained bending oscillations have been recorded. The oscillations can have four effects: a) they can ruin the seal or stuffing box at the top mounting of the anchor mixer shaft, leading to contamination of contents or leakage of possibly hazardous or toxic fumes; b) the anchor arms can contact the vessel wall leading to corrosion problems if the glass lining/coatings are ruptured; c) the dip tubes can contact either the vessel wall or the anchor mixer depending on location, causing problems similar to b); and d) fatigue failure of the components may occur.

Vessels are expensive, and their contents are often extremely valuable; loss of either can be costly and inconvenient. A number of ad hoc solutions have been found for specific problems and there are still many unknowns. This paper draws together the experimental results from work undertaken largely at BHRA and presents a consistent pattern of behaviour for the configurations tested.

1.1 Previous Work

Probably one of the earliest demonstrations of vortex excited oscillations of a cylinder dipping into rotating flow was that of Lord Rayleigh [1] who in 1915 ran a series of fairly rudimentary tests using a rotating bath of water to show that coincidence of vortex shedding frequency and natural frequency of a pendulum cylinder dipping into the water gave rise to sustained oscillations. He demonstrated that the pendulum oscillated cross-flow (i.e. radially) and that maximum oscillation amplitude was recorded for an apparent Strouhal number of 0.14. This may be interpreted as maximum amplitude occurring at a Reduced Velocity (V_r) of 7; he repeated the tests in heated water (60° C) and recorded results that were insensitive to this change of temperature and consequent change in Reynolds number.

Bearman and Zdravkovich [2] measured the pressure distribution around a rigid cylinder placed near a plane boundary. As the cylinder was moved towards the wall the front stagnation point was displaced towards the gap and the cylinder experienced a force expelling it from the wall. Goktun [3] showed that the frequency of vortex shedding between a rigid cylinder and the wall was different from that from the top surface of the cylinder, and this may have been associated with changes in location of the separation and stagnation points as noted by Bearman and Zdravkovich [2]. Although there are obvious differences (notably in Reynolds number) between the various references, there is a general concensus that for rigid cylinders, regular vortex shedding ceases at $G/D \approx 0.5$ and that the isolated cylinder condition is reached for $G/D \approx 1$. [2-6].

Although rigid cylinders would not necessarily exhibit vortex shedding patterns that are representative of those from flexible cylinders (such as dip tubes) under otherwise similar conditions, the brief literature survey on proximity tests provided a useful pointer on what to observe in the work described in this paper.

2. EXPERIMENTAL ARRANGEMENTS

Two mixing vessels and a flume were used in the work described here.

The anchor hydroelastic model (built to a linear scale of approximately 2.25:1 was tested in a 600 mm diameter perspex mixing vessel with a rounded base (Fig. 1). The gap between the arms and the wall was varied in two steps by inserting liners. Based on the diameter of the arms (57 mm) the range of gaps tested was $G/D = 0.39, 0.14, 0.07$.



Fig. 1. The hydroelastic model anchor mixer in the 0.6 m diameter mixing vessel.

The central shaft of the anchor was strain-gauged to sense torsion and strain in two orthogonal planes of bending (radial and tangential). The sets of strain gauges each formed part of a separate, tuned high frequency (RF) circuit and changes of strain were interpreted as changes in frequency. Each of three battery-powered frequency transmitters was clamped to the shaft and thus rotated with it. Each unit transmitted signals through an antenna concentric with the shaft and these were received by a stationary pick-up mounted close to the shaft. Thus the torsion and bending strains could be monitored whilst the shaft was ro-

tating. The instrumentation worked equally well when the shaft was not rotating and the dynamic tests were preceded by a short investigation into added mass and frequency variation over the range of gaps available. Speed of rotation was monitored automatically on-line using a toothed wheel interrupting a light source.

The perspex mixing vessel used for the dip tube experiments and later for flow visualisation, was of square plan 680 mm deep and having a clear circular insert of 762 mm diameter to avoid refraction when viewed from outside. The base of the vessel was flat and made from perspex, and mounted beneath the vessel on a turntable was a TV camera which rotated synchronously with the central mixer shaft. The TV signals were connected through a slip-ring arrangement to a video recorder and monitor. By this means, the observer could see what the flow patterns were at the mixer (which for the majority of tests was a 4-bladed impeller). In later tests, the central mixer was removed and replaced by an adjustable cross member to which a vertical cylinder was connected to simulate one of the anchor arms sweeping near the vessel wall (Fig. 2), to enable flow visualisation studies to be made of the vortex shedding processes for this arrangement.

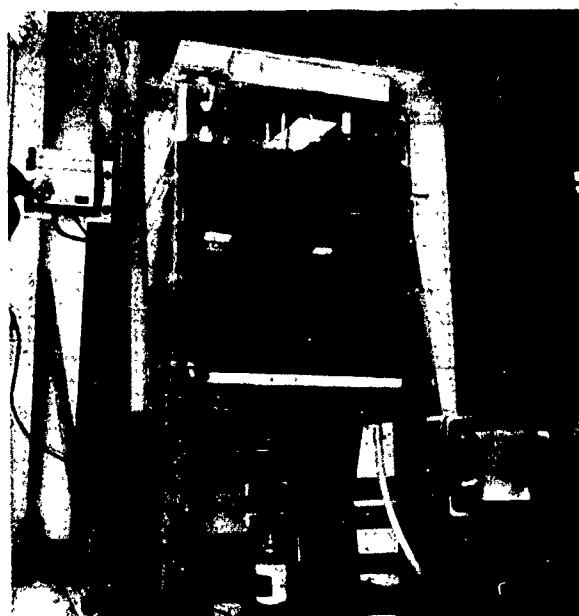


Fig. 2. The mixing vessel used for the dip tube tests. Note the rotating TV camera, monitor and cylinder used for flow visualisation.

For the dip tube tests, each dip tube was strain-gauged in two bending planes (X, Y; tangential and radial) and mounted from above the vessel at various clearances from the wall in the range $0.16 \leq G/D \leq 5.58$. The signals from the strain gauge amplifier were fed into an oscilloscope for visual observation and into a PDP11/03 computer for analysis using an HP 5420 digital signal analyser, which gave rms amplitudes and frequency composition. In the tests two 800 mm long parallel sided (plain) dip tubes of diameter 9.4 mm and 12.7 mm respectively were investigated, and one stepped dip tube, having diameters of 9.4 mm and 12.7 mm on the same cylinder. The step length was 300 mm. The dip tubes were tested for only one fixed depth of partial immersion (600 mm measured from the free end) and the influence of variable immersion was investigated more thoroughly in the flume tests ($G/D \rightarrow \infty$) using three different plain dip tubes having diameters of 16.5, 25.4 and 30 mm respectively. The depth of immersion of these tubes was varied by adjusting the water level in the flume over which the strain-gauged dip tubes were mounted. The instrumentation for these tests was fairly simple, consisting of strain gauge amplifier and UV chart recorder, yielding amplitudes (as bending moment) and frequencies of oscillations.

3. RESULTS

3.1 Anchor

In the original configuration, the anchor vibrated with increasing violence over a wide velocity range, in a radial (cross-flow) direction and the speed of rotation was restricted to prevent damage to the perspex vessel or to the anchor. In this respect the model anchor reproduced the behaviour of the fullscale anchor both in the type of response and in the scaled rotational speed at which oscillations were first recorded [7]. As in the fullscale tests, the addition of a trailing splitter plate projecting for one diameter from each of the arms almost completely suppressed the oscillations and this was taken as a confirmation that vortex shedding was the cause of the excitation. The trailing splitter was not a practical solution because it gave a streamlined contour to each arm, thus reducing the drag coefficient and mixing efficiency of the anchor.

A series of investigations was made using the anchor, to determine the dependence of the results on Reynolds number, to gain some basic design data for future use and finally to find an acceptable way of reducing the oscillations to reasonable levels. The velocity distribution in the vessel was determined by using a miniature propeller meter for each test set up over a range of anchor speeds to yield the slip or relative velocity between the fluid and the anchor arms. The appropriate slip velocity was used throughout the subsequent analyses.

3.1.1 Varying the gap. The liners were inserted in sequence and the anchor response noted for each condition. Table 1 summarises the results showing that the onset of oscillations was recorded for progressively lower values of Reduced Velocity V_{rc} as the gap was decreased. This indicates that Strouhal vortex shedding frequency and size of gap are related by an inverse power law. The reduction in natural frequency (f_n) with reduction in gap indicates not unreasonably that the added mass coefficient is also a function of gap size.

Table 1: Onset of oscillations for variable gap

G/D	f_n (Hz)	V_{rc}
0.396	3.13	3.31
0.140	2.99	2.29
0.075	2.92	1.50

3.1.2 Varying the Reynolds number. The question of Reynolds number dependence inevitably arises when the results of model tests are applied to the full size equivalent. In this section, the response of the anchor was measured in a dilute solution of glycerol having a viscosity of 57 cP, (water = 1 cP).

It will be seen from Fig. 3 that the velocity at onset of large amplitude oscillations in glycerol is very close to that recorded in pure water, although the Reynolds numbers of the comparable cases are 400 and 23,000 respectively. These effects are similar to previous research with oscillating cylinders in flowing water in which Reynolds number was shown to have secondary importance in determining criteria for the onset of oscillations [8].

3.1.3 The stabilising effect of fins. In a brief exploratory test, it was shown that fins projecting for $3D/8$ mounted in pairs at $\pm 90^\circ$ from the leading stagnation point of each arm completely suppressed the oscillations. The fins gave a very small running clearance at the vessel wall which could cause problems in industrial use. The tests in this section were arranged to determine the optimum location and minimum size of fins to suppress oscillations consistent with providing an adequate drag coefficient and an acceptable running clearance.

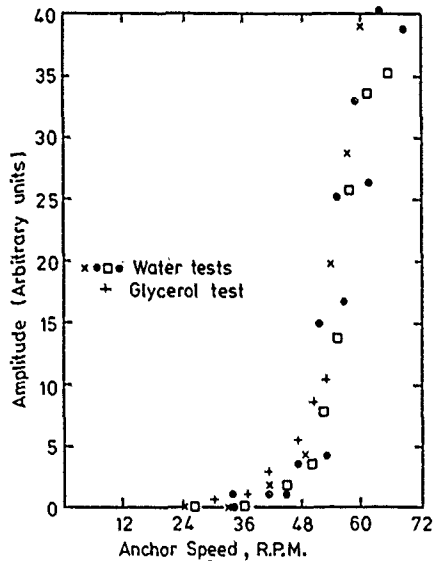


Fig. 3. Flow-induced oscillations of the anchor mixer in water and in glycerol solution.

A wide range of fin sizes and locations were investigated and the results showed that the amplitude of oscillation decreased as the fin sizes were increased; the D/16 fins gave results similar to those recorded for the bare anchor, the D/8 fins showed little improvement and the 3D/16 fins caused considerable reduction both in amplitude and rate of onset of oscillations. However, the D/4 fins set at 245° gave a yet more dramatic reduction; they also increased the drag coefficient (and thus the power consumption) by 40% relative to the bare anchor and this configuration was adopted for the fullscale anchor.

The D/4 fins were fitted to the fullscale mixer which has operated satisfactorily from vibration and mixing considerations for several years. The design is accepted as the standard for this class of mixer.

3.1.4 Flow visualisation. The flat-bottomed mixing vessel equipped with the synchronously rotating TV camera was used to study the vortex shedding process. The arm of the anchor was simulated by a vertical cylinder mounted from the rotating cross-member. Flow visualisation was achieved using a dye tracer supplied from a reservoir on the cross-member through a small bore pipe inside the cylinder and emerging through an outlet hole on the downstream (suction) side of the cylinder. The potassium permanganate dye very rapidly discoloured the vessel contents, imposing frustratingly short time limits on the length of each test. To overcome this, the potassium permanganate was mixed with dilute sulphuric acid in the reservoir, and sodium thiosulphate solution added to the water. By this means, the dye trace remained extant for sufficient time to film but was so rapidly decoloured in the vortex wakes that the vessel contents generally remained clear.

The average vortex shedding frequency was determined by counting the vortices as recorded on the video tape over a given time. The water speed was measured using a miniature propeller meter mounted in the gap between the cylinder and the vessel wall; the slip or relative velocity was deduced by subtracting the water speed from the cylinder speed.

Several cylinder speeds and gaps were covered and the results are shown in Table 2. This confirms that the vortex shedding frequency increases with decreas-

ing gap as inferred from the anchor tests in 3.1.1. However, the flow visualisation also supported [2, 3] by confirming that the vortex shedding from the cylinder surface near the vessel wall was significantly different from the surface of the cylinder furthest from the wall and varied with G/D . The separation points were not diametrically opposite and at times as G/D was decreased, vortices apparently were shed in a mixture of alternate and symmetric pairs.

Table 2: Apparent Strouhal number as a function of G/D - anchor arm and dip tube tests

G/D	S	Comment
0.16	0	no regular vortex shedding
0.47	0.35	intermittent shedding
0.62	0.26	more regular shedding
0.97	0.206	regular shedding
3.15	0.204	regular shedding
5.58	0.203	regular shedding

3.2 Dip Tubes

3.2.1 Plain dip tubes in a mixing vessel. The dip tube was tested at five radial positions, $G/D = 5.58, 3.15, 0.79, 0.39$ and 0.16 ; in the tests the paddle speed was increased gradually from zero until either the end of the tube began to hit the tank wall, or high sloshing waves were developed [9].

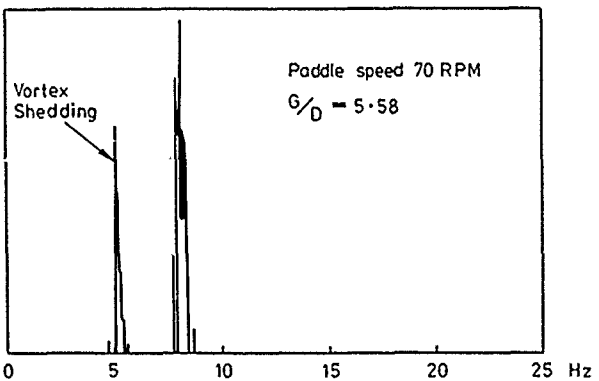


Fig. 4. Power spectral density (PSD) recorded on a plain dip tube for $G/D = 5.5$.

Fig. 4 shows a typical power spectrum of the strain gauge signals for a paddle speed of $N = 70$ rpm for $G/D = 5.58$. At lower paddle speed, $N = 40$ rpm, the power spectrum shows a fairly narrow band response and the tube vibrates at a frequency very close to its still water natural frequency. Thus, the tube behaves as a narrow band filter, responding to the pseudo-random excitation caused by turbulence in the tank. The strength and frequency of vortices being shed along the tube length depend on the flow velocity and the diameter of the tube, which is subjected to fluctuating forces caused by the change in drag and lift each time a vortex is shed. At $N = 70$ rpm, the peak on the left of Fig. 4 is caused by vortex shedding and the peak on the right is the response (to random excitation) of the tube at its 'natural' frequency. As the paddle speed increases, so do the tangential flow velocity and the frequency of vortex shedding. The two peaks finally coincide, and at $N = 100$ rpm, the tube vibrates at one dominant frequency and the response is fairly broad band.

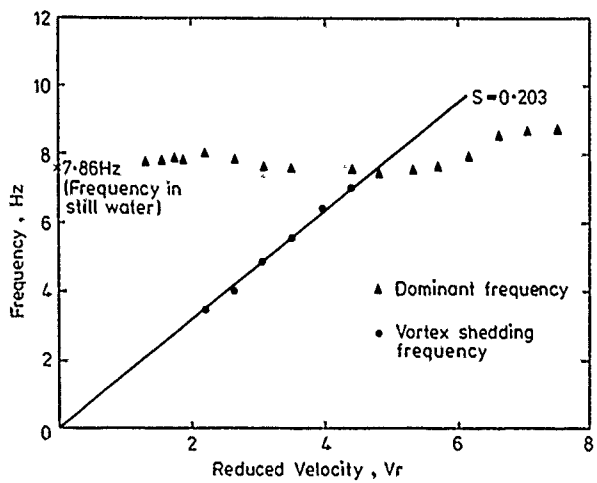


Fig. 5. Vortex shedding frequencies and dominant response frequencies against V_r for the plain dip tube at $G/D = 5.5$.

Fig. 5 shows the variation of the dominant and vortex shedding frequencies with V_r for $G/D = 5.58$. When V_r is below 2.2 the tube is excited by symmetric vortex shedding and vibrates predominantly in the direction of the flow (i.e. tangentially). At higher V_r the symmetric pattern breaks down and vortices are shed alternately from either side of the tube which then oscillates predominantly in the cross-flow direction (i.e. radially).

The frequency of alternate vortex shedding could be picked up when the Reduced Velocity V_r was above 2.2 or $G/D > 0.39$. The shedding frequency increased linearly with flow velocity and the corresponding Strouhal numbers for $G/D = 5.58$, 3.15 and 0.79 were 0.203, 0.204 and 0.236 respectively; these results are similar to those recorded for the anchor agitator.

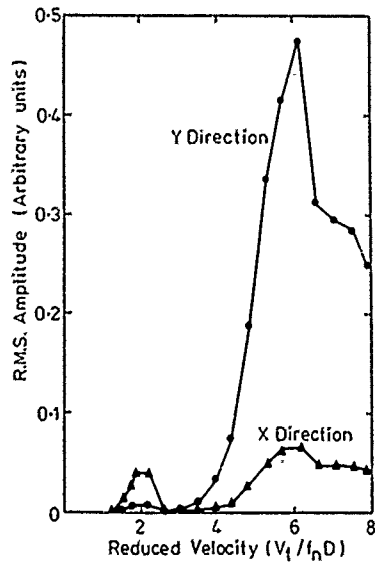


Fig. 6. Amplitude response in the X and Y directions as a function of V_r ; plain dip tube.

The RMS amplitude of the dip tube in both X and Y directions is plotted in Fig. 6 for $G/D = 5.58$. For $V_r < 2.5$ the amplitude in the X direction is higher than in the Y direction. The situation is reversed with $V_r > 2.5$. This is analogous to cylinders in two-dimensional flow which oscillate in-line with the flow for $V_r < 2.5$ and in the transverse direction for $V_r > 3.5$ although these values are highly dependent upon mass and damping levels [8]. The dip tube in the mixing vessel however, is subjected to a different flow field; instead of purely two-dimensional flow, fluid is moving in a circular path about the centre of the tank. The tangential velocity profile is roughly that of a free vortex, hence the dip tube is subjected to a 'circular', shear flow. This velocity profile will alter the points of separation and the direction of the resultant lift and drag forces. The tube, therefore, vibrates at an angle, instead of in-line or perpendicular to the flow. As the tube is moved near the tank wall, the presence of a solid boundary will again modify the flow field. The angle between the plane of vibration and the X-axis increased as the gap G/D decreased, being 10° for $G/D = 5.58$ and 50° for $G/D = 0.16$. The change in direction may be explained by the change in the front stagnation point and the separation points, as shown in Bearman and Zdravkovich's pressure distribution measurements [2].

The collected RMS amplitudes of vibration are shown in Fig. 7. There are two regions of amplitude response for G/D other than 0.16; the amplitude reaches a peak in the first region at $V_r \approx 2.0$, although the value of V_r depends on the gap/diameter ratio and is lower for smaller G/D , consistent with an increase in Strouhal number as G/D is reduced. The peak amplitude occurs when the vortex shedding frequency is just under one half the dominant frequency. The magnitude of the peak amplitude decreases with G/D and for $G/D = 0.16$ the proximity effects are such as to modify or suppress the vortex shedding process and the exciting forces are insufficient to cause oscillations in the first amplitude region.

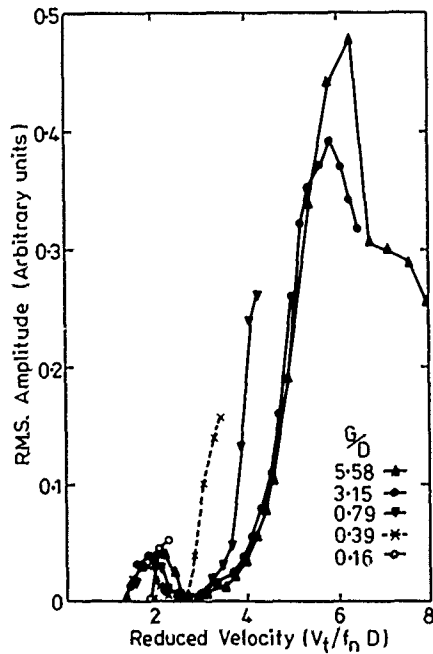


Fig. 7. Collected RMS amplitude response as functions of V_r and G/D for the plain dip tube.

After the first maximum, the amplitude of vibration drops to a very small value. When the second critical velocity is reached, the vibration amplitude increases very rapidly. The second maximum, for $G/D = 5.58$ and 3.15 occurs at about

$V_r = 6.0$. The critical velocity for this second amplitude increase depends very much on G/D . The critical Reduced Velocity drops from 3.9 when $G/D = 5.58$ to only 1.9 when $G/D = 0.16$, as demonstrated with the anchor agitator, although the configurations and the flow patterns in the two mixing vessels were quite different. However, both the dip tube and anchor results indicate that the critical or threshold velocity is lowered when the gap between the cylinder and the tank wall is decreased, consistent with a corresponding increase in Strouhal shedding frequency.

The collected results for dip tubes and anchor mixer are given in Fig. 8 as a graph of V_{rc} plotted against G/D .

3.2.2 Stepped dip tube. In these tests a stepped cylinder of diameters 9.5 mm and 12.7 mm was tested at a fixed clearance ($G/D = 4.3$) to examine the influence of the step on subsequent oscillatory motion [10].

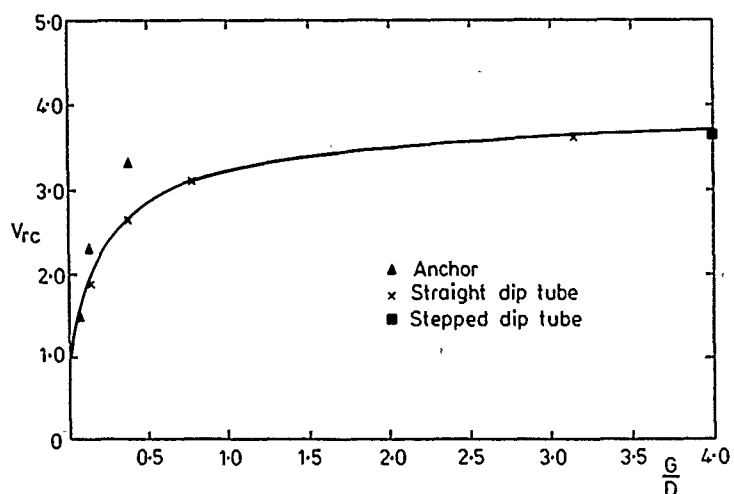


Fig. 8. Collected results from the anchor and dip tube tests; V_{rc} as a function of G/D .

a) Vorticity response

Three frequencies could be identified in the frequency spectra. The highest frequency is the tube natural frequency and the two lower frequencies increase almost linearly with flow velocity. These latter two were attributed to Strouhal vortex shedding from the two diameters of the tube, giving $S = 0.202$ and 0.198 for the 9.5 mm and 12.5 mm diameters respectively. Once the critical V_r has been reached, the various components of frequency disappear, and the tube vibrates at one dominant frequency, which is itself a function of V_r (see Fig. 9).

b) Amplitude response

Fig. 10 shows the amplitude response for the stepped dip tube which is characterised by two large amplitude peaks, not usually present in tests with parallel sided cylinders. The first peak is caused by Strouhal vortex shedding from the 9.7 mm diameter portion of the tube coinciding with the tube natural frequency and the second is caused by similar vortex shedding from the 12.7 mm diameter length. For a parallel sided tube the amplitude of oscillation reaches a peak and usually falls fairly rapidly to zero. However, with the stepped tube, the amplitude response is seen to be much broader, extending over a much wider V_r range. The peak amplitudes are smaller than for parallel sided cylinders of similar diameter although they are still large enough to cause problems in many applications.

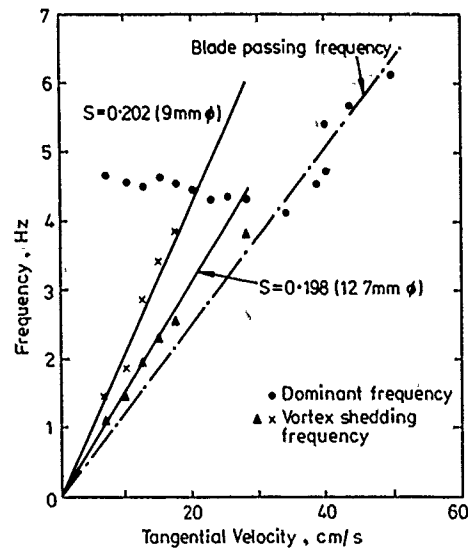


Fig. 9. Vortex shedding frequencies and dominant response frequencies against velocity for the stepped dip tube.

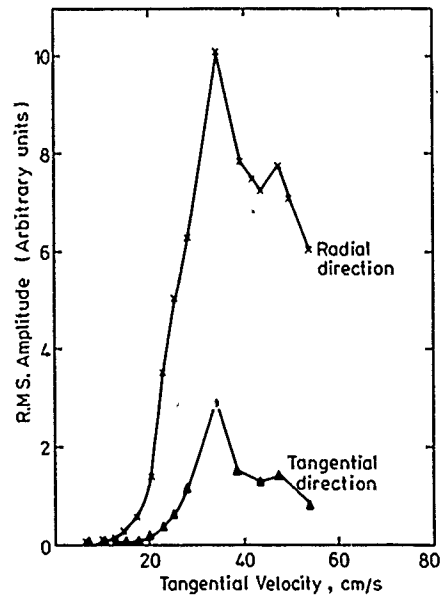


Fig. 10. Amplitude response, stepped dip tube.

c) Comment

It is recognised that these results are somewhat restricted because the phenomena observed and recorded are almost certainly functions of step size, length/diameter ratio of each step, and numbers of steps for a given cylinder length. In the limit, the steps may be regarded as forming parts of a tapered cylinder. Such cylinders are known to oscillate in a number of normal modes,

with the vortex shedding 'locking-on' to different diameters as a function of velocity and mode number [11].

3.3 Cylinder Dipping into Flowing Water

These tests were conducted using three different cylinders in sequence, dipping into a water flume in which steady two-dimensional flow could be generated. The tests were devised to investigate the similarity between the criteria governing the excitation of oscillations of cylinders dipping into water with those determined from the more conventional surface piercing pile arrangement [12].

3.3.1 Response. The results showed that cylinders dipping into water could be excited to oscillate in-line and cross-flow and that the Reduced Velocity range over which this motion occurred were similar to those established from surface-piercing piles.

Three-dimensional flow effects about the end dipping into water make it difficult to compare amplitudes of cylinders of equal Stability Parameter K_s but of different diameter. Maximum amplitudes of the fully immersed cylinders could however be predicted from the amplitudes of fully immersed piles at the same K_s . For fully immersed cylinders or piles K_s is given by

$$K_s = \frac{2\delta}{\rho D^2} (m_a + m_s)$$

and the corresponding limit amplitude of oscillation (A) is:

$$A = (2 - \sqrt{K_s}/2)D \quad \text{cross flow}$$

$$A = (0.2 - \sqrt{K_s}/5)D \quad \text{in-line}$$

Thus, the maximum amplitudes of fully immersed cylinders will not exceed ± 0.2 diameters in-line and ± 2.0 diameters cross-flow.

3.3.2 Added mass. The added mass per unit length of an infinitely long cylinder oscillating in water is ideally equal to the mass of fluid displaced by the cylinder outer diameter. For piles, the ideal added mass function can be assumed for all depths of immersion greater than about ten diameters. In this exercise with cylinders dipping into water, the added mass coefficient was demonstrated to decrease rapidly for very shallow depths of immersion. For all practical purposes the ideal solution can be used for all depths of immersion greater than about five diameters.

4. DISCUSSION OF RESULTS

The various sets of tests with the anchor mixer and dip tubes gave relatively consistent results. They also demonstrated how these geometrical arrangements are influenced by vortex shedding and how estimates can be made of potential problems prior to installation.

Specifically, the following points were noted:

- a) The Strouhal vortex shedding frequency of a cylinder near a solid boundary in linear or rotating flow can be determined by considering the local relative flow past the cylindrical member. For large gaps ($G/D = 4$) the Strouhal number is approximately equal to the isolated cylinder value of $S = 0.198$. At smaller gaps, the Strouhal number increases rapidly, reaching $S = 0.260$ at $G/D = 0.62$. Regular shedding ceases for G/D less than about 0.5.
- b) The plain dip tube was excited to oscillate for $G/D = 0.16$, and the anchor excited to oscillate for $G/D = 0.07$, confirming that vortex shedding does occur from elastic cylinders at these very small clearances from solid boundaries. The results thus show considerable difference from those recorded with rigid cylinders

for which arrangement vortex shedding ceased at $G/D \approx 0.5$. However, the flow visualisation studies with a rigid rotating anchor arm gave qualified support to the general observations of the rigid cylinder work (see a) above).

c) The Critical Reduced Velocity (V_{rc}) at which large amplitudes of dip tubes and the anchor were excited is a function of G/D (see Fig. 8). For an isolated cylinder, V_{rc} is approximately 5; however, the tests described here showed that V_{rc} can be as low as 1.5 for $G/D = 0.07$. In the one test in which Reynolds number was changed from 23,000 to 400 at a fixed G/D , the critical V_{rc} remained unaltered. For stepped dip tubes the smaller diameter should be used for calculating the lower critical V_{rc} .

d) Maximum amplitudes of oscillation can be predicted conservatively from isolated cylinder data at equal values of Stability Parameter K . Maximum amplitudes of isolated cylinders coincide with $6 < V_m < 8$. As G/D is reduced, the maximum amplitudes theoretically possible in the radial (cross-flow) direction may equal or exceed the gap; the cylinder will then either strike the side of the vessel or oscillate at some angle intermediate between the radial and cross-flow directions.

e) The vortex excited oscillations of the anchor mixer in the radial direction could be suppressed by fitting two fins to each arm projecting for $D/4$ and mounted at $\pm 45^\circ$ from the front stagnation point. The fins increased the drag coefficient of the arms and thus improved the mixing efficiency of the anchor. It is probable that this expedient could be adopted for the dip tubes also.

f) The added mass coefficient (C_m) is approximately unity for G/D larger than 4; C_m increases with decreasing G/D and was approximately 1.5 for $G/D = 0.4$ (for both the anchor and the dip tubes).

5. REFERENCES

1. Rayleigh, Lord 'Aeolian Tones' Philosophical Magazine 29. pp. 433-444, 195 (1915).
2. Bearman, P.W. and Zdravkovich, M.M. "Flow around a circular cylinder near a plant boundary". J. Fluid Mechanics, (1978).
3. Goktun, S. "The drag and lift characteristics of a cylinder placed near a plane surface". Aeronautical Quarterly pp. 305-321 (1975).
4. Buresti, G. "Vortex shedding from smooth and roughened cylinders in cross-flow near a plane surface". Aeronautical Quarterly pp. 305-321 (1979).
5. Roshko, A. et al. "Flow forces on a cylinder near a wall or near another cylinder". Proc. 2nd US Conf. Wind Res. Eng. Fort Collins, Paper IV-15 (1975).
6. Sarpkaya, T. "In-line and transverse forces on cylinders near a wall in oscillatory flow at high Reynolds numbers". Proc. Offshore Technology Conference, USA. Paper OTC 2898 (1977).
7. King, R. and Jones, R.J. "Flow Induced Vibrations of an anchor agitator". Symposium on Practical Experiences with Flow-Induced Vibrations, Karlsruhe W. Germany. Paper B15 pp. 323-332. Proceedings published by Springer-Verlag, Berlin (1979).
8. King, R. "Hydroelastic Oscillations of marine Piles - a comparison of Model and Fullscale Tests". BHRA Report RR 1254 (1974).

9. Yeung, H.C. "Vibration of Plain Dip Tubes in Mixing Vessels". BHRA Report RR 1668 (1981).

10. Yeung, H.C. "Flow-Induced Vibrations of Plain and Stepped Dip Tubes in an Unbaffled Mechanically Agitated Mixing Vessel". Fourth European Conference on Mixing, Leeuwenhurst, The Netherlands, Paper K2, pp. 371-382. Proceedings published by BHRA (1982).

11. Walshe, D.E. and Whitbread, R.E. "The Aerodynamic Investigation for a Stack for Canada-India Reactor Project". NPL Aero Report 395 (1959).

12. King, R. "Vortex Excited Oscillations of a Cylinder Dipping into Water". BHRA Report 1460 (1978).

LIST OF SYMBOLS

A	Amplitude of oscillations (zero to peak)	(m)
C_m	Added mass coefficient	(-)
D	Representative outer diameter of cylinder	(m)
f_n	Natural frequency of cylinder in still fluid	(Hz)
f_v	Frequency of vortex shedding	(Hz)
G	Gap between cylinder surface and vessel wall	(m)
K_s	Stability Parameter = $2 m_e \delta / \rho D^2$	(-)
m_a	Added mass/unit length	(kg/m)
m_e	Equivalent mass/unit length	(kg/m)
m_s	Structural mass/unit length	(kg/m)
N	Rotational speed of mixer	(rpm)
S	Strouhal Number = $f_v D / V$	(-)
V, V_t	Representative local velocity or tangential velocity	(cm/s)
V_r	Reduced velocity ($V / F_n D$)	(-)
V_{rc}	Critical Reduced Velocity (i.e. V_r at onset of unacceptable oscillations)	(-)
δ	Damping : logarithmic decrement	(-)
ρ	Fluid density	(kg/m ³)

WIND EFFECTS ON HIGH COOLING TOWERS

J. F. Sageau and M. Robert
Electricité de France
Chatou, France

ABSTRACT

In 1974, in parallel with the spreading of cooling towers and their increasing height, Electricité de France (E.D.F.), initiated a wide programme of experimental and numerical studies about the behaviour of large cooling towers.

The objectives of this programme were to provide E.D.F. with design criteria adapted to the new generation of cooling towers, after the validity of the assumptions used for small size structures, or structures with different shapes (chimneys), has been systematically questioned.

This programme included three components : (i) the determination of loadings, (ii) the static response of the tower, (iii) the dynamic response of the tower.

Many results are presented, some of them somehow unexpected. The consequences for the design of the current E.D.F. cooling towers are then discussed.

1. INTRODUCTION

The safety margin factor concept plays an essential part now in the design of modern structures. This margin helps to counterbalance the imperfections of numerical modelling, without modifying the nature of usually applied building codes. Generally, the less a phenomenon is known by theoretician, the wider must be the safety margin chosen by the designer to deal with the phenomenon in question.

As far as cooling towers are concerned, safety margins are proposed in the E.D.F. technical specifications which should be applied when the various phenomena, that may result in failures or shorten the lifetime of the towers, are taken into account. These safety margins have been derived from the results obtained in the framework of a research program, launched in 1979, concerning the feasibility and behaviour of large cooling towers.

The main features of this program, founded on experimental "in situ" studies, on wind-tunnel tests and on the development of numerical means are described in this paper and the main results obtained from 1976 to 1983 are presented.

2. AVAILABLE MEANS

2.1. Available means on site ; chosen sites and configurations

Four cooling towers have been instrumented in three different sites. The sites and the towers have been chosen in such a way that at least one of the three following parameters : height, surface condition, configuration - that may play an important part in the wind-shell interaction-varies from one site to another and from one tower to another. The tower erection schedule and the requirement of a windy site are two other limiting factors in these choices. The geometry and configurations of the instrumented towers are given in tables 1 and 2. These studies and the studies conducted in other countries are compared in figure 1.

SITE	Tower Geometry			Meteo mast Height (m)	Number of channels						
	Height (m)	D Neck (m)	D Base		Pressure			Wind		Tempera-ture	
					P _e	P _i	D _P = P _e - P _i	Speed	Direction		
GARDANNE (1975-1978)	123	50	84	140	44	3	-	3	3	1	
BUGEY (1978-1981)	128	61	108	140	68	68	68	6	3	2	
CRUAS (1981)	155	78	136	160	76	76	76	8	3	3	

Table 1 : Towers'geometry and instrumentation.

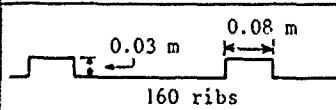
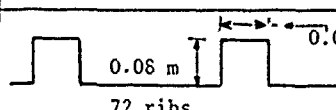
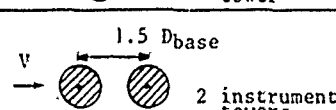
Site	Roughness	Configuration
GARDANNE	SMOOTH	1 tower
BUGEY		
CRUAS		

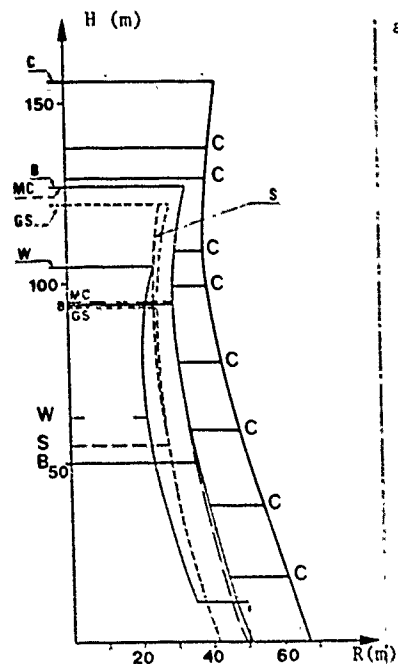
Table 2 : Towers'roughness and configuration.

2.2. Instruments used on site.

Two types of measurements are systematically used in the in-situ tests : pressure measurements on the cooling tower shell and wind measurements recorded upwind on a meteorological mast of at least the same height as the tower.

At any point on the shell three parameters can be measured :

- the instantaneous internal pressure field P_i (t),
- the instantaneous external pressure field P_e (t),
- the instantaneous pressure difference D_P (t) = P_e (t) - P_i (t).



S : SCHMEKAUSEN (1)
 MC : MARTIN'S CREEK (2)
 W : WEISWEILER (3)
 G : GARDANNE
 B : BUGEY (4)
 C : CRUAS

Fig. 1 : Comparison between "in-situ" tests.

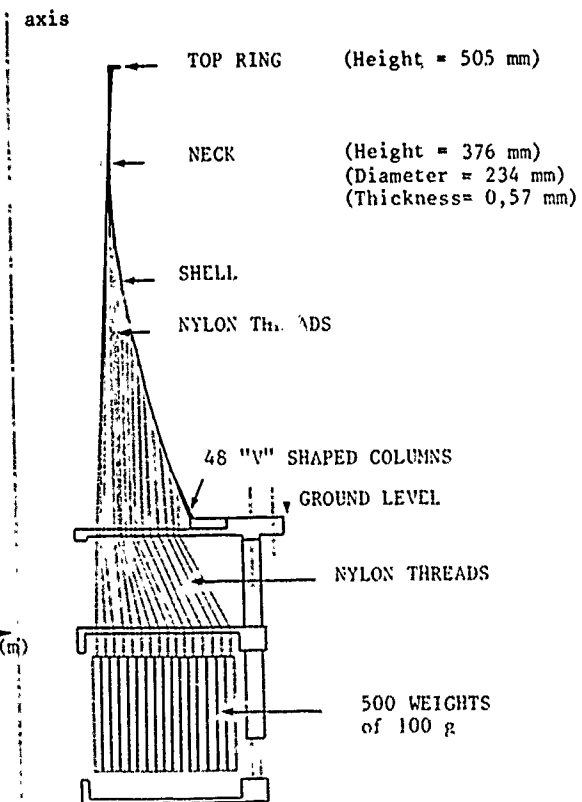


Fig. 2 : Aeroelastic model (one half), with weight simulation.

with transducer boxes incorporating a differential pressure transducer that may be calibrated from the ground before every recording. A monitoring system, automatically controlled by a computer located on site, is used for the digital acquisition of simultaneous recordings of all the channels (pressure, wind speed and direction) over 5 hours. The various characteristics of the instrumentation provided on each site are described in the table 1.

Moreover, natural frequencies are measured on the cooling tower with servo-accelerometers ; the excitation imparted by wind fluctuations is used.

2.3. Laboratory means.

The tests conducted in the laboratory or wind-tunnel serve to determine the pressure loads applied on the shell, the structure natural frequencies and the stress field and to study the tower instability.

Assessment of the pressure loads. Pressure measurements are conducted on rigid models fitted with pressure taps on their outer and inner surfaces. These are performed in the wind tunnels at the CSTB "Centre Scientifique et Technique du Bâtiment" in Nantes and at the V.K.I. "Von Karman Institute" in Brussels. The test section is 4 m wide, 3.5 m high at the C.S.T.B. and 3 m wide, 2 m high at the V.K.I. In both wind tunnels the atmospheric boundary layer is

simulated but the Reynolds number cannot be satisfied (roughness elements glued on the shell surface artificially reproduce hypercritical flow conditions). With regard to the tests on tower groups, the streamlines on the shell surface of the downwind tower are visualized on the model itself, which is covered with a special coating.

Assessment of the stress fields and natural frequencies. Aeroelastic models of 1/400 scale, made of gravity-fed, cold-cast epoxy resin are used for the tests.

Stresses are measured in the same wind tunnels on models fitted with inner and outer strain gauges. Conventional or semi-conductor strain gauges are used in which temperature compensation is provided when temperature control is inadequate in the wind tunnel. At the laboratory, the modal analysis of models subjected to harmonic vibration is based on both conventional accelerometer techniques and holographic interferometry which permits visualization of eigenmodes.

Failure tests. Aeroelastic models which are to undergo buckling tests are also equipped with a special device used to simulate the self-weight which is made up of more than 500-weights of 100 g hanging on to wires glued all over the inner surface of the shell (figure 2). The failure tests are performed in the ONERA "Office National d'Etudes et de Recherches Aérospatiales", pressurized wind tunnel F1 in Toulouse, which is maintained at a 4 bar pressure. The test section is 4.5 m wide and 3.5 m high. High speed films are made at a speed of 500 pictures per second to observe the collapse phenomenon.

Numerical means. Several finite-element codes have been used for the numerical computations in order to perform modal analysis, Eulerian buckling analysis, and to determine the stress fields under static loadings. These codes are the three-dimensional ASKA code, and two axisymmetric codes with five degrees of freedom which were developed at EDF : the so-called COQREV and CODEM codes.

3. WIND-LOADINGS.

Beside the Reynolds number - always above 10^8 - the characteristics of the pressure field are determined by two phenomena :

- the flow separation at the top of the tower partly determines the values of the mean pressure inside the tower, as well as outside in the wake area, since the ratio length over width of the tower, is not large.
As a result, the mean load is equal to zero all over the part of the shell which is in the wake,
- the large eddies within the atmospheric turbulence, with a size similar to that of the shell, determine the overall characteristics of the fluctuating pressure field around the tower and together with the three-dimensional character of the tower, hinder the formation of Von Karman vortex streets.

From one tower to another, the differences observed as regards wind-induced pressure fields will be minor and mainly due to :

- the changes in height, lessened by the constant value of H/D,
- the changes in surface condition(although roughness remains small),
- the environment and especially the downwind towers.

On the contrary, when the structure is in the wake of a cooling tower located upwind, the flows to which it is exposed have not the same characteristics as the wind, and very important perturbations are observed in that case in the induced pressure field.

3.1. The isolated tower.

The pressure field on the surface of an isolated tower may be divided into four areas. These four areas are shown in figures 3 and 4 (for ribbed cooling towers (table 2)) with the "in-situ" mean pressure values, the standard deviation and the spectrum. These areas (or zones) correspond to :

- (i) The upwind area ($0-70^\circ$) : the mean pressure varies with height as the mean wind and the fluctuating pressure has the same characteristics as the atmospheric turbulence (constant standard deviation). The fluctuation frequency range is however less wide.
- (ii) The minimum pressure and boundary layer separation area ($70-95^\circ$) : because the vortex shedding is well-correlated vertically, periodic fluctuations are observed in this area and measurements are quite dispersed in the minimum pressure area.
- (iii) The post-separation area ($95-125^\circ$) : this area, which is not readily affected by upwind flow parameters, is characterized by pressure fluctuations at relatively high frequencies.
- (iv) The wake area ($125-180^\circ$).

Note that the maximum pressures are recorded in the neck area of the tower.

3.2. Influence factors.

The following parameters have been found to influence the results.

Roughness. On the site, the surface roughness created by the ribs always remains slight. No important impact is therefore observed as the minimum of pressure is masked by the measurement dispersion and its favourable effect counteracted by the pressure gradient increase in the separation area.

In the wind tunnel, it is only when roughness elements are introduced all over the upwind part of the tower that real loads can be reproduced (figure 5).

Height increase. When height was increased from 128 m (Bugey) to 160 m (Cruas), no perceptible difference was noticed in the pressure fields : only the wind speed that must be taken into account in the design is increased.

Presence of towers downwind. When towers are located downwind, the pressure in the wake varies (decreases) and a slight decrease in the pressure minima is observed.

Interaction. Interaction phenomena can be shown by plotting the deflexion of the stagnation point as a function of the respective position of the towers (figure 6).

There are two types of interaction : (i) a strong interaction (area A, figure 6), determined by the angle between the axis of the towers and the mean direction of the wind, (ii) a slight interaction (area B, figure 6), determined by the distance.

In both cases, but to a lesser degree when the interaction is slight, a very important increase in the induced pressure fluctuations can be observed on the downwind tower and the pressure field is noticed to be asymmetrical.

As a result, dynamical stresses in the shell increase greatly (§ 5.1.).

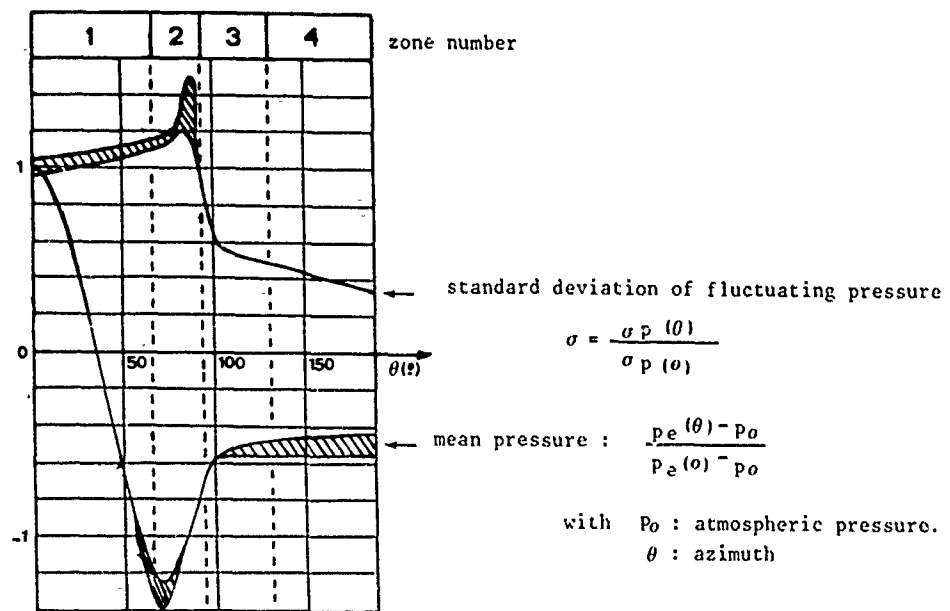


Figure 3. Pressure around isolated tower.

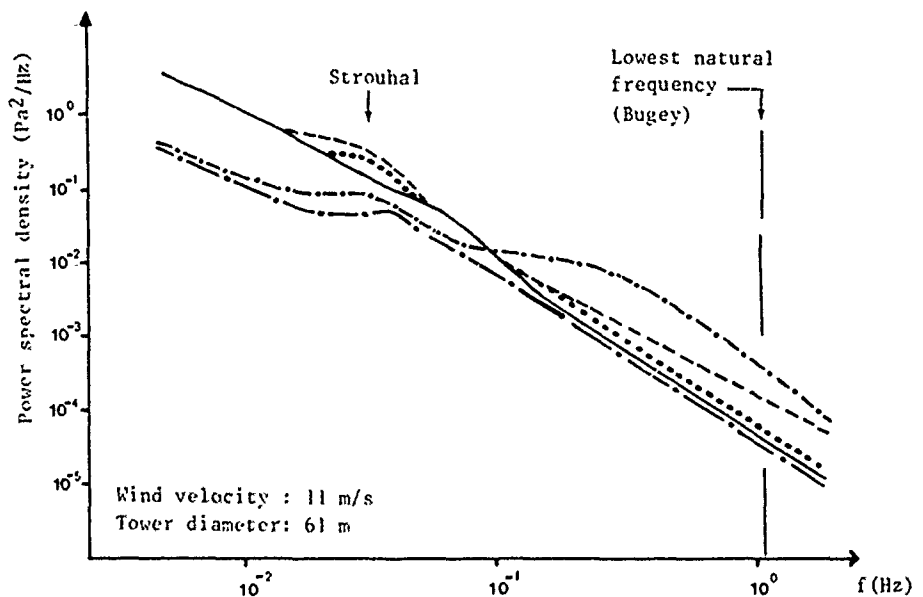
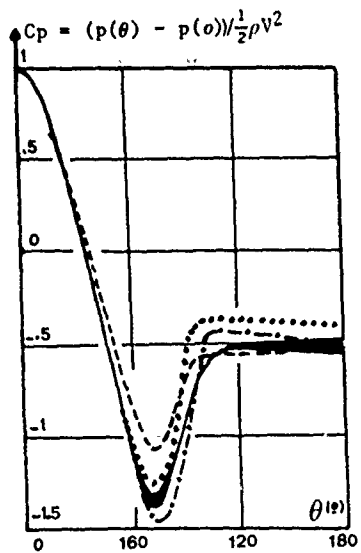


Figure 4. Pressure spectrum.

— Stagnation point	----- Separation (zone 2)
..... Maximum suction After separation (zone 3)
	— Wake (zone 4)



in-situ Bugey	Model 1/400 Onera	Model 1/400 CSTB	Model 1/400 VKI-Cruas
height of the tower			
128 m	505 mm	505 mm	387 mm
atmospheric boundary layer			
yes	not simulated	simulated	simulated
Reynolds number			
10^8	$4.3 \cdot 10^6$	$3.5 \cdot 10^5$	$5.3 \cdot 10^5$
Roughness			
RIBS 8cm thick 3cm wide angular spacing : 2.25°	NO RIBS SMOOTH	RIBS .5 mm thick 10 mm wide angular spacing: 5°	GRANULAR $500 \mu\text{m}$ along 55° from the stagnation point

Fig. 5. Comparison of pressure measurements around cooling towers (neck level).

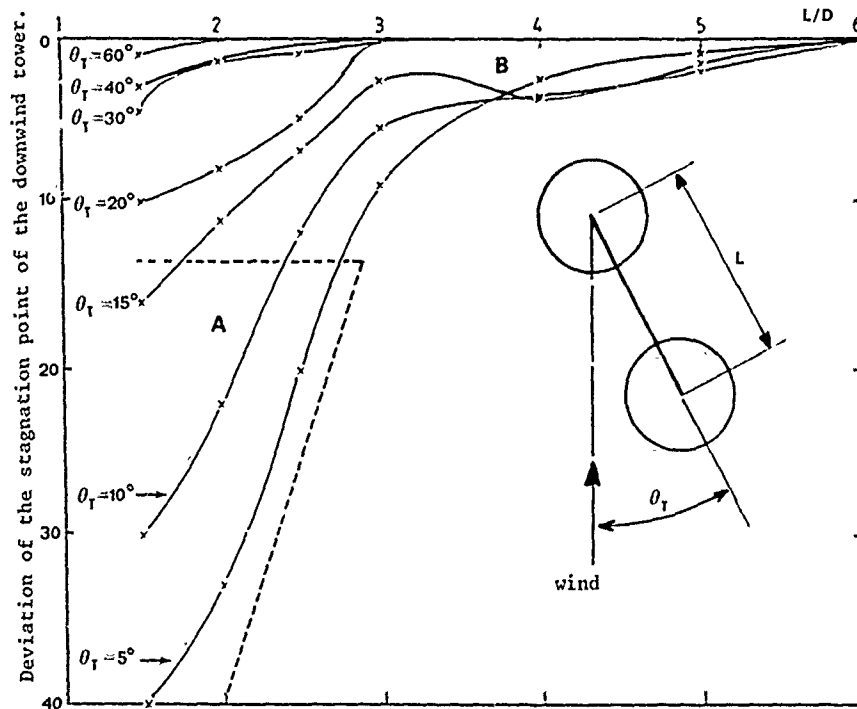


Fig. 6. Strong interaction (zone A), and weak interaction (zone B).

3.3. Analytical model.

The proposed model applies only to an isolated tower. For the mean pressure field, we have :

$$P_i(\theta, z) = P_i(z) = P_s$$

$$DP(\theta, z) = P_e(\theta, z) - P_i(z) = 1/2 \rho v_h^2 \frac{(DP(\theta, z))}{1/2 \rho v_h^2} y(\theta, z)$$

where : $y(\theta, z) = A(z) + B(z) [\sin(\theta, C(z))]$ $E(z)$ is independent of Reynolds number and wind characteristics.

with : P_i, P_e, P_s : internal, external and wake pressure.

ρ : air mass density.

v_h : wind speed at top level.

A, B, C, E : are linear functions of z .

For the fluctuating field, we have :

$$\sigma_p(\theta, z) = K(\theta) \times \rho V(z) \sigma_v(z)$$

where $K(\theta)$ assumes the values 1.3, 1.5, 0.85 and 0.5 in the four zones, at the neck in Bugey, with :

σ_p and σ_v : standard deviation of pressure and wind speed.
 $V(z)$: wind speed at the z -level.

and for the power spectral density of the pressure S_{pp} :

$$\frac{f \cdot S_{pp}(\theta, z, f)}{\sigma_p^2(\theta, z)} = g \left(\frac{f \cdot D(z)}{V(z)} \right)$$

with : $D(z)$: tower diameter, and g shown in figure 7.

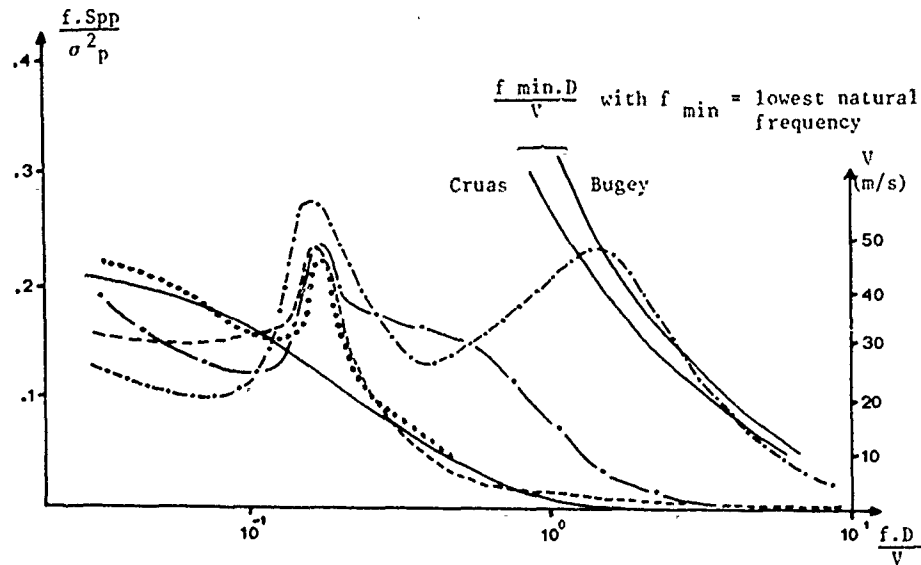


Fig. 7. Dimensionless pressure power spectral density (left and bottom scales)
Dimensionless natural frequency versus wind speed (bottom and right scales). (same legend as fig.4).

4 THE STRUCTURE.

The tower modal analysis program includes about twenty full-scale tests on five different sites, a dozen tests on aeroelastic models and a systematic computation for all towers.

The first eigenmodes correspond to mode shapes exhibiting two or three nodes along the generatrix, according to the type of upper ring provided, and generally 4 to 5 loops in the circumferential direction (mode shape of the type $\cos n\theta$, $n = 4$ or 5). Field measurements made on cooling towers 124-165 m high and 0.18-0.21 m thick at the neck provide values of the first natural frequency of the completed tower, which ranges from 0.82 to 1.27 Hz.

Some quantitative data concerning the influence of several parameters on the tower first natural frequency can be derived from the study.

Upper ring (Cruas)	+ 14 %
Slip forms (jumping beams)	- 4 %
Lower part reinforcement	Slight for V shaped diagonal support columns, strong for X shaped diagonal support columns.
Self weight	- 3 %
Concrete hardening (checked over time)	+ 1/100 Hz in the first four months Stable after one year.
Poisson's ratio	Variation below that of the $(1-\nu^2)^{-1/2}$ law

Table 3 : Variation of the first natural frequency with different parameters

The effect of the upper ring is determined from field measurements made before and after the ring was built (the result was corrected to counterbalance the influence of the slip forms). The impact of additional stiffening rings was tested by computation and on aeroelastic models. The impact of a ring in the lower part of the tower depends appreciably on the nature and flexibility of the support structures.

Rings with cross sections of a conventional type, when installed in places where the two loops of the first mode are recorded, contribute to increase the first two frequencies up to the level of the third.

The Poisson's ratio of the shell has a negligible influence on the first natural frequency. For the modes in which membrane energy is predominant (less circumferential harmonic waves than with lowest frequencies), an increase in the Poisson's ratio results in a slight decrease in the frequency. The opposite effect is obtained for modes in which bending prevails and, when loops are numerous, this effect approaches the $(1 - \nu^2)^{-1/2}$ law which applies to pure bending modes.

The ground elasticity in the vertical direction which has been demonstrated to prevail over horizontal and rotatory elasticities, results in a small decrease in the first natural frequency for hard soils : less than a 4 % decrease for soils with a vertical elasticity coefficient above 20 bars/cm, but 17 % for soils with an elasticity below 2 bars/cm.

The effect seems more pronounced on modes with few circumferential loops.

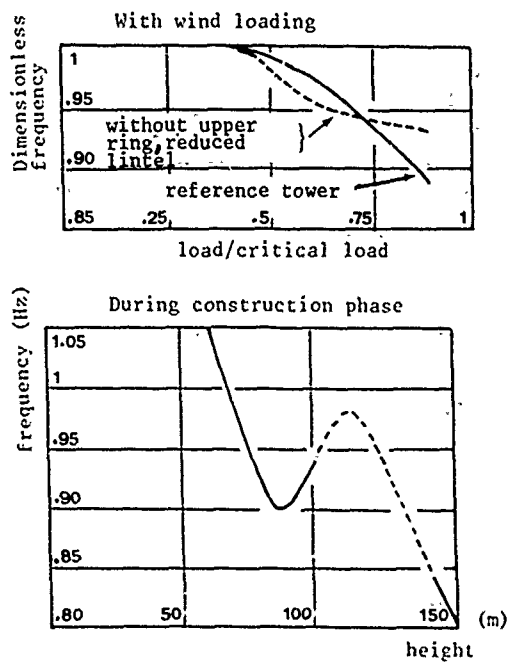


Fig. 8. Variation of the first natural frequency.

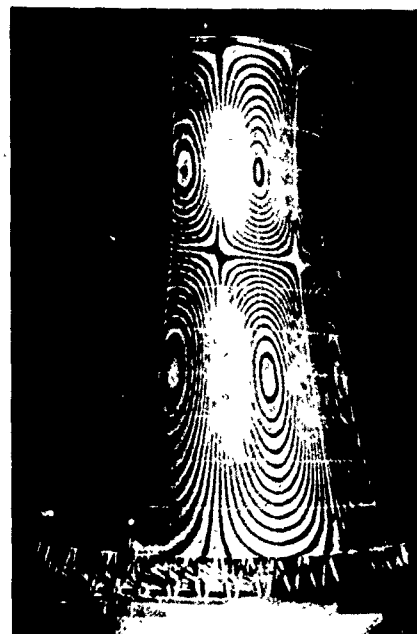


Fig. 9. Mode shape shown by holographic interferometry.

5. STUDY OF FAILURE INDUCING PHENOMENA.

5.1. Shell vibration.

To study the shell vibration as a function of tower configurations, aeroelastic models fitted with strain gauges (§ 2.2.) were placed in the boundary-layer wind tunnels at the C.S.T.B. in Nantes.

Stress field characteristics. (i) When the tower stands alone, the stress field is symmetrical. Static meridional stresses have the highest amplitude and they develop around the shell in the same way as the static pressure field. Circumferential stresses remain small (figure 10). Maximum static stresses are not influenced by the presence of upper rings or lintels. Dynamic stresses remain small at usual wind speeds and are not very likely to induce the shell vibration at its eigenmodes. The dynamic component increases with the wind speed and can become significant in the azimuth direction. (ii) When the tower stands among a group of towers, a double amplification of the stress field is observed (see figure 11).

- A static amplification due to accelerated flow areas which results in a significant assymmetry and high local maximum stresses.
- A dynamic one, always significant, can produce stress levels 3-6 times as high as those recorded in an isolated tower.

This amplification, though always significant, varies with the configuration of the towers grouping. It contributes to vibration induced fatigue of the veil.

Dynamic effect modelling and incorporation. According to their frequency range, pressure fluctuations acting upon the shell are known to produce either quasi-static or resonant stresses (figure 11).

- Quasi-static stresses are associated with slow displacements and are undergone by the shell as additional static stresses. Like static stresses, they vary as V^2 .
- Resonant stresses, which are strongly amplified when the tower vibrates at its natural frequencies, vary as V^6 but are equal to zero at usual wind speeds.

To take these various stresses into account, maximum 10 second values of the stress σ (θ, z, t) induced in the shell over a given time can be considered.

$$\sigma_{\text{MAX}} = \max_P \max_t \sigma(P, t) \quad \text{where MAX is the maximum value over the shell and}$$

$$\max_t \sigma(P, t) \quad \text{MAX is the maximum value in time.}$$

When the tower is not subjected to wind fluctuations, the maximum value of the stress equals the maximum static stress : the dynamic amplification factor is 1.

$$\sigma_{\text{MAX}} = \frac{\sigma}{P} \text{MAX}$$

When the tower is isolated and subjected to wind fluctuations, dynamic components in the stress modify and increase this maximum value. This amplification can be written as follows :

$$\sigma_{\text{MAX}} = (1 + (g_{QS} - 1) g_R) \frac{\sigma}{P} \text{MAX} = G \frac{\sigma}{P} \text{MAX}$$

Where g_{QS} and g_R are the quasi-static and resonant amplification coefficients respectively. They depend on the stress direction.

g_{QS} does not depend on the wind speed and its value is of the order of 1.3.

g_R is highly dependent on the wind speed and is equal to 1 at low wind speed. For instance :

$$\begin{array}{lll} \bar{V} = 25 \text{ m/sec} & G(Z) = 1.27 & G(\theta) = 1.33 \\ \bar{V} = 50 \text{ m/sec} & G(Z) = 1.31 & G(\theta) = 3.13. \end{array}$$

When the tower stands among a group of towers, an overall amplification coefficient is defined in the same way :

$$\sigma_{\text{MAX}} = I \cdot \frac{\sigma}{P} \text{MAX} \text{ (isolated)} = K \times G \times \frac{\sigma}{P} \text{MAX} \text{ (isolated).}$$

K is a static amplification factor accounting for the upwind flow acceleration and for separation areas. G is the dynamic amplification factor as defined above. Both factors are highly dependent on the configuration. Table (4) summarizes some values of G , K and I .

Configuration	Isolated			0°			1.5 D			15°			1.5 D			15°			3 D		
	K	G	I	K	G	I	K	G	I	K	G	I	K	G	I	K	G	I	K	G	I
Meridian	1	1.27	1.27	0.5	1.6	0.8	1.5	1.38	2.07	1.2	1.41	1.69									
Circumferential	1	1.54	1.54	1	1.98	1.98	2.2	1.94	4.27	1.9	1.94	3.69									

Table 4. Tensile stress amplification in case of interaction
for wind speed below 25 m/s.
K, G, I : static, dynamic and total factors.

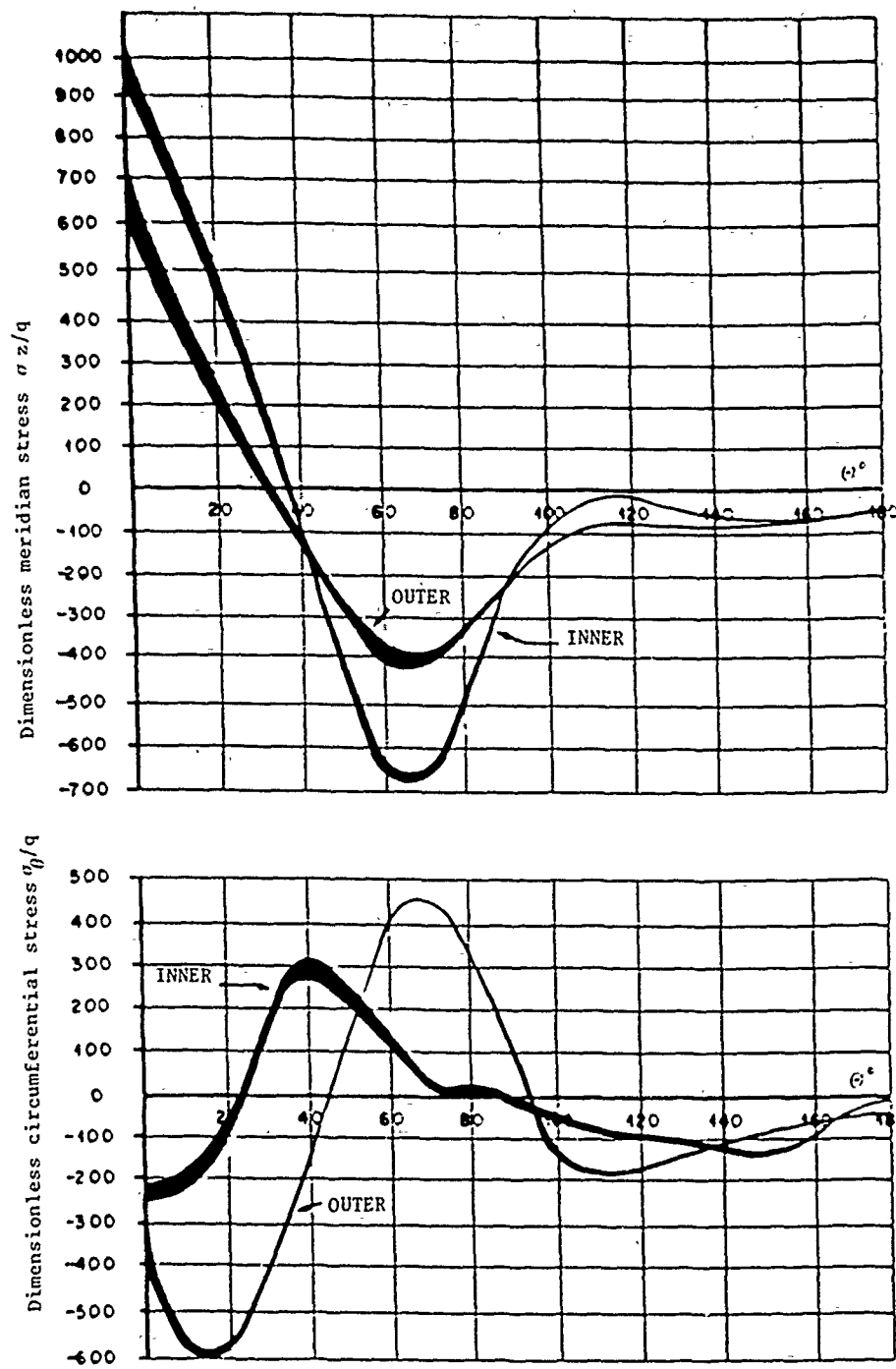


Fig. 10. Static stress. Isolated tower $z/H = 0.48$
 q : dynamic pressure at neck level.

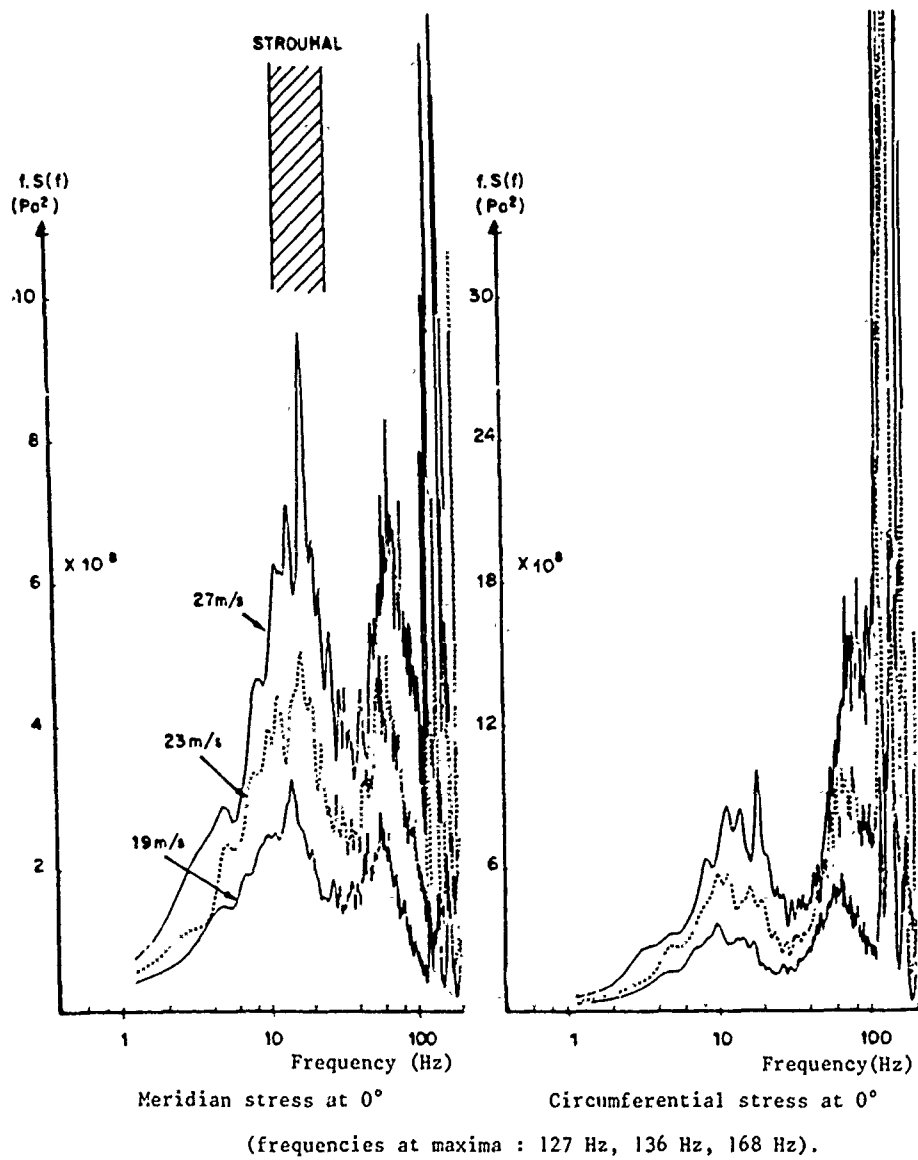


Fig. 11. Stress spectrum, recorded on aeroelastic model.

Interaction : $L = 1.5 D$
 $\theta_T = 15^\circ$

5.2. Instability.

The tower instability is studied by making failure tests on models placed in wind tunnels. Our aim is to study the static buckling of the tower by precisely modelling the geometry and the wind+weight loading and to obtain reference values against which to validate numerical models.

The atmospheric boundary layer is not modelled and the upwind turbulence level is reduced to a minimum (<0.1 %) in order to emphasize static buckling as opposed to other failure modes (fatigue failure...).

Results are obtained in terms of loadings leading to the model failure, and the impact on critical loadings of reinforcements and tower configuration is determined.

Table 5. Experimental critical loads.

q_{cr} : critical dynamic pressure
 ρ_s : structure mass density (simulated)
 E : Young's modulus
 H : height of the tower
 g : gravity acceleration.

		Normalized experimental critical load	
		Weight $\rho_s gH$ E	Wind q_{cr} E
Isolated tower	Reference tower	1.17×10^{-4}	11×10^{-7}
	Tower with wide lintel	"	11×10^{-7}
	Tower with 2 additionnal rings	"	12×10^{-7}
	Tower with half weight	5.85×10^{-5}	97×10^{-8}
	Tower with reduced lintel	1.17×10^{-4}	65×10^{-8}
	Tower with reduced lintel and no weight	0	50×10^{-8}
	Tower with reduced lintel and without upper ring	1.17×10^{-4}	59×10^{-8}
Interaction	Reference tower : 0° 1.5 D	"	14×10^{-7}
	Reference tower : 15° 1.5 D	"	96×10^{-8}
	Reference tower : 15° 3 D	"	94×10^{-8}

A numerical study must be made prior to applying these results to real cooling towers. As a matter of fact, direct extrapolation to full-scale structures is difficult since the laws governing the behaviour of reinforced concrete and epoxy resins are different and the atmospheric boundary layers as well as the upwind turbulence are not modelled.

Visualization reveals that the veil vibrates at high wind speeds as confirmed by the readings of accelerometers. Failure modes, which cannot be always easily characterized begin with a depression, or a crack in an area of the shell which depends on configuration (7). The reproducibility of critical loadings is tested for 7 out of the 10 configurations studied. An attempt to determine the phenomenon responsible for the collapse of the towers is made by comparing experimental data with numerical values derived from both Eulerian buckling and non linear computations. Another indication is given by the analysis of the stress level in the reference tower model, (isolated configuration), at the moment of the failure. It is assessed by a conventional static computation and augmented to take dynamic effects into account, and it seems to rule out the hypothesis of ultimate stress failure and fatigue failure.

This study is still to be supplemented by further analysis and computations.

6. CONCLUSION.

The purpose of this paper is the presentation of the different methods, mainly experimental, developed by E.D.F. to determine the real wind-induced effects in high cooling towers.

These studies were first devoted to isolated towers. In a second stage, the emphasis was put on interaction effects analysis.

Reference data have been collected through an important programme of full scale measurements, supplemented by model tests in wind tunnels. The general outlines of the results are given in this paper. Interaction configuration of the towers is shown to be an important factor to be considered, as opposed to isolated configuration.

The significant effects that may result from critical interactions are mainly :

- an increase in pressure fluctuations applied to the shell, and the asymmetry of the pressure field,

- the static and dynamic amplification of the stresses induced in the structure,

- a change of instability phenomena and of related critical loads (analysis still in progress).

Some of the outcomes derived from these studies can be directly applied to tower design and construction.

REFERENCES.

1. Niemann, H.J. and Ruhwedel, J., "Full scale and model tests on wind induced, static and dynamic stresses in cooling tower shells", Eng. Struct. Vol. 2 April 1980.

2. Scanlan, R.H. and Sollenberger, N.J., "Pressure difference across the shell of a hyperbolic natural draft cooling tower", "4th International Conference on Wind Effects on Buildings and Structures", London 1975.

3. Niemann, H.J., "On the stationary wind loading of axisymmetric structures in the transcritical Reynolds number region", Report n° 71-2 March 1971, Institut für Konstruktiven Ingenieurbau, Ruhr Universität, Bochum.

4. Sageau, J.F. and Grovalet, Y., "Mean wind loading and stresses on cooling tower shell", Société hydrotechnique de France, XVIe Journées de l'Hydraulique, Paris, 16-17-18 Sept. 1980, Question II, rapport 4.

5. Sageau, J.F. and Auclair, D., "Some aspects of the dynamic action of wind on cooling towers shells", Société hydrotechnique de France, XVIe journées de l'Hydraulique, Paris 16-17-18 Sept. 1980, Question II, rapport 5.

6. Sageau, J.F. "Characterization of average and fluctuating pressure fields on the surface of large air-air heat-exchangers", La Houille Blanche, N° 1/2-1980.

7. E.D.F. film, "For a few meters more", (12 minutes), SODEL.

DYNAMICAL BEHAVIOR OF SUSPENDED PIPE IN THE SEA

T. Kawashima and T. Shimogo
Department of Mechanical Engineering
Faculty of Science and Technology
Keio University
Yokohama, Japan

ABSTRACT

The dynamical behavior of a long pipe, which is vertically suspended in the sea water by a single-moored-buoy, was analysed, and the dynamical stability of the pipe excited by a random motion of the buoy was examined in a theoretical manner. In this study, an analytical model of the pipe is constructed from several rigid pipe sections, which are serially linked by universal joints. As a result of this study, the influences of the number of pipe sections, the total length of the pipe system, the steady current of the sea water, the flow speed in the pipe, the power spectral density of the heaving motion of the buoy, the natural frequency of the pipe system and the dynamical properties of universal joints upon the covariance stability of lateral displacement of the pipe system were clarified by the simplified analytical model.

1. INTRODUCTION

A long pipe vertically suspended in the sea is usually available to take deep sea water and resources, especially used as a cold water pipe at the ocean thermal energy conversion plant and other facilities of offshore structures. When a pipe is suspended by a single-moored-buoy, the random motion of the buoy, excited by sea waves, gives a bending vibration to the suspended pipe. A vertical motion of the buoy may be the cause of instability in the pipe motion in some situations.

Several analytical methods have been developed during past few years to predict the hydroelastic response of suspended long pipes in the ocean environment. Paulling, J. R.[1],[2], Chou, D. Y., et al.[3], and Chang, P. Y.[4] studied coupled responses of the OTEC cold water pipe and platform to ocean currents and random sea waves by using of two-dimensional beam theory, and some of them used an equivalent linearization technique based on statistics of the random response to approximate the nonlinearities associated with the pipe damping due to fluid drags. In these analyses, computer programs were developed by using the finite element method or the transfer matrix method.

On the other hand, Iso, S., et al.[5] treated the same response problems in continuous elastic pipes in a theoretical manner, and recently Chung, J. S., et al.[6] examined the axial stretching oscillation of the long vertical pipe.

If the pipe is constructed from several rigid pipe sections serially linked by universal joints, it has a very low bending stiffness as compared with the

continuous elastic pipe. In such an articulated pipe, the bending stress produced in each pipe section is reduced and the requirement of the pipe strength is alleviated. In the articulated pipe, however, stability problems are particularly important due to the low flexibility of the pipe. Paidoussis, M. P., et al.[7] studied a stability of the articulated pipe conveying fluid, but an instability produced by a vertical motion of the pipe supporting point are not treated so far.

This study intends to provide stability conditions of the suspended articulated pipe, which is vertically excited by a heaving motion of a buoy. A simple analytical model is formulated on the assumptions of the two-dimensional motion of the pipe, small lateral displacement of the pipe, and so on. The critical power spectral density and its frequency on the covariance stability are found by two methods. The one is the application of the covariance equation for Gaussian white noise input, and the other is the application of the perturbation technique to the statistical moment equation, which is derived on the assumption of uncoupled modes of the pipe, for the colored noise input. The influences of the number of pipe sections, the total length of the pipe system, the steady current of the sea water, the flow speed in the pipe, the power spectral density of the heaving of the buoy, the natural frequency of the pipe system and the dynamical properties of the universal joints upon the covariance stability of lateral displacement of the pipe system are examined.

2. ANALYTICAL MODEL

2.1 Assumptions

The scheme of the analytical model of the buoy and the pipe system are shown in Fig.1. To simplify a theoretical treatment, the analytical model is formulated on the following assumptions:

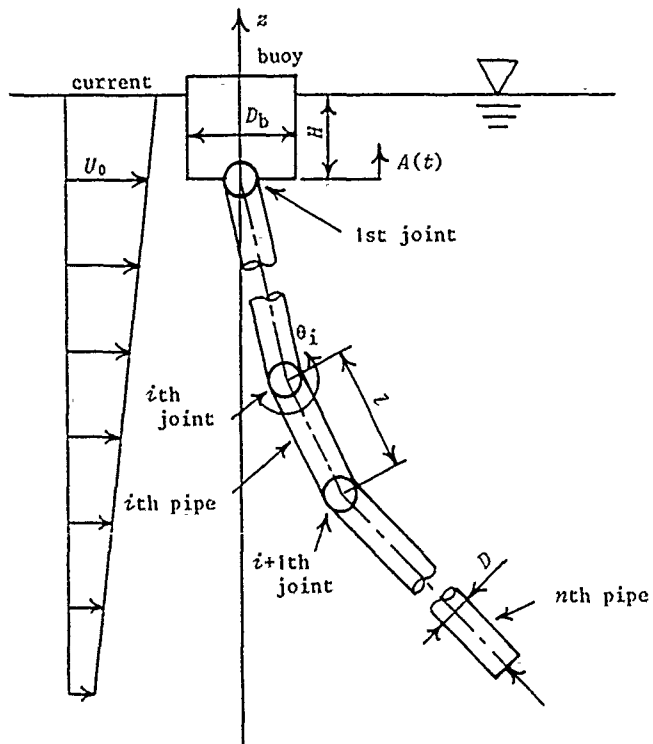


Fig.1 Analytical model

(1) The pipe system is constructed from n sections of pipes, which are serially linked by universal joints, and every pipe section has a uniform cross section and the same length, and make the two-dimensional movement in the vertical plane.

(2) Every universal joint has a concentrated mass and a damping being proportional to the relative rotation velocity.

(3) The steady current of the sea water decreases linearly with the sea depth, and the static displacement of the pipe in the horizontal direction caused by the steady current is relatively small compared with the pipe length.

(4) The dynamical lateral displacement of the pipe around the static equilibrium position is much smaller than the static displacement, and does not affect a motion of the buoy.

(5) The upward flow speed in the pipe is constant.

(6) The sea wave is given by linear wave theory at the deep sea.

(7) The effects of a fluid motion caused by the wave on the pipe are neglected.

(8) The buoy is shaped as a circular cylinder, with vertical axis, and is symmetrically moored. The buoy moves only in the vertical direction, under wave excitation, i.e., only the heaving motion is taken into account, and the effects of sway and roll are neglected.

(9) The heaving motion of the buoy is relatively small and the effects of the mooring are neglected.

2.2 Buoy

From assumptions (6), (8) and (9), the equation of heaving motion $A(t)$ of the buoy is given as follows:

$$(m_b + m_w)\ddot{A}(t) + c_w\dot{A}(t) + k_w A(t) = \rho_w(\pi D_b^2/4)\partial\phi(z, t)/\partial t|_{z=-H} + m_w\partial^2\phi(z, t)/\partial t\partial z|_{z=-H}, \quad (1)$$

where m_b = mass of the buoy, D_b = diameter of the buoy, H = draft of the buoy, ρ_w = density of the sea water, $m_w = \rho_w(\pi/12)D_b^3$ = added mass of the sea water, $k_w = \rho_w g(\pi D_b^2/4)$ = restoring coefficient of buoyancy, $\phi(z, t) = -(ag/\omega)\exp(\omega^2 z/g)\sin(\omega t)$ = velocity potential for the sea wave, (a = wave amplitude, g = gravitational acceleration, ω = angular frequency), c_w = damping coefficient related to heaving motion, which is approximately proportional to the angular frequency ω .

2.3 Pipe

From assumptions (1), (2), (3), (4), (5) and (7), the equation of lateral motion of the pipe system is given as follows:

$$[M]\{\ddot{\theta}(t)\} + [C]\{\dot{\theta}(t)\} + ([K] + \ddot{A}(t)[K_A])\{\theta(t)\} = \{0\}, \quad (2)$$

where $\{\theta(t)\} = \{\theta_i(t)\}$ ($i=1, 2, \dots, n$), $\theta_i(t)$ = an angular displacement of the i th pipe section from the static equilibrium position, $[M]$ = mass matrix including added mass of water, $[C]$ = damping matrix including fluid drag force, damping at the universal joints, and Coriolis force by internal flow, $[K]$ = stiffness matrix including gravitational force, buoyancy, momentum change of internal flow at the universal joints, $[K_A]$ = mass matrix of parametric excitation. The right hand side of equation (2) is not $\{0\}$, if the static equilibrium displacement of the pipe is not zero. However, the nonhomogeneous term of $\{\theta(t)\}$ can be neglected, if only the stability condition is examined.

The expression of $[M]$, $[C]$, $[K]$ and $[K_A]$ are given as follows:

$$[M] = \begin{bmatrix} M_{i,k} (k < i) & = (\rho_p + \rho'_p)l^3(n-i+1/2) + ml^2(n-i) \\ M_{i,i} & = (\rho_p + \rho'_p)l^3(n-i+1/3) + ml^2(n-i) \\ M_{i,k} (i < k) & = (\rho_p + \rho'_p)l^3(n-k+1/2) + ml^2(n-k) \end{bmatrix}, \quad (1 \leq i, k \leq n) \quad (2a)$$

$$[C] = \begin{bmatrix} C_{i,k} (k < i) & = C_D \rho_w D l^3 \{U_2(i) + \sum_{j=i+1}^n U_1(j)\} - \delta_{i-1,k} c \\ C_{i,i} & = C_D \rho_w D l^3 \{U_3(i) + \sum_{j=i+1}^n U_1(j)\} - (2 - \delta_{i,n}) c - \rho_w (\pi/4) d^2 v_p l^2 \\ C_{i,k} (i < k) & = C_D \rho_w D l^3 \{U_2(k) + \sum_{j=k+1}^n U_1(j)\} - \delta_{i+1,k} c - 2 \rho_w (\pi/4) d^2 v_p l^2 \end{bmatrix},$$

$$U_1(i) = U_0 - \alpha(i-1/2)l, \quad U_2(i) = \{U_0 - \alpha(i-1/3)l\}/2, \quad U_3(i) = \{U_0 - \alpha(i-1/4)l\}/3,$$

(1 $\leq i, k \leq n$) (2b)

$$[K] = \begin{bmatrix} K_{i,k} (k < i) & = 0 \\ K_{i,i} & = w_p l^2/2 + (n-i)(w_p l^2 + mg l) - (1 - \delta_{i,n}) \rho_w (\pi/4) d^2 v_p^2 l \\ K_{i,k} (i < k) & = \delta_{k,n} \rho_w (\pi/4) d^2 v_p^2 l \end{bmatrix},$$

(1 $\leq i, k \leq n$) (2c)

$$[K_A] = \begin{bmatrix} K_{Ai,k} (k < i) & = 0 \\ K_{Ai,i} & = (\rho_p + \rho'_p) l^2/2 + (n-i)(\rho_p l^2 + m l) \\ K_{Ai,k} (i < k) & = \rho'_p l^2 \end{bmatrix},$$

(1 $\leq i, k \leq n$) (2d)

where ρ_p = mass of the pipe including internal water per unit length, ρ'_p = added mass of water to the pipe per unit length, w_p = gravity of the pipe in water per unit length, l = length of each pipe section, m = concentrated mass at the universal joint, c = rotational damping coefficient at the universal joint, D = outer diameter of the pipe, d = inner diameter of the pipe, v_p = flow velocity in the pipe, C_D = fluid drag coefficient of the pipe, U_0 = horizontal steady current velocity at the top of the pipe system, α = proportionality constant for the current velocity $U = U_0 - \alpha h$ (h = depth from the top of the pipe system), $\delta_{k,n}$ = Kronecker delta.

Equation (2) is rewritten by multiplying $[M]^{-1}$, that is

$$\{\ddot{\theta}(t)\} + [C']\{\dot{\theta}(t)\} + ([K'] + \ddot{A}(t)[K_A])\{\theta(t)\} = \{0\},$$
(3)

where $[C'] = [M]^{-1}[C]$, $[K'] = [M]^{-1}[K]$, $[K_A] = [M]^{-1}[K_A]$. Furthermore the above equation is reduced to the equation of state vector

$$\frac{d}{dt} \left\{ \begin{bmatrix} \theta(t) \\ \dot{\theta}(t) \end{bmatrix} \right\} = \left(\begin{bmatrix} [0] & [I] \\ [-[K'] - [C']] & [0] \end{bmatrix} + \ddot{A}(t) \begin{bmatrix} [0] & [0] \\ [-[K'_A]] & [0] \end{bmatrix} \right) \left\{ \begin{bmatrix} \theta(t) \\ \dot{\theta}(t) \end{bmatrix} \right\}.$$
(4)

3. COVARIANCE EQUATION FOR GAUSSIAN WHITE NOISE INPUT

Assuming that the heaving acceleration of the buoy $\ddot{A}(t)$ is Gaussian white noise, equation (4) can be regarded as a random differential equation of Ito's type, so that the covariance equation of the angular displacement $\theta_i(t)$ and velocity $\dot{\theta}_i(t)$ of the pipe is obtained as follows:

$$\frac{d}{dt} \{V(t)\} = \begin{bmatrix} [0] & [I] + [\alpha] & [0] \\ [\beta] & [\beta'] & [I] \\ [Y_G] & [Y_A] + [Y_B] & [Y'_A] + [Y'_B] \end{bmatrix} \{V(t)\},$$
(5)

where $\{V(t)\} = \begin{Bmatrix} \{E[\theta_i \theta_j]\} \\ \{E[\theta_i \dot{\theta}_j]\} \\ \{E[\dot{\theta}_i \dot{\theta}_j]\} \end{Bmatrix}$, $(1 \leq i, j \leq n)$

$$[\alpha] = [\alpha_{i,j}] = [\delta_j, i - ((i-1)/n)n-1, n + ((i-1)/n)+1],$$
(1 $\leq i, j \leq n^2$)

$$[\beta] = [\beta_{i,j}] = [-\delta_j, ((i-1)/n)n+k, i - ((i-1)/n)n, k],$$
(1 $\leq i, j \leq n^2, 1 \leq k \leq n$)

$$[\beta'] = [\beta'_{i,j}] = [-\delta_j, ((i-1)/n)n+k, C'_{i - ((i-1)/n)n, k}],$$
(1 $\leq i, j \leq n^2, 1 \leq k \leq n$)

$$\begin{aligned}
[\gamma_A] &= [\gamma_{Ai,j}] = [-\delta_{j,i-((i-1)/n)n+(k-1)n}^{K'}((i-1)/n)+1,k] , \quad (1 \leq i, j \leq n^2, 1 \leq k \leq n) \\
[\gamma'_A] &= [\gamma'_{Ai,j}] = [-\delta_{j,i-((i-1)/n)n+(k-1)n}^{C'}((i-1)/n)+1,k] , \quad (1 \leq i, j \leq n^2, 1 \leq k \leq n) \\
[\gamma_B] &= [\gamma_{Bi,j}] = [-\delta_{j,((i-1)/n)+1+(k-1)n}^{K'}i-((i-1)/n)n,k] , \quad (1 \leq i, j \leq n^2, 1 \leq k \leq n) \\
[\gamma'_B] &= [\gamma'_{Bi,j}] = [-\delta_{j,((i-1)/n)+1+(k-1)n}^{C'}i-((i-1)/n)n,k] , \quad (1 \leq i, j \leq n^2, 1 \leq k \leq n) \\
[\gamma_G] &= [\gamma_{Gi,j}] = [(1+\delta_{((i-1)/n)+1,i-((i-1)/n)n})^{(2/n)S_0K'}_{Ai-((i-1)/n)n,j-((j-1)/n)n}] , \quad (1 \leq i, j \leq n^2)
\end{aligned}$$

and S_0 = power spectral density of the heaving acceleration of the buoy. Unless the subscript $(i-1)/n$ or $(j-1)/n$ is an integer, omit the figure below decimals.

Since the covariance equation was reduced to a 1st order differential equation with constant coefficients, the stability of the covariance is investigated by solving the eigenvalue problem of the coefficient matrix, that is, the condition that every real part of eigenvalue is negative is the stability condition for the covariance of the dynamical displacement of the pipe.

4. EQUATION OF STATE FOR COLORED NOISE INPUT

4.1 Power Spectral Density of Input

When the heaving acceleration of the buoy $\ddot{A}(t)$ is Gaussian colored noise, the ISSC power spectral density function with the significant wave height $h_{1/3}$ and the characteristic wave period T_1 is used as a typical power spectral density of the sea wave height, that is

$$S_w(\omega) = (A/\omega^5) \exp(-B/\omega^4) , \quad \text{in } \text{m}^2/\text{s} , \quad (\omega \geq 0) \quad (6)$$

where $A = 173h_{1/3}^2/T_1^4$ in m^2/s^4 , $B = 691/T_1^4$ in s^{-4} . In Fig.2, the power spectral density of the sea wave is shown for $T_1 = 11$ s, $h_{1/3} = 11$ m.

From equation (1), a frequency response function of the heaving displacement of the buoy to the sea wave height is

$$H(\omega) = \frac{-(m_b\omega^2 + \rho_w g \pi D_b^2/4) \exp(-\omega^2 h/g)}{-(m_b + m_w)\omega^2 + i c_w \omega + k_w} , \quad i = \sqrt{-1} . \quad (7)$$

As a numerical example, the values of parameters indicated in Table 1 are used to calculate equation (7), and the gain $|H(\omega)|$ is plotted against $T = 2\pi/\omega$ in Fig.3.

The power spectral density of the heaving acceleration of the buoy is given by the expression

$$S_{\ddot{A}}(\omega) = \omega^4 |H(\omega)|^2 S_w(\omega) , \quad (\omega \geq 0) . \quad (8)$$

A numerical example of $S_{\ddot{A}}(\omega)$ calculated for the parameters in Table 1 is shown as a solid line in Fig.4.

In order to determine a shaping filter as a simple transfer function, equation (8) is approximated by the expression

$$S_{\ddot{A}}(\omega) = C_1 \omega^2 / (\omega^4 + C_2 \omega^2 + C_3) , \quad (\omega \geq 0) . \quad (9)$$

To fit equation (9) to the result given by a solid line in Fig.4, parameters C_1 , C_2 and C_3 are selected as follows: $C_1 = 1/9 \text{ m}^2/\text{s}$, $C_2 = -0.5458 \text{ s}^{-2}$, $C_3 = 0.08037 \text{ s}^{-4}$. The approximated result given by equation (9) is shown as a broken line in Fig.4.

If the shaping filter corresponding to the power spectral density of heaving motion of the buoy is determined and an augmented system including the shaping filter is introduced, then the system is formulated by the stochastic differential equation with a white noise input.

Table 1. Typical numerical example (1MW OTEC Plant)

Pipe	outer diameter $D = 1.845$ m inner diameter $d = 1.8$ m number of the pipe sections $n = 2$ length of the pipe section $l = 400$ m	mass per unit length $\rho_{\text{pipe}} = 986$ kg/m mass of the universal joint $m = 9860$ kg damping of the universal joint $c = 0$ flow velocity in the pipe $v_p = 1$ m/s
Buoy	diameter $D_b = 10$ m draft $H = 28$ m mass $m_b = 2260$ t damping coefficient $c_w = 680\omega$ kg/s	including mass of the pipe
Current	current velocity at the top of the pipe system $U_0 = 0.5$ m/s proportionality constant $\alpha = 0.3125 \times 10^{-3}$ s ⁻¹ density of the sea water $\rho_w = 1027$ kg/m ³	
Wave	characteristic period $T_1 = 11$ s significant height $h_{1/3} = 11$ m	

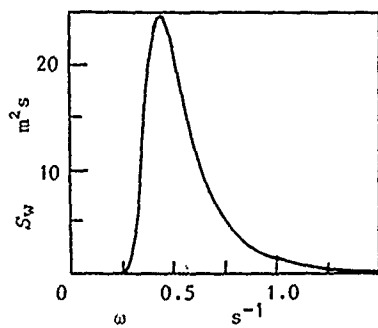


Fig.2 ISSC wave power spectral density

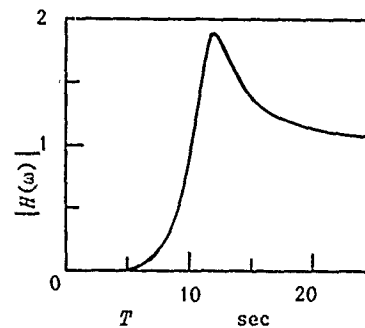


Fig.3 Gain of transfer function of buoy

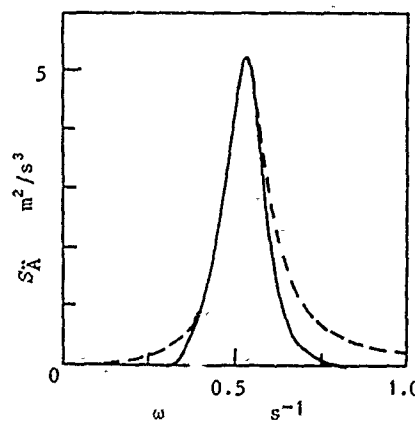


Fig.4 Power spectral density of heaving acceleration of buoy
(—:exact, - - -:approximate)

4.2 Equation of State

A covariance equation of the response will be very complex in the case of a colored noise input, because the term of parametric excitation in the equation of state becomes nonlinear. Therefore, the equation of motion (3) is approximately separated into n uncoupled equations by the disregard of coupled terms, in order to apply the modal analysis. As a result of the approximation, the covariance equation for each mode is established and the stability condition for each mode is obtained by the perturbation technique under the assumption of small nonlinearity[8].

In order to apply modal analysis, the eigenvalue problem is first solved in the case of no damping and no parametric excitation in equation (3), and then the modal matrix $[\Phi]$ is applied to diagonalize the stiffness matrix $[K']$ in equation (3). The matrices of damping and parametric excitation are approximated by the disregard of coupled terms, and the equation for each mode $\theta_i(t)$ is found to be as follows:

$$\ddot{\theta}_i(t) + C''_{i,i} \dot{\theta}_i(t) + (K''_{i,i} + \ddot{A}(t)K''_{A,i,i})\theta_i(t) = 0, \quad (i=1,2,\dots,n) \quad (10)$$

where $C''_{i,i}$, $K''_{i,i}$ and $K''_{A,i,i}$ are diagonal elements of $[\Phi]^{-1}[C'][\Phi]$, $[\Phi]^{-1}[K'][\Phi]$ and $[\Phi]^{-1}[K'][\Phi]$, respectively.

5. STABILITY FOR GAUSSIAN COLORED NOISE INPUT

5.1 Moment Equation

Now we consider a stability problem of covariance of a function satisfying a differential equation

$$\ddot{y}(t) + 2\xi\omega_n\dot{y}(t) + \{\omega_n^2 + \epsilon_0 x(t)\}y(t) = 0, \quad (11)$$

where a parametric excitation $x(t)$ has a power spectral density

$$S_x(\omega) = (\sigma^2/\pi) \sum_{k=0}^p \beta_k (i\omega)^{p-k} / \sum_{j=0}^q \alpha_j (i\omega)^{q-j} |^2, \\ \sigma = \text{constant}, \quad \alpha_0 = \beta_0 = 1, \quad q > p, \quad (\omega \geq 0) \quad (12)$$

The function $x(t)$ is given as a function satisfying a differential equation

$$x^{(q)}(t) + \alpha_1 x^{(q-1)}(t) + \dots + \alpha_q x(t) \\ = \sigma \{ \dot{B}^{(p)}(t) + \beta_1 \dot{B}^{(p-1)}(t) + \dots + \beta_p \dot{B}(t) \}, \quad (13)$$

where $\dot{B}(t)$ is Gaussian white noise with mean zero and autocorrelation function $\delta(t)$ (= Dirac delta function). Equation (13), which represents a shaping filter giving a parametric excitation $x(t)$, is rewritten as an equation of state vector

$$d\{X_1(t)\}/dt = \{A\}\{X_1(t)\} + \{B\}\dot{B}(t), \quad (14a)$$

$$x(t) = \{C\}^T \{X_1(t)\}, \quad (14b)$$

where $\{X_1(t)\} = \{x'(i-1)(t)\}$, $1 \leq i \leq q$; $x'(t)$ = solution of equation (13), and only $\sigma\dot{B}(t)$ remains on the right hand side; also

$$\{A\} = \begin{bmatrix} 0 & 1 & \dots & 0 \\ \vdots & \vdots & \ddots & \vdots \\ \vdots & \vdots & \ddots & \vdots \\ 0 & 0 & \dots & 1 \\ -\alpha_q & -\alpha_{q-1} & \dots & -\alpha_1 \end{bmatrix}, \quad \{B\} = \begin{Bmatrix} 0 \\ \vdots \\ 0 \\ \sigma \end{Bmatrix}, \quad \{C\} = \begin{Bmatrix} \beta_p \\ \beta_{p-1} \\ \vdots \\ \beta_0 \\ 0 \\ \vdots \\ 0 \end{Bmatrix}.$$

Reducing the coefficient matrix in equation (14) to a diagonal matrix, we have

$$\begin{aligned} d\{X_2(t)\}/dt &= [T]^{-1}[A][T]\{X_2(t)\} + [T]^{-1}[B]\dot{B}(t) \\ x(t) &= [C]^T[T]\{X_2(t)\} = \sum_{i=0}^p \beta_{p-i} \sum_{i=1}^q \lambda_i^1 x_i''(t) \end{aligned} \quad (15)$$

where $\{X_2(t)\} = \{x_i''(t)\}$, $1 \leq i \leq q$,

$$[T]^{-1}[A] = \begin{bmatrix} \lambda_1 & 0 \\ \vdots & \ddots \\ 0 & \lambda_q \end{bmatrix}, \quad [T] = \begin{bmatrix} 1 & 1 & \cdots & 1 \\ \lambda_1^2 & \lambda_2^2 & \cdots & \lambda_q^2 \\ \lambda_1^3 & \lambda_2^3 & \cdots & \lambda_q^3 \\ \vdots & \vdots & \ddots & \vdots \\ \lambda_1^{q-1} & \lambda_2^{q-1} & \cdots & \lambda_q^{q-1} \end{bmatrix},$$

and λ_i = roots of characteristic equation of $[A]$, i.e., functions of α_j ($j=1, 2, \dots, q$).

Similarly, replacing equation (11) by a state equation and reducing its coefficient matrix to a diagonal matrix, we have

$$\frac{d}{dt}\{y_1(t)\} = \left(\begin{bmatrix} v_1 & 0 \\ 0 & v_2 \end{bmatrix} + (i\epsilon_0 x(t)/2\omega_n') \begin{bmatrix} 1 & 1 \\ -1 & -1 \end{bmatrix} \right) \{y_1(t)\}, \quad (16)$$

where $v_{1,2} = (-\zeta \pm i\sqrt{1-\zeta^2})\omega_n$, $\omega_n' = \omega_n\sqrt{1-\zeta^2}$.

Therefore, the stochastic differential equations in our problem are formulated from equations (15) and (16) as follows:

$$\left. \begin{aligned} \dot{y}_1(t) &= v_1 y_1(t) + (i\epsilon_0/2\omega_n') \sum_{i=0}^p \sum_{j=1}^q \lambda_i^1 x_i''(t) \{y_1(t) + y_2(t)\}, \\ \dot{y}_2(t) &= v_2 y_2(t) - (i\epsilon_0/2\omega_n') \sum_{i=0}^p \sum_{j=1}^q \lambda_i^1 x_i''(t) \{y_1(t) + y_2(t)\}, \\ \dot{x}_i''(t) &= \lambda_i x_i''(t) + (\Delta_{q,i}/\Delta_T) \sigma \dot{B}(t), \quad (1 \leq i \leq q), \end{aligned} \right\} \quad (17)$$

where Δ_T = determinant of matrix $[T]$, $\Delta_{q,i}$ = cofactor determinant of (q,i) element of matrix $[T]$.

From equation (17), the moment equations for $y_1(t)$, $y_2(t)$ and $x_i''(t)$ ($i=1, 2, \dots, q$) are obtained, that is

$$\begin{aligned} (1/2\omega_n') d\{m_{k_1, \dots, k_q}(t)\}/dt &= [A_{k_1, \dots, k_q}] \{m_{k_1, \dots, k_q}(t)\} \\ &+ \epsilon [R] \sum_{i=1}^q \sum_{j=1}^p \beta_{p-i} \lambda_i^1 \{m_{k_1, \dots, k_{i+1}, \dots, k_q}(t)\} \\ &+ (\sigma^2/4\omega_n' \Delta_T^2) \left[\sum_{i=1}^q k_i (k_i-1) \Delta_{q,i}^2 \{m_{k_1, \dots, k_{i-2}, \dots, k_q}(t)\} \right. \\ &\left. + \sum_{i=1}^q \sum_{l=1}^{k_i} 2k_i k_{i-1} \Delta_{q,i} \{m_{k_1, \dots, k_{i-1}, \dots, k_{l-1}, \dots, k_q}(t)\} \right], \end{aligned} \quad (18)$$

$$\text{where } \{m_{k_1, \dots, k_q}(t)\} = \begin{cases} E[y_1 y_1 x_1'' \dots x_q''] \\ E[y_1 y_2 x_1'' \dots x_q''] \\ E[y_2 y_2 x_1'' \dots x_q''] \end{cases}, \quad (19)$$

$m_{k_1, \dots, k_q}(t) > 0$, only if $k_i \geq 0$ for $i=1, 2, \dots, q$, otherwise $m_{k_1, \dots, k_q}(t) = 0$,

$$[A_{k_1, \dots, k_q}] = \begin{bmatrix} -\zeta\sqrt{1-\zeta^2} + i + \eta_{k_1, \dots, k_q} & 0 & 0 \\ 0 & -\zeta\sqrt{1-\zeta^2} + \eta_{k_1, \dots, k_q} & 0 \\ 0 & 0 & -\zeta\sqrt{1-\zeta^2} - i + \eta_{k_1, \dots, k_q} \end{bmatrix},$$

$$\eta_{k_1, \dots, k_q} = \sum_{i=1}^q k_i \lambda_i / 2\omega_n', \quad \epsilon = \epsilon_0 / \omega_n'^2, \quad [R] = (i/2) \begin{bmatrix} 1 & 1 & 0 \\ -1/2 & 0 & 1/2 \\ 0 & -1 & -1 \end{bmatrix}.$$

5.2 Perturbation Technique

Equation (18) is iteratively solved for values of k_1, k_2, \dots, k_q and the covariances are also obtained. If a parameter ϵ is small, an approximate solution is obtained by the perturbation technique.

Putting

$$\{m_{k_1, \dots, k_q}(t)\} = \{c_{k_1, \dots, k_q}\} \exp(2\omega_n' st) \quad (20)$$

and expanding $\{c_{k_1, \dots, k_q}\}$ and s into power series of ϵ ,

$$s = s^{(0)} + \epsilon s^{(1)} + \dots + \epsilon^r s^{(r)} + \dots$$

$$\{c_{k_1, \dots, k_q}\} = \{c_{k_1, \dots, k_q}^{(0)}\} + \epsilon \{c_{k_1, \dots, k_q}^{(1)}\} + \dots + \epsilon^r \{c_{k_1, \dots, k_q}^{(r)}\} + \dots \quad (21)$$

and substituting equations (20) and (21) in the moment equation (18), then we obtain iterative equation with respect to $\{c_{k_1, \dots, k_q}^{(r)}\}$ and $s^{(r)}$ ($r=0, 1, 2, \dots$), that is

$$\begin{aligned} & (s^{(0)}[I] - [A_{k_1, \dots, k_q}]) \{c_{k_1, \dots, k_q}^{(r)}\} + \sum_{i=0}^{r-1} s^{(r-i)} \{c_{k_1, \dots, k_q}^{(i)}\} \\ & = [R] \sum_{i=1}^q \sum_{l=0}^p \beta_{p-l} \lambda_i^{l-1} \{c_{k_1, \dots, k_{i+1}, \dots, k_q}^{(r-1)}\} \\ & + (\sigma^2/4\omega_n'^2 T^2) \sum_{i=1}^q k_i (k_{i-1}) \Delta_{n,i}^2 \{c_{k_1, \dots, k_{i-2}, \dots, k_q}^{(r)}\} \\ & + \sum_{i=1}^q \sum_{l=1, i < l}^{2k_i} k_i \Delta_{q,i} \{c_{k_1, \dots, k_{i-1}, \dots, k_{l-1}, \dots, k_q}^{(r)}\} . \end{aligned} \quad (22)$$

By solving equation (22) iteratively, eigenvalues of s are obtained, and the stability condition for covariances of $y_1(t)$ and $y_2(t)$ is determined by examining the maximum real part of the eigenvalues of s . Since the stability condition is determined for parameters λ_i and β_i ($i=1, 2, \dots$), the stability condition for the power spectral density $S_X(\omega)$ can be obtained by considering equation (12). The result is

$$S_X(2\omega_n\sqrt{1-\zeta^2}) < 4\zeta\omega_n^3(1-\zeta^2)/\pi\varepsilon_0^2 . \quad (23)$$

From the above expression, it is seen that the stability condition is determined by the frequency component of parametric excitation at twice the natural frequency $\omega_n\sqrt{1-\zeta^2}$. This result can be predicted from the fact that the equation of motion is reduced to Mathieu's equation in the case of harmonic excitation.

6. STABILITY OF COVARIANCE

6.1 The Case of a Single Pipe ($n = 1$)

The covariance equation of the angular displacement $\theta(t)$ and velocity $\dot{\theta}(t)$ for a single pipe under excitation of Gaussian white noise is derived from equation (5).

$$\frac{d}{dt} \begin{Bmatrix} E[\theta\theta] \\ E[\theta\dot{\theta}] \\ E[\dot{\theta}\dot{\theta}] \end{Bmatrix} = \begin{bmatrix} 0 & 2 & 0 \\ -K' & -C' & 1 \\ -K_A'^2 \pi S_0 & -2K' & -2C' \end{bmatrix} \begin{Bmatrix} E[\theta\theta] \\ E[\theta\dot{\theta}] \\ E[\dot{\theta}\dot{\theta}] \end{Bmatrix} , \quad (24)$$

where

$$\begin{aligned} C' &= 3\sqrt{g/l} \{ (C_D D/3l) \{ \rho_w l^2 / (\rho_p + \rho_p') \} (U_0 / \sqrt{lg} - 3\alpha l / 4\sqrt{lg}) + \{ c / l^2 \sqrt{lg} (\rho_p + \rho_p') \} \\ &\quad - \{ \rho_w l^2 / (\rho_p + \rho_p') \} (3d^2 / 4l^2) v_p / \sqrt{lg} \} , \end{aligned}$$

$$K' = (3g/2l) w_p / (\rho_p + \rho_p') g , \quad K_A' = 3/2l .$$

The stability condition for the covariance is easily determined from the eigenvalue of coefficient matrix in equation (24), that is

$$S_0 < 2C'K'/\pi K_A'^2 . \quad (25)$$

On the other hand, rewriting equation (23) by introducing the expressions $x(t) = (\sqrt{\omega_n}/C_1)\ddot{A}(t)$, $c_0 = K_A C_1 / \sqrt{\omega_n}$, $\zeta = C'/2\omega_n$, $\omega_n = \sqrt{K'}$, $\omega_n' = \omega_n \sqrt{1-\zeta^2}$, the stability condition in the case of colored noise input is reduced to

$$S_A(2\omega_n) < 2C'K'(1-\zeta^2)/\pi K_A'^2. \quad (26)$$

From comparison of equation (26) with equation (25), it is seen that the stability condition for the colored noise input is different from that for the white noise input by a factor $(1-\zeta^2)$ in the case of a single pipe. Therefore, the critical value of power spectral density of the colored noise input is lower than that of the white noise input, especially in the case of large damping ratio. If the damping ratio is large, the amount of $\epsilon = \epsilon_0/\omega_n^2(1-\zeta^2)$ is large, so the error caused by the perturbation technique may be large. From this fact, the stability condition (23) is valid only for the small damping ratio ($\zeta \ll 1$), although the safety-side result is given.

In a numerical example given by Table 1, equations (25) and (26) are

$$\begin{aligned} S_0 (= S_A(\omega)) &< 41.1 \text{ m}^2/\text{s}^3 & \text{(white noise input)} \\ S_A(\omega = 0.0384 \text{ s}^{-1}) &< 6.13 \text{ m}^2/\text{s}^3 & \text{(colored noise input)} \end{aligned} \quad (l = 800 \text{ m})$$

The large difference between the two results comes from the large damping ratio $\zeta = 0.922$ in this example. Such a large damping is mainly caused by the fluid resistance in the sea. A frequency component of the heaving motion for $\omega = 0.0384 \text{ s}^{-1}$ is critical for the stability in this example. But the power spectral density of the heaving motion is distributed over the frequency range $0.3 \text{ s}^{-1} < \omega < 0.9 \text{ s}^{-1}$ as indicated in Fig.4. Even if $\omega = 0.0384 \text{ s}^{-1}$ were involved in this range, the maximum value of the power spectral density, $5.2 \text{ m}^2/\text{s}^3$ in this example, satisfies the stability conditions.

If the length of pipe is shorter, say $l = 100 \text{ m}$, the damping ratio ζ becomes small, $\zeta = 0.462$ in this example, and the natural frequency ω_n' becomes high, because the gravitational effect is relatively large. The stability conditions are

$$\begin{aligned} S_0 (= S_A(\omega)) &< 7.28 \text{ m}^2/\text{s}^3 & \text{(white noise input)} \\ S_A(\omega = 0.250 \text{ s}^{-1}) &< 5.73 \text{ m}^2/\text{s}^3 & \text{(colored noise input)} \end{aligned} \quad (l = 100 \text{ m})$$

In this case, the difference between the two results is not so large. From comparison of the above results with the power spectral density shown in Fig.4, it is seen that this case is also stable.

6.2 The Case of Two Pipe Sections ($n = 2$)

For two pipe sections ($n = 2$), the critical power spectral density of the heaving acceleration $\ddot{A}(t)$ is shown in Figs.5(a) and (b). In the case of colored noise input, two groups of solid line represent the critical levels for the 1st and the 2nd modes, respectively. In these figures, the effects of the rotational damping at the universal joint are presented. The damping of the long pipe system ($2 \times 400 \text{ m}$) has an inverse effect of the short pipe system ($2 \times 50 \text{ m}$) for the 1st mode critical level, because the critical level is proportional to $\zeta(1-\zeta^2)$ from equation (23). In the case of short pipe system, $\zeta < 0.7$, so the critical level increases as ζ increases, while in the case of long pipe system, $\zeta > 0.7$, so the critical level decreases as ζ increases. In the case of white noise input, the damping at the universal joint was neglected, i.e., $c = 0$.

From comparison of these results with Fig.4, the system is unstable for the white noise input, while it is stable for the colored noise input, because the frequency range of the heaving motion is out of the critical frequencies.

Fig.6 shows the effects of mass and damping at the universal joint, fluid velocity in the pipe, current velocity in the sea, total length of the pipe and the number of the pipe sections on the critical power spectral density of heaving acceleration of buoy. The critical level of the 2nd mode is generally lower than that of the 1st mode, because the lateral displacement or the fluid drag of the 2nd mode is smaller than that of the 1st mode. Therefore, the final critical level is usually determined by the 2nd mode, and in fact the critical level of the 2nd mode is near that of the white noise input.

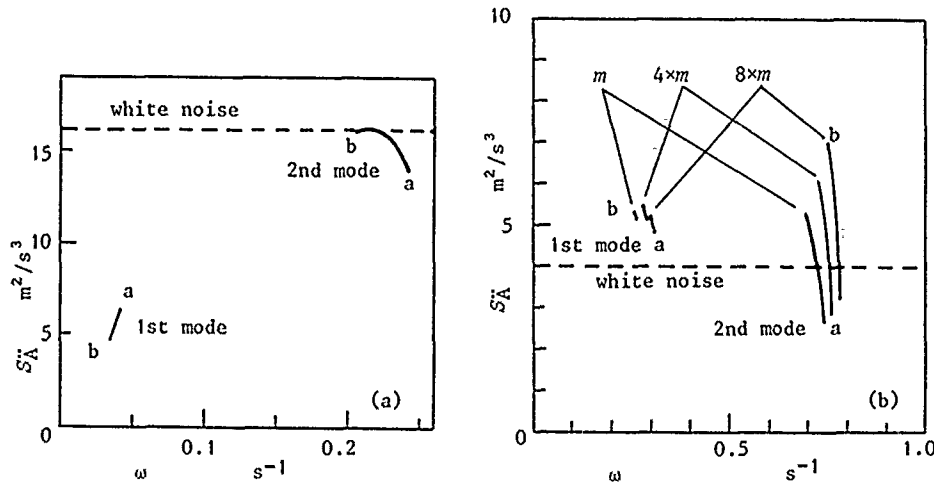


Fig.5 Critical power spectral density S_A'' of heaving acceleration of buoy
 (—:colored noise, - - -:white noise) ; $n = 2$
 Damping of the joint : $c/(\rho_p + \rho'_p)l^2\sqrt{lg} = 0$ at point a
 $= 0.025$ at point b
 (a) Effect of ω , total length = 2×400 m = 800 m
 (b) Effect of ω , total length = 2×50 m = 100 m

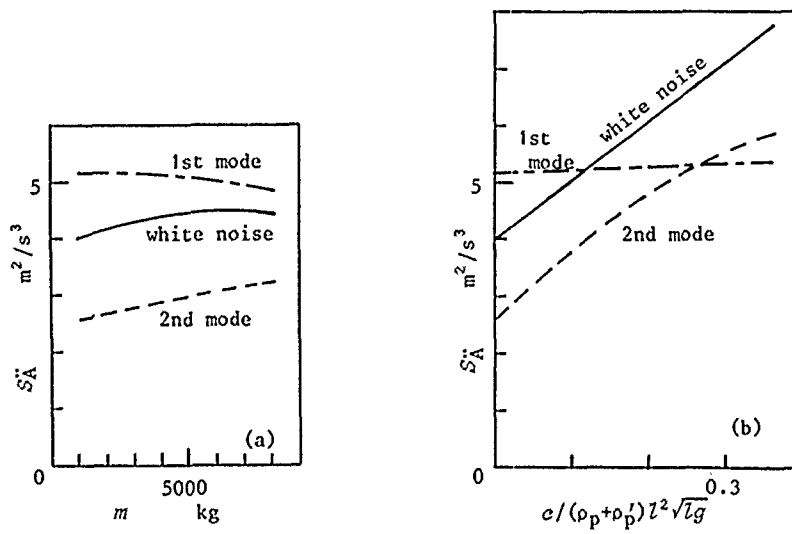


Fig.6 Critical power spectral density S_A'' of heaving acceleration of buoy
 (—:white noise, - - -:colored noise) ; $n = 2$
 (a) The effect of mass of the joint ($n \times l = 2 \times 50$ m)
 (b) The effect of damping of the joint ($n \times l = 2 \times 50$ m)

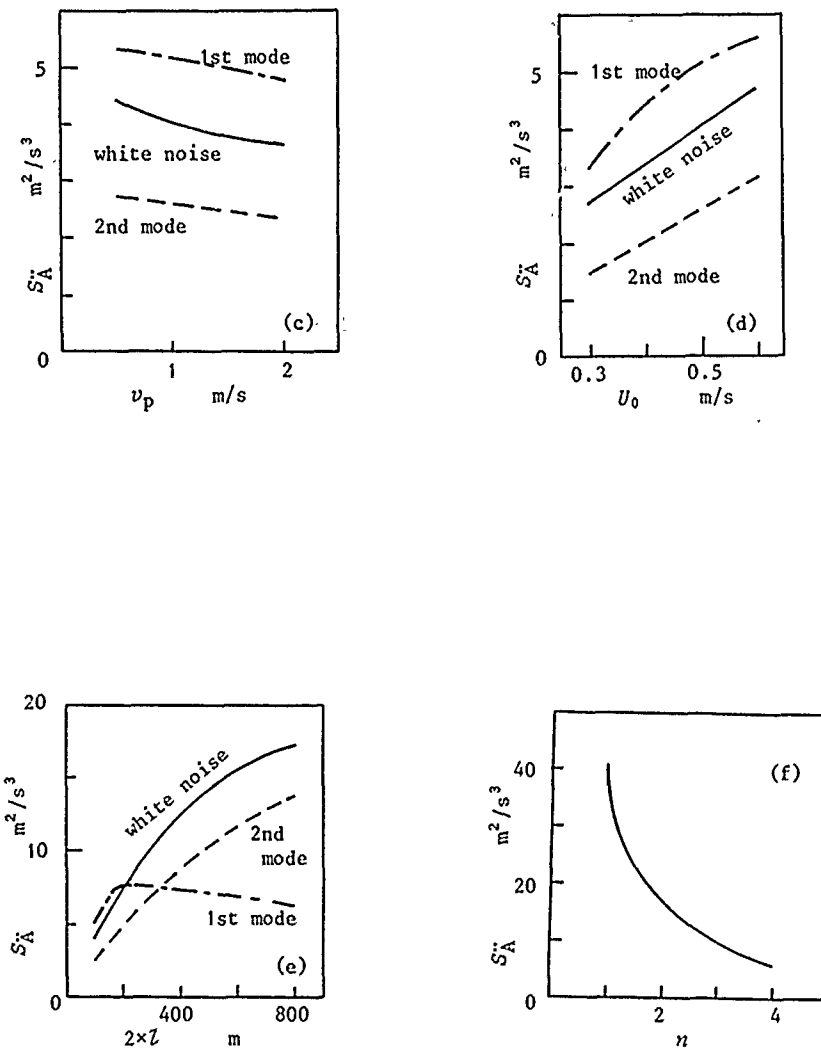


Fig.6 Critical power spectral density S_A'' of heaving acceleration of buoy
 (—:white noise, - - -:colored noise) ; $n = 2$
 (c) The effect of fluid velocity in the pipe ($n \times l = 2 \times 50 \text{ m}$)
 (d) The effect of current velocity in the sea ($n \times l = 2 \times 50 \text{ m}$)
 (e) The effect of total length of the pipe ($n \times l = 2 \times 50 \text{ m}$)
 (f) The effect of the number of the pipe sections ($n \times l = 2 \times 400 \text{ m}$)

Fig.6(a) shows that the critical level of the 1st mode drops, while that of the 2nd mode rises, as the mass of the joint increases, because the amplitude of the joint in the 2nd mode is larger than that in the 1st mode.

Further, the critical frequency becomes high as the mass of the joint increases as shown in Fig.5(b). The result of the white noise input is similar with that of the 2nd mode.

Fig.6(b) shows that the critical level rises for large damping of the joint, because the 2nd mode is suppressed by the joint damping. The 1st mode does not so markedly change that the 1st mode becomes critical above some amount of damping.

Fig.6(c) shows that the critical level drops for large fluid velocity in the pipe, because the momentum change of internal flow at the joint decreases a restoring force and Coriolis force decreases a damping force of the pipe in the case of upward flow.

Fig.6(d) shows that the critical level drops for small current velocity in the sea, because the fluid drag decreases. In this example, it was assumed that the decreasing rate of U_0 is the same with that of α . In the case of colored noise input, the critical frequency hardly changes, even if the fluid velocity in the pipe, the current velocity in the sea and the damping of the joint change.

Fig.6(e) shows that the critical level rises for the long pipe, because the effect of heaving motion becomes relatively small for the long pipe.

Fig.6(f) shows that the critical level drops for a large number of pipe sections, because the higher order modes appear and the lateral displacement or the fluid drag decreases in the higher order modes.

7. CONCLUSIONS

In this study, the stability condition of the suspended articulated pipe, which is vertically excited by the random heaving motion of the buoy, were examined in a theoretical manner, and the critical power spectral density of the heaving acceleration of the buoy and its frequency for the stability of the response covariance of the pipe were obtained.

The effects of the mass and damping at the pin-joints of the pipe, the fluid velocity in the pipe, the ocean current velocity, the pipe length, and the number of the pipe sections on the stability condition were clarified, and it was found that the long articulated pipe is fairly stable, while unstable for large number of the pipe sections, say more than 4 sections.

The stability condition of a continuous elastic pipe could be obtained by the same method as described in this study, if the bending modes of the pipe are assumed to be uncoupled. When the articulated pipe has equivalent stiffness and damping at every pin-joint corresponding to the bending stiffness and damping of the continuous pipe, then its stability condition, in the case of large number of the pipe sections, would coincide with that of the continuous pipe. In the articulated pipe, the stiffness and damping, accordingly the bending stress, can be more easily reduced than in the continuous pipe. However, its stability decreases as the stiffness and damping are reduced. In this study, the critical conditions for the stability were clarified to make the best use of the articulated pipe.

To evaluate the response of the articulated pipe is also important, though this study is limited in scope to consideration of the stability. In order to analyze response displacements of the pipe, more detailed model should be established, for example, not only heaving motion of the buoy, but also sway and roll, furthermore phase difference between them should be found, and coupled effects between the pipe and the buoy should be taken into account owing to the finite displacement of the pipe.

ACKNOWLEDGMENT

The authors are grateful to Dr. Yoshida, K., Assistant Professor of Mechanical Engineering, Keio University, for valuable discussions on the analytical method.

REFERENCES

1. Paulling, J. R., "Frequency-Domain Analysis of OTEC Cold Water Pipe and Platform Dynamics," OTC Paper 3543, Proceedings of the Offshore Technology Conference, Houston, Texas, May 1979, pp.1641-1651.
2. Paulling, J. R., "An Equivalent Linear Representation of the Forces Exerted on the OTEC Cold Water Pipe by Combined Effects of Waves and Currents," Energy-Sources Technology Conference, Sponsored by Ocean Engineering Division of ASME, New Orleans, Louisiana, February 1980, pp.21-28.
3. Chou, D. Y., et al., "Dynamic Analysis of Coupled OTEC Platform - Cold Water Pipe System," OTC Paper 3338, Proceedings of the Offshore Technology Conference, Houston, Texas, May 1978, pp.2489-2498.
4. Chang, P. Y., and Barr, R. A., "The NOAA/DOE Frequency Domain Methods for Analysis of OTEC Plant CWP and CWP/Platform Static and Dynamic Responses," Energy-Sources Technology Conference, Sponsored by Ocean Engineering Division of ASME, New Orleans, Louisiana, February 1980, pp.7-20.
5. Iso, S., Yamashita, Y., Shimogo, T., and Yoshida, K., "A Study on Dynamical Behavior of OTEC 1MW CWP in Japan," Proceedings of 8th Ocean Energy Conference, Washington D. C., June 1981, pp.61-68.
6. Chung, J. S., and Whitney, A. K., "Axial Stretching Oscillation of an 18,000-Ft Vertical Pipe in the Ocean," ASME Journal of Energy Resources Technology, Vol.105, 1983, pp.195-200.
7. Paidoussis, M. P., and Deksnis, E. B., "Articulated Models of Cantilevers Conveying Fluid : the Study of a Paradox," Journal of Mechanical Engineering Science, Vol.12, 1970, pp.288-300.
8. Sugimoto, S., Ito, K., and Sugiyama, H., "On the Moment Stability of the Second Order Linear Systems with Colored Noise Coefficients," Transaction of the Society of Instrument and Control Engineers, Vol.15, 1979, pp.171-177 (in Japanese).

VIBRATION OF TURBOMACHINE-BLADE DUE TO VISCOUS WAKES

K. Ishihara
Strength Research Laboratory
Technical Institute
Kawasaki Heavy Industries, Ltd.
Akashi, Japan

ABSTRACT

The present paper deals with blade vibration due to the unsteady forces generated by the wake shed from the preceding blade row and presents a method which can evaluate the resonant stress of the blade.

The closed-loop vibration system takes into account not only the unsteady force due to the wake but also the one caused by blade vibration, as the forces acting on the blade are first analyzed by the Transfer Matrix Method.

Next, the experiment is carried out using the rotating-cascade test rig, in order to confirm the validity of this method. Since the results obtained by this analysis are in good agreement with the experimental ones, the resonant stress, which could not be predicted up to this time, now enables prediction before actual occurrence; hence this method will be useful to the design of turbomachine blades.

NOMENCLATURE

$w_p(t)$: wake distribution
 $u_p(t), v_p(t)$: gust fluctuation parallel and normal to an undisturbed flow respectively
 ω : circular frequency of fluctuating gust
 $y_o(x)$: camber line ($y_o(x) = f(1 - x^2)$ for parabolic blade)
 $\bar{y}, \bar{\psi}$: bending and torsional displacement of blade respectively
 Y_b, Y_f : bound vortex, free vortex
 K : reduced frequency
 μ : mass ratio
 c, b : chord length, half chord length
 ρ, V : air density, relative inlet velocity of rotor blade
 U, V_s : rotor speed, absolute outlet velocity of stator blade
 α, f : angle of attack, ratio of maximum camber over the half-chord length
 t_r, t_s : pitch of rotor cascade, pitch of stator cascade
 ϕ : angle made by rotor blade and outlet velocity vector
 m, J_o : concentrated mass and inertia moment of blade respectively
 EI, GJ : bending and torsional stiffness of blade
 c_d, δ : concentrated damping coefficient, logarithmic decrement
 Y_i, A_i : angle made by principal axis of i -th cross section and x -axis of basic coordinate, cross sectional area

X-Y : basic coordinate of blade
 $\xi-\eta$: coordinate along principal axis of each cross section
 $x-y$: nondimensional coordinate made by half-chord length

Subscript

$\bar{\cdot}$: implies the complex number
 s : steady component
 t : unsteady component
 n : n-th harmonic
 i : i-th element
 o : implies fundamental component
 j : imaginary unit $=\sqrt{-1}$

1. INTRODUCTION

In an axial-flow turbomachine, it is well known that blades are subjected to unsteady forces, because of it being operated in unsteady flow fields. Especially as the unsteady force arising through passing the wakes shed from the preceding blade row has a frequency proportional to a rotating speed, the resonant phenomenon occurs under the condition that the blade natural frequency coincides with the exciting frequency, and the blades suffer very large stresses which leads to fatigue failure. It is very important for designing turbomachinery to predict the resonance stress due to the wake, but this has not been taken into account up to the present.

The unsteady force due to the wake can be considered to be one arising on a blade in a periodic fluctuating flow field. Such kind of studies have been carried out theoretically by many authors [1]-[6]. Karman and Sears [1] first analyzed the unsteady flow around airfoils using the prevailing vortex theory. Sears [2] obtained the unsteady forces on an isolated airfoil in a sinusoidal travelling gust in which the velocity perturbation is normal to the undisturbed flow. Horlock [4] investigated the unsteady forces on an isolated airfoil with an angle of attack due to a longitudinal (i.e., parallel to the undisturbed flow) gust and pointed out that this gust gave the very important effect to the unsteady force. Naumann and Yeh [5] considered the effect of camber on the unsteady force due to parallel and normal gusts and presented the design method for reducing the unsteady force to a minimum. Analyses previously mentioned are valid only for cascades with low solidity, because they are based on the isolated airfoil theory. Whitehead [6] investigated the unsteady forces arising on a blade in a cascade due to a sinusoidal gust, together with the unsteady force due to blade vibration.

As mentioned above, unsteady aerodynamic forces due to the gust have been studied by many authors. However there has been few investigations on an unsteady force on blade vibration. Moreover, experimental investigations being fewer than theoretical ones, it is difficult to apply these theoretical results to the blade design with confidence.

The present paper is trying to establish the method of evaluation of the resonant stress by comparing the theoretical results with experimental ones. First, stress evaluation method is presented, which analyzes the closed-loop system of blade vibration, containing not only the fluctuating force due to the gust (i.e., external force) but also the fluctuating one caused by its own vibration (i.e., aerodynamic damping), by the Transfer Matrix Method. Second, the wake distribution, the logarithmic decrement and the resonant stress are obtained experimentally using the rotating cascade test equipment. The universal validity of the stress evaluation method presented here is confirmed by comparing the theoretical result with the experimental one.

2. DERIVATION OF UNSTEADY FORCE

The assumptions used here are as follows:

- (a) The flow is two-dimensional, inviscid and incompressible
- (b) The unsteady aerodynamic forces arising on a blade consist of those due to the gust and the vibration of blade itself

(c) The fluctuating velocity is very small compared with the mean velocity

2.1 Expression of Fluctuating Gust due to Wakes

As shown in Fig.1, a rotor blade subjected to a fluctuating gust when it passes through the wake shed from the preceding blade row. The wake is periodic and its period is given by.

$$T_0 = t_s/U, \quad \omega_0 = 2\pi \frac{U}{t_s} \quad (1)$$

Regarding the wake as a time function with a frequency ω_0 , it can be Fourier expanded as follows:

$$w_p(t) = \sum_{-\infty}^{\infty} \bar{w}_{pn} e^{jn\omega_0 t} \quad (2)$$

Normal and parallel components of gust to the undisturbed flow are

$$v_p(t) = \sum_{-\infty}^{\infty} \bar{v}_{pn} e^{jn\omega_0 t} \quad u_p(t) = \sum_{-\infty}^{\infty} \bar{u}_{pn} e^{jn\omega_0 t} \quad (3)$$

respectively. Where $\bar{v}_{pn} = w_{pn} \sin \phi$, $\bar{u}_{pn} = \bar{w}_{pn} \cos \phi$.

Adopting blade center as a basis, the gust at an arbitrary point x on a blade can be expressed as follows.

$$v_p(x, t) = \sum_{-\infty}^{\infty} \bar{v}_{pn} e^{jn\omega_0 (t - x/V)} = \sum_{-\infty}^{\infty} \bar{v}_{pn} e^{-jnk_0 x} e^{jn\omega_0 t} \quad (4)$$

Similarly

$$u_p(x, t) = \sum_{-\infty}^{\infty} \bar{u}_{pn} e^{-jnk_0 x} e^{jn\omega_0 t} \quad (5)$$

where argument φ_n of \bar{v}_{pn} , \bar{u}_{pn} , indicates the phase difference between the wake fluctuation and its n -th fourier component.

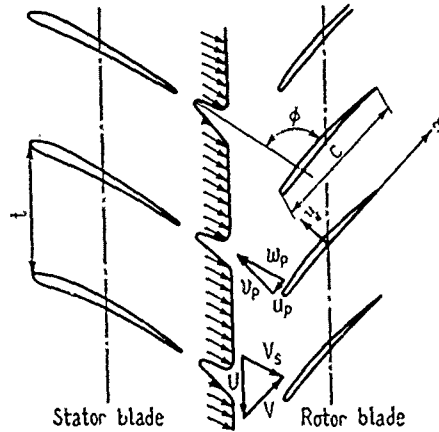


Fig.1 Rotor blade passing through wakes

2.2 Boundary Condition on a Blade surface

As shown in Fig.2(a), the coordinate of the blade vibrating in a pure bending mode is given as follows.

$$y(x, t) = y_0(x) + \sum_{-\infty}^{\infty} y_n e^{jn\omega_0 t} \quad (6)$$

where $\theta_n = \arg \bar{y}_n$ is a phase difference between the n -th component of gust fluctuation and its response displacement. From now on, the suffix is omitted

because only one component is considered.

The velocity vector V_1 at a point on a blade and the velocity vector V_2 of a fluid are

$$V_1 = \{0, \frac{\partial Y(x, t)}{\partial t}\} \quad V_2 = \{V + u_p, V\alpha + v_p + v\} \quad (7)$$

respectively. Where v is an induced velocity and consists of steady and unsteady components; then

$$v(x, t) = v_s(x) + v_t(x, t) \quad (8)$$

In indicid fluid, the normal components of V_1 and V_2 to the blade must be equal to each other, then

$$V_1 \cdot n = V_2 \cdot n \quad (9)$$

where n is the normal vector and defined such as $n = (-\partial Y / \partial x, 1)$. If Eq.(9) is expressed by vector components, it becomes

$$\frac{\partial Y}{\partial x} = \frac{V\alpha + v_p + v_s + v_t}{V + u_p} - \frac{1}{V + u_p} \frac{\partial v}{\partial t} \quad (10)$$

Subtracting the mean-flow relation

$$\frac{\partial Y}{\partial x} = \frac{V\alpha + v_s}{V} \quad (11)$$

from Eq.(10), results in

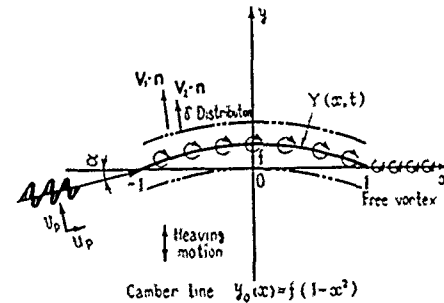
$$\tilde{v}_t = (\bar{u}_p \frac{\partial Y}{\partial x} - \bar{v}_p) e^{-jkx} + j\omega \bar{y} \quad (v_t = \bar{v}_t e^{j\omega t}) \quad (12)$$

On the other hand, the coordinate of the blade vibrating in a pure torsional mode is given as follows:

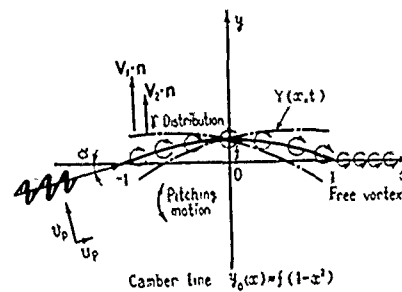
$$Y(x, t) = y_0(x) - \sum_{n=0}^{\infty} \tilde{v}_n x e^{jn\omega_0 t} \quad (13)$$

Similar to the case of pure bending vibration, the boundary condition on a blade surface is given by Eq.(9). Then fluctuating induced velocity is

$$\tilde{v}_t = (\bar{u}_p \frac{dy_0}{dx} - \bar{v}_p) e^{-jkx} - (V + j\omega x) \tilde{v} \quad (14)$$



(a) Pure bending mode



(b) Pure torsional mode

Fig.2 Coordinates of vibrating blade

2.3 Unsteady Aerodynamic Force arising on a Vibrating Blade Subjected to a Gust
The bound vortex distribution arising on a blade due to the unsteady induced velocity \tilde{v}_t can be obtained by using Söhngen's reciprocal formula and

putting $x = -\cos\theta$
The result is

$$Y_b(\theta) = 2f\bar{v}_p[\bar{F}(k) \cot\frac{\theta}{2} + \frac{4}{k} \sum_{n=1}^{\infty} j^{n-1} J_n(k) \sin n\theta] + 2\bar{v}_p \bar{S}(k) \cot\frac{\theta}{2}$$

$$+ \left\{ \begin{array}{l} 2wk \sin\theta \bar{y} - j2w\cot\frac{\theta}{2} \bar{C}(k) \bar{y} \quad (\text{pure bending vibration}) \\ \frac{2\bar{v}\ddot{\psi}}{\pi} [jk\pi \sin\theta + \pi\cot\frac{\theta}{2} \bar{C}(k) + \frac{k^2}{4}\pi \sin 2\theta + \pi jk \sin\theta] \end{array} \right. \quad (15)$$

$$- \frac{\pi jk}{2} (1 - \bar{C}(k)) \cot\frac{\theta}{2} \quad (\text{pure torsional vibration}) \quad (16)$$

where $\bar{F}(k) = \{2\bar{C}(k) - 1\} [J_0(k) - J_1(k)/k - jJ_1(k)] - [J_0(k) - J_1(k)/k + jJ_1(k)]$;
 $\bar{S}(k)$ $\bar{C}(k)$ are Sears function and Theodorsen function respectively and given as follows:

$$\bar{S}(k) = [J_0(k) - jJ_1(k)] \bar{C}(k) + jJ_1(k) \quad (17)$$

$$\bar{C}(k) = H_1^{(2)}(k) / \{H_1^{(2)}(k) + jH_0^{(2)}(k)\} \quad (18)$$

and H_0 , H_1 are Hankel functions.

Unsteady forces arising on a blade surface due to this $\bar{Y}_b(\theta)$ are given as follows by applying Euler's equation of motion to the flow around the blade:

$$L(t) = \pi\rho c V_w \sin\phi [\cot\phi \{f\bar{F}_f(k) + \alpha\bar{F}_\alpha(k)\} + \bar{S}(k)] e^{j\omega t}$$

$$+ \left\{ \begin{array}{l} -\pi\rho b^2 \ddot{\psi} - 2\pi\rho b V \bar{C}(k) \dot{\psi} \quad (\text{pure bending vibration}) \\ \pi\rho b V \dot{\psi} + 2\pi\rho b V^2 (1 + \frac{jk}{2}) \bar{C}(k) \psi \quad (\text{pure torsional vibration}) \end{array} \right. \quad (19)$$

$$+ \left\{ \begin{array}{l} -\pi\rho b^2 V \bar{C}(k) \dot{\psi} \quad (\text{pure bending vibration}) \\ -\frac{\pi\rho b^3 V}{2} \ddot{\psi} - \frac{\pi\rho b^4}{8} \dot{\psi} + \pi\rho b^2 V^2 (1 + \frac{jk}{2}) \bar{C}(k) \psi \quad (\text{pure torsional vibration}) \end{array} \right. \quad (20)$$

The above result consists of a lift fluctuation due to the gust and one due to blade vibration. Besides, moment fluctuation can also be obtained, as follows:

$$M(t) = \frac{1}{4} \pi \rho c V_w \sin\phi [\cot\phi \{f\bar{F}'_f(k) + \alpha\bar{F}'_\alpha(k)\} + \bar{S}(k)] e^{j\omega t}$$

$$+ \left\{ \begin{array}{l} -\pi\rho b^2 V \bar{C}(k) \dot{\psi} \quad (\text{pure bending vibration}) \\ -\frac{\pi\rho b^3 V}{2} \ddot{\psi} - \frac{\pi\rho b^4}{8} \dot{\psi} + \pi\rho b^2 V^2 (1 + \frac{jk}{2}) \bar{C}(k) \psi \quad (\text{pure torsional vibration}) \end{array} \right. \quad (21)$$

$$+ \left\{ \begin{array}{l} -\frac{\pi\rho b^3 V}{2} \ddot{\psi} - \frac{\pi\rho b^4}{8} \dot{\psi} + \pi\rho b^2 V^2 (1 + \frac{jk}{2}) \bar{C}(k) \psi \quad (\text{pure torsional vibration}) \end{array} \right. \quad (22)$$

where

$$\bar{F}_f = \bar{F}(k) + \frac{4}{k} J_1(k), \quad \bar{F}_\alpha(k) = J_0(k) + jJ_1(k) \quad (23)$$

$$\bar{F}'_f(k) \approx \bar{F}(k) + \frac{6}{k} j[-J_0(k) + 2J_1(k)/k], \quad (24)$$

$$\bar{F}'_\alpha(k) = 2[J_0(k) - J_1(k)/k + jJ_1(k)]$$

In Eq.(19)-Eq.(22), the first term is an unsteady force acting on a rigid blade in gust flow and plays the role of a forced external force in vibration analysis. Let these forces be expressed by L_g , M_g hereafter. On the other hand, the other terms show the forces produced by a blade vibration and act as the aerodynamic damping.

3. RESPONSE OF BLADE DUE TO UNSTEADY FORCE

There are many calculation methods by which blade response due to a known external force can be obtained. The Transfer Matrix Method is used in this analysis because it is simple to treat and gives enough precision in engineering. The following are considered in this analysis: (1) initial torsion, (2) centrifugal effect and shear deformation, (3) bending and torsion coupling.

As the Transfer Matrix Method is used, the blade which is a continuous system is divided into many elements approximately in a span-wise direction and

replaced by a Myklestad model which consists of the concentrated mass and the massless shaft as shown in Fig.3(a).

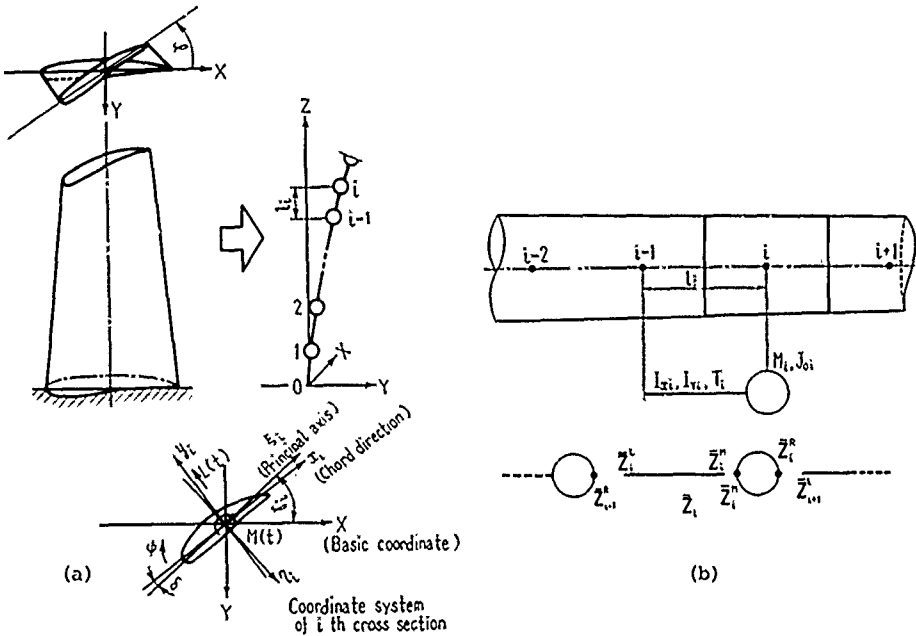


Fig.3(a) Modelling of blade and coordinate system; (b) Model element and state vector

The cross sectional constants (A_i , I_{xi} , I_{qi} , J_i etc.) at each cross section are different in a blade with ununiform cross section, and torsion is assumed to change stepwise at each section. Modelling of a blade and the coordinate system are shown in Fig.3.

3.1 Unsteady Force

Unsteady forces have already been obtained and given by Eq.(19)-(22). Adopting ξ , η component of these forces

$$L_\xi(t) = L(t) \sin\delta', \quad L_\eta(t) = L(t) \cos\delta' \quad (25)$$

and

$$\xi = y \sin\delta', \quad \eta = -y \cos\delta', \quad \text{then}$$

$$L_\xi(t) = \tilde{L}_g \sin\delta' e^{j\omega t} - \pi \rho b^2 \ddot{\xi} - 2\pi \rho b V \tilde{C}(k) \dot{\xi} + \\ [\pi \rho b V \dot{\psi} + 2\pi \rho b V^2 (1 + \frac{jk}{2}) \tilde{C}(k) \psi] \sin\delta' \quad (26)$$

Similary

$$L_\eta(t) = \tilde{L}_g \cos\delta' e^{j\omega t} + \pi \rho b^2 \ddot{\eta} + 2\pi \rho b V \tilde{C}(k) \dot{\eta} + \\ [\pi \rho b V \dot{\psi} + 2\pi \rho b V^2 (1 + \frac{jk}{2}) \tilde{C}(k) \psi] \cos\delta' \quad (27)$$

and the aerodynamic moment is

$$\bar{M}(t) = \tilde{M}_g e^{j\omega t} - \pi \rho b^2 V \tilde{C}(k) \times [\xi \sin\delta' - \eta \cos\delta'] j\omega - \frac{\pi}{2} \rho b^3 V \dot{\psi} \\ - \frac{\pi}{8} \rho b^4 \ddot{\psi} + \pi \rho b^2 V^2 (1 + \frac{jk}{2}) \tilde{C}(k) \psi \quad (28)$$

3.2 State Vector, Element of Each Kind of Matrix and Transfer Matrix

In the coordinate system shown in Fig.3(a), defining i -th divided point as in Fig.3(b), the state quantities representing the vibration at this point are as follows:

- \bar{x}, \bar{y} : displacement in X and Y direction
- $\bar{\theta}_x, \bar{\theta}_y$: slopes in X and Y direction
- \bar{M}_x, \bar{M}_y : moments around Y and X axis
- \bar{s}_x, \bar{s}_y : shearing force in X and Y direction
- $\bar{\psi}, \bar{T}$: torsional displacement and torque

These are all complex quantities which can be described as $x = \bar{x}e^{j\omega t}$
Representing these quantities by \bar{z}

$$\bar{z}_i = [\bar{y}, \bar{\theta}_y, \bar{M}_x, \bar{s}_y, \bar{x}, \bar{\theta}_x, \bar{M}_y, \bar{s}_x, \bar{\psi}, \bar{T}, 1]^T \quad (29)$$

By the way, the dynamical relation between both ends of a elastic beam in Fig.3 (b) is formed as follows:

$$\bar{z}_i^M = \bar{F}_i \bar{z}_i^L \quad (30)$$

\bar{F} is called "Field Matrix". On the other hand, the dynamical relation between the two ends of the mass element is also formed as follows:

$$\bar{z}_i^R = \bar{P}_i \bar{z}_i^M \quad (31)$$

\bar{P} is called "Point Matrix". Last, the coordinate translation matrix associated with torsion angle γ is given by T .

From matrices mentioned above, the Transfer Matrix between \bar{z}_{i+1} and \bar{z}_i becomes as follows:

$$\bar{z}_{i+1} = \bar{U}_i \bar{z}_i \quad \text{where} \quad \bar{U}_i = \bar{P}_i T_i \bar{F}_i T^{-1} \quad (32)$$

Representing the state vectors at the root and tip of the blade by \bar{z}_0 and \bar{z}_n respectively, we can obtain the next equation

$$\bar{z}_n = \bar{U}_n \cdot \bar{U}_{n-1} \cdot \dots \cdot \bar{U}_1 \cdot \bar{U}_0 \cdot \bar{z}_0 = \bar{V} \cdot \bar{z}_0 \quad \text{where} \quad \bar{V} = \prod_{i=0}^n \bar{U}_i \quad (33)$$

3.3 Boundary Condition and Simultaneous Equation

The following boundary conditions are adopted in Eq.(33):

Displacement and slope are zero (fix) at $Z = 0$
Moment and shearing force are zero (free) at $Z = L$

Applying these boundary conditions to Eq.(33), a non-homogeneous simultaneous equation with order 5 is obtained. The state vector \bar{z}_0 can be gotten by solving this equation, and state vectors at each points \bar{z}_i ($i=1 \sim n$) can also be calculated sequentially by using \bar{z}_0 .

4. EXPERIMENT

4.1 Outline of Rotating Cascade Test Rig

In order to compare with the theoretical result, the test rig (Fig.4) is designed so as to realize assumptions used in the present analysis. That is :

- (a) Boss ratio being large and having many blades to get two-dimensionality.
- (b) Relative inlet velocity of rotor blade being about 100 m/sec, in order to insure incompressibility and the amount of the exciting force.
- (c) The resonant phenomenon of 1st bending mode occurs.

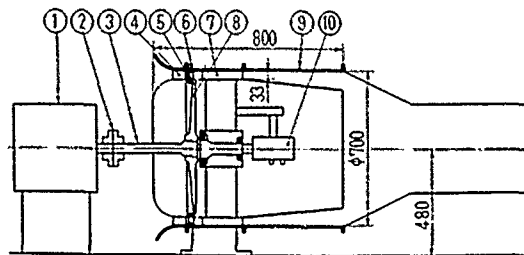
Table 1 shows the rotating cascade test rig designed with the above conditions. The rotating cascade test rig is driven by DC-motor (25KW) ① and the compressed air is released in atmosphere through the diffuser ②. Inlet guide vanes ④ and outlet guide vanes ⑦ are rigid blades fixed at the upper and the lower casing. The blade height is 32.5 mm, aspect ratio and boss ratio are 1.3

and 0.9, respectively. The velocity triangle and the stagger angle at mid span at the design point are shown in Fig.5.

4.2 Experimental Method and Results

In this experiment, the wake distribution, the logarithmic decrement of the test blade and its resonant stress are measured. The wake distribution and the logarithmic decrement play the role of input information in the present analysis, and the resonant stress is the output information for comparison with the theoretical results.

The measuring method of wake distribution is first described. A lot of measurements of wake distribution have been carried out in two-dimensional cascade, but few in the rotating cascade. Anemometer or pilot tube are well used as a sensor. However, in the present test rig, the distance between the inlet guide vane and the rotor blade is so small that the pilot tube could not be used. Then the total pressure distribution was measured by the cylindrical total pressure tube as shown in Fig.6.



(1) D.C. motor	(6) Rotor blade
(2) Shaft coupling	(7) Outlet guide vane
(3) Shaft	(8) Blade disk
(4) Inlet guide vane	(9) Diffuser
(5) Strain gauge	(10) Slipring

Fig.4 Rotating cascade test rig

Table 1 Items of rotating cascade

Chord length c mm	Inlet guide vane			Rotor blade		
	67			25		
Numbers of blade Z	36			98		
Position	Boss	Center	Tip	Boss	Center	Tip
Solidity c/t	1.244	1.180	1.125	1.25	1.188	1.131
Radius R mm	312	328.5	345	312	328.5	345
Turning angle θ°	29.87	31.61	33.56	16.54	14.91	12.97
Angle of attack α°	19.0	20.0	21.60	11.1	10.0	9.1
Stagger angle ξ°	19.20	20.00	21.65	33.5	36.5	40.2
Lift coeff. C_{l0}	1.50	1.63	1.9	0.84	0.765	0.67
Casing dia.	Inner dia. = 624			Outer dia. = 690		
Natural freq. of rotor blade				2000 Hz		
Tip clearance mm				0.4 ~ 0.8		

On the other hand, static pressure was measured at the upper and lower wall surfaces. The velocity distribution can be obtained from these results. The exciting frequency f_c due to the preceding blade row's wake is given by

$$f_c = K \frac{NZ}{60} \quad (34)$$

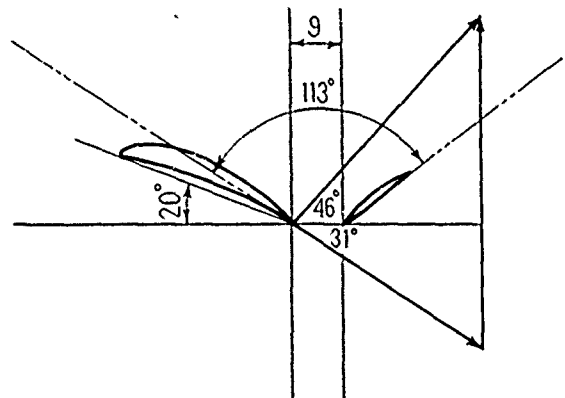


Fig.5 Velocity triangle and stagger angle at mean radius

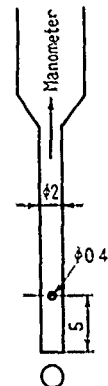
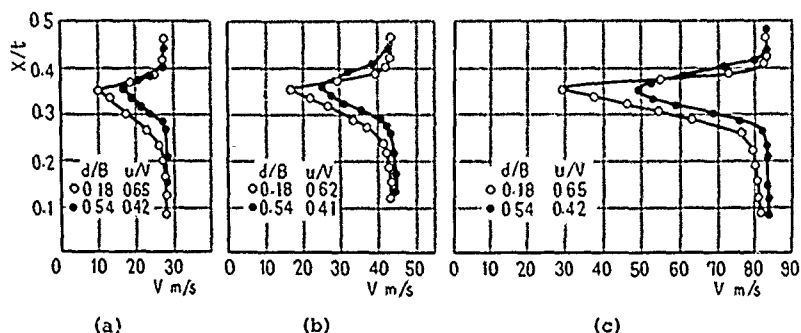


Fig.6 Cylindrical total pressure tube (dimensions are in mm)

where N is a rotating speed (rpm), Z is the number of inlet guide vanes and K is the harmonic number of the periodic force. As the natural frequency of the test blade is 2010 Hz and there are 36 inlet guide vanes, so the rotating speeds at which the resonance due to the wake occurs becomes 3350 rpm (1st harmonic), 1675 rpm (2nd harmonic) and 1117 rpm (3rd harmonic), respectively. Then the wake distribution was measured at these three rotating speeds, Fig.7 shows the measurement results of the wake distribution of the inlet guide vanes.



d : Distance from trailing edge to measuring point t : Pitch
 B : Half chord of inlet guide vane u : Velocity defect

Fig.7 Wake distribution of inlet guide vane

Next, the experimental method for logarithmic-decrement measurement, are described. It is necessary to grasp the logarithmic decrement of the blade beforehand, in order to get the resonance stress of the blade by the calculation. This logarithmic decrement consists of the material damping, the structural damping and the aerodynamic damping. In these three dampings, only the aerodynamic damping can be obtained theoretically and others have to be gotten experimentally. Let the damping except the aerodynamic one be represented by δ_s ; it is usually obtained by the following methods:

$$(a) \text{Free-damped oscillation method : } \delta_s = -\lambda_n \frac{x_{n+1}}{x_n} \quad (35)$$

(b) Resonance curve method $\delta_s = \frac{\Delta f}{f_0}$ (36)

Method (b) was adopted in this experiment. Fig.8 shows δ_s of the test blade and it is seen that it tends to increase linearly with the stress amplitude.

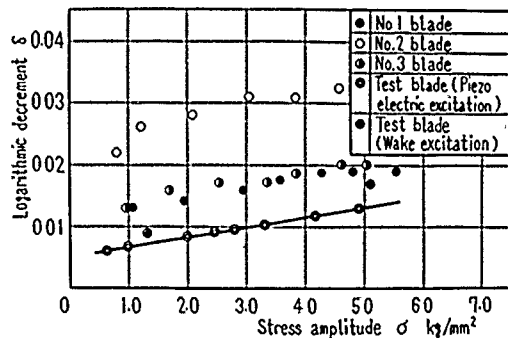


Fig.8 Logarithmic decrement of test blade

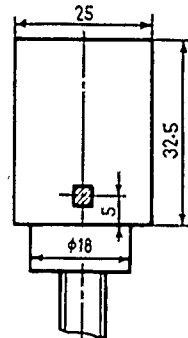
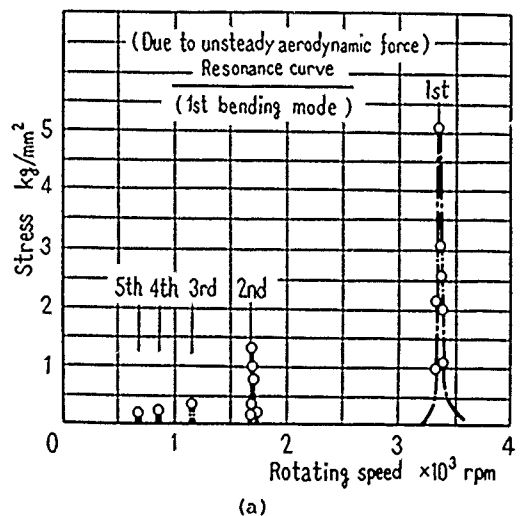


Fig.9 Position of strain gauge stuck of blade

Last, the measurement of the resonant stress of the blade is described. The stress is measured by a strain gauge stuck to the blade, as shown in Fig.9. Outputs from the strain gauge are led to a slirring and amplified by a dynamic strain meter. Fig.10(a) shows the resonance curve of stress due to the wake and Fig.10(b) shows the resonant stress waves at each harmonic.



(a)

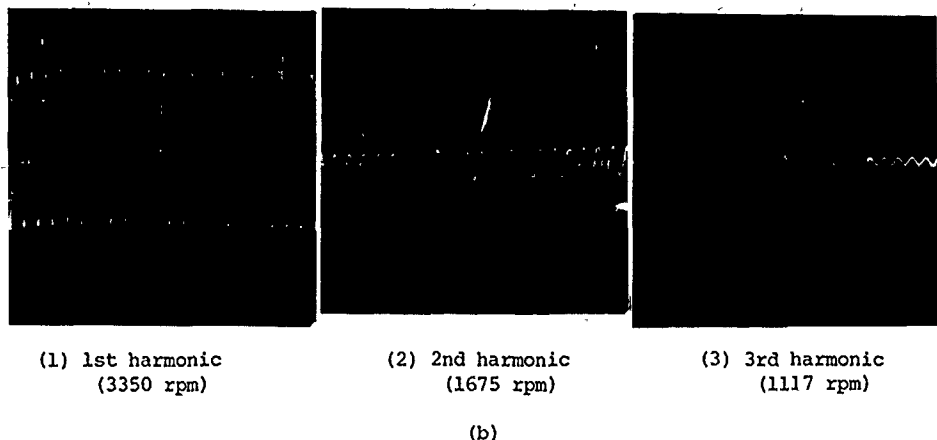


Fig.10 (a) Resonance curve of stress due to the wake ; (b) Resonant stress waves at each harmonic

5. COMPARISON OF CALCULATED RESULTS WITH EXPERIMENTAL ONES

In this chapter, the validity of the present theory is discussed by comparing calculation results with experimental ones. Fig.11(a) shows a resonance curve of blade vibration due to the 1st harmonic component of the wake. The natural frequency of the test blade is 2010 Hz and the logarithmic decrement is 0.013. The logarithmic decrement used here is the value obtained experimentally beforehand.

In Fig.11(a), the curve which indicates high stress level is the calculation result without the aerodynamic damping and another curve is the one with the aerodynamic damping; the circles indicate experimental values. The calculation value taking into account the aerodynamic damping is in good agreement with the experimental one, but if not the calculation result is inclined to be greater than an actual one. Fig.11(b) shows the result in the case due to the 2nd harmonic component of the wake. This result also indicates the same tendency as in Fig.11(a). This fact means that aerodynamic damping acts on a blade as a positive damping, but the damping effect is dependent on the reduced frequency. The damping effect becomes larger with smaller reduced frequency. This fact will be explained next by using a simplified system.

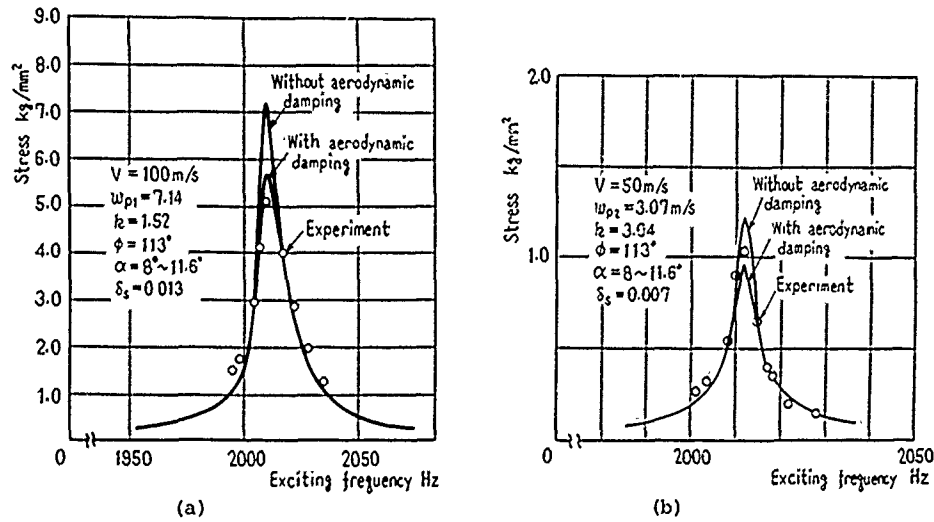


Fig.11 Comparison between the theoretical results and the experimental ones for the resonance curve due to the wake excitation

(a) Due to 1st component of the wake; (b) Due to 2nd component of the wake

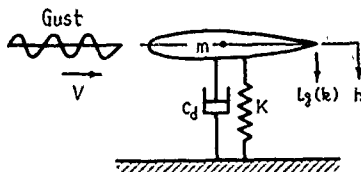


Fig.12 Simplified model of vibrating blade subjected to gust

The equation of motion for the vibration system shown in Fig.12 is given by Eq.(37)

$$\ddot{h} + c_d \dot{h} + Kh = \tilde{L}_g(k) e^{j\omega t} - \pi \rho b^2 \ddot{h} - 2\pi \rho b V C(k) \dot{h} \quad (37)$$

Moving the right hand term to the left and considering $C(k) = F(k) + jG(k)$ we get

$$(m + \pi \rho b^2) \ddot{h} + [C_d + 2\pi \rho b V F(k)] \dot{h} + [K - 2\pi \rho b V G(k)] h = \tilde{L}_g(k) e^{j\omega t} \quad (38)$$

As the resonant amplitude (corresponding to the stress) against $\tilde{L}_g(k)$ is inversely proportional to the damping coefficient, if we express the resonant stress due to only C_d by σ_o and the one due to $[C_d + 2\pi \rho b V F(k)]$ by σ_a , then we get the next equation:

$$\frac{\sigma_a}{\sigma_o} = \frac{C_d}{C_d + 2\pi \rho b V F(k)} \quad (39)$$

Using the relation $C_d = m \omega_n \delta_s / \pi$, $V = \omega_n b / k$, Eq.(39) can be rewritten as follows:

$$\frac{\sigma_a}{\sigma_o} = \frac{\delta_s}{\delta_s + (2\pi/\mu) \{F(k)/k\}} \quad (40)$$

Fig.13(a) shows the above relation in the case of $\mu = 637$ (experimental value) by using δ_s as a parameter. In order to get the validity of this figure, the logarithmic decrement of the test blade in rotation was measured. Fig.14 shows the experimental results. For example, the resonant stress due to the 1st component of the wake is about 5 Kg/mm^2 as shown in Fig.11(a). In this case, the logarithmic decrement δ_s and reduced frequency k are about 0.013 and 1.52 respectively. Obtaining the logarithmic decrement δ including the aerodynamic damping from Fig.13(a), we get $\delta = 0.0165$. On the other hand, the logarithmic decrement δ obtained from Fig.14 is about 0.017 and this value means total dampings (i.e., $\delta_s + \delta_a$, where δ_a represents aerodynamic damping). This value (0.017) being in good agreement with the value previously mentioned (0.0165), the relation indicated by Fig.13 can be thought to be reasonable.

It can be seen from Fig.13(a) that when μ is constant, the aerodynamic damping effect on the stress increases with δ_s , k becoming small. On the other hand, Fig.13(b) shows the relation of Eq.(40) in the case of $\mu = 20$ and indicates that the aerodynamic damping effects are important even in a region of large k when μ is small. These figures are results in the case of $\phi = 90^\circ$ but these are the same too for other ϕ values.

Finally, the theoretical and experimental values of resonant stress due to each harmonic components of the wake in the case of $d/B = 0.18$, $d/B = 0.54$ is shown in Table 2. It is seen from this table that the theoretical values are in very good agreement with the experimental ones.

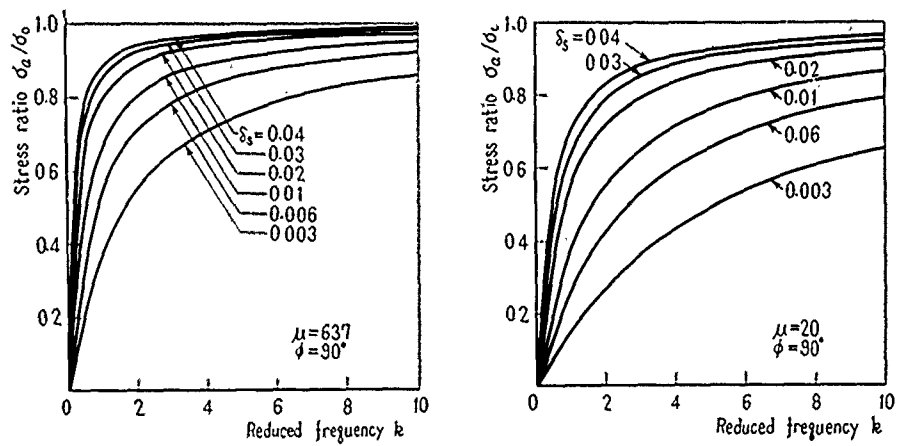


Fig.13 Effect of aerodynamic damping δ_s on resonant stress

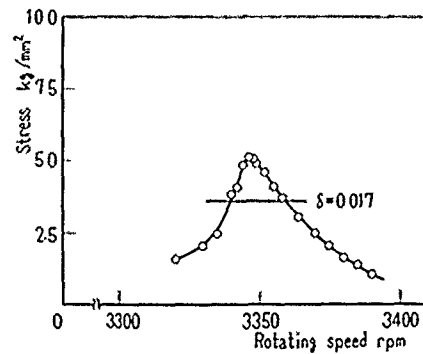


Fig.14 Measurement of total logarithmic decrement of rotating blade

Table 2 Theoretical and experimental values of resonant stress due to each harmonic component

n	V_{rn} m	W_{pn} m	k_n	δ_s	σ_n (Th) kg/mm ²	σ_n (Ex) kg/mm ²
1	100	7.24	1.52	0.013	5.72	5.1
2	50	1.04	3.04	0.007	0.95	1.06
3	33	0.65	4.56	0.006	0.26	0.3

(d / B = 0.18)

n	V_{rn} m	W_{pn} m	k_n	δ_s	σ_n (Th) kg/mm ²	σ_n (Ex) kg/mm ²
1	100	5.56	1.52	0.012	4.69	4.0
2	50	1.02	3.04	0.007	0.61	0.64
3	33	0.42	4.56	0.006	0.17	0.2

(d / B = 0.54)

Th : Theoretical value

Ex : Experimental value

6. CONCLUSION

The present paper treats the vibration of the compressor blade with large mass ratio and small camber when the rotor blade passes through the wake shed from the preceding blade row. The stress evaluation method was presented and its validity was confirmed by comparing with experiment.

The following conclusions were obtained:

- (1) The unsteady force derived from isolated airfoil theory can be used as the external force in predicting the resonant stress of the blade, but this approach tends to over-predict the actual values.
- (2) As the present analytical result, obtained by also considering the unsteady force due to the blade vibration, is in good agreement with the experimental one, we can expect to get a more accurate evaluation than the analysis which ignored the aerodynamic damping.
- (3) It is clarified that the effect of aerodynamic damping on the resonant stress is large for small structural (with material damping) damping and small reduced frequency, and that if μ becomes small, the aerodynamic damping effect appears in the region of large reduced frequency. This fact is independent of the angle ϕ which is made by the rotor blade and the stator blade.

Since the unsteady aerodynamic force used in the present analysis was derived from an isolated airfoil theory, this force can be applied only to a cascade with low solidity. However in a real cascade, the natural frequency of each blade is not always the same, so the vibrational phase difference between adjacent blades varies with time and the amplitude is not always the same too. Then it is thought to be difficult to examine these effect in detail.

From above reason, the present analysis is useful for predicting the resonant stress of the blade in engineering because it is in good agreement with the experiment.

REFERENCES

1. Karman, Th. and Sears,W.R., "Airfoil Theory for Non-uniform Motion", Journal of The Aeronautical Science, Vol.5, No.10, 1938, pp. 379-390.
2. Sears,W.R., "Some Aspects of Non-stationary Airfoil Theory and Its Practical Application", Journal of the Aeronautical Sciences, Vol.8, No.3, 1941, pp. 104-108.
3. Kemp.N.H. and Sears.W.R., "The Unsteady Forces due to Viscous Wakes in Turbomachines", Journal of the Aeronautical Sciences, Vol.22, No.7, 1955, pp.477-483.
4. Horlock,J.H., "Fluctuating Lift Forces on Aerofoils Moving Through Transverse and Chordwise Gust", Transactions of ASME, Series D, Vol.90, No.4, 1968, pp.494-500.
5. Naumann, H. and Yeh,H., "Lift and Pressure Fluctuations of a Cambered Airfoil under Periodic Gusts and Applications in Turbomachinery", Transactions of ASME, Series D, Vol.90, No.4, 1973, pp.1-10.
6. Whitehead,D.S., "Force and Moment Coefficients for Vibrating Airfoils in Cascade, Report and Memoranda, A.R.C. No.3254, 1960, pp.1-37.
7. Kemp.N.H. and Sears.W.R., "Aerodynamic Interference Between Moving Blade Rows", Journal of Aeronautical Sciences, Vol.20, No.9, 1953, pp.583-597.

NUTATION DAMPERS AND SUPPRESSION OF WIND INDUCED INSTABILITIES

V. J. Modi and F. Welt
Department of Mechanical Engineering
University of British Columbia
Vancouver, B. C., Canada

ABSTRACT

Performance of a set of torus-shaped nutation dampers, suitable for arresting relatively low frequency oscillations, is studied experimentally using a simple test facility. Results suggest damping characteristics to be particularly sensitive to physical properties of the liquid used, its height in the torus, damper geometry, and dynamical parameters representing amplitude and frequency. Among the configurations studied, dampers with perforated inside tubes, baffles, horizontal layers and floating rectangular pieces of wood in flow showed most favorable performance in terms of energy dissipated per unit volume. Tests on two and three dimensional models in smooth flow and boundary layer tunnels, with the models undergoing vortex-induced resonance and galloping conditions, suggest that nutation dampers can effectively suppress both forms of instabilities over a wide range of wind velocity. The concept is likely to be suitable in industrial aerodynamics, earthquake and ocean engineering problems.

1. INTRODUCTION

Response of aerodynamically bluff bodies when exposed to a fluid stream has been a subject of considerable study for quite some time. The prevention of aero-elastic vibrations of smokestacks, transmission lines, suspension bridges, tall buildings, etc., is of particular interest to engineers. Ever since the pioneering contribution by Strouhal, who correlated periodicity of the vortex shedding with the diameter of a circular cylinder and velocity of the fluid stream, there has been a continuous flow of important contributions resulting in a vast body of literature. This has been reviewed rather adequately by Cermak [1]. In general, the oscillations may be induced by vortex resonance or geometric-aerodynamic instability called galloping.

Several passive devices such as helical strakes, shrouds, slats, tuned mass dampers, etc., have been proposed over years and have exhibited a varying degree of success in minimizing the effects of vortex induced and galloping types of

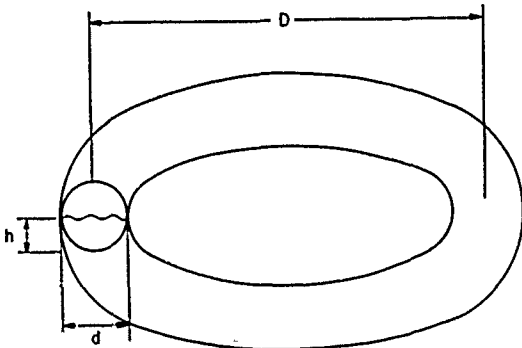


Figure 1 Nutation damper configuration

encountered in wind induced instability of bluff bodies, earthquake response of buildings, and wave excited vibrations of off-shore structures is relatively small, it was thought appropriate to explore applicability of nutation dampers to this class of problems.

2. DAMPING RATIO AND ENERGY DISSIPATION

A nutation damper can be characterized by its dimensions, physical properties of the liquid contained, oscillation characteristics as well as the system inertia under which the damper responds. The variables involved may be classified as follows:

• Geometrical Dimensions	:	ring diameter	D
		cross-section diameter	d
		surface roughness	ϵ
		liquid height	h
• Physical Properties of Liquid	:	density	ρ
		viscosity	μ
		surface tension	σ
• System Dynamical Properties	:	frequency	f
		amplitude	a
		total mass	M
		inherent damping	η_s
• Natural Parameter	:	gravitational acceleration	g

The twelve basic variables with three dimensions lead to nine dimensionless members:

dimensionless amplitude of oscillations	$\pi_1 = a/d$
dimensionless liquid height	$\pi_2 = h/d$
dimensionless surface roughness	$\pi_3 = \epsilon/d$
inertia stress/viscous stress (Reynolds number)	$\pi_4 = \rho d^2 f / \mu$
shape factor	$\pi_5 = D/d$
liquid fraction, mass of liquid/total mass	$\pi_6 = \rho d^3 / M$
inherent damping ratio	$\pi_7 = \eta_s$

$$\begin{array}{ll} \text{inertia force/surface tension force (Weber number)} & \pi_8 = \rho d^3 f^2 / \sigma \\ \text{inertia force/gravity force (Froude number)} & \pi_9 = f^2 d / g \end{array}$$

Note, these represent only the parameters associated with the fundamental geometry of the damper. Any modification to the internal geometry would add to the variables and the corresponding group of the π -numbers. The list of parameters given below refers to specific changes in the basic internal configuration aimed at increasing the damping due to sloshing motion of the liquid:

• Spheres (Balls) in the Flow	:	number of balls	n
		ball diameter	d_b
• Screens	:	number of screens	n
		open area	A
• Inside Tube with Perforations	:	tube diameter	d_t
		tube height	h^*
		hole size	q
	:	number of holes	n_o
• Baffles	:	baffle height	h'
		baffle area	b
	:	number of baffles	n
• Horizontal Layers	:	number of layers	n_L
• Pieces of Wood in Flow	:	volume	v
		number	n_w

The corresponding π numbers are readily obtained as the variables are mostly dimensionless or have the dimension of length. They were nondimensionlized with respect to 'd'. Damping characteristics were assessed through the use of two criteria: the damping ratio η and the dimensionless energy dissipation parameter

$$\bar{E}_{a,f} = E_d / f^2 a^2, \text{ where:}$$

$$\begin{aligned} E_d &= (E - E_s) M_L ; \\ E &= \text{total energy dissipated per cycle} = [(k/2)(x_1^2 - x_{m+1}^2)]/m ; \\ k &= \text{spring stiffness;} \\ x_1 &= \text{spring amplitude of oscillation after } i \text{th cycle;} \\ E_s &= \text{energy dissipated by the system alone (excluding damper);} \\ M_L &= \text{mass of the liquid in damper;} \\ m &= \text{number of cycles;} \\ f &= \text{damped natural frequency;} \\ a &= \text{initial displacement of damper.} \end{aligned}$$

The two criteria are related.

2.1 Static Stand Test Facility and Models

To assess effectiveness of the damper during nutational motion, a static stand was designed. Essentially it consisted of a 1.2 m swing arm pivoted by a ball bearing at one end and supported by two springs whose stiffness and locations can be changed so as to provide a desired range of natural frequencies. The frequency of oscillation was monitored through a strain gauge, mounted on a clamp connected to one of the springs, in conjunction with a bridge amplifier meter and a Brüel and Kjaer type 2305 level recorder (Figure 2), which also provided the time history of the amplitude decay.

A family of twenty-seven dampers was designed to carry out the parametric study. Details of the models which proved to be relatively more effective are given in Table I. Characteristics of nutation dampers were studied through a

systematic variation of nine dimensionless parameters including h/d ; Reynolds, Froude and Weber numbers; D/d ; frequency parameter; etc.

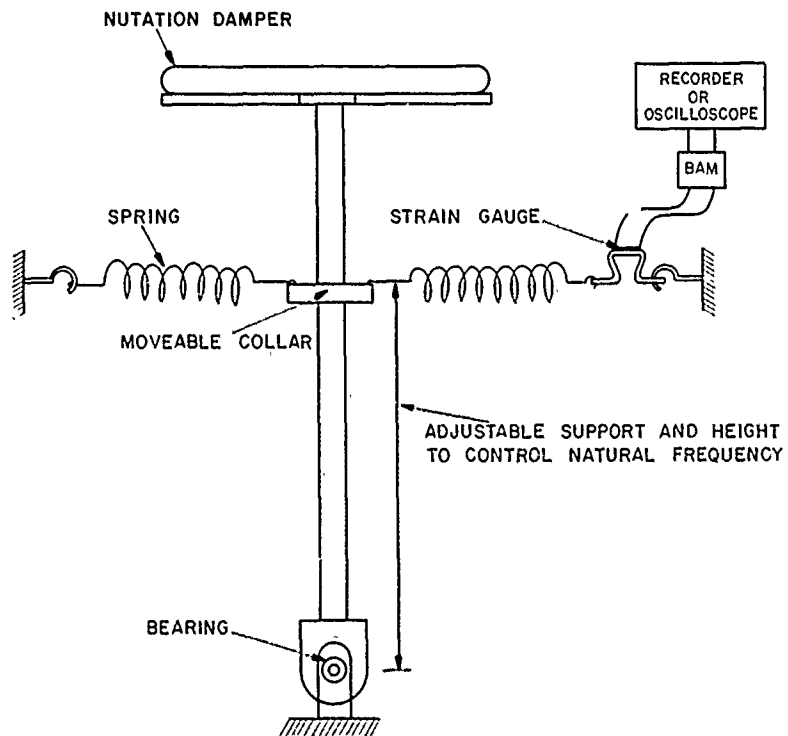


Figure 2 A schematic diagram of the static stand test facility

Table I Details of some of the damper models used in the test program

Damper	Dimensions		Description				
	d (cm)	D (cm)	Internal Configuration	Cross-Section	Material	Weight (gms)	Capacity (ml)
1	2.4	33.1	plain	circular	rubber	914	422
2	3.4	15.9	plain	square	plexiglas	1710	640
7	2.6	6.65	plain	circular	plastic	26	167
7A	3.0	8.3	plain	circular	plastic	27	184.1
7B	2.8	7.6	plain	circular	plastic	18	157.6
7C	2.4	5.5	plain	circular	plastic	12	78
8	1.9	28.9	plain	circular	copper	842	235
9	1.55	23.6	plain	circular	polyethylene	215	136
16	3.5	15.9	perforated tube	square	plexiglas	1740	635
17	3.5	15.9	baffles	square	plexiglas	1710	640
18	3.5	15.9	middle layer	square	plexiglas	1771	589
19	3.5	15.9	pieces of wood in flow	square	plexiglas	1710	640

2.2 Damper Characteristics

The amount of information collected through a planned variation of the system parameters is rather extensive; however, for conciseness, only a sample of data suggesting trends is presented here.

2.2.1 Effect of height/section diameter (h/d) ratio

Damping ratio η and energy dissipation rate $\bar{E}_{a,f}$ are highly dependent on the liquid height. For the circular cross-section damper (Damper 1 in Figure 3), optimum value of the liquid height parameter leading to a maximum η was found to be in the range $3/4 - 1$. The parameters $\rho d^3 f^2 / \sigma$ (Weber number) and $f^2 d / g$ (Froude number) have only a slight effect on this optimum value. However, $\bar{E}_{a,f}$ has a tendency to be maximum for low values of h/d , typically equal to $1/8$. In other words, the increase in damping η with h/d , as observed in Figures 3(a) and (b), is at a cost of an increase in the amount of liquid.

The square cross-section damper (Damper 2) showed similar trends at relatively high values of $\rho d^2 f / \mu$, $\rho d^3 f^2 / \sigma$ and $f^2 d / g$ (i.e., higher frequencies), where η reached a maximum for h/d close to 1 (Figure 3c). However, at lower values of $\rho d^3 f^2 / \sigma$ and $f^2 d / g$ (lower frequencies), η and $\bar{E}_{a,f}$ are both optimal for h/d around $1/8$ (Figure 3d). It should be mentioned that experiments with viscous engine oils (i.e., very small $\rho d^2 f / \mu$) showed similar trends, suggesting that the optimal damping as a function of h/d is essentially unaffected by the $\rho d^2 f / \mu$ parameter.

In summary, there is a value of h/d for which the damping is optimal. It depends on $\rho d^3 f^2 / \sigma$, $f^2 d / g$ (frequency), D/d and cross-sectional shape (geometry). This value is typically in the range $3/4 - 1$, although it is shifted towards the lower end in some cases due to reduced contribution of the top surface at lower frequency and liquid height. Energy dissipation rate was found to be generally maximum at low h/d , typically $< 1/8$, when there is high contact surface area per unit volume of water.

2.2.2 Reynolds number ($\rho d^2 f / \mu$)

To assess the effect of Reynolds number, liquid viscosity (μ) was changed using water and various types of engine oils in Damper 2, for selected frequencies. This helped isolate the influence of surface tension (σ) and gravity (g) at a given value of the Reynolds number. Results showed damping coefficient η and energy dissipation rate $\bar{E}_{a,f}$ to increase slowly as the Reynolds number decreased except for $\rho d^3 f^2 / \sigma = 0.61$. Similar trends were observed for constant values of $f^2 d / g$ (Froude number). The reversal of trend for $\rho d^3 f^2 / \sigma = 0.61$ at low values of $\rho d^2 f / \mu$ would suggest a change in damping and energy dissipation mechanism which is now governed by the liquid resonance as against viscosity.

2.2.3 Influence of ring diameter/section diameter (D/d) ratio

Figure 4 shows the effect of ring diameter (D) on the dissipation process in high and low frequency regimes with the tube cross-sectional diameter (d) held fixed. At a relatively higher frequency ($f = 2.27$ Hz), both the damping ratio and the energy dissipation function decrease with an increase in the ring to tube diameter ratio ($D/d < 10$). Note, at higher D/d , the damping ratio increases due to a larger volume of the liquid, however, more accurate assessment of the efficiency is reflected by $\bar{E}_{a,f}$ which remains essentially constant in this

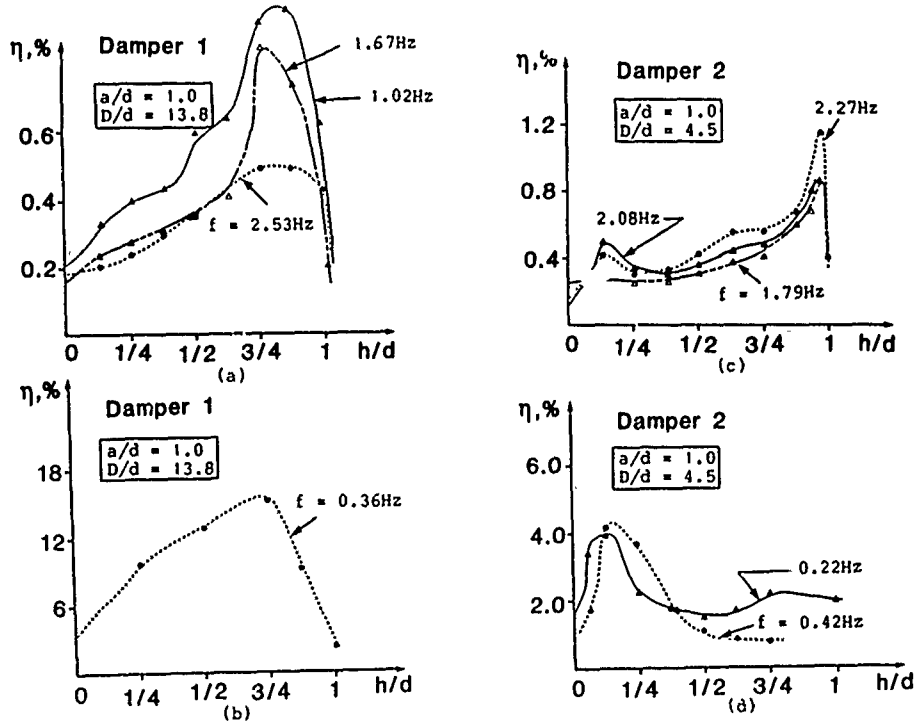


Figure 3 Variation of the damping ratio with the liquid height

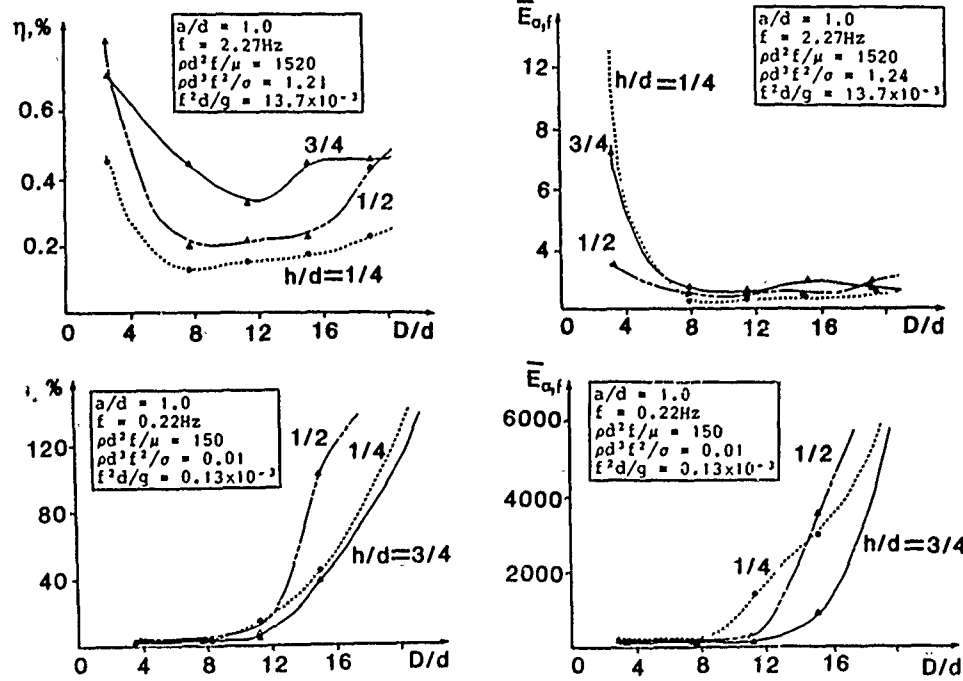


Figure 4 Effect of ring diameter on dissipation characteristics in high and low frequency regimes

range ($D/d > 10$). At low frequency ($f = 0.22$ Hz) this trend is reversed. η and $E_{a,f}$ remain essentially constant over a range of D/d extending from 0 to 8 (slight variation in location of the critical point according to liquid height h/d), and suddenly rise to much higher values at larger D/d . Again this may be attributed to the liquid resonance condition.

2.2.4 Weber number ($\rho d^3 f^2 / \sigma$) and Froude number ($f^2 d / g$)

Keeping the Reynolds number ($\rho d^2 f / \mu$) constant permits a study of the combined effect of Weber and Froude numbers. The results showed that there is a critical region where η and $E_{a,f}$ are much higher. The critical range associated with the liquid resonance was around $0.4 - 1.0$ for the Weber number and $(1.5 - 4.0)10^{-3}$ for the Froude number. This dependence on the Weber and Froude numbers, regardless of the viscous contribution, points out the importance of the free surface. Surface tension and gravity forces appearing in the Weber and Froude numbers, respectively, indeed affect the oscillatory motion of the free surface. However, contribution of the surface tension force is expected to be insignificant here. On the other hand, gravity represents the restoring force during sloshing motion, hence, the Froude number should be predominant. The effect of the Froude number is primarily confined to the critical region only, where the natural frequency of the sloshing liquid (which is a function of gravity and therefore of the Froude number) coincides with the excitation frequency leading to maximum $E_{a,f}$ and η .

2.2.5 Effect of excitation frequency (f)

Additional sets of experiments were carried out to measure the influence of frequency alone (for the same liquid), which involves a variation of the η -numbers in $\rho d^2 f / \mu$, $\rho d^3 f^2 / \sigma$ and $f^2 d / g$ simultaneously. Dampers 1, 2, 7, 8 and 9 were used to this end (Figure 5). Since the influence of $\rho d^2 f / \mu$ is quite smooth (continuous) and surface tension is not an important parameter here, the effect of a change in frequency is mostly reflected through the Froude number. For a given D/d ratio, corresponding to a given damper, there is a region for which damping is significantly higher. This region is the low frequency area for high D/d ratios (e.g., $D/d = 15.2$), and is shifted to higher frequencies as D/d decreases (e.g., $D/d = 4.5$ and 2.65). This reinforces the conclusion arrived at earlier. Changes in damping in this critical region are again sudden and drastic and therefore there is a relationship between the critical region location, D/d ratio and Froude number $f^2 d / g$, corresponding presumably to the first natural frequency of the sloshing liquid. A series of tests separately undertaken (not discussed here) verified this premise. It is interesting to note that Damper 2 (i.e., $D/d = 4.5$) shows a second peak at $f = 2.10$ Hz, which corresponds to the second natural frequency of the liquid.

2.2.6 Modified internal configurations

A large number of tests aimed at assessing the influence of modifications in the internal geometry on the energy dissipation process were undertaken. They included introduction of: (i) surface roughness; (ii) spheres in flow; (iii) screens; (iv) perforated tube; (v) baffles; (vi) horizontal partition; (vii) floating pieces of wood. Some of the more promising results are summarized here (Figure 6). In the high frequency range, perforated inside tube device and floating pieces of wood exhibit highest peak values of η , while baffles show more consistent improvement over the entire range of h/d . The two layer damper is not competitive at high frequency, but is most successful in the low frequency range ($f = 0.22$ Hz). As can be expected, the energy dissipation

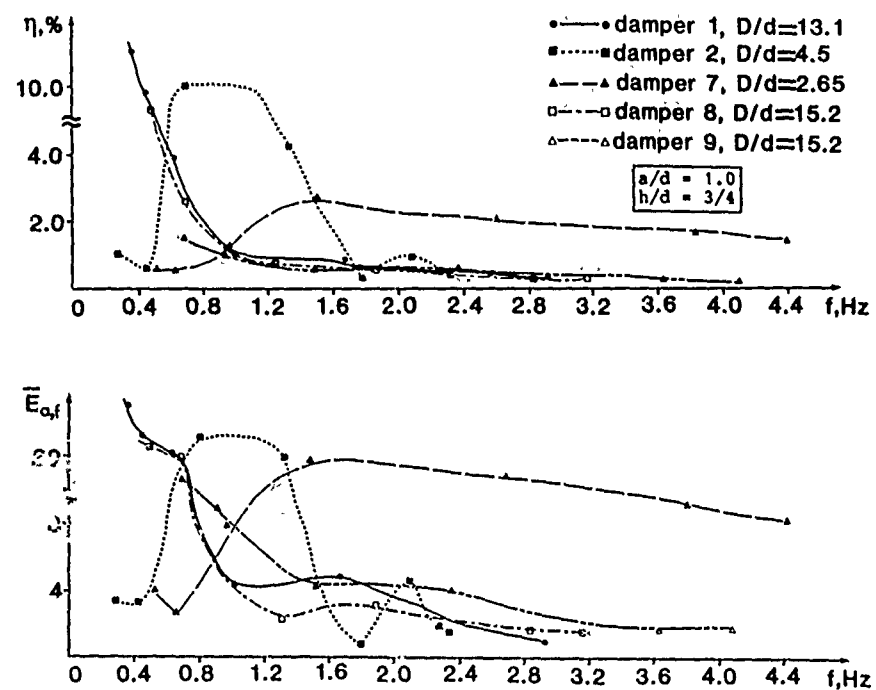


Figure 5 Effect of frequency and damper diameter ratio D/d on the dissipation functions η and $E_{a,f}$

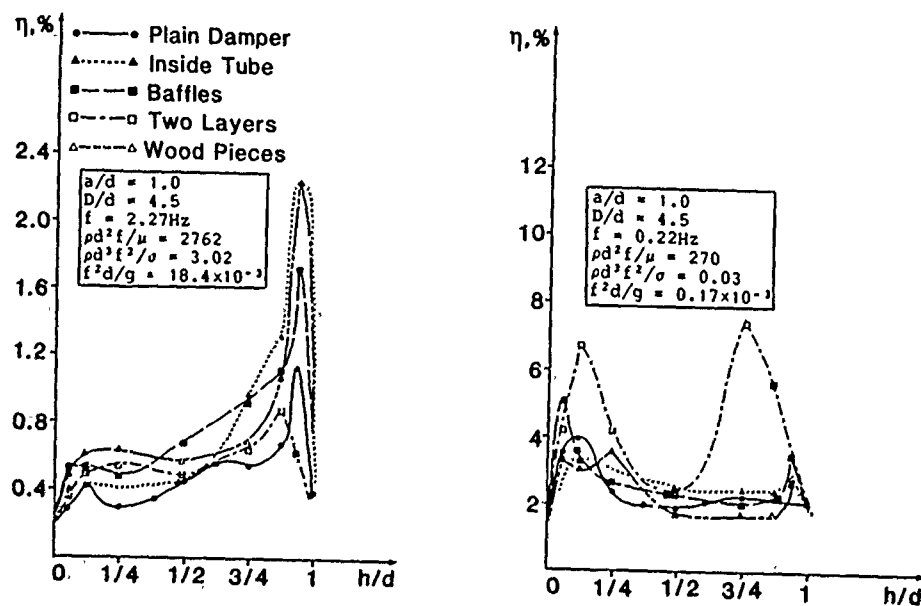


Figure 6 Comparative performance of several more promising damper configurations

rate $E_{a,f}$ showed peak values in the low range of h/d where this class of nutation dampers are most efficient, whereas, Figure 6 emphasizes high values of h/d where damping ratios are maximum. Thus, design of a damper will be a compromise dictated by the structural frequency together with the physical constraint represented by D/d . The ultimate objective would be to minimize the damper mass and yet attain the liquid resonance for optimal damping.

3. WIND INDUCED INSTABILITY STUDIES

Effectiveness of the dampers in controlling vortex resonance and galloping instabilities for a family of two and three dimensional models was studied in both laminar and turbulent flows. A closed circuit laminar flow wind tunnel with a test-section of $0.69 \times 0.91 \times 2.44$ m is able to produce a stable flow with velocity ranging from $0.3 - 30$ m/s and turbulence level of less than 0.1%. Turbulent flow tests were conducted in a boundary layer tunnel ($1.58 \times 2.44 \times 24.4$ m) with 20.74 m of roughness board installed in the test-section upstream of the model to produce desired boundary layer thickness and turbulence intensity.

Two different air-bearing systems were used during the test programme. The first system was essentially composed of four bearing blocks located outside the tunnel test-section, two on the top and two at the bottom, carrying sliding shafts which in turn support the model under test (Figure 7). The system enables the model to travel transverse to the direction of the free stream thus simulating a two-dimensional plunging motion. The second air-bearing system supports a shaft which is free to rotate about its longitudinal axis (Figure 8). When attached to a model the shaft acts as a free pivot point and provides a rigid body rotational motion with one degree of freedom. The longitudinal displacement of the model in plunging was measured by an electromagnetic transducer. The time history of the model displacement in the second case was obtained using a simple strain gauge device.

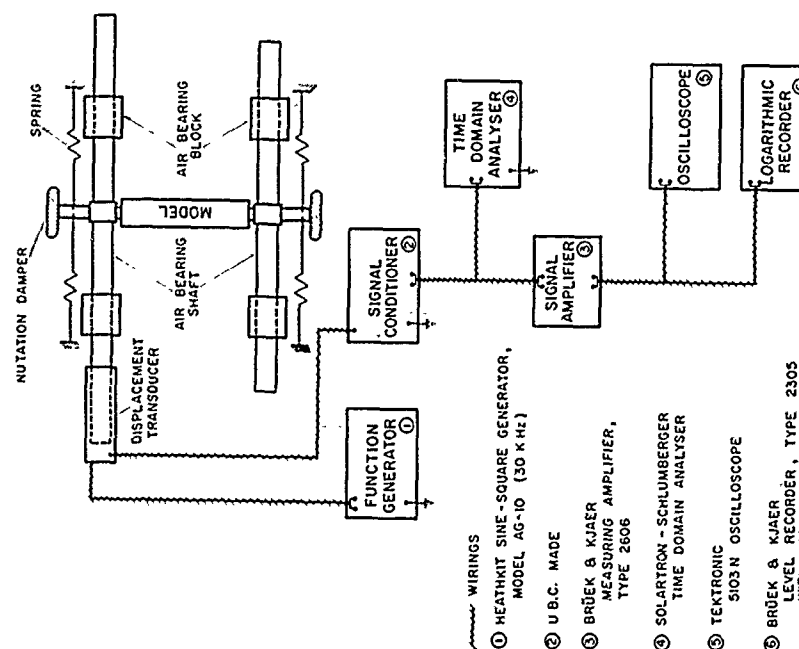
The dampers were mounted on a variety of different models during the tests. The models had either circular or square cross-section. The two-dimensional models essentially spanned the height of the tunnel (0.69 m) while the models of finite span simulated three dimensional conditions (Table II).

Table II Physical description of aerodynamic models

MODEL	I, 2-D	II, 2-D	III, 3-D	IV, 3-D	V, 3-D	VI, 2-D
CROSS-SECTIONS						
LENGTH (mm)	686	686	483	705	483	686
MATERIAL	ALUMINUM	BALSA	BALSA	BALSA	BALSA	BALSA
MASS (g)	383	234	253	VARIABLE	376	124

3.1 Damper Performance in Smooth Flow

The aerodynamic instability for a circular cylinder exposed to a fluid stream is due to vortex shedding. In this set of tests, Models I, IV and V



182

Figure 7 The air-bearing system used to support a model during plunging tests with associated instrumentation

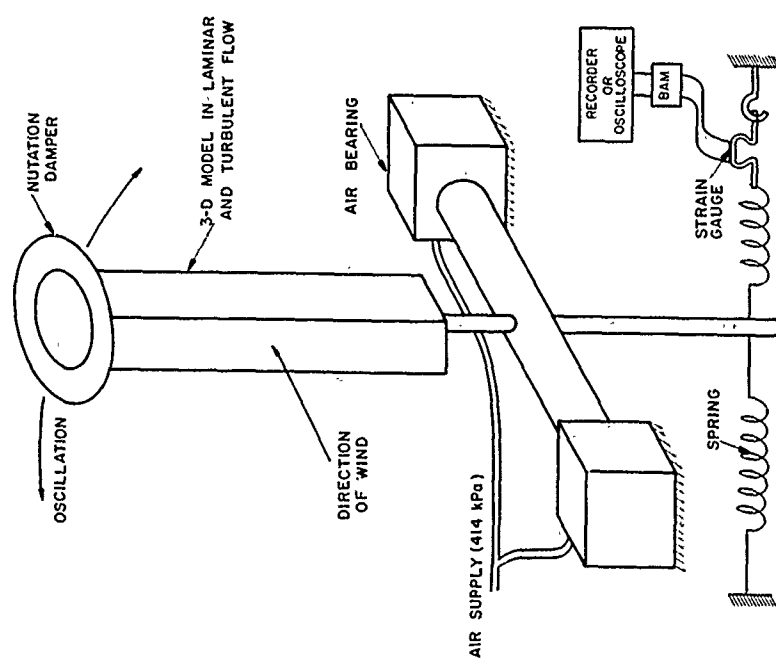


Figure 8 Static stand test facility used during the wind tunnel tests

were used in conjunction with several dampers at different natural frequencies of the model and system mass parameter $M/L_m \rho_a d_m^2$ (where M = total system mass, L_m = model length, ρ_a = air density, d_m = model diameter or width). Typical results are shown in Figures 9 and 10. Here U , the dimensionless free stream velocity is defined as $U_\infty/\omega_n d_m$ where U_∞ represents the free stream velocity and ω_n is the system's natural frequency. Note, with the plain damper 7B ($D = 76$ mm, $d = 29$ mm) the dimensionless amplitude Y (y/model width) at resonance is dramatically reduced from around 0.575 for the empty damper to 0.02 when half-filled with water, a 96.5% reduction. The performance remains equally impressive even with the smaller damper 7C (Figure 9).

Figure 10 shows vortex resonance response in the presence of two different dampers with modified internal configuration. The results are presented for two aerodynamic models having different values of mass parameter and natural frequency. As the objective is to assess relative effectiveness of the damper configurations, the liquid height was held fixed during a set of tests. To facilitate comparison, corresponding results for the plain damper are also included.

At a high frequency ($f = 3.17$ Hz, Model VI), the effect of internal modification in the damper geometry through introduction of baffles or perforated tube on amplitude of oscillations appears to be insignificant when the liquid depth is small ($h/d = 1/4$). However, for $h/d = 3/4$, the situation changes dramatically. With the plain damper, the amplitude resonance is reduced by around 12%. The damping effectiveness improves with baffles and the oscillations are virtually arrested completely with the perforated tube.

At a relatively low frequency of $f = 1.9$ Hz (Model V), the damper configurations are sensitive to even small h/d of $1/4$. However, at $h/d = 3/4$ there is

MODEL I (0,2-D)

$K = 212 \text{ N/m}$, $f = 4.8 \text{ Hz}$

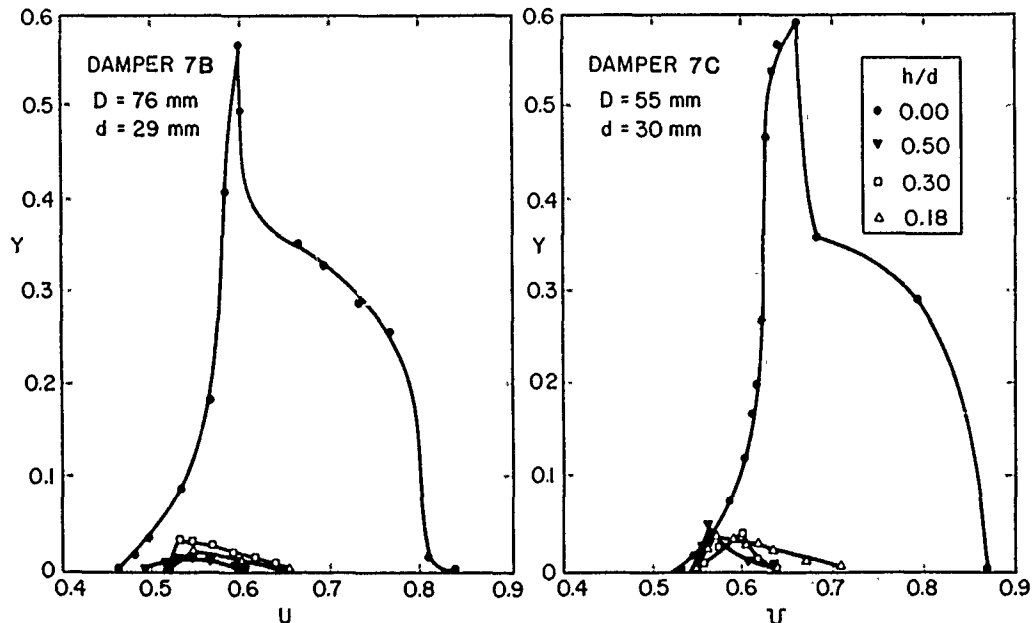


Figure 9 Plots showing effectiveness of dampers 7B and 7C in controlling vortex induced instability of a two dimensional circular cylinder

little difference in the response and all configurations damp the motion successfully. Thus appropriate choice of damper configuration and liquid height for a given situation will be governed by the natural frequency of the system.

For square prisms, galloping occupies a more important position than vortex resonance so far as the aerodynamic instabilities are concerned. Effectiveness of the ring dampers in controlling galloping motion is illustrated in Figure 11. Oscilloscope records of the vibratory response are displayed at appropriate locations to facilitate understanding. The results show the nutation damper to be remarkably effective even for water level as low as $h/d = 0.18$. Note, in absence of the damping fluid, the classical vortex resonance peak appears at around $U = 1.25$ followed by a hysteresis loop indicating two equilibrium positions. In this region, equilibrium state of the model jumps from a low level to a high value when subjected to an external disturbance. At $U \approx 5$, large amplitude oscillations set in which quickly exceeded the limit of the test arrangement. However, with damping, not only the vortex resonance is

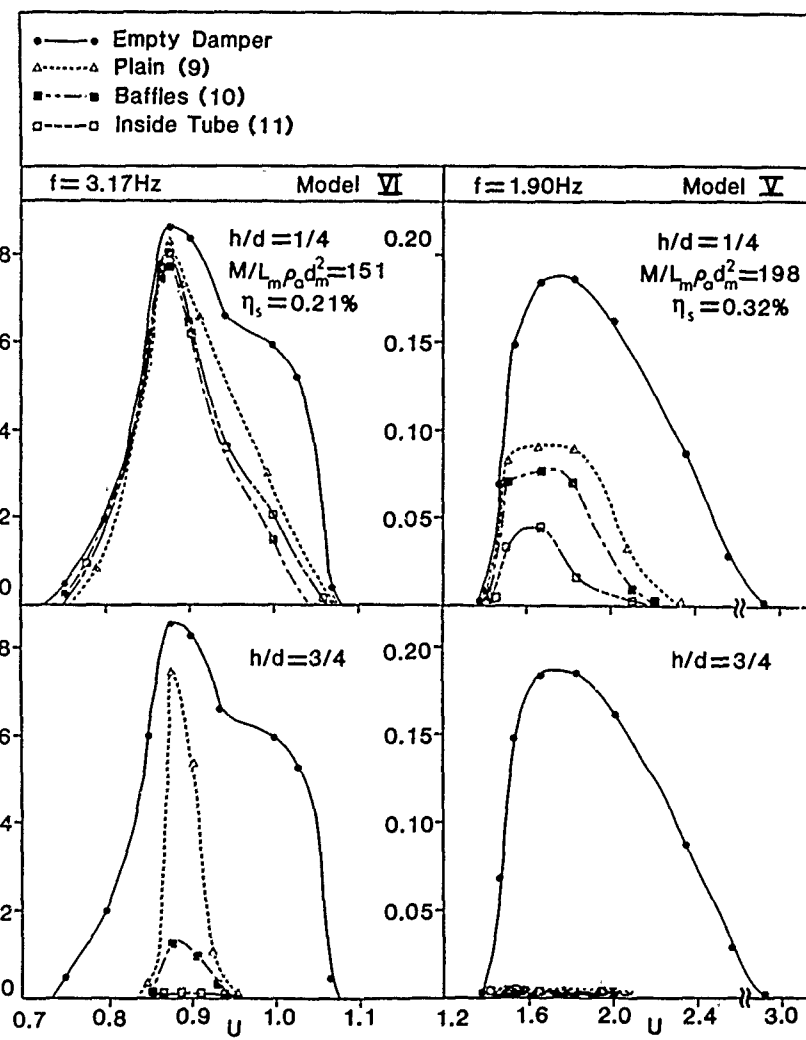


Figure 10 Effect of damper configurations on vortex resonance

essentially eliminated but also the onset of galloping is delayed or suppressed completely over the entire operating range of the tunnel velocity. Even with the water level as low as $h/d = 0.18$, onset of the galloping instability as indicated by the start of a hysteresis loop is delayed to U as large as 22. Results with the larger nutation damper 7A were even more spectacular.

Figure 12 attempts to assess influence of modifications in the damper's internal geometry on galloping response of a three dimensional model. It is apparent that irrespective of the liquid heights used both the dampers, with baffles and perforated tube, remain equally effective in suppressing galloping instability over a wider range of wind speeds. The same is true with the plain damper. However, the amplitudes of oscillations here are relatively small suggesting smaller excitation force compared to the weight of the model. Damping required to arrest the motion being small, the role of configuration becomes unimportant. Experiments with a larger model resulting in higher excitation force and hence larger galloping amplitude confirmed this observation. The results (not presented here) showed perforated tube configuration to perform better also during galloping.

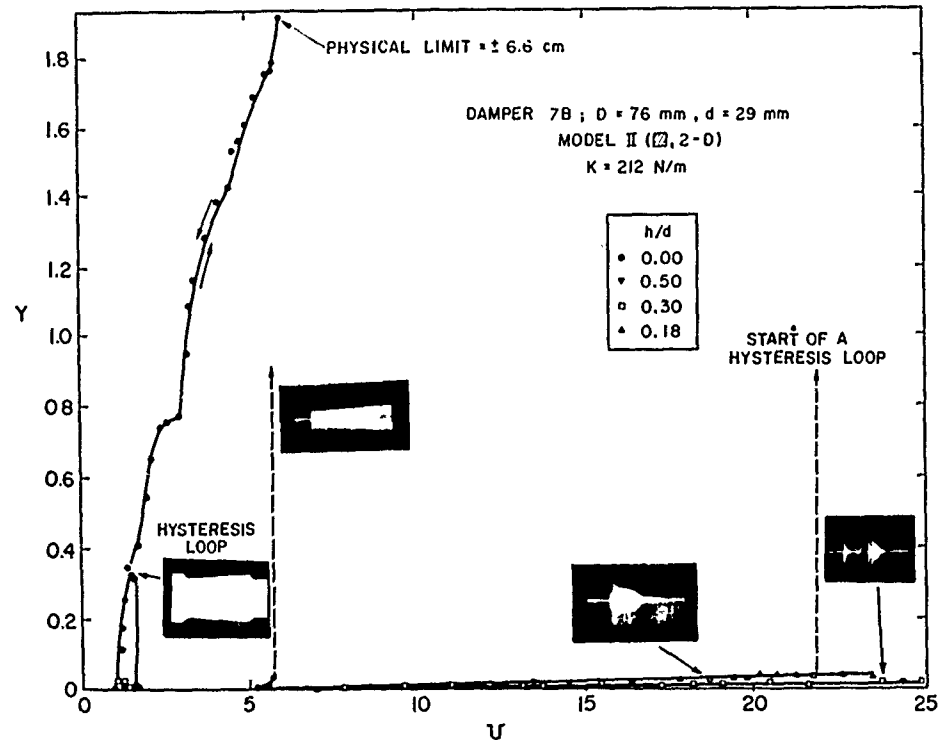


Figure 11 Damper effectiveness in controlling galloping response of a two-dimensional square prism in laminar flow

3.2 Damper Performance in Turbulent Flow

As in the actual practice, an engineering structure (smokestacks, buildings, bridges, etc.) is generally exposed to a turbulent boundary layer, it was essential to study system response under similar simulated condition. Typical results under this condition are displayed in Figure 13, which also accounts for three dimensional character of the prototype.

In absence of any damping liquid, the galloping instability sets in at $U \approx 8.2$. However, with damper 7A half-full, the galloping oscillations are completely suppressed over the entire range of the tunnel velocity. The response remains unaltered even for $h/d = 0.3$. Note, with h/d as low as 0.18, onset of the hysteresis loop is delayed to $U \approx 16.4$. As anticipated, galloping amplitudes were found to be smaller in the turbulent flow compared to those observed in the laminar case. This may be attributed to a reduction in the organized energy input to the system.

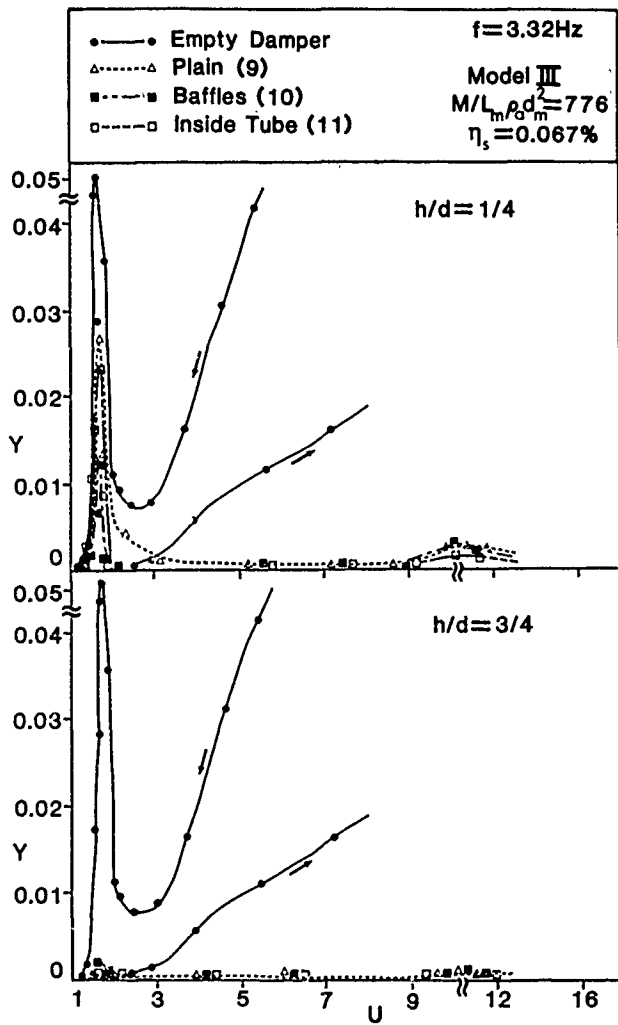


Figure 12 Effect of damper configurations on galloping response

4. CONCLUDING REMARKS

The experimental program has attempted to assess the influence of more significant parameters on the energy dissipation process. The amount of information obtained is rather extensive and would be useful in the design of efficient dampers for a wide range of applications. The proposed nutation dampers

represent a useful concept in minimizing the effects of wind induced instabilities. They showed encouraging performance during both vortex induced and self-excited galloping type of oscillations. The experiments also demonstrated effectiveness of the dampers for either two dimensional plunging motion or pivoted rigid body rotation for three dimensional models both in laminar and turbulent flows.

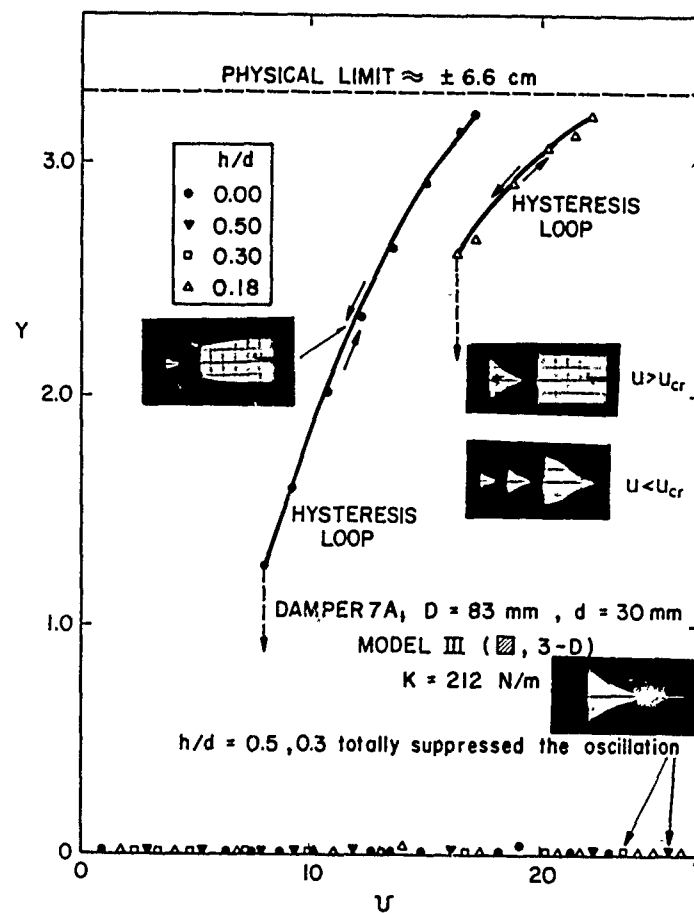


Figure 13 Galloping response of a three dimensional square prism in a turbulent flow

REFERENCES

- [1] Cermak, J.E., "Application of Fluid Mechanics to Wind Engineering," Freeman Scholar Lecture, Transactions of ASME, Journal of Fluids Engineering, Vol. 97, No. 1, March 1975, pp. 9-38.
- [2] Zdravkovich, M.M., "Review and Assessment of Effectiveness of Various Aero and Hydromechanic Means for Suppressing Vortex Shedding," Proceedings of the 4th Colloquium on Industrial Aerodynamics, Aachen, West Germany, Part 2, Editors: C. Kramer et al., 1980, pp. 29-46.

TRANSIENT LOADING OF PILE-SHELL-TYPE SUPPORTED OFFSHORE STRUCTURES

V. A. Dzhupenov, D. D. Karagozova, and V. M. Vassilev
Bulgarian Academy of Sciences
Institute of Mechanics and Biomechanics
Sofia, Bulgaria

ABSTRACT

The description of an offshore scaffold bridge consisting of bridge desk supported by row of pile-shells is given. The transient loadings are discussed. The problem of the dynamical structure-liquid interaction is solved by a method of successive approximations. Engineering estimations are presented.

1. INTRODUCTION

1.1. General Considerations

Circular cylindrical structural components are widely used in offshore engineering structures (ocean scaffold bridges for petroleum production, piers, ocean oil platforms, etc.). The calculation of such structures is always connected with estimations of hydrodynamical loadings of different nature. These loads result from the dynamical liquid-structure interaction. The structural component vibrations can be forced as a consequence of any technological processes connected with the operation of the equipment which is disposed on the bridge deck, in other cases the vibration can be produced by earthquake waves propagating along the ideal ocean bottom; the last case is when the vibration excitation is produced by waves propagating in ocean water stratum (due to underwater explosions, earthquakes, etc.). In every one of these three excitation cases the hydrodynamical loading determination must be made separately taking into account the specific peculiarities of the system.

1.2. Structural Description

In shallow water with constant depth h a scaffold bridge is built. It consists from a row long cylindrical shells serving as supports of the bridge deck. The geometrical dimensions and their designations are given in Fig.1. The shells are linearly elastic, and clamped on the ocean bottom.

1.3. Pile-Shells

Usually the circular cylindrical structural components (used as supports) have been produced in shape of tubes, or (if radius R is larger) in shape of shells. Thus their floating transport to the

assembly place is easier. But after sinking into place they are filled with well compacted sand - to be heavier and to turn into piles. The piles have uniform cross sections, and as a consequence - better rigidity.

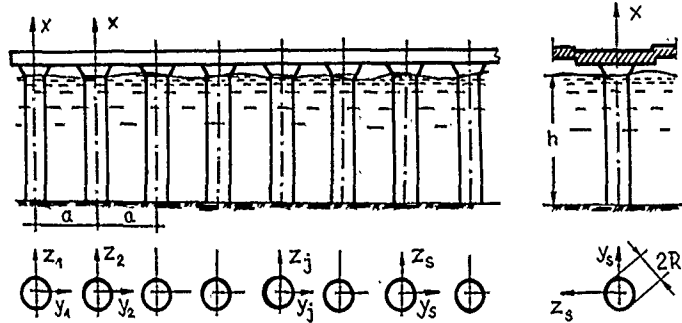


Fig.1. Scaffold bridge in shallow water.

1.4. Superstructure Rigidity

One would underline that the bridge deck has very great rigidity in the horizontal plane. It is presumed that the bridge deck synchronizes the vibrations of the whole row of piles. Of course, due to the large length of the row, the bridge deck is not practically infinitely rigid, Fig.2. The prerequisite that all piles are vibrating in the y-direction is supposed, when the deck is taken as absolutely rigid. Otherwise, the phase displacements of the consequent pile vibrations must be taken into account.

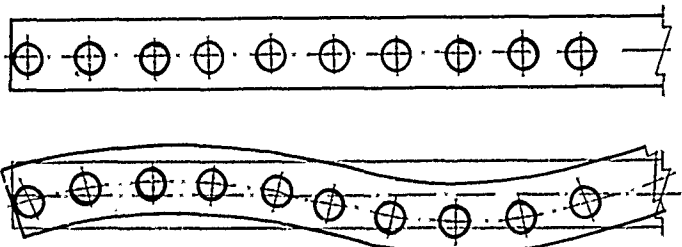


Fig.2. Rigidity of the superstructure.

1.5. Indices

The row piles are identified by the running index $j=1, 2, 3, \dots$. The index s denotes the pile considered.

1.6. Co-ordinates

The investigations are made in local cylindrical co-ordinates (r_s, θ_s, x) , obtained from the rectangular ones by the transforms, Fig.3.,

$$r_s^2 = y_s^2 + z_s^2, \quad \theta_s = \arctg(z_s/y_s). \quad (1)$$

An arbitrary point S of the liquid stratum can be identified by the co-ordinates of an arbitrary of the local systems, i.e. one can write $S = S(r_j, \theta_j, x, t)$, $j = 1, 2, \dots$. Then the investigator will need the transforms $(j \rightarrow s)$, Fig.3.,

$$r_s^2 = r_j^2 + (|s-j|a)^2 + 2r_j(|s-j|a)\cos\theta_j, \quad \theta_s = \arcsin(r_j/r_s)\sin\theta_j. \quad (2)$$

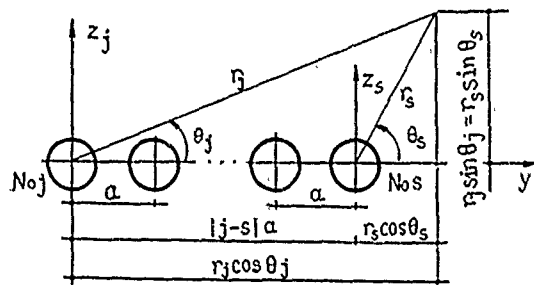


Fig.3. To the summation formulae.

1.7. Water

The water is assumed to be compressible with sound velocity $c \sim 1450$ m/s (at 20°C). Besides that, it is assumed to be ideal.

1.8. Short Review

The structures of the type under consideration have been the object of scientific investigations for a long time [1-8, etc.], but the systematic investigation of their interaction with the liquid, in which they are vibrating, is far from being closed. Usually with the help of the solution for one shell (or pile) [6,9-13] the solutions for groups of components have been constructed.

In Ref.[6] the following approach is accepted: (i) a solution is obtained for a group of two components vibrating along the main axes of the group; (ii) then follows a solution for a group of two components, but vibrating in one arbitrary direction; (iii) each of the two components in the group is vibrating in its own direction; (iv) vibrations in arbitrary directions of more than two arbitrarily disposed vertical shell-piles. This logical scheme has large generality and permit the construction of the solutions for arbitrarily disposed groups of supports. In Ref.[10-12] the problem on the hydroelasticity of a two-component group is developed fully. In Ref. [13] the infinite row of piles is considered. The method of successive approximations was suggest first in Ref.[14] for the vibrations of inner tubes of nuclear reactor vessel and in Ref.[15] for the external problem. Refs.[16,17] are connected and contain estimations of the "influence matrix" for a semi-infinite row of piles.

Here some books and articles, characteristic of the Russian School on hydroelasticity of offshore structures are referred to. They include the fundamental works of Ishkov[1], Kulmatch[18], Has-kind[3], Sheinin[5].

Comparatively full reviews on the corresponding stages the curious reader can find in the special reviews of Wiegel[7], Wootton [19], Shaw[20], Plate[21], edited by Naudascher[22], and Naudascher & Rockwell[23], as well as in Brebbia & Walker's book[24].

2. THE PROBLEM

2.1. Excitations

The wave loadings onto the offshore structures have a very large frequency spectrum. Any of the perturbation frequencies periodically may be found to coincide with the natural frequencies of an arbitrary part of the structural components. In such cases, because of the response phenomena, the full dynamical analysis of the liquid-structure interaction is necessary. As the structural natural frequency spectrum is a discrete one, the uniform spectrum of special excitations of the water wave fields (explosive, earthquake, etc.), will be filtered by the structure. Hence, always the resonance picture described above will exist.

2.2. Transient or Stationary Excitations?

The problems of the interaction between the incident wave field and the system of cylindrical components occur in the array design. There, however, as in the majority of the previous papers of the first of the authors, the incident field is approximated by a system of stationary waves and the interaction between the structure and the field is considered as a stationary process. This is done with the purpose of simplifying the interpretation of the problem. But these solutions are exceptionally voluminous and cumbersome for an analytical solution and very difficult for computing. The reasons are earlier discussed, but the most important are: (1) infinite sequence of Bessel's functions, which are slowly converging, and (2) infinite algebraic systems with coefficients expressed in Bessel's functions, which are difficult to be solved (even by a computer). Another important reason is, that for stationary disturbances, a stationary process of vibration is obtained an infinitely long time after the beginning of the interaction, while in real life most interest is very often precisely in the unstationary processes commencing from the start of the application of the disturbing load. All this presupposes the search for another approach for the solution of the hydroelastic problem in cases of impulsively initiated loadings.

2.3. Incident Field Spectra

It is further assumed, that far from the structure under consideration, a source of impulsively excited acoustical field is disposed. The plane waves in the water attack the pile-shell row of the scaffold bridge. Let the incident field be representable in general form

$$\psi_0(S, t) = \sum_{m=0}^{\infty} C_m(f) \Phi_m(S) T(\omega_m t), \quad 0 \leq t \leq t^*, \quad (3)$$

where $S = S(x, y, z) = S(r_i, \theta_i, x)$ is a point of the liquid stratum, Φ_m is a function of the spatial co-ordinates, T -time function, t - time, ω_m - m th circular frequency of the spectrum performing the loading, $f_m = \omega_m / 2\pi$, $[f] = \text{Hz}$, $C_m(f)$ - Fourier's transform of the incident field.

Skudrzyk in his book [25] shows more than ten characteristic impulses, the corresponding resulting spectra $C(f)$, and their phase characteristics. The prerequisite that the characteristic time t^* of the impulse action is well accented will furthermore be taken into account. Evidently, this will give rise to a discrete spectrum of Fourier's transformants. On Fig.4. four impulses with accented time interval t^* are shown.

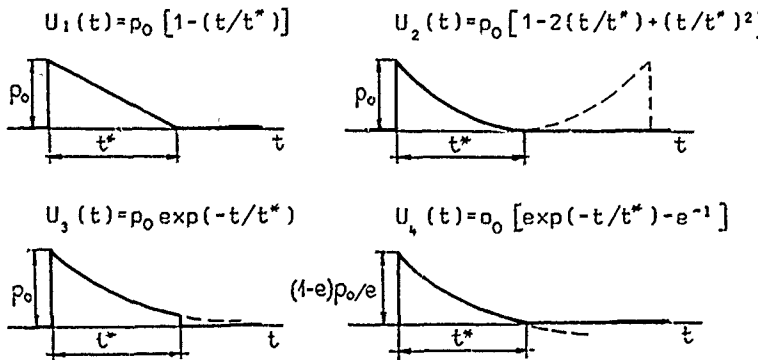


Fig.4. Characteristic burst impulses [15].

Their spectra are:

$$\begin{aligned} C_{1m} &= p_0/m\pi, & C_{2m} &= p_0(m\pi\sqrt{1+m^2\pi^2})^{-1} \\ C_{3m} &= C_{4m} = 2(e-1)p_0(e\sqrt{1+4m^2\pi^2})^{-1} \end{aligned} \quad (4)$$

if $\omega = 2m\pi/t^*$ and p_0 is characteristic pressure.

Then the general solution will be a sum of all harmonics, or of several of them, thus providing the main part of the solution. All previous problems considering stationary excitation have been based on the same idea. However, as these solutions are of a stationary type they retain all difficulties we accounted above.

The purpose of the present investigation is to give a simpler and more convenient, but at the same time sufficiently exact method to determine the structural behavior in case of the aforementioned types of wave loading.

2.4. The Idea of Successive Approximations

The idea of the successive approximations, applied previously to solve the analogous problem in the closed volume of reactor vessel [14], solves the problem here. The difference (here) is that the problem is expressed in Hankel's functions and the problem is the outside one. The possibility of representing the total wave field as a sum of three fields is used. They are: (i) the incident one, (ii) the scattered field (considering the cylindrical structural components as absolutely rigid obstacles), and (iii) the field due to the structural components emission, considering their elastic vibration (as really are not absolutely rigid).

Firstly, the shells are considered as absolutely rigid, and the scattered field due to the incident wave is determined. At the next step, the field determined on the previous step as a scattered one, is now used as the incident field. For the neighbouring structural components the scattered field is determined. On each successive step as an incident wave is taken the determined scattered field of the previous step. All this procedure can be repeated till the precision sought has been reached [14]. The main advantage of this method is that for every approximation the independent equations are obtained, and only two unknown constants must be determined. Of course, they are complex constants, but there are not any great difficulties for their determination.

As a consequence of both fields (the incident and the scattered), the structural components will be loaded by forces due to the hydrodynamical pressure. They will start to move and to emit additional waves in the liquid. But this will change the hydrodynamical forces. With the new forces the structural motion will change slightly, etc.

In Ref.[14] as a criterion to stop the procedure, the comparison of two forces, determined by two successive approximations, was used. (Here, the forces acting onto the surface of an arbitrary structural component, is meant.) Such a criterion is very convenient because it has an integral character. Analogous is the criterion on taking into account the interaction energies (between an arbitrary component and liquid), determined from two successive approximations, Ref.[15]. In the investigation presented here the first of them is used.

3. ANALYTICAL FORMULATION

3.1. Velocity Potential Function

The whole problem will be investigated in terms of velocity potentials. If, as was done above, the incident wave field is described in pressure terms, i.e. if the pressure $p_0 = p_0(x, y, z, t)$ satisfies the acoustical equation

$$\Delta p_0 - c^2 \ddot{p} = 0 \quad (5)$$

then recalling the linear relations

$$p_0 = -\rho (\partial \psi_0 / \partial t) \quad [\vec{v}_0 = \text{grad} \psi_0] \quad (6)$$

one can translate the problem in the space of velocity potential terms. Hence, within an additive constant, one can write

$$\Delta \psi_0 - c^2 \ddot{\psi}_0 = 0 \quad (7)$$

Analogously, the full velocity potential function, ψ , in near vicinity of an arbitrary component (after every approximation, e.g. the j th) must satisfy the acoustical equation

$$\Delta \psi^j - c^2 \ddot{\psi}^j = 0, \quad [\vec{v}^j = \text{grad} \psi^j]. \quad (8)$$

3.2. Boundary Conditions

The boundary conditions for full determination of ψ^j are separated into two groups. If ψ^j is a general velocity potential after the j th approximation, i.e. if

$$\psi_m^j = \psi_{0m} + \sum_{x=1}^j \psi_m^x + \sum_{x=1}^j \psi_{m(el)}^x, \quad (9)$$

where ψ_{0m} is incident wave potential, ψ_m^x the potential if the scattered field after the x th approximation, $\psi_{m(el)}^x$ the potential due to elastic vibration after the x th approximation, then from the separation

$$\psi_m^j = [\psi_{0m} + \sum_{x=1}^j \psi_m^x + \sum_{x=1}^j \psi_{m(el)}^x] x_m(k_m x) \dot{\psi}(w_m t), \quad (9^*)$$

where k_m is the wave number along the x -axis it is seen that the conditions along the x -axis are general for all problem. These conditions are

$$\left(\frac{\partial^2 \psi^j}{\partial t^2} + g \frac{\partial \psi^j}{\partial x} \right)_{x=h} = 0, \quad \frac{\partial \psi^j}{\partial x} \Big|_{x=0} = 0. \quad (10)$$

On the moving surfaces Σ of the piles, the general condition

$$(\vec{n} \cdot \text{grad} \psi)_{\Sigma} = \vec{v}_{\text{structure}} \quad (11)$$

must be satisfied. It can be decomposed taking

$$\vec{n} \cdot \text{grad} [\psi_{0m} + \sum_{x=1}^j \psi_m^x]_{\Sigma} = 0 \quad (12)$$

$$\vec{n} \cdot \text{grad} [\sum_{x=1}^j \psi_{m(el)}^x]_{\Sigma} = w_{\Sigma} \quad (13)$$

and these are already special conditions for different groups of the functions. In the last three equations \vec{n} is an unit vector, normal to the surface of the components; w_{Σ} is displacement function over the surfaces Σ .

Another special condition which must be satisfied by the functions

$$\left[\sum_x^j \psi_m^x + \sum_x^j \psi_{m(el)}^x \right] \dot{\psi}(w_m t) \equiv (\phi_m^j \dot{\psi}(t)) \equiv \psi_m^j \quad (14)$$

is Sommerfeld's principle (in cylindrical co-ordinates)

$$\lim_{r_s \rightarrow \infty} \sqrt{r_s} \left[\frac{\partial \psi_m^j}{\partial r_s} + i \psi_m^j \right] = 0, \quad (15)$$

where ψ_m is the general wave number, being expressed by the formula

$$\psi_m = [(\omega_m/c)^2 - k_m^2]^{1/2}, \quad [\psi_m] = L^{-1} \quad (16)$$

Obviously, when the domain considered includes the source of the φ_0 -field, the last condition will be satisfied by all potential (9).

3.3. What is Sought?

The incident wave is given. The dynamic loading of the structure and the structural motion are sought. Similarly, the following are sought: (i) the displacement of the vibration spectrum of the construction, (ii) the vibration spectra displacements of the structural components, (iii) the water damping (for all structure and for its components). Obviously, the multitude of all problems is almost innumerable.

4. SOLUTION

4.1. Spatial or Plane Problem?

It is better to decompose suddenly the problem as follows. Let the general velocity potential satisfying the acoustical equation be φ_m . Taking

$$\varphi_m = \mathcal{C}_m(s) X_m(x) T(t), \quad (17)$$

and satisfying the boundary conditions along the x -axis, one can transform into a two-dimensional one. The conditions (10) will be satisfied if

$$(k_m h) \cdot \text{th}(k_m h) = \omega_m^2 h / g \quad \text{or} \quad (k_m h) \cdot \text{th}(k_m h) = -\omega_m^2 h / g \quad (18)$$

In the present investigation only the first of the two conditions (18) is considered, taking

$$X_m = \cosh(k_m x) / \cosh(k_m h). \quad (19)$$

4.2. Plane Wave Decomposition

Let the incident field be represented by a system of plane acoustic waves with circular frequencies $\omega_m = 2\pi m / t^*$. Their propagation direction, as mentioned above, is inclined to the row axis (y-axis) at an angle θ . Then the incident field will be

$$\varphi_0 = \sum_{m=0}^{\infty} \varphi_{mo} = \sum_{m=0}^{\infty} (i\omega_m) \exp[i\psi_m r_s \cos(\theta_s - \theta)] \frac{\cosh(k_m x)}{\cosh(k_m h)} V_m(t),$$

$$V_m(t) = C_m(f) \exp(i\omega_m t), \quad \dot{V}_m(t) = i\omega_m \exp(i\omega_m t). \quad (20)$$

As is well known, the function $\exp[i\psi_m r_s \cos(\theta_s - \theta)]$ is representable as

$$\exp[i\psi_m r_s \cos(\theta_s - \theta)] = \sum_{n=0}^{\infty} \epsilon_n(i)^n J_n(\psi_m r_s) \cos n(\theta_s - \theta), \quad (21)$$

where $J_n(\psi_m r_s)$ is Bessel's function, order n , and $\epsilon_n = 1$ for $n=0$, and $\epsilon_n = 2$ for $n \neq 0$.

4.3. Scattered Field

As the function $(\cosh(k_m x) / \cosh(k_m h))$ is one and same for all stages of the solution, it can be removed from further consideration by taking the problem in its plane version. Then

$$\varphi_0(r, \theta, h) = \sum_{m=0}^{\infty} \sum_{n=0}^{\infty} \epsilon_n(i)^n C_m J_n(\psi_m r_s) \cos n(\theta_s - \theta) \dot{V}_m(t). \quad (22)$$

The scattered field must satisfy the acoustical equation, and it can be sought in the form

$$\varphi_{ms}^{(1)} = \sum_{n=0}^{\infty} \epsilon_n A_{mn}^{(1)} H_n^{(2)}(\psi_m r_s) \cos n(\theta_s - \theta) \dot{\tau}(t), \quad (23)$$

where $A_{mn}^{(1)}$ is an integration constant, and $H_n^{(2)}(\psi_m r_s)$ is Hankel's function of second kind and order n , $n=1, 2, \dots$. Namely this function satisfies the Sommerfeld's principle (15), i.e.

$$\lim_{r_s \rightarrow \infty} r_s \left\{ \frac{\partial}{\partial r_s} [H_n^{(2)}(\psi_m r_s) \exp(i\omega_m t)] + i\psi_m [H_n^{(2)}(\psi_m r_s) \exp(i\omega_m t)] \right\} = 0 \quad (24)$$

The unknown constant $A_{mn}^{(1)}$ can be determined from the boundary condition on the absolutely rigid surface of every pile-shell (e.g. the s th one).

$$[(\partial \varphi_{om} / \partial r_s) + (\partial \varphi_m^{(1)} / \partial r_s)]_{r_s=R} = 0. \quad (25)$$

Then

$$A_{mn}^{(1)*} = -(i)^n C_m J_n'(\psi_m R) / H_n^{(2)}(\psi_m R) \quad (26)$$

and the scattered field velocity potential becomes

$$\varphi_{ms}^{(1)} = \sum_{n=0}^{\infty} \epsilon_n \left[-(i)^n C_m \frac{J_n'(\psi_m R)}{H_n^{(2)}(\psi_m R)} \right] H_n^{(2)}(\psi_m r_s) \cos n(\theta_s - \theta) \dot{\tau}(t). \quad (27)$$

The asterisk in Eq(26) means that $A_{mn}^{(1)*}$ has been determined already. So the first approximation is over. After the incident wave passed, in the near vicinity of every pile the velocity potential must be

$$\varphi_{ms} = \varphi_{om} + \varphi_{ms}^{(1)}. \quad (28)$$

Of course, the real part Eq(28) should be taken.

4.4. Second Approximation

The scattered field (27) will propagate to the neighbouring piles, and reaching their rigid surfaces will give rise to a secondary scattering. Here the incident field will be

$$\varphi_{mj}^{(1)} = \sum_{n=0}^{\infty} \epsilon_n A_{mn}^{(1)*} H_n^{(2)}(\psi_m r_j) \cos n(\theta_s - \theta) \dot{\tau}_m(t) \quad (29)$$

Applying the summation formulas [26], one can rewrite this expression in the s th co-ordinate system, i.e.

$$\varphi_{m(j-s)}^{(1)} = \sum_{n=0}^{\infty} \epsilon_n \epsilon_{\lambda} A_{mn}^{(1)*} \left[\left(\mathcal{G}_{js}^{n\lambda} \right)_{\mu} \cos \lambda \theta_s - \left(\mathcal{G}_{js}^{n\lambda} \right)_{\mu} \sin \lambda \theta_s \right] J_{\lambda}(\psi_m r_s) \dot{\tau}_m(t) \quad (30)$$

where $\epsilon_{\lambda} = 1$ for $\lambda = 0$, and $\epsilon_{\lambda} = 2$ for $\lambda \neq 0$,

$$\left(\mathcal{G}_{js}^{n\lambda} \right)_{\mu} = H_{n-\lambda}^{(2)}(\psi_m a_{js}) \cos \beta_1 - (-1)^{\lambda+\mu} H_{n+\lambda}^{(2)}(\psi_m a_{js}) \cos \beta_2,$$

$$\left(\mathcal{G}_{js}^{n\lambda} \right)_{\mu} = H_{n-\lambda}^{(2)}(\psi_m a_{js}) \sin \beta_1 + (-1)^{\lambda+\mu} H_{n+\lambda}^{(2)}(\psi_m a_{js}) \sin \beta_2, \quad (31)$$

$$\mu = 1 \text{ or } 2, \quad \beta_1 = (n-\lambda)\theta, \quad \beta_2 = (n+\lambda)\theta, \quad a_{js} = |s-j|a$$

Let the secondary scattering field is

$$\varphi_{ms}^{(2)} = \sum_{\lambda=0}^{\infty} \epsilon_{\lambda} H_{\lambda}^{(2)}(\psi_m r_s) [A_{m\lambda}^{(2)} \cos \lambda \theta_s + B_{m\lambda}^{(2)} \sin \lambda \theta_s] \dot{T}(t). \quad (32)$$

Then, after the satisfaction of boundary condition (25) the constants

$$\begin{aligned} A_{m\lambda}^{(2)*} &= - \sum_{n=0}^{\infty} \epsilon_n A_{mn}^{(1)*} J_{\lambda}'(\psi_m R) \left(\mathcal{E}_{js}^{n\lambda} \right)_1 / \bar{H}_{\lambda}^{(2)}(\psi_m R), \\ B_{m\lambda}^{(2)*} &= \sum_{n=0}^{\infty} \epsilon_n A_{mn}^{(1)*} J_{\lambda}'(\psi_m R) \left(\mathcal{F}_{js}^{n\lambda} \right)_1 / \bar{H}_{\lambda}^{(2)}(\psi_m R), \end{aligned} \quad (33)$$

$$J_{\lambda}'(\psi_m R) = \psi_m^{-1} [\partial J_{\lambda}(\psi_m r_s) / \partial r_s]_{r_s=R},$$

$$\bar{H}_{\lambda}^{(2)}(\psi_m R) = \psi_m^{-1} [\partial H_{\lambda}^{(2)}(\psi_m r_s) / \partial r_s]_{r_s=R}$$

are obtained. $A_{mn}^{(1)*}$ can be substituted from Eq(26), yielding

$$\begin{aligned} A_{m\lambda}^{(2)*} &= \sum_{n=0}^{\infty} \epsilon_n (i)^n C_m \frac{J_n'(\psi_m R)}{H_n^{(2)}(\psi_m R)} \frac{J_{\lambda}'(\psi_m R)}{\bar{H}_{\lambda}^{(2)}(\psi_m R)} \left(\mathcal{E}_{js}^{n\lambda} \right)_1, \\ B_{m\lambda}^{(2)*} &= - \sum_{n=0}^{\infty} \epsilon_n (i)^n C_m \frac{J_n'(\psi_m R)}{H_n^{(2)}(\psi_m R)} \frac{J_{\lambda}'(\psi_m R)}{\bar{H}_{\lambda}^{(2)}(\psi_m R)} \left(\mathcal{F}_{js}^{n\lambda} \right)_1. \end{aligned} \quad (34)$$

4.5. The Third Approximation

The third approximation will be given by the chain of transforms

$$\begin{aligned} \varphi_{m(j+s)}^{(2)} &= \dot{T}(t) \sum_{\lambda=0}^{\infty} \sum_{v=0}^{\infty} \epsilon_{\lambda} \epsilon_v \left\{ A_{m\lambda}^{(2)*} \left[\left(\mathcal{E}_{js}^{\lambda v} \right) \cos v \theta_s - \left(\mathcal{F}_{js}^{\lambda v} \right) \sin v \theta_s \right] J_{\lambda}(\psi_m r_s) + \right. \\ &\quad \left. + B_{m\lambda}^{(2)*} \left[\left(\mathcal{E}_{js}^{\lambda v} \right) \sin v \theta_s + \left(\mathcal{F}_{js}^{\lambda v} \right) \cos v \theta_s \right] J_{\lambda}(\psi_m r_s) \right\}, \end{aligned} \quad (35)$$

$$\varphi_{ms}^{(3)} = \sum_{v=0}^{\infty} \epsilon_v H_v^{(2)}(\psi_m r_s) [A_{mv}^{(3)} \cos v \theta_s + B_{mv}^{(3)} \sin v \theta_s] \dot{T}(t), \quad (36)$$

$$A_{mv}^{(3)} = - \sum_{\lambda=0}^{\infty} \epsilon_{\lambda} [A_{m\lambda}^{(2)*} \left(\mathcal{E}_{js}^{\lambda v} \right)_1 + B_{m\lambda}^{(2)*} \left(\mathcal{F}_{js}^{\lambda v} \right)_2] J_{\lambda}'(\psi_m R) / \bar{H}_v^{(2)}(\psi_m R), \quad (37)$$

$$B_{mv}^{(3)} = \sum_{\lambda=0}^{\infty} \epsilon_{\lambda} [A_{m\lambda}^{(2)*} \left(\mathcal{F}_{js}^{\lambda v} \right)_1 - B_{m\lambda}^{(2)*} \left(\mathcal{E}_{js}^{\lambda v} \right)_2] J_{\lambda}'(\psi_m R) / \bar{H}_v^{(2)}(\psi_m R),$$

$$\begin{aligned} A_{mv}^{(3)} &= - \sum_{n=0}^{\infty} \sum_{\lambda=0}^{\infty} \epsilon_n \epsilon_{\lambda} (i)^n C_m \frac{J_n(n_m)}{H_n^{(2)}(n_m)} \frac{J_{\lambda}'(n_m)}{\bar{H}_{\lambda}^{(2)}(n_m)} \frac{J_v'(n_m)}{\bar{H}_v^{(2)}(n_m)} \times \\ &\quad \times \left[\left(\mathcal{E}_{js}^{n\lambda} \right)_1 \left(\mathcal{E}_{js}^{\lambda v} \right)_1 - \left(\mathcal{F}_{js}^{n\lambda} \right)_2 \left(\mathcal{F}_{js}^{\lambda v} \right)_2 \right], \end{aligned} \quad (38)$$

$$\begin{aligned} B_{mv}^{(3)} &= \sum_{n=0}^{\infty} \sum_{\lambda=0}^{\infty} \epsilon_n \epsilon_{\lambda} (i)^n C_m \frac{J_n(n_m)}{H_n^{(2)}(n_m)} \frac{J_{\lambda}'(n_m)}{\bar{H}_{\lambda}^{(2)}(n_m)} \frac{J_v'(n_m)}{\bar{H}_v^{(2)}(n_m)} \times \\ &\quad \times \left[\left(\mathcal{E}_{js}^{n\lambda} \right)_1 \left(\mathcal{F}_{js}^{\lambda v} \right)_1 + \left(\mathcal{F}_{js}^{n\lambda} \right)_2 \left(\mathcal{E}_{js}^{\lambda v} \right)_2 \right]. \end{aligned}$$

where $\epsilon_v = 1$ for $v=0$, and $\epsilon_v = 2$ for $v=0$, $n_m = \psi_m R$.

4.6. Convergence of the Method

The distributed loading along the x-axis of the shells may be calculated as follows:

$$F_{sm}(x) = - \int_0^{2\pi} p_{sm} \bar{n} R d\theta = p \int_0^{2\pi} \frac{\partial \psi_{sm}}{\partial t} \bar{n} R d\theta , \quad (39)$$

where \bar{n} is the unit normal vector to the surface of the column.

It is seen, from (27), (30), (38), that every new specification of the velocity potential ($\psi_{sm}^{(j)}$) differs from the previous one by a factor

$$[J'_v(n_m)/\bar{H}_v^{(2)}(n_m)] \left(\mathcal{E}_{js}^{\lambda v} \right)_u \text{ or } [J'_v(n_m)/\bar{H}_v^{(2)}(n_m)] \left(\mathcal{F}_{js}^{\lambda v} \right)_u . \quad (40)$$

It is proved [16], that for these factors

$$K_{js,1} = \left| \sum_{v=0}^{\infty} \left(\mathcal{E}_{js}^{\lambda v} \right)_u J'_v(n_m)/\bar{H}_v^{(2)}(n_m) \right| \approx u_{js}/(1-u_{js})^2 < 1, \quad u_{js} = \frac{R}{|j-s|a} , \quad (41)$$

$$K_{js,2} = \left| \sum_{v=0}^{\infty} \left(\mathcal{F}_{js}^{\lambda v} \right)_u J'_v(n_m)/\bar{H}_v^{(2)}(n_m) \right| \approx u_{js}/(1-u_{js})^2 < 1.$$

Such factors are obtained for every new specification of the forces along the x-axes of the shells. In this way, the force $F_{sm}^{(j)}(x)$ may be represented as

$$F_{sm}^{(j)}(x) \leq F_{sm}^{(1)}(x) + K_{sq}^2 + \dots + K_{sq}^{(j-1)} . \quad (42)$$

It is seen, that the procedure of calculation is convergent and it may be interrupted at every step with a given precision.

Of course, in order to account for the mutual influence of the shells, it is necessary to summarize all potentials (forces), due to the interaction between the shells and the waves, in the corresponding co-ordinate system of any one shell

$$F_{sm}^{(j)} = \sum_q F_{sm}^{(j)}_q \quad (43)$$

4.7. Elastic Motion

By wave forces the pile under consideration set in motion which in its turn radiates waves. This wave radiation carries away a momentum thus causing damping of the pile motion. It is important to estimate this damping force in comparison with the force emitted from neighbouring piles. It is not difficult to prove that in our case the force due to the emitted field is appreciably smaller than that due to the incident and scattered fields. Therefore, the damping force due to the neighbouring piles can be neglected.

The equilibrium equation for a beam element is

$$EI \frac{\partial^4 w_s}{\partial x^4} + M \frac{\partial^2 w_s}{\partial t^2} = F_{sm}(x, t) , \quad (44)$$

where E is the modulus of elasticity, I the moment of inertia of the cross section, and M the mass density per unit length; $w_s(x, t)$ are the transverse displacements. $F_{sm}(x, t)$ are the forces applied along the pile:

$$F_{sm}(x, t) = F_{sm}^r(x, t) + F_{sm}^f(x, t) , \quad (45)$$

where $F_{sm}^r(x, t)$ is the force obtained at the final approximation, $F_{sm}^f(x, t)$ the damping force (emitted from the s-th pile). The pile will vibrate in the direction of the wave propagation, and following [4] it can be calculated as

$$F_{sm}^f(x, t) = \rho c R \frac{\partial w_s}{\partial t} . \quad (46)$$

The corresponding initial and boundary conditions are added to Eq (44):

$$w_s(x,0)=0, \quad \partial w_s(x,0)/\partial t=0. \quad (47)$$

In this case the structural damping is neglected in order to estimate the maximum magnitude of $F_f^s(x,t)$. In the case where the structural damping has to be taken into account, Eq (44) turns into:

$$EI \frac{\partial^4 w_s}{\partial x^4} + M \frac{\partial^2 w_s}{\partial t^2} + \beta \frac{\partial w_s}{\partial t} = F_{sm}(x,t), \quad (48)$$

where β is the structural damping. As it is well known the structural damping and the water damping are additive.

5. EXAMPLE

The structure in Fig.1. has the following parameters: $R=1m$, $h=20m$, $a=10m$, the number of the piles is ten, $EI=1,57 \cdot 10^{10} \text{ Nm}^2$, $M=7863,4 \text{ kg/m}$. The time step is chosen to be $t=a/c$, $c=1500 \text{ m/s}$. The incident wave field is a single plane pressure wave of amplitude p_0 and frequency ω . Four examples are computed taking four single waves of frequencies $\omega=\pi; 1,2\pi; 1,5\pi; 2\pi$ and of the same amplitude p_0 . The angle θ is zero. The boundary conditions are

$$w'''(h,t)=0, \quad w'(h,t)=0; \quad w'(0,t)=0, \quad w(0,t)=0. \quad (49)$$

Table 1. The influence coefficients K_{sq}

ω	π	$1,2\pi$	$1,5\pi$
$K_{1,2}$	0,0742	0,0658	0,0448
$K_{1,4}$	0,0278	0,0243	0,0158
$K_{1,6}$	0,0171	0,0148	0,0094
$K_{1,8}$	0,0123	0,0107	0,0069
$K_{1,10}$	0,0096	0,0083	0,0053

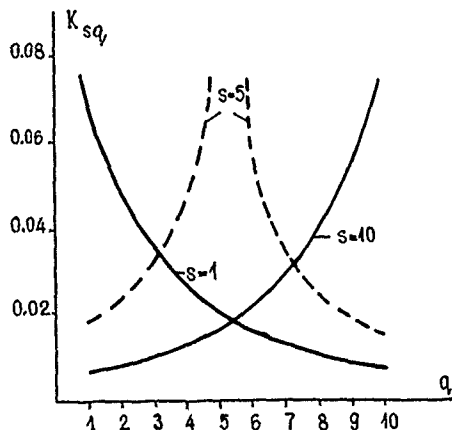


Fig.5. The influence coefficients

In Fig.5. and Table 1 are shown the influence coefficients K_{sq} as functions of the disposition of the piles and the frequency of the incident wave. The forces $F_r(h,t)$ and $F_f^s(h,t)$ are respectively shown in Fig.6. and Fig.7. The computational procedure is realized in FORTRAN-IV on HP-1000.

6. CONCLUSION

The demonstrated example shows that the coefficients K_{sq} are much less than 1 and that they strongly decrease with increasing frequency of the incident wave.

The results obtained show that the method is quickly converging and, in this case, two approximations are quite enough to obtain satisfactory solution.

The force F_f^s is much smaller than the force F_r because the

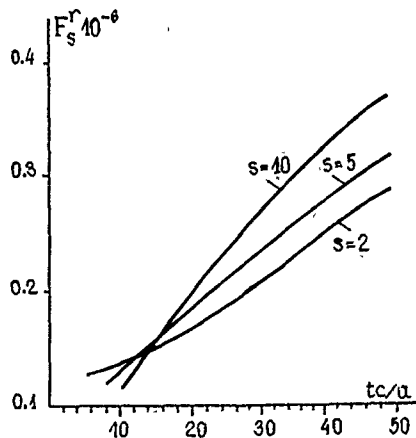


Fig.6. The forces $F_s^r(h, t)$ due to the incident and scattered field

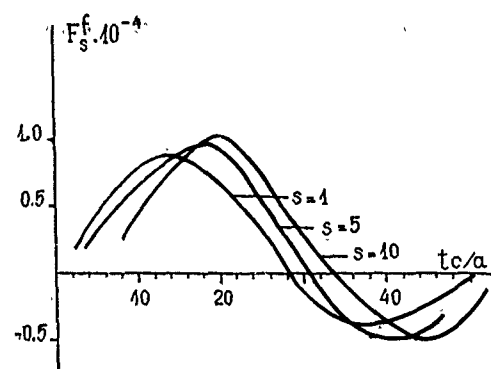


Fig.7. The forces $F_s^f(h, t)$ due to the emitting field.

last includes the incident field. F_s^f is comparable with the forces due to some of the scattered fields F_s^m /Table 1/.

REFERENCES

1. Ishkov, P.K., "Determination of the In-Liquid Vibration Frequencies of Compliant Piles", PMM, Vol.1, 1937 (Moscow, USSR).
2. Morrison, J.R., "The Force Exerted by Surface Waves on Poles" Petroleum Transactions American Institute of Mining Engineers, Vol. 189, 1959, pp. 145-154.
3. Haskind, M.D., "Diffraction of Moving Waves around Vertical Barrier in Heavy Liquid", Izvestia AN SSSR, OTM, N8, 1957 (Translation of Ac. Sci. of USSR, Division of Technical Sciences, N8, 1957).
4. Mindlin, R.D., and Bleich, H.H., "Response of an Elastic Cylindrical Shell to a Transverse Step Shock Wave", J. Appl. Mech., 20, N2, 1953.
5. Sheinin, I.S., "Vibration of Hydraulic Structures in Liquid", Hand book on Dynamics of Hydraulic Structures, Pt.1, Leningrad, Energia, 1967.
6. Dzhupanov, V.A., "Dynamical Interaction of Groups of Vertical Cylindrical Shells with Liquid" (Doctoral Thesis), Moscow, 1969.
7. Wiegel, R.L., "Ocean Wave Spectra, Eddies, and Structural Response", Paper F-1 in [22], pp. 531-586.
8. Borgman, L.E., "Ocean Wave Simulation for Engineering Design" Journal of Water Waves and Harbors Division, ASCE, Vol.1 95, N WW4, Nov. 1969, pp. 557-583.
9. Dzhupanov, V.A., "On the Analysis of the Dynamic Interaction of Circular Cylindrical Shell with Liquid", Theor. and Appl. Mech., Bulg. Ac. of Sci., Vol.2 (1971), N3.
10. Dzhupanov, V.A., "On the Problem of a Dynamical Interaction of Two Roundcylindrical Shells with Compressible Liquid", Theor. and Appl. Mech., Bulg. Ac. of Sci., Sofia, Vol.5 (1974), N1.
11. Dzhupanov, V.A., "An External Hydroelastic Problem of Two Circular Cylindrical Supports", Paper F-5 in [22], pp. 622-630.
12. Dzhupanov, V.A., "Hydroelastic Interaction of Two Bars", Mathematica Balkanica, 4.28 (Beograd, 1974), pp. 159-172.
13. Dzhupanov, V.A., "In-Liquid Vibration of Infinite Row of Compliant Piles", II National Acoustical Conference, 1975, Varna, Bulgaria.
14. Dzhupanov, V.A., "On the problem of the Transient Post-Failure Pressure Waves", B.N.E.S. Vibration in Nuclear Plant, May

1978, Keswick, U.K.

15. Dzhupanov, V.A., "Transient Wave Diffraction on Rows of Compliant Cylinders" (Unpublished, 1981).
16. Dzhupanov, V.A., and Karagözova D.D., "Dynamical Interaction between Liquid and a Semi-Infinite Equidistant Row of Cylindrical Shells", Theor. and Appl. Mech., Bulg. Ac. of Sci., Sofia, Vol. 14 (1983) N 3.
17. Dzhupanov, V.A., and Karagözova, D.D., "Quantitive Estimation of the Mutual Influence of the Shells in a Semi-Infinite Equidistant Row trough Acoustical Liquid", Theor. and Appl. Mech., Bulg. Ac. of Sci., Sofia, Vol. 14 (1983), N 3.
18. Kulmatch, P.P., "In-Liquid Vibration of Elastic Cylindrical Piles", Izvestia VNIIG, Vol. 79, 1965 (Leningrad, USSR).
19. Wootton, L.R., "Dynamics of offshore Structures: Problems, Solutions, and Benefits", Paper E-1 in [23], pp. 555-557.
20. Shaw, T.L., "Wave-Induced Vibration of offshore Structures", Paper E-2 in [23], pp. 558-569.
21. Plate, E., "Marine Structures", Paper in [22], pp. 528-530.
22. Naudascher, E. (Editor), "Flow-Induced Vibration", Proceedings of IAHR-IVTAM Symposium, Karlsruhe, 1972, BRG, Springer - Verlag; Berlin, Heidelberg-New-York, 1974.
23. Naudascher, E., and Rockwell D., (Eds), "Proceedings of IAHR-UTAM Symposium", Karlsruhe, 1979, BRG, Springer-Verlag; Berlin, Heidelberg - New-York, 1980.
24. Brebbia, C.A., and Walker, S., "Dynamic Analysis of offshore Structures", Newnes-Butterworths, 1979.
25. Skudzik, E., "The Foundation of Acoustics", Vol. 1, Moscow, 1976.
26. Dzhupanov, V.A., "On the Summation Formulas of the Bessel's Functions", Technicheska Misal (Technical Reflection), Bulg. Ac. of Sci., Vol. 9 (1972), N 2.